Coded-OFDM for PLC Systems in Non-Gaussian Noise Channels

Ghanim A. Al-Rubaye

Newcastle University

Newcastle upon Tyne, UK.

A thesis submitted for the degree of

Doctor of Philosophy

September 2017

To the Messenger of Allah (Mohammed) the praying and peace upon him. Also, I dedicate this thesis to my precious wife, children and brothers who have supported me throughout the years of my study, especially in the years that I was working on this thesis. With all my love.

Declaration

NEWCASTLE UNIVERSITY

SCHOOL OF ELECTRICAL AND ELECTRONIC ENGINEERING

I, Ghanim A. Al-Rubaye, declare that this thesis is my own work and it has not been previously submitted, either by me or by anyone else, for a degree or diploma at any educational institute, school or university. To the best of my knowledge, this thesis does not contain any previously published work, except where another persons work used has been cited and included in the list of references.

Signature:

Student: Ghanim A. Al-Rubaye

Date:

SUPERVISOR'S CERTIFICATE

This is to certify that the entitled thesis "Coded-OFDM for PLC Systems in Non-Gaussian Noise Channels" has been prepared under my supervision at the school of Electrical and Electronic Engineering / Newcastle University for the degree of PhD in Electrical Engineering.

Signature:

Supervisor: Dr. Charalampos Tsimenidis

Date:

Signature:

Student: Ghanim A. Al-Rubaye

Date:

Acknowledgements

First of all, thanks are due to the Almighty God for giving me the strength and patience to complete my studies and write this dissertation.

It is a pleasure to thank those who made this thesis possible. I would like to express my special appreciation and thanks to my first supervisor, Dr. Charalampos Tsimenidis, for the continuous support of my PhD study and research, for his patience, motivation, enthusiasm and his knowledge and priceless advice has largely contributed for focusing my research towards my goal. His guidance helped me throughout the research and writing of this thesis.

I would like to thank my second supervisor Dr. Martin Johnston whose always encouraged me to work in new areas, his guidance and his support from the initial to the final level to develop the subject.

Lastly, I would like to express my sincere gratitude to my sponsor the Ministry of Higher Education in Iraq who have given me the opportunity of an education at the best universities in the UK.

Abstract

Nowadays, power line communication (PLC) is a technology that uses the power line grid for communication purposes along with transmitting electrical energy, for providing broadband services to homes and offices such as high-speed data, audio, video and multimedia applications. The advantages of this technology are to eliminate the need for new wiring and AC outlet plugs by using an existing infrastructure, ease of installation and reduction of the network deployment cost. However, the power line grid is originally designed for the transmission of the electric power at low frequencies; i.e. 50/60 Hz. Therefore, the PLC channel appears as a harsh medium for low-power high-frequency communication signals. The development of PLC systems for providing high-speed communication needs precise knowledge of the channel characteristics such as the attenuation, non-Gaussian noise and selective fading. Non-Gaussian noise in PLC channels can classify into Nakagami-m background interference (BI) noise and asynchronous impulsive noise (IN) modelled by a Bernoulli-Gaussian mixture (BGM) model or Middleton class A (MCA) model. Besides the effects of the multipath PLC channel, asynchronous impulsive noise is the main reason causing performance degradation in PLC channels.

Binary/non-binary low-density parity check B/NB-(LDPC) codes and turbo codes (TC) with soft iterative decoders have been proposed for Orthogonal Frequency Division Multiplexing (OFDM) system to improve the bit error rate (BER) performance degradation by exploiting frequency diversity. The performances are investigated utilizing high-order quadrature amplitude modulation (QAM) in the presence of non-Gaussian noise over multipath broadband power-line communication (BB-PLC) channels. OFDM usually spreads the effect of IN over multiple sub-carriers after discrete Fourier transform (DFT) operation at the receiver, hence, it requires only a simple single-tap zero forcing (ZF) equalizer at the receiver.

The thesis focuses on improving the performance of iterative decoders by deriving the effective, complex-valued, ratio distributions of the noise samples at the zero-forcing (ZF) equalizer output considering the frequency-selective multipath PLCs,

background interference noise and impulsive noise, and utilizing the outcome for computing the *apriori* log likelihood ratios (LLRs) required for soft decoding algorithms.

On the other hand, Physical-Layer Network Coding (PLNC) is introduced to help the PLC system to extend the range of operation for exchanging information between two users (devices) using an intermediate relay (hub) node in two-time slots in the presence of non-Gaussian noise over multipath PLC channels. A novel detection scheme is proposed to transform the transmit signal constellation based on the frequency-domain channel coefficients to optimize detection at the relay node with newly derived noise PDF at the relay and end nodes. Additionally, conditions for optimum detection utilizing a high-order constellation are derived. The closed-form expressions of the BER and average BER upper-bound (AUB) are derived for a point-to-point system, and for a PLNC system at the end node to relay, relay to end node and at the end-to-end nodes. Moreover, the convergence behaviour of iterative decoders is evaluated using EXtrinsic Information Transfer (EXIT) chart analysis and upper bound analyses. Furthermore, an optimization of the threshold determination for clipping and blanking impulsive noise mitigation methods are derived. The proposed systems are compared in performance using simulation in MATLAB and analytical methods.

Contents

List of Figures

List of Tables

Nomenclature

ADSL Asynchronous digital subscriber line

AF Amplify and Forward

AMM Automated Meter Management

AMR Automated Meter Reading

APP A *posteriori* probability

AUB Average upper bound

AUBs Average upper bounds

AWGN Additive White Gaussian Noise

BB Broad-Band

BB-PLC Broad-Band Power Line Communication

BC Broadcast

BCJR Bahl, Cocke, Jelinek, and Raviv

BER Bit Error Rate. Probability of a data word being transmitted in error

BFA Bit-Flipping Algorithm

BGMIN Bernoulli-Gaussian Mixture Impulsive Noise

BI Background Interference

BPSK Binary Phase Shift Keying

BW Bandwidth

CBN Colored Background Noise

CDF Cumulative Distribution Function

CFR Channel Frequency Response

CIR Channel Impulse Response

CLT Central Limit Theorem

CND Check node decoder

VND Variable node decoder

CP Cyclic Prefix

CWEF Conditional Weight Enumerating Function

DAB Digital Audio Broadcasting

DF Decode and Forward

DFT Discrete Fourier Transform

DNF Denoise and Forward

DVB Digital Video Broadcasting

DVB-C2 Second Generation Digital Video Transmission over Cable

DVB-S2 Digital Video Broadcasting - Satellite - Second Generation

DVB-SH Digital Video Broadcasting - Satellite services to Handhelds

ED Euclidean distance

EXIT EXtrinsic Information Transfer

FEC Forward Error Correction

FR Frequency Response

HV High-voltage

ICI Inter-Carrier Interference

IDFT Inverse Discrete Fourier Transform

IFFT Inverse Fast Fourier Transform

IN Impulsive Noise

IR Irregular

IR-B-LDPC Irregular Binary Low Density Parity Check

IR-NB-LDPC Irregular Non-Binary Low Density Parity Check

IRWEF Input Redundancy Weight Enumerating Function

ISI Inter-symbol Interference

LAN Local Area Network

LBL Link-By-Link

LF Low Frequency

LLR Log-Likelihood Ratio

LV Low-voltage

MA Multiple Access

Max-Log-MAP Maximum-Log-Maximum A Posteriori

MCAIN Middleton Class A Impulsive Noise

MCM Multi-Carrier Modulation

MF Medium Frequency

ML Maximum Likelihood

MPA Message Passing Algorithm

M-PAM M-ary Pulse Amplitude Modulation

M-QAM M-ary Quadrature Amplitude Modulation

MSE Mean Squared Error

MV Medium-voltage

NB Narrow-Band

NBN Narrow-Band Noise

NB-PLC Narrow-Band Power Line Communication

NGN Non-Gaussian Noise

NGNs Non-Gaussian Noises

NRC Non-Recursive Convolutional

OFDM Orthogonal Frequency Division Multiplexing

PCCC Parallel Concatenated Convolutional Code

PDF Probability Density Function

PEG Progressive Edge-Growth

PEP Pairwise Error Probability

PL Power-Line

PLC Power-Line Communication

PLNC Physical Layer Network Coding

PSD Power Spectral Density

QPSK Quadrature Phase Shift Keying

R-B-LDPC Regular Binary Low Density Parity Check

RSC Recursive Systematic Convolutional

RVs Random Variables

SC Single-Carrier

SER Symbol Error Rate

SIF Soft Information Forwarding

SINR Signal-to-Impulsive-Noise Ratio

SLF Super Low Frequency

SL-FFT Signed Log Fast Fourier Transform

SNR Signal-to-Noise Ratio

SPA Sum Product algorithm

TC Turbo Code

TCs Turbo Codes

ULF Ultra Low Frequency

UNB Ultra Narrow-Band

VLF Very Low Frequency

VND Variable Node Decoder

ZF Zero Forcing

Notations

$_1F_1(a;b;z)$ Confluent hypergeometric function

$_2F_1(a;b;c;z)$ Gauss hypergeometric function

A Impulsive index

a_0, a_1 Attenuation parameters

$\tilde{b}_n$ Envelope of the BI noise in the time-domain

$\mathcal{C}_0$ Speed of the light in the vacuum

C_P Cyclic prefix

$\mathbf{c}$ Codeword

C_k^{ZF} Complex-valued of the ZF equalizer

$\mathbf{d}$ Information bits

d_i Length of path i

d_c Cheak node degree

d_v Variable node degree

E_b Energy per transmitted bit

erfc Complementary error function

$\mathbb{F}_q$ Fields of q

$F_{q,k}^a$ LLR of symbol a over fields q for NB-LDPC code

$\mathbf{G}$ Generator matrix

g_i Weighting factor of path i

g_n Complex white Gaussian process with mean zero

$\mathbf{H}$ Sparse parity-check matrix

$I_{A,VND}/I_{A,CND}$ a priori information coming out from VND/CND

$\mathrm{I_{E_1}}/\mathrm{I_{E_2}}$ $extrinsic$ output of the first/second decoder is used as *a priori* input to $\mathrm{I_{A_2}}/\mathrm{I_{A_1}}$ of the second/first decoder

$\mathrm{I_{E_2}}/\mathrm{I_{E_1}}$ $extrinsic$ output of the second/first decoder is used as *a priori* input to $\mathrm{I_{A_1}}/\mathrm{I_{A_2}}$ of the first/second decoder

$H_{A\to R}(k), H_{B\to R}(k)$ The complex-valued channel coefficients in the frequency domain from A to R and from B to R, respectively

H_k Channel transfer function for the k-th sub-carrier

$I(X,Y)$ Mutual information

$I_{E,VND}/I_{E,CND}$ *extrinsic* information coming out from $\mathrm{VND}/\mathrm{CND}$

$i.i.d.$ Independent and identically distributed

i_n Impulsive noise sample

$k \in [0.5, 1]$ Exponent of the attenuation factor

k_c Information length of the code

$K_0(\cdot)$ Modified Bessel function of the second kind of order zero

$K_1(\cdot)$ Modified Bessel function of the second kind of order one

L Channel length

m Nakagami-m parameter

N Number of sub-carriers

n_c Codeword length

R Relay

R_c Coding rate

r_c Redundancy bits

$r = \{\Re, \Im\}$ Real and imaginary components, respectively

τ_i Propagation delay of path i

T_b	Blanking threshold
T_c	Clipping Threshold
v_p	Propagation velocity
w_c	Column weight
w_r	Row weight
W_R	Complex additive white Gaussian noise at the Relay
W_D	Complex additive white Gaussian noise at the end nodes
X_k	Modulated symbols
x_n	Complex base-band OFDM signal in the time domain
$Y_D(t_2, k)$	Received signal in the frequency domain at the end nodes A and B
Y_k	Received signal in the frequency domain
$\hat{Y}_k$	Complex-valued equalized received signal
Z_k	Complex-valued equalized non-Gaussian noise samples
α	Probability of impulsive occurrence for the BGMIN model
ℓ	Number of impulsive noise sources
$\Gamma(\cdot)$	Gamma function
$\{h_i\}_{i=0}^{L-1}$	Coefficients of the discrete impulse response of the multipath PLC channel
κ_i	Fraction of check nodes
$L_{m,in}$	The m-th *priori* LLRs going into the VND
$L_{n,out}$	The n-th *extrinsic* LLRs coming out of the VND
Λ_k	Total non-Gaussian noise samples in the frequency domain
$\lambda_n^{\Im}$	Imaginary component of non-Gaussian noise in the time-domain
$\lambda_n^{\Re}$	Real component of non-Gaussian noise in the time-domain
$\mathbb{E}\{\cdot\}$	Expectation of a random process

$\mathcal{M}_n$ Set of checks connected to the coded bit

$\mathcal{M}_n \backslash m$ Set of $\mathcal{M}_n$ except the check bit m

$\mathcal{N}(\cdot)$ Gaussian density

$\mathcal{N}_m$ Set of coded bits connected to parity check

$\mathcal{N}_m \backslash m$ Set of $\mathcal{N}_m$ except the coded bit n

μ_A Mean value of MCAIN model

μ_a Mean value of the channel LLR values

μs Microseconds

ms Milliseconds

ν_i Fraction of variables nodes

Ω Mean power of the random variable $\tilde{b}_n$

ϕ_{H_k} Phase of the modified power line communication channel

ρ Gaussian-to-Impulsive Noise Power Ratio (GINPR)

σ_A^2 Variance of MCAIN model

σ_a^2 Variance of the $a\ priori$ LLRs

σ_b^2 Variance of background noise

σ_{ch}^2 Variance of the channel

σ_N^2 Variance of BGMIN model

σ_w^2 Gaussian noise power

σ_β^2 Variance of non-Gaussian noise

σ_ℓ^2 Noise power associated with the simultaneous emission from ℓ noise sources

σ^2 Total noise power

τ_i Propagation delay of path i

θ_n Phase of the BI

$\tilde{\rho}$ Impulsive-to-Gaussian Noise Power Ratio (IGNPR)

ε_r Dielectric constant for isolation material

$|H_k|$ Magnitude of the modified PLC channel

$\max(x, y)$ Maximum between x and y

$Q(\cdot)$ Q function

$T_{ML}^{opt.}$ Optimal maximum likelihood threshold

$P_b(R)$ Bit error rate for the relay node

$P_b(D)$ Bit error rate for the end node A or B

$P_b(E2E - D)$ End to end bit error rate at the end node A or B

$P_b(E2E)$ Average end to end bit error rate

Chapter 1

Introduction

Recently, high-speed broadband communications on the existing Power-Line (PL) grid have received a great amount of interest from both academia and industry. The greatest advantage of Power Line Communication (PLC) is the existing power grid network infrastructures which can significantly reduce the cost required for the installation of new infrastructure to the system and leads to deployment costs similar to wireless communication. PLC technology is very important for high-speed transmissions such as broadband Internet access, audio and video applications. PLC can be divided into Narrow-Band (NB) and Broad-Band (BB). Narrow-Band PLC (NB-PLC) utilizes the frequency band 3-500 kHz and achieves a theoretical bit rate of up to 2 Megabits per second (Mbps). It has been extensively employed for smart metering around the world for low and medium voltage distribution networks such as Automated Meter Reading (AMR) and Automated Meter Management (AMM). On the other hand, the Broad-Band PLC (BB-PLC) utilizes the frequency Bandwidth (BW) 0.5-34 MHz to achieve a theoretical bit rate of up to 200 Mbits/s [1]. It is exploited by utilizing low-voltage (LV) distribution networks such as a Local Area Network (LAN). However, high-speed data communications over PLC channels are feasible and a series of more recent standards such as HomePlug AV series, IEEE 1901 and ITU-T G.hn for BB-PLC applications and IEEE 1901.2 and ITU-T G.hnem have emerged for NB-PLC applications.

1.1 Motivation and Challenges

The PL grid is different to other conventional wired communication channels such as coaxial, fibre-optic or twisted-pair cables. It was originally designed for the transmission of electric power at low frequencies, i.e. 50/60 Hz. Hence, it has hostile properties for low-power

high-speed communication signals due to the fluctuating nature of the PL environment, such as reflection points (multipath fading), attenuation and impulsive noise (IN), which may yield lower data throughput and high Bit Error Rate (BER) degradation. The channel attenuation is frequency-dependent which increases with frequency and distance. Moreover, several electromagnetic reflections are generated between the channel and the connected electrical appliances giving rise to multipath fading.

The noise at any power outlet in PLC is a mixture of coloured noise, narrowband noise and IN, representing the sum of Non-Gaussian Noises (NGNs) that are either connected or in closeness to the PLC transmission medium. The experimental results in the frequency band 1-30 MHz, show that the envelope of the background noise in PLC channels in the time-domain follows the Nakagami-m distribution [2, 3]. Several known models have been proposed to model the impulsive noise, such as the Middleton Class A, B, C, Bernoulli-Gaussian mixture model and symmetric alpha stable models [4–7]. The Middleton Class A impulsive noise (MCAIN) model and it is simplified version, Bernoulli-Gaussian Mixture Impulsive Noise (BGMIN) model, are accurate models used to model the thermal background noise and impulsive noise in PLC channels. The IN represents the main challenge for PLC that causes degradation in the BER performance of the system. The IN is generally the result of switching transients in power appliances for short durations of some microseconds up to a few milliseconds with random occurrences and high amplitudes. The Power Spectral Density (PSD) of IN exceeds the PSD of the background noise by 10-15 dB and may reach up to 50 dB, and may cause bit or burst errors especially in BB data transmissions. The presence of an individual or combined non-Gaussian noise (NGN) can severely degrade the communication over a PLC system since many decoders assume the noise is Gaussian.

Forward Error Correcting (FEC) codes such as Binary-Low Density Parity Check (B-LDPC) codes, Non Binary-Low Density Parity Check (NB-LDPC) codes and Turbo Codes (TCs) with iterative soft decoding algorithms can achieve a performance close to the Shannon limit capacity on the AWGN channel. Therefore, in this thesis, these codes have been proposed to address the challenges of PLC channels and to resist the channel impairments due to NGN. Many decoders assume the noise has a Gaussian distribution at the equalizer output for the log-likelihood ratio LLR computations, however, LLR computations are highly sensitive to the effective noise samples distribution in the frequency domain at the equalizer output. For example, the BER performance of the Coded OFDM (COFDM) system utilizing LLRs computed from a Gaussian noise distribution degrades quickly in the presence of NGN. The optimal LLR computations have not been computed in closed-form for COFDM systems and COFDM-PLNC systems at

the equalizer output over PLC channels contaminated by NGN in the literature. Due to these adverse effects, researchers only recently considered the PL grid as a medium for communication. Hence, the first motivation in this thesis is the BER analysis for OFDM systems over PLC channels in the presence of NGN based on optimal noise distributions at the Zero-Forcing (ZF) equalizer output. Moreover, it motivates us to examine the performance of different FEC codes for COFDM systems over PLC channel contaminated by different scenarios of NGN with LLRs computed based on optimal noise distribution. In addition to motivate the convergence behaviour using EXtrinsic Information Transfer (EXIT) chart analysis for a given E_b/N_0 value based on derived distributions and the Average Upper Bound (AUB).

Physical Layer Network Coding (PLNC) can be used to exchange information between two users (devices) using an intermediate relay (hub) node in two-time slots. To the best of our knowledge, there is no research on FEC for COFDM-PLNC over PLC channels in the presence of NGN with optimal LLR computations from optimal derived noise distributions at the equalizer output. The derived noise distributions are obtained for a new mapping method at the relay node and at the end nodes. It can improve the performance of the FEC codes applied to the end nodes as well as at the relay node to perform link-by-link (LBL) COFDM-PLNC system by computing optimum LLR values. Hence, it motivates us to examine the performance of B/NB-LDPC and TC codes for COFDM-PLNC systems over PLC channels in the presence of NGN by utilizing the derived PDFs at the relay node and Broadcast (BC) nodes with analysis and evaluation of End-to-End (E2E)-BER and E2E-AUB.

Furthermore, the conventional receiver utilizes non-linear IN mitigation techniques in the time domain to zero and/or clip the incoming samples when exceeding a certain threshold value at the receiver. This motivates us to examine the performance of conventional COFDM system and COFDM-PLNC systems by optimizing the threshold for clipping and blanking techniques with the help of a maximum likelihood (ML) detector based on derived PDFs.

1.2 Aim and Objectives

The research aim of this thesis is to improve the performance of COFDM communication systems and COFDM-PLNC communication systems over multipath PLC channels. The BER performances of both systems are analysed and evaluated in the presence of background noise and impulsive noise utilizing high order M-ary Quadrature Amplitude Modulation (M-QAM). The research chapters of this thesis are organized as follows

- Chapter 2: originally PLs were not designed for the purpose of high-speed data transmission like other wired communication such as coaxial cables and fibre optics. This chapter presents a brief literature survey on the PLC channels, structures and physical properties with suitable multipath channel model, as well as their advantages and disadvantages, background noise model and impulsive noise models over PLC channels. This chapter also describes orthogonal frequency division multiplexing (OFDM) as a modulation technique for high-speed data transmission over PLC channels and finally, the IN mitigation methods in the time domain such as clipping, blanking and combined clipping blanking method in additional to coding methods are presented in this chapter.

- Chapter 3: presents an introduction to different forward error correcting codes such as B-LDPC codes with the iterative Sum-Product decoding Algorithm (SPA), NB-LDPC codes with iterative Signed-Log Fast Fourier Transform (SL-FFT) decoding algorithm and binary TC with iterative Max-Log Maximum A Posteriori (Max-Log-MAP) decoding algorithm. In addition to discuss the EXIT chart analyses for B-LDPC code and TC in addition to AUB computation for TC are discussed. This chapter also considers a two-time slot PLNC system to exchange the information between two end nodes through a relay node when no direct link is present.

- Chapter 4: focuses on the analysis and evaluation of the BER performance for an uncoded OFDM (UOFDM) system. The effective noise distributions have been derived at the Zero Forcing (ZF) equalizer output over the PLC channel in the presence of different scenarios of individual and the combination of Nakagami-m BI noise and IN modelled either by MCAIN model or BGMIN model. Moreover, to examine the performance of the derived receivers, the ML detectors (optimal detectors) with BER computation and thresholds optimization have been derived in the presence of different scenarios of NGN based on the derived distributions and compared to sub-optimal detectors.

- Chapter 5: the main goal of this chapter is to improve the BER performance of the B/NB-LDPC codes and TCs for COFDM system by computing optimal log-likelihood ratios (LLRs) that are used as input for iterative decoders. The optimal LLRs are computed for two different scenarios. The first scenario has been computed by utilizing the distribution of the received signal at the OFDM modulator output based on Euclidean Distance (ED), while the second scenario is based on the derived complex-valued ratio distributions of the noise samples at the ZF equalizer output from Chapter 4. In addition, an analysis and

evaluation of the iterative receivers by using EXIT chart and AUBs are presented.

- Chapter 6: this chapter provides the analysis and simulation results of the BER for B/NB-LDPC and TC for the coded-OFDM-PLNC system over PLC channels in the presence of different scenarios of NGN. All systems utilize the LLRs at the relay node computed from the new derived noise PDF based on a novel mapping method at the relay and utilize LLRs at the BC nodes computed in Chapter 5. Moreover, the E2E-BER, E2E-AUB and thresholds optimization have been derived in the presence of different scenarios of NGN.

- Chapter 7: this chapter concludes the important findings in this thesis with new research directions for future work.

1.3 Novel Contributions of the Thesis

This thesis is based on a number of related publications in addition to unpublished material. It is focused on the performance analysis and evaluation of UOFDM systems, COFDM systems and COFDM-PLNC systems. The novel contributions in this research over PLC channels with NGN are listed as follows

- In Chapter 4, the effective complex-valued ratio distributions of the noise samples at the zero-forcing (ZF) equalizer output, considering both frequency-selective multipath PLCs and NGN are derived for the MCAIN model, BGMIN model, Nakagami-m BI noise, combined BI noise and MCAIN and finally for combined BI noise and BGMIN. Moreover, the condition for optimum ML detectors and exact BER are derived based on the derived PDFs utilizing high order M-QAM constellation. The performance of the OFDM system over PLC channels in the presence of different scenarios of NGN have been examined based on derived PDFs. The derived receivers performances are compared against the conventional OFDM receiver that utilizes optimized thresholds for clipping or blanking non-linearity IN mitigation methods and LLRs computed from a Gaussian distribution (sub-optimal detector) for different scenarios of NGN.

- In Chapter 5, two methods are presented to compute the LLRs required for soft decoding in COFDM systems over PLC channel in the presence of different NGN scenarios. The first method is based on ED and the second one is based on the derived PDFs at the ZF equalizer output in Chapter 4. The computed LLR achieved significant improvement in BER performance for NB-LDPC code with SL-FFT decoding algorithm, B-LDPC code

with SPA and TC with Max-Log-MAP algorithm. The performance of the COFDM systems is demonstrated with optimal and sub-optimal receivers. The B-LDPC COFDM system utilizing the derived LLRs can increase the data throughput by 111 Mbps compared to the conventional B-LDPC COFDM system, while the NB-LDPC COFDM system utilizing the derived LLRs increased the data throughput by 963 Mbps compared to the conventional B-LDPC COFDM system. The EXIT chart analysis and the derived AUBs are also derived for PLC channel in the presence of different scenarios of individuals and combined BI noise and IN. It is demonstrated that the proposed approach requires fewer iterations for convergence and close to the AUB results compared to the conventional receiver.

- In Chapter 6, A novel detection scheme is introduced to transform the transmit signal constellation based on the frequency-domain channel coefficients. This mapping method is used to improve the performance of the COFDM-PLNC systems at the relay node and at the end nodes, respectively, on a LBL basis utilizing newly derived noise distribution at the relay node and the derived noise distributions at the end nodes in Chapter 4. Hence, the BER performance of COFDM-PLNC systems have been improved by computing optimal LLRs at the relay node and at the end nodes. Moreover, the general closed-form expressions of the BER at the relay, end nodes and E2E, E2E-AUB, thresholds optimization and ML detectors are also derived for the novel derived distribution over PLC channel in the presence of different scenarios of NGN.

1.4 Publications Related to the Thesis

1. G. A. Al-Rubaye and C. C. Tsimenidis and M. Johnston,"Non-binary LDPC coded OFDM in impulsive power line channels", 2015 23rd European Signal Processing Conference (EUSIPCO), IEEE, 2015, pp.1431-1435.

2. G. A. Al-Rubaye and C. C. Tsimenidis and M. Johnston,"Improved performance of TC-OFDM-PLNC for PLCs using exact derived impulsive noise PDFs", 2017 IEEE International Conference on Communications Workshops (ICC Workshops), IEEE, 2017, pp. 1271-1276.

3. G. A. Al-Rubaye and C. C. Tsimenidis and M. Johnston,"LDPC-COFDM for PLC in Non-Gaussian Noise Using LLRs Derived from Effective Noise PDFs", published in IET on commun., 10.1049/iet-com.2017.0265, https://doi.org/10.1049/iet-com.2017.0265, 2017.

4. G. A. Al-Rubaye and C. C. Tsimenidis and M. Johnston,“Average Upper Bounds for Turbo Coded OFDM for Power Line Communication in Non-Gaussian Noise”, Under review of IEEE Access.

Chapter 2

BB-PLC Channel Model and IN Cancellation for OFDM System

2.1 Introduction

Nowadays, the demand for broadband multimedia applications has been rising significantly due to broadband technology becoming more sophisticated. The Internet has become an indispensable part of our daily lives, especially for homes and businesses. The variety of technologies leads to a higher expectation of utilizing the PL grid as a new technology to provide the broadband Internet access from every socket in every room in the building.

PLC exploits the indoor electrical wiring as a LAN to deliver high-speed communications such as broadband Internet access, voice and video. However, the original purpose of PL channel is optimized for the transmission of high voltages at low frequencies, 50/60, Hz throughout the world. This technology acts as a harsh environment for high-speed communication at low voltage and high frequencies, which leads to unusual channel characteristics that affect the transmission performance and result in BER degradation due to frequency-dependent attenuation, multipath fading and impulsive noise. All the above factors make data transmission over such a medium a very difficult task. PLC differs from conventional wired communication such as coaxial, twisted-pair and fibre-optic cables. Therefore, it is important to deeply characterize the topology of a local electric power grid to combat the hostile transmission environment.

After the general introduction of PLC systems, this chapter focuses on the major features and characteristics of the PL as a communication medium. The multipath PL channel transfer function is modelled by the Zimmermann and Dostert model, whereas the noise is classified into two main noise classes: BI noise in which the envelope is modelled by Nakagami-m distribution

and the IN modelled as a Gaussian mixture model or Middleton's class A model. This chapter also presents IN mitigation techniques, namely clipping, blanking and clipping/blanking for OFDM systems.

2.2 Brief Historical Evolution of Communications over Power-Lines

With the advent of advanced technology, people require reliable high-speed data communication in-home and in-building. PLC is a technology offering telecommunication service delivery for the "last mile" access, that allows data transmission and electrical energy transmission over the public electric power distribution wiring, which can be used as a LAN, without requiring the installation of new infrastructure. PL technologies can be grouped into NB-PLC, which enables data transfer at NB speeds at frequencies below 500kHz, and BB-PLC, which enables data transfer at BB speeds at frequencies above 500 kHz [8] or above 1.8MHz [9].

Many efforts have been made to improve the performance and reliability in both BWs. As a result, the BB-PLC system can achieve a maximum speed of 200 Mbps for high-speed internet access applications [1, 10] compared to a maximum speed of 2 Mbps offered by the NB-PLC systems. As a result, the growing technology is evolving towards broadband local networks which will achieve higher data rates than the NB-PLC systems.

2.3 PLC Networks Characterization

PLC utilizes the electrical grid as a transmission medium and makes use of the existing wiring to transmit communication signals, delivering different broadband services. The fundamental purpose of PLC technology is to carry the communication signal along with the AC power signals. Typically AC power signals are at 60 Hz in North America and at 50 Hz in Europe and the rest of the world. There are different of challenges facing transmission of data through the PLC channel due to differing topology, structure and physical characteristics compared with traditional communication channels such as Ethernet cables and optical fibres. Hence, it is important to study the typical power supply topologies to check their viability as a high-speed communication medium for data transmission. The characteristics of PL cable based on the voltage levels is an important function for choosing the kind of communication technology that needs to be used. Generally, the AC power supply networks can be divided into three regions

based on voltage levels of networks supply [11–13]:

- The High-voltage (HV) networks utilize the voltage level 110-380 kilo-Volts (kV).
- The Medium-voltage (MV) networks utilize the voltage level 10-30 kV.
- The LV networks utilize the voltage level 110 V in USA and 230/400 V for the rest of the world.

The LV level is needed for transmission the communication signal.

2.4 Power Line Communication Standards

A series of standards have been developed by different industrial companies to help promote of the data communications over both BB-PLC and NB-PLC channels, which was proposed for different application scenarios. These technologies which are available nowadays can be divided into three classes of PLC technologies depending on the utilizing BW as [9, 12]

- Generally, Ultra Narrow-Band (UNB)-PLC technologies provides very low data rate ($\sim$ 100 bps) in the Ultra Low Frequency (ULF) from $0.3 - 3$ kHz band or in the upper part of the Super Low Frequency (SLF) $30 - 300$ Hz band.
- NB-PLC Technologies provides higher data rates for communication. The current NB solutions operating in the Very Low Frequency/Low Frequency/Medium Frequency (VLF/LF/MF) bands from $3 - 500$ kHz include the European Committee for Electro technical Standardization such as EN 50065 specifies a frequency band of $3 - 148.5$ kHz, the US FCC (Federal Communications Commission) utilize the band of $9 - 490$ kHz, the Japanese ARIB (Association of Radio Industries and Businesses) used the band of $10 - 450$ kHz, and the Chinese band of $3 - 500$ kHz for NB transmissions over PLs, and provides a data rates up to several kilo-bits per second only, which can be utilized for voice channels and power supply utilities [14].
- Evolution of the PLC systems standardization towards BB-PLC Technologies is started initially for internet access applications and then for LAN applications. It is operating in the High Frequency/ Very High Frequency (HF/VHF) bands of $1.8 - 250$ MHz for providing several Mbps to several hundred Mbps such as the TIA-1113 (HomePlug 1.0), IEEE 1901, ITU-T G.hn (G.9960/G.9961) recommendations, HomePlug AV 2.0, HomePlug Green PHY, UPA Powermax, and Giggle MediaXtreme [15–17].

BB-PLC usually used the frequency band of $1.8-250$ MHz for high-speed communications. Recently, the performance of many applications on BB-PLC that works in the frequency band up to 30 MHz has been investigated completely for channel modelling, channel environments, and network topology. Nowadays, the PLC channel has been modelled up to 100 MHz BW due to increase the demand for BB Internet access services in indoor buildings [18, 19]. Therefore, several techniques have been adopted as communication standards for BB-PLC such as IEEE P1901 [15,16,20], ETSI [21], ITU G.hn. [22] and HomePlug Powerline Alliance series [17,23].

2.5 Indoor PLC Networks Characterization

A simplified indoor PL network can be expressed by a number of branching points, with various multimedia terminal equipment which is usually connected directly to the PLC modem or by plugging into any indoor AC PL outlet. However, the Wireless Local Area Networks (WLAN) operates inside buildings to cover a small area in a "last mile" PLCs network [12]. While, in the second scenario, the indoor AC PL outlet can be used as a LAN, which matches the indoor PLC solution [12]. For this purpose, the PLC modem performs a coupling operation between the communication appliances and PL medium [13].

2.5.1 PLC Channel Description

The BB-PLCs use the existing electrical PL networks for communication purposes, which significantly differ in topology from conventional wired communication such as twisted pair, coaxial, fiber-optic cables [8]. It is a harsh and hostile medium for high-speed communication due to its fluctuating nature. The PLC channel suffers from frequency-dependent attenuation which increases with frequency and transmission distance. Moreover, the indoor PLC grid connects numerous appliances through AC outlets. Thus, the PLC impedance exhibits a highly time-varying feature due to changing the load which leads to impedance mismatches which leads to multipath fading. Furthermore, branches and line length in the in-house wiring usually lead to several electromagnetic reflections that result in multipath propagation scenario with frequency selectivity [24].

Additionally, some deep narrowband notches appear in the transfer function due to occurring frequency selective fading. The notches spread over the frequency band up to 30 MHz with phase non-linearities observed at those notches decreasing with respect to frequency. The characterization of the PL topology for typical channels can be found in the literature [8, 11, 24, 25].

Therefore, the changing of the transfer characteristics of PL channels can be assumed as quasi-stationary, due to the changes in the network topology and the connecting or switching of electrical devices that causes load changes [26].

2.5.2 Channel Modeling

The development of any communication system requires sufficient characteristics knowledge of the transmission medium. In general, the design of a reliable communication system requires an appropriate transmission technique based on the channel transfer properties and the capacity offered by the channel. This requires appropriate models that can adequately describe the transmission behavior over the communication channel. The PL system was not designed for high-speed data transmission, so modeling this channel is a complex task and constitutes one of the main technical challenges [27].

In addition, there are some other impairments that affect the transmission in PLC channels resulting in a significant degradation in transmission quality, such as complex distribution structures, background noise, impulsive noise, where attenuation increases with frequency and transmission distance, and finally the multipath propagation delay due to reflections from different load points. There are many models utilized to model the PLC channels such as the Zimmermann and Dostert model [8], Philipps model [26] and the Anatory model [28]. Also, many Rayleigh fading models have been proposed to model the PLC channel in the literature [19, 29, 30]. Between these models, Zimmerman's multipath model that utilizes to model the PLC channel is now a generally accepted model, and therefore adopted in this thesis.

2.5.2.1 Multipath Channel Model

In PL transmission, the data signals follow multipath (echoes) propagation caused by numerous mismatch joints of cables with different characteristic impedances [31,32]. Indeed, the received signal can be regarded as the sum of delayed and attenuated copies of the transmitted signal. The duplicates of the transmitted signal will cause deep nulls at some frequencies of the received signal due to the destructive interference between propagation paths from frequency selective fading.

The BB-PLC medium can be analyzed as a multipath channel model because of its specific topology as proposed in [31, 32]. The PLC has been studied in the Zimmermann and Dostert model [8] by utilizing a simple topology network consisting of only three segments as illustrated in Fig. 2.1.

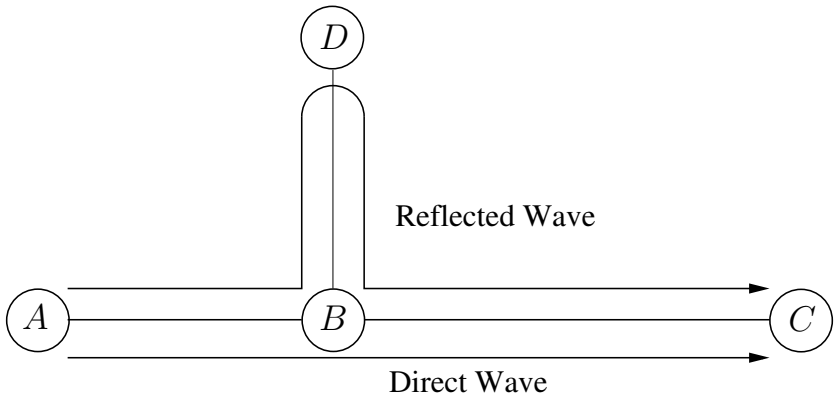

Figure 2.1: Multipath signal propagation for cable with one tap.

The information signal is supposed to be carried out from the transmitter in position A to the receiver in position C. In this case, an infinite number of reflections are caused by the joints which can be written as:

- Path 1: $A \rightarrow B \rightarrow C$
- Path 2: $A \rightarrow B \rightarrow D \rightarrow B \rightarrow C$
- Path 3: $A \rightarrow B \rightarrow D \rightarrow B \rightarrow D \rightarrow B \rightarrow C$
  $\vdots$
- Path N: $A \rightarrow B \rightarrow D \rightarrow B \rightarrow D \rightarrow \ldots \rightarrow C$

Zimmermann and Dostert [8] have been proposed a generalized multipath model describing a complex transfer function of a typical PLC channel exhibiting L paths using a limited set of parameters expressed as

$$H(f) = \sum_{i=1}^{L} \underbrace{g_i}_{\substack{\text{weighting} \\ \text{factor}}} \underbrace{e^{-(a_0+a_1 f^k)d_i}}_{\substack{\text{attenuation} \\ \text{portion}}} \underbrace{e^{-j2\pi f \frac{d_i}{v_p}}}_{\substack{\text{delay} \\ \text{portion}}}, \tag{2.1}$$

where $H(f)$ is the Channel Frequency Response (CFR), g_i is the weighting factor of path i which is assumed to be real-valued, a_0 and a_1 are the attenuation parameters, $k \in [0.5, 1]$ is the exponent of the attenuation factor, d_i is the length of path i and $\tau_i = \frac{d_i}{v_p} = \frac{d_i\sqrt{\varepsilon_r}}{\mathcal{C}_0}$ is the propagation delay of path i, where $v_p = 1.5 \times 10^8$ is the propagation velocity of the wave colorgreen along the PL cable, $\mathcal{C}_0$ is the speed of the light in the vacuum, and $\varepsilon_r = 4$ is the dielectric constant for isolation material. The attenuation actually corresponds to cable losses in the PLC network which increases with length and frequency of the cable. The model parameters

can be obtained by measurement fitting, as detailed in [8]. However, the BER and the received signal power at point C will depend on the number of propagation paths selected and also the path length.

The drawback of Zimmermann's multipath model appears when a large number of propagation paths are yielded. The Zimmermann model will need more calculations to estimate the gain, attenuation and delay of each path [33]. Therefore, many researchers have adopted this model in the research area with a small number of paths. Based on the measurement results, the Channel Impulse Response (CIR) of the PLC can be implemented as the sum of the reflections using an echo-based channel model expressed as

$$h(t) = \sum_{i=1}^{L} C_i \delta(t - \tau_i) \;\Leftrightarrow\; H(f) = \sum_{i=1}^{L} C_i e^{-j2\pi f \tau_i}, \tag{2.2}$$

where i is the path index, τ_i is the path delay and C_i is the attenuation path.

2.6 Noise in Power Line Communications

Besides the hostile environment of the PLC channel, the source of the noise can be classified as internal noise (inside the network) or external noise (outside the network). Overall, the additive noise in PLC channels is not white Gaussian noise as usually assumed for other communication systems. The additive noise is mostly dominated by NB interference and impulsive noise, which can be grouped according to their origins and their physical properties into five different classes, as follows [34, 35]:

- Colored background noise (CBN) (type 1): This type of noise is mainly caused by the addition of multiple noise sources with low PSD, varies with frequency and increases toward lower frequencies. Typically common household appliances such as lamps, heaters, light dimmers and microwave ovens can generate disturbances in the frequency range of up to 30 MHz. Even though it varies over time, it can be regarded as stationary since it varies very slowly over periods of minutes or even hours [2, 35, 36].

- Narrow band noise (type 2): this type of noise is generated from amplitude modulated signals or frequency modulated signals due to the interference of radio sources in the typical frequency band of 1-22 MHz [37]. The level of this type of noise varies very slowly over the day and becomes higher during the night [12]. The power levels of the

noise reach up to 30 dB greater than the background noise over frequencies greater than 1 MHz [38].

- Periodic impulse noise asynchronous to the main frequency (type 3): impulses noise are characterized by a lower repetition rate between 50 kHz and 200 kHz, generating an impulse spectrum spaced according to the repetition rate [13]. It can be considered as a part of the background noise and usually remains stationary over periods of seconds, minutes or hours. This type of noise is due to switching of the power supplies in various household appliances [12, 37].

- Periodic impulsive noise synchronous to the mains frequency (type 4): This noise originates from switching actions of rectifier diodes that are found in many electrical appliances connected to the power supplies and operating synchronously with the main frequency of 50/100 Hz in Europe and 60/120 Hz in the US. Its PSD decreases with the frequency. The repetition rate of this noise is 50 Hz or 100 Hz for a short time duration from 10-100 μs [12, 37].

- Asynchronous Impulsive Noise (type 5): It is caused by unpredictable switching transients that occur in different parts of the distribution network, which leads to the noise time duration from several microseconds (μs) up to several milliseconds (ms) [37]. This type of noise may occur either as random impulses or as bursts impulses with the PSD reaching values of up to 50 dB greater than the background noise.

The first three types of noise usually remain stationary over periods of seconds and minutes or sometimes an hour and can be regarded as a background noise. While the last two types of noise are time variant in terms of microseconds and milliseconds. Hence, the noise in a PLC is the sum of the background noise and impulsive noises from all neighbouring devices [39]. Therefore, the BER performance will be degraded during the occurrence of IN. The PSD of the IN has a perceptibly high amplitude and may cause bit or burst errors in data transmission [37]. The additive noise types in PLC environment are shown in Fig. 2.2

2.6.1 Background Interference Noise Model

The BI noise model in a PLC environment is considered as the sum of the CBN and the Narrow-Band Noise (NBN). The CBN is usually approximated by several Gaussian sources such as hair dryers, computers or dimmers, which is characterized by the PSD decreasing with increasing frequencies from 0-100 MHz. While the NBN can characterize by a very low PSD in the

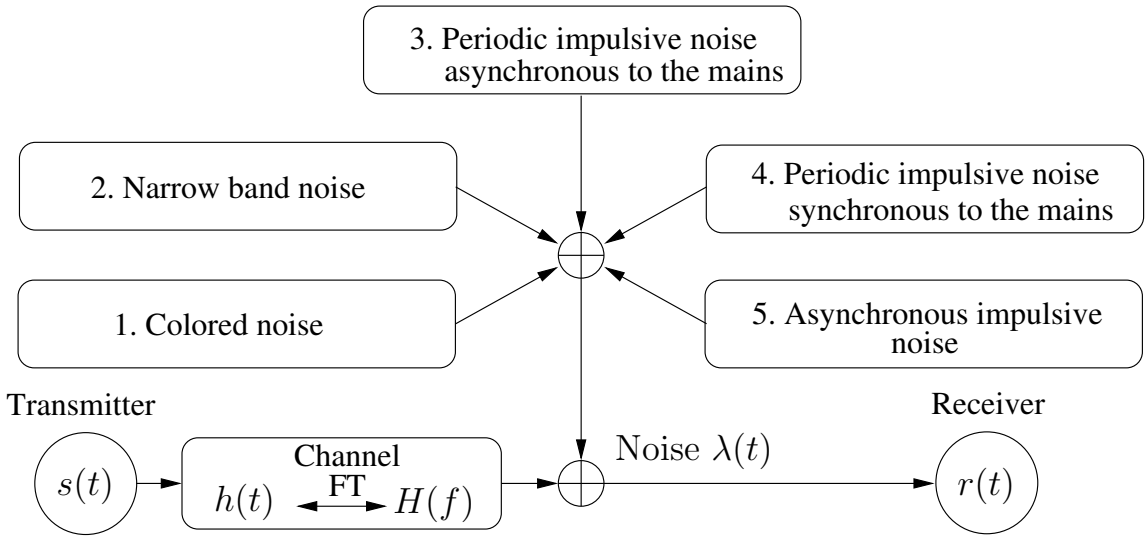

Figure 2.2: The types of additive noise in PLC environments.

same frequency band [40–42]. Several efforts have been made to characterize and model the individual and combined BI noise and IN noise over PLC channels. The experimental results in the frequency band 1-30 MHz [2, 3], shows the envelope of the BI noise,$\tilde{b}_n$, in PLC system in the time-domain can be modelled by Nakagami-m distribution expressed as [2, 3, 43]

$$p(\tilde{b}_n) = \frac{2}{\Gamma(m)} \left(\frac{m}{\Omega}\right)^m \tilde{b}_n^{2m-1} e^{\left(-\frac{m \times \tilde{b}_n^2}{\Omega}\right)}, \tag{2.3}$$

where n is the index of noise samples in the time domain, $\Gamma(\cdot)$ is the Gamma function and m is the Nakagami-m shaping parameter expressed as

$$m = \frac{\left(\mathbb{E}\{\tilde{b}_n^2\}\right)^2}{\mathbb{E}\{(\tilde{b}_n^2 - \mathbb{E}\{\tilde{b}_n^2\})^2\}} > 0.5, \tag{2.4}$$

which denotes the closeness between the Nakagami and Rayleigh PDFs, $\Omega = \mathbb{E}\{\tilde{b}_n^2\}$ is the mean power of the random variable $\tilde{b}_n$ and $\mathbb{E}\{\cdot\}$ is the expectation operator. The complex BI noise in the time domain can be expressed as

$$\lambda_n = \lambda_n^{\Re} + j\lambda_n^{\Im}, \tag{2.5}$$

where $\lambda_n^{\Re} = b_n^{\Re} = \tilde{b}_n \cos(\theta_n)$ and $\lambda_n^{\Im} = b_n^{\Im} = \tilde{b}_n \sin(\theta_n)$ are the real and imaginary components of BI noise, respectively, θ_n is the phase of the BI noise given by (2.3) and is uniformly distributed in $[-\pi, \pi)$. The Fig.2.3 demonstrates simulation plot of Nakagami-m distribution for

different values of m and for $\Omega = 1$. It can be seen from the figure that the value of the noise distribution m can control the shape of the distribution, the distribution becomes one-sided Gaussian distribution for $m = 0.5$ and becomes Rayleigh distribution for $m = 1$.

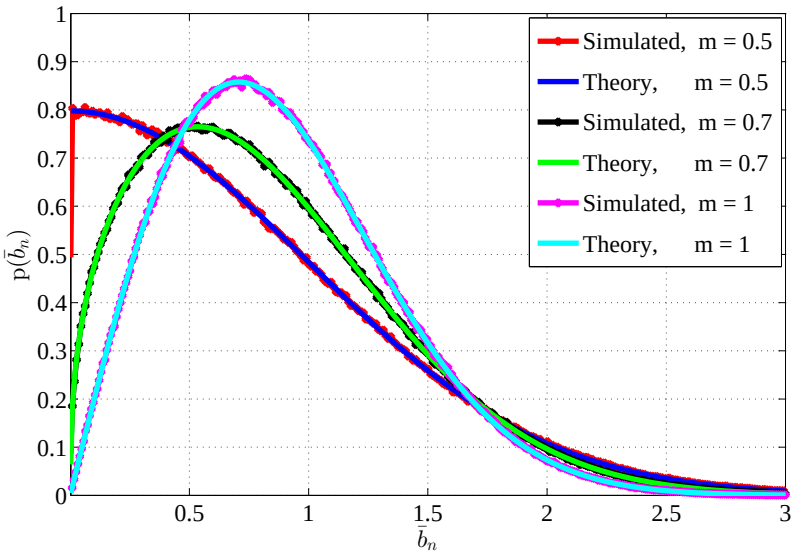

Figure 2.3: Nakagami-m distributions for $m = 0.5, 0.7, 1$ and $\Omega = 1$.

The Probability Density Function (PDF) of the real part of the BI noise, $\lambda_n^{\Re}$, conditioned on the phase of the background noise θ_n can be expressed as [2]

$$\begin{aligned} p_\lambda(\lambda_n^{\Re}|\theta_n) &= \frac{1}{|\cos(\theta_n)|} p(\tilde{b}_n)\Big|_{\tilde{b}_n=\frac{\lambda_n^{\Re}}{\cos(\theta_n)}} \\ &= \frac{2}{|\cos(\theta_n)|} \frac{(\lambda_n^{\Re})^{2m-1}}{\Gamma(m)\cos^{2m-1}(\theta_n)} \left(\frac{m}{\Omega}\right)^m e^{-\left(\frac{m\times(\lambda_n^{\Re})^2}{\Omega\cos^2(\theta_n)}\right)} \\ &= \frac{2(\lambda_n^{\Re})^{2m-1}}{\Gamma(m)\cos^{2m}(\theta_n)} \left(\frac{m}{\Omega}\right)^m e^{-\left(\frac{m\times(\lambda_n^{\Re})^2}{\Omega\cos^2(\theta_n)}\right)}, \end{aligned} \tag{2.6}$$

while the distribution of the imaginary part of the BI noise, $\lambda_n^{\Im}$, conditioned on θ_n can be expressed as [44]

$$\begin{aligned} p_\lambda(\lambda_n^{\Im}|\theta_n) &= \frac{1}{|\sin(\theta_n)|} p(\tilde{b}_n)\Big|_{\tilde{b}_n=\frac{\lambda_n^{\Im}}{\sin(\theta_n)}} \\ &= \frac{2}{|\sin(\theta_n)|} \frac{(\lambda_n^{\Im})^{2m-1}}{\Gamma(m)\sin^{2m-1}(\theta_n)} \left(\frac{m}{\Omega}\right)^m e^{-\left(\frac{m\times(\lambda_n^{\Im})^2}{\Omega\sin^2(\theta_n)}\right)} \\ &= \frac{2(\lambda_n^{\Im})^{2m-1}}{\Gamma(m)\sin^{2m}(\theta_n)} \left(\frac{m}{\Omega}\right)^m e^{-\left(\frac{m\times(\lambda_n^{\Im})^2}{\Omega\sin^2(\theta_n)}\right)}. \end{aligned} \tag{2.7}$$

The closed-form expressions of the real part of the distribution, $p_\lambda(\lambda_n^{\Re})$, utilizing (2.6) and the imaginary part distribution, $p_\lambda(\lambda_n^{\Im})$, utilizing (2.7) for $0 < m < 1$, $m \neq \frac{1}{2}$, $-\infty < \lambda_n^{\Re} < \infty$ and $-\infty < \lambda_n^{\Im} < \infty$, can be expressed as [3, 44]

$$p_\lambda(\lambda_n^{\Re}) = \frac{e^{-\frac{m\times(\lambda_n^{\Re})^2}{\Omega}}}{\sqrt{\pi}\Gamma(m)}\sqrt{\frac{m}{\Omega}}\left[\frac{\Gamma(\frac{1}{2}-m)}{\Gamma(1-m)}\left(\frac{m\times(\lambda_n^{\Re})^2}{\Omega}\right)^{m-\frac{1}{2}}{}_1F_1\left(\frac{1}{2},\frac{1}{2}+m,\frac{m\times(\lambda_n^{\Re})^2}{\Omega}\right)+\right.$$
$$\left.\frac{\Gamma(m-\frac{1}{2})}{\sqrt{\pi}}{}_1F_1\left(1-m,\frac{3}{2}-m,\frac{m\times(\lambda_n^{\Re})^2}{\Omega}\right)\right], \tag{2.8}$$

$$p_\lambda(\lambda_n^{\Im}) = \frac{e^{-\frac{m\times(\lambda_n^{\Im})^2}{\Omega}}}{\sqrt{\pi}\Gamma(m)}\sqrt{\frac{m}{\Omega}}\left[\frac{\Gamma(\frac{1}{2}-m)}{\Gamma(1-m)}\left(\frac{m\times(\lambda_n^{\Im})^2}{\Omega}\right)^{m-\frac{1}{2}}{}_1F_1\left(\frac{1}{2},\frac{1}{2}+m,\frac{m\times(\lambda_n^{\Im})^2}{\Omega}\right)+\right.$$
$$\left.\frac{\Gamma(m-\frac{1}{2})}{\sqrt{\pi}}{}_1F_1\left(1-m,\frac{3}{2}-m,\frac{m\times(\lambda_n^{\Im})^2}{\Omega}\right)\right], \tag{2.9}$$

and for $m = \frac{1}{2}$ as

$$p_\lambda(\lambda_n^{\Re}) = \frac{1}{\pi}\sqrt{\frac{1}{2\pi\Omega}}e^{-\frac{(\lambda_n^{\Re})^2}{4\Omega}}K_0\left(\frac{(\lambda_n^{\Re})^2}{4\Omega}\right), \tag{2.10}$$

$$p_\lambda(\lambda_n^{\Im}) = \frac{1}{\pi}\sqrt{\frac{1}{2\pi\Omega}}e^{-\frac{(\lambda_n^{\Im})^2}{4\Omega}}K_0\left(\frac{(\lambda_n^{\Im})^2}{4\Omega}\right), \tag{2.11}$$

where ${}_1F_1(a;b;z)$ is the confluent hypergeometric function expressed as [45, Eq.(9.210^{10})]

$${}_1F_1(a;b;z) = 1 + \frac{a}{b}\frac{z}{1!} + \frac{a(a+1)}{b(b+1)}\frac{z^2}{2!} + \frac{a(a+1)(a+2)}{b(b+1)(b+2)}\frac{z^3}{3!} + \ldots, \tag{2.12}$$

and $K_0(\cdot)$ is the modified Bessel function of the second kind of order zero expressed as [46]

$$K_0(x) = \sqrt{\frac{\pi}{2x}}e^{-x}\left[1 - \frac{1}{8x}\left(1 - \frac{9}{16x}\left(1 - \frac{25}{24x}\right)\right)\right]. \tag{2.13}$$

Several works have been made to detect the transmitted signal in the presence of Nakagami-m distributed additive noise over PLC system by utilizing sub-optimal detector [47]. The average symbol error rate (SER) in the presence of Nakagami-m BI noise over PLC channels has been derived by utilizing sub-optimal detector for the Quadrature Phase Shift Keying (QPSK) signal in [44]. While the optimal detector based on the ML detector with BER performance analysis have been obtained in [48] by utilizing the Nakagami-m model proposed in [2, 3] for BPSK

modulation with neglecting the multipath Rayleigh fading effects.

2.6.2 Middleton Class A Impulsive Noise Model

MCAIN model is the most popular and important model that is useful to describe the statistical features of IN in PLC environments [5–7, 49]. The main advantage of Middleton's model is that it requires few parameters and an analytically tractable PDF formula [6]. The mathematical expression of this model incorporates both background Gaussian noise ($\ell = 0$) and IN sources ($\ell \neq 0$). According to this model, the overall noise samples are a sequence of independent and identically distributed (i.i.d.) complex Random Variables (RVs). The PDF of the in-phase and quadrature-phase components of this model can be expressed as a weighted sum of Gaussian distributions with zero mean as [5, 7]

$$p_A(i_n^{\Re}) = \sum_{\ell=0}^{\infty} \frac{e^{-A}A^{\ell}}{\ell!} \frac{1}{\sqrt{2\pi\sigma_\ell^2}} e^{\left(-\frac{(i_n^{\Re})^2}{2\sigma_\ell^2}\right)}, \tag{2.14}$$

$$p_A(i_n^{\Im}) = \sum_{\ell=0}^{\infty} \frac{e^{-A}A^{\ell}}{\ell!} \frac{1}{\sqrt{2\pi\sigma_\ell^2}} e^{\left(-\frac{(i_n^{\Im})^2}{2\sigma_\ell^2}\right)}. \tag{2.15}$$

The joint PDF of MCAIN can be expressed as [50]

$$p_A(i_n^{\Re}, i_n^{\Im}) = \sum_{\ell=0}^{\infty} \frac{e^{-A}A^{\ell}}{\ell!} \frac{1}{2\pi\sigma_\ell^2} e^{\left(-\frac{(i_n^{\Re})^2+(i_n^{\Im})^2}{2\sigma_\ell^2}\right)}, \tag{2.16}$$

where $\sigma_\ell^2 = \sigma^2\left(\frac{\frac{\ell}{A}+\rho}{1+\rho}\right)$ denotes the noise power associated with the simultaneous emission from ℓ noise sources that contribute to the IN, and the parameter A is called the impulsive index which denotes the average number of impulses during interference time, $\rho = \frac{\sigma_w^2}{\sigma_i^2}$ is the Gaussian to Impulsive Noise Power Ratio (GINPR), with Gaussian noise power σ_w^2 and IN power σ_i^2, and $\sigma^2 = \sigma_w^2 + \sigma_i^2$ is the total noise power. Sources of IN have a Poisson distribution expressed as $\frac{e^{-A}A^{\ell}}{\ell!}$. The number of IN sources is ℓ, which is characterized by a Poisson distribution with mean value A expressed as $A = \mathbb{E}\{\ell\} = \sum_{\ell=0}^{\infty} \frac{\ell e^{-A}A^{\ell}}{\ell!}$. The noise variance at the receiver can

be expressed by a Gaussian PDF as

$$\sigma_\ell^2 = \sigma^2 \left(\frac{\frac{\ell}{A} + \rho}{1 + \rho} \right) = (\sigma_w^2 + \sigma_i^2) \left(\frac{\frac{\ell}{A} + \rho}{1 + \rho} \right)$$
$$= \sigma_w^2 \left(1 + \frac{1}{\rho} \right) \left(\frac{\frac{\ell}{A} + \rho}{1 + \rho} \right) = \sigma_w^2 \left(1 + \frac{\ell}{A\rho} \right). \tag{2.17}$$

Practically, for smaller values of A, the characteristic of noise become close to impulsive noise, while for larger values of A; for example(A = 10), the characteristic of noise will be more continuous and become close to Gaussian noise [51, 52].

The cross correlation between the real and imaginary components of this model can be expressed utilizing the joint noise PDF as [53]

$$\overline{i_n^{\Re} i_n^{\Im}} = \int_{-\infty}^{\infty} \int_{-\infty}^{\infty} i_n^{\Re} i_n^{\Im} p_A(i_n^{\Re}, i_n^{\Im}) di_n^{\Re} di_n^{\Im}$$
$$= \int_{-\infty}^{\infty} \int_{-\infty}^{\infty} i_n^{\Re} i_n^{\Im} \sum_{\ell=0}^{\infty} \frac{e^{-A} A^\ell}{\ell!} \frac{1}{2\pi\sigma_\ell^2} e^{\left(-\frac{(i_n^{\Re})^2 + (i_n^{\Im})^2}{2\sigma_\ell^2} \right)} di_n^{\Re} di_n^{\Im}$$
$$= 0. \tag{2.18}$$

Therefore, the pair of the in-phase and quadrature components are uncorrelated but dependent, which is mean that both components of MCAIN are not statistically independent because $p_A(i_n^{\Re}, i_n^{\Im}) \neq p(i_n^{\Re}) p(i_n^{\Im})$ as given in (2.16) [50, 53].

According to the noise PDF expression (2.14) and (2.15), the Middleton Class A model requires three parameters of A, ρ and σ for computation of the impulsive noise. These parameters depend on the measurement of the statistical behaviour of the electromagnetic noise environments [5], and can be computed by empirical or analytical calculation [6]. The MCAIN is caused due to switching transients or lightning phenomena within the PLC network. The PSD for IN has maximum amplitude of 40 dBm/Hz above BI noise. While the PSD of BI noise decreases with increasing frequencies from $0 - 100$ MHz, and it is usually around -145 dBm/Hz [12]. This is about 30 dB higher than the thermal noise floor [54].

2.6.3 Bernoulli Gaussian Mixture Impulsive Noise Model

Another well-known model, a special case of MCAIN model which is widely used to model the IN in communication systems, is the BGMIN model [4]. The noise samples at the receiver in the time domain represent the sum of the Additive White Gaussian Background Noise (AWGN) and IN. The IN occurs randomly with high PSD and narrow pulses [55]. According to this model,

the total complex NGN samples, λ_n, over PL channels can be expressed as

$$\begin{aligned} \lambda_n &= w_n + i_n, \\ \lambda_n^{\Re} + \mathrm{j}\lambda_n^{\Im} &= w_n^{\Re} + \mathrm{j}w_n^{\Im} + i_n^{\Re} + \mathrm{j}i_n^{\Im}, \end{aligned} \tag{2.19}$$

where w_n is a complex AWGN sample and i_n is an independent complex IN sample that arises primarily by switching the electric equipment in the PLC grid [56]. The time arrivals of IN in a two-component BGMIN is given by [4, 57, 58]

$$i_n = i_n^{\Re} + \mathrm{j}i_n^{\Im} = b_n(g_n^{\Re} + \mathrm{j}g_n^{\Im}), \tag{2.20}$$

in which g_n is a complex white Gaussian process with mean zero and variance σ_i^2, and $\mathbf{b} = \{b_0, b_1, \ldots, b_{N-1}\}$ is a vector of a Bernoulli process that consists of N i.i.d sequence of zeros and ones with probability mass function [55]

$$p_r(b_n) = \begin{cases} \alpha & b_n = 1 \\ 0 & b_n = 0 \end{cases} \quad n = 0, 1, \ldots, N-1, \tag{2.21}$$

where α is referred to as the IN probability of occurrence. For the sake of clarity, each transmitted data symbol is affected independently by IN with probability α and with random amplitude g_n. Moreover, all the above RVs are assumed to be independent RVs with respect to each other and to the time index n. The total complex noise components in (2.19) at the receiver can be expressed as

$$\lambda_n^{\Re} + j\lambda_n^{\Im} = w_n^{\Re} + jw_n^{\Im} + b_n(g_n^{\Re} + jg_n^{\Im}). \tag{2.22}$$

The distribution of the in-phase component, $\lambda_n^{\Re}$, and quadrature component, $\lambda_n^{\Im}$, and the joint PDF, $p_{BG}(\lambda_n^{\Re}, \lambda_n^{\Im})$, of the total noise samples in the time domain can be expressed as [4]

$$\begin{aligned} p_{BG}(\lambda_n^{\Re}) &= (1-\alpha)\mathcal{N}(\lambda_n^{\Re}, 0, \sigma_w^2) + \alpha\mathcal{N}(\lambda_n^{\Re}, 0, \sigma_w^2 + \sigma_i^2), \\ p_{BG}(\lambda_n^{\Im}) &= (1-\alpha)\mathcal{N}(\lambda_n^{\Im}, 0, \sigma_w^2) + \alpha\mathcal{N}(\lambda_n^{\Im}, 0, \sigma_w^2 + \sigma_i^2), \end{aligned} \tag{2.23}$$

$$p_{BG}(\lambda_n^{\Re}, \lambda_n^{\Im}) = (1-\alpha)\mathcal{N}(\lambda_n^{\Re}, 0, \sigma_w^2)\mathcal{N}(\lambda_n^{\Im}, 0, \sigma_w^2) + \alpha\mathcal{N}(\lambda_n^{\Re}, 0, \sigma_w^2 + \sigma_i^2)\mathcal{N}(\lambda_n^{\Im}, 0, \sigma_w^2 + \sigma_i^2), \tag{2.24}$$

where the notation $\mathcal{N}(\cdot)$ denotes the Gaussian density defined by

$$\mathcal{N}\left(x, \mu_x, \sigma_x^2\right) = \frac{1}{\sqrt{2\pi\sigma_x^2}} e^{\left(-\frac{(x-\mu_x)^2}{2\sigma_x^2}\right)}, \tag{2.25}$$

σ_w^2 and σ_i^2 represent the AWGN and IN variances, respectively. These variances define the input Signal-to-Noise Ratio (SNR) and Signal-to-Impulsive-Noise Ratio (SINR) as in $\mathrm{SNR} = 10\log_{10}\left(\frac{E_s}{2\sigma_w^2}\right)$ and $\mathrm{SINR} = 10\log_{10}\left(\frac{E_s}{2\sigma_i^2}\right)$, respectively, and the Impulsive to Gaussian Noise Power Ratio (IGNPR) can be expressed as $\tilde{\rho} = \frac{\sigma_i^2}{\sigma_w^2}$.

2.6.4 Approximation of the MCAIN Model

The two component BGMIN model is a very simple model that is used to simulate the IN in PLC channels. This model requires only two components $\tilde{\rho}$ and α. Therefore, the BGMIN model is a good model can be used to approximate the MCAIN model. The approximation model has been presented by the Spaulding and Middleton model in [59]. The real, imaginary and the joint distributions can be expressed as

$$\begin{aligned} p_A(\lambda_n^{\Re}) &= e^{-A}\mathcal{N}(\lambda_n^{\Re}, 0, \sigma_w^2) + (1-e^{-A})\mathcal{N}(\lambda_n^{\Re}, 0, \zeta^2), \\ p_A(\lambda_n^{\Im}) &= e^{-A}\mathcal{N}(\lambda_n^{\Im}, 0, \sigma_w^2) + (1-e^{-A})\mathcal{N}(\lambda_n^{\Im}, 0, \zeta^2), \end{aligned} \tag{2.26}$$

$$p_A(\lambda_n^{\Re}, \lambda_n^{\Im}) = e^{-A}\mathcal{N}(\lambda_n^{\Re}, 0, \sigma_w^2)\mathcal{N}(\lambda_n^{\Im}, 0, \sigma_w^2) + (1-e^{-A})\mathcal{N}(\lambda_n^{\Re}, 0, \zeta^2)\mathcal{N}(\lambda_n^{\Im}, 0, \zeta^2), \tag{2.27}$$

where $\zeta^2 = \sigma_w^2\left(1 + \frac{1}{A\rho}\right)$, $\rho = \frac{\sigma_w^2}{\sigma_i^2}$ is the GINPR and $\mathcal{N}(\cdot)$ is given in (2.25).

2.7 Orthogonal Frequency Division Multiplexing

The multipath effects and impulsive noise are the most dominant factors that causes performance degradation in PLC. Most research in the literature selects OFDM as an appropriate modulation technique to reduce the errors in data transmission over PLC channels. OFDM is a Multi-Carrier Modulation (MCM) technique which commonly used with a cyclic prefix (CP) to achieve the highest robustness against frequency-selective fading, Inter-symbol Interference (ISI), Inter-Carrier Interference (ICI) and IN in wired and wireless channels; hence, requiring only a simple single-tap equalizer at the receiver [56]. Moreover, the orthogonality between the sub-carriers allows excellent BW efficiency due to the overlap between them. Due to these ad-

vantages, OFDM was adopted as a modulation scheme for Digital Audio Broadcasting (DAB), Digital Video Broadcasting (DVB) and Digital Video Broadcasting - Satellite services to Handhelds (DVB-SH) in Europe and Japan [60–62]. On the other hand, OFDM has been adopted for different standards such as IEEE802.11a, IEEE802.16, IEEE802.20 and IEEE802.11n [63]. Generally, OFDM can perform better than single carrier modulation over PLC contaminated by IN because the OFDM spreads the effect of IN over large number of sub-carriers, which leads to the noise on each sub-carrier exhibiting a Gaussian distribution. Therefore, a variety of standards have adopted OFDM as one of the most promising modulation techniques in many wired communication channels for BB-PLC and for NB-PLC applications [64], such as the Asymmetric Digital Subscriber Line (ADSL) [65], Second Generation Digital Video Transmission over Cable (DVB-C2) [66] and home networking over PLC [67].

2.7.1 OFDM Signalling

OFDM is one of the main techniques for high rate data transmission over PLC channels. OFDM offers great advantages for combating multipath frequency-selective PLC channels and IN over Single-Carrier (SC) transmission systems [58].

A high-speed serial data stream is usually mapped to equiprobable complex data symbols using one of the modulation technique such as M-QAM or M-ary Phase Shift Keying (M-PSK) modulations. Subsequently, the high data rate information stream is then modulated into base-band symbols of a lower rate information stream by means of N orthogonal sub-carriers using an Inverse Discrete Fourier Transform (IDFT), increasing the symbol period. If N is a multiple number of 2, the data symbols can be modulated efficiently using an N-point Inverse Fast Fourier Transform (IFFT) process to produce an OFDM symbol expressed as $\mathbf{x} = [x_0, x_1, \ldots, x_{N-1}]$, which reduces the complexity of operations from N^2 in the case of IDFT to $N \log_2 N$ in the case of IFFT. Thus, IFFT/FFT is widely used in practical measurements due to simpler hardware implementation than the IDFT/DFT. To eliminate the Inter-Symbol-Interference (ISI) completely between consecutive OFDM symbols, a time-domain CP of length N_{CP} samples which is designed to exceed the maximum PLC channel delay spread is inserted at the beginning of each OFDM symbol by copying the last N_{CP} samples of the IFFT output block $\mathbf{x}$ and appending them at the beginning of $\mathbf{x}$ to produce the transmitted symbol $\tilde{\mathbf{x}}$ of length $N_t = N + N_{CP}$ samples expressed as $\tilde{\mathbf{x}} = [x_{N-N_{CP}}, x_{N-N_{CP}+1}, \ldots, x_{N-1}, x_0, x_1, \ldots, x_{N-1}]$. Moreover, to eliminate the ICI, the OFDM symbol is cyclically extended in the guard time; which ensures the OFDM symbol always has an integer number of cycles within the FFT inter-

val as long as the delay is smaller than the guard time. At the receiver front-end, the transmitted symbol, $\tilde{x}_n$, is distorted by multipath frequency-selective PLC channel contaminated by the NGN which includes the combined BI noise and IN. The n-th sample of the complex received signal in the time domain can be expressed as

$$\tilde{\mathbf{y}}_n = \sum_{i=0}^{L_h-1} h_i \tilde{x}_{n-i} + \lambda_n, \;\; 0 \leq n \leq N + N_{CP} - 1, \tag{2.28}$$

where $\{h_i\}_{i=0}^{L_h-1}$ are the coefficients of the discrete channel impulse response of the multipath PLC channel of length L_h and $\boldsymbol{\lambda} = [\lambda_0, \lambda_1, \ldots, \lambda_{N+N_{CP}-1}]$ denotes the total NGN samples in the time domain, which is modeled as an individual noise or as a combined noise of Nakagami-m background noise, BGMIN or MCAIN models. The inverse operations are done at the receiver side to detect the transmitted data. Assuming perfect time synchronization between the transmitter and the receiver, the received signal in the time domain after CP removal can be expressed as $\mathbf{y} = [y_0, y_1, \ldots, y_{N-1}]$, and in the frequency domain after FFT operation can be expressed as

$$\begin{aligned} Y_k &= \frac{1}{\sqrt{N}} \sum_{n=0}^{N-1} y_n e^{-\frac{j2\pi kn}{N}}, \\ &= H_k X_k + \Lambda_k, \; k = 0, 1, \ldots, N-1, \end{aligned} \tag{2.29}$$

where H_k is the FFT of the CIR samples, X_k is the FFT of the transmitted signal samples, Λ_k is the FFT of the total NGN samples λ_k.

In probability theory, the Central Limit Theorem (CLT) is a statistical theory that states, when independent and identically distributed random variables $X_1, \cdots, X_n$ of size n with expected values or mean values are given by $\mathbb{E}\{X_i\} = \mu$ and variances are given by $Var\{X_i\} = \sigma^2$ are added, the sample average of these random variables can be expressed as

$$S_n = \frac{X_1 + \cdots + X_n}{n} \tag{2.30}$$

For large enough n, the distribution of the random variables $\sqrt{n}(S_n - \mu)$ converge in distribution to a normal distribution even if the original variables themselves are not normally distributed with mean $\mu = 0$ and variance σ^2 as $\mathcal{N}(0, \sigma^2)$. Therefore, the noise distribution of Λ_k^r in the frequency domain will be approaching a normal distribution [2], with zero mean and variance σ_λ^2 as $\mathcal{N}(0, \sigma_\lambda^2)$. Indeed, the distortion introduced by the channel can be compensated by using

a simple frequency domain equalizer (FEQ) [27].

2.8 Mitigating the Effect of Impulsive Noise in indoor PLC Channels

Among all the additive NGN types, IN causes a significant degradation in BER performance, therefore, it is the limiting factor for broadband communication over PLs [27, 58]. Such as in DVB systems, the IN is often randomly generated by various sources connected to the PL, for example, switching power supplies and indoor electrical appliances [68]. Different methods have been developed in the literature to mitigate IN effects over PLC channels for achieving high-speed data transmission. It can be roughly divided into four classes, time-domain methods which operate on the received signal magnitude after exceeding a certain threshold level [69–71], the iterative frequency domain method, where the IN cancellation is processed in the frequency domain [72], and the combination of both methods, i.e. the time and frequency domain methods [73,74]. Finally, one can utilize powerful error correcting codes such as LDPC codes or TCs to mitigate the IN in BB-PLC systems [52, 75–79]. The attention is now focusing on the existing methods that are used to mitigate the impact of IN in the time domain, while the coding techniques will be presented in the next chapter.

2.8.1 Time-Domain Methods

Different non-linearity based IN mitigation methods with different degrees of complexity are used in the time domain to reduce the impact of IN samples before the OFDM demodulator. For the sake of simplicity, the non-linearity mitigation methods are applied to Nyquist rate sampled signals to ensure all distortion components fall within the range. In practical applications, number of non-linear techniques with different degrees of complexity have been proposed to reduce the effect of IN, which including clipping, blanking, and their combination [69, 72, 80, 81]:

a) **Blanking nonlinearity**:

$$r_n = \begin{cases} y_n & \text{if } |y_n| \leq T_b \\ 0, & \text{otherwise} \end{cases}, \quad n = 0, 1, \cdots, N-1, \tag{2.31}$$

where T_b is the blanking threshold. The complex received signal magnitudes whose values exceed T_b are replaced by zero.

b) **Clipping nonlinearity**:

$$r_n = \begin{cases} y_n & \text{if } |y_n| \leq T_c \\ T_c e^{j \arg(y_n)}, & \text{otherwise} , \end{cases} n = 0, 1, \cdots, N-1, \tag{2.32}$$

where T_c is the Clipping Threshold. The complex received signal magnitudes whose values exceeding T_c are replaced by the clipping value.

c) **c) Clipping/blanking nonlinearity**:

$$r_n = \begin{cases} y_n & \text{if } |y_n| \leq T_c \\ T_c e^{j \arg(y_n)}, & T_c < |y_n| \leq T_b, \\ 0, & \text{if } |y_n| > T_b , \end{cases} \quad n = 0, 1, \cdots, N-1. \tag{2.33}$$

The clipping/blanking technique is a combination of clipping and blanking non-linearities. This hybrid technique offers better performance than the other non-linear techniques [69], where the blanking threshold is usually greater than the clipping threshold, i.e. ($T_b > T_c$) under the similar NGN scenario. In this method, the complex received signal magnitude whose values are greater than T_b are replaced by zero while medium magnitudes whose values greater than T_c are clipped.

In general, two major drawbacks of the blanking or clipping methods are:

- if T_b or T_c has a small value, most of the OFDM samples are blanked or clipped, which can be harmful to the desired signal and the original signal samples cannot be recovered.
- if T_b or T_c has a very large value, the non-linear preprocessor will have no impact on the OFDM samples contaminated by IN.

This leads to degradation in the BER performance of the system. Therefore, reliable broadband communication over PLC channels in the presence of IN will depend on the selection of threshold values. The basic strategy uses to improve the performance of these time-domain non-linearities is based on maximizing the signal-to-noise ratio at the output of the non-linearity IN mitigation methods. A comprehensive study on threshold optimization and theoretical performance analysis based on SNR computation at the clipping scheme, the blanking scheme, and clipping/blanking output have been presented by Zhidkov in [69, 80]. The optimization has been done based on the BGMIN model and the MCAIN model. Moreover, simplified analytical expressions of the clipping and blanking threshold based on the combination criterion and the

Siegert ideal criterion [82] with a reasonable complexity are presented in [83–85] for BPSK modulation over uncoded OFDM system.

On the other hand, different works have been proposed in the literature to reduce the impact of the impulsive noise, these research can be summarized as

- In [86], the closed-form expression for the probability of blanking error has been derived for the proposed blind blanking technique, in addition to addressing the problem of threshold optimization in the presence of different scenarios of IN and Peak-to-Average Power Ratio (PAPR).

- In [87], the Single-Carrier Frequency Division Multiple Access (SC-FDMA) has been proposed to reduced the effect of PAPR and to optimize the blanking threshold.

- In [88], the lookup table with uniform quantization levels has been proposed to estimate the PAPR at the receiver, which is allowed to compute the optimal blanking threshold without needing any information knowledge of the IN parameters.

- In [89], it has been showed that the performance of the combination blanking and clipping in a hybrid technique utilizes two thresholds T_1 and $T_2 = \alpha T_1$ is sensitive to the threshold T_1 and the scaling factor α.

- In [90], a method for blanking IN mitigation method has been proposed to minimize both probabilities of blanking error and missed blanking and maximize the probability of successful detection, which has been made by applying the partial transmit sequence scheme at the transmitter to enhance the capability of the conventional dynamic peak-based threshold estimation technique.

- In [91], a method for computing the optimal blanking threshold (OBT) has been proposed for the OFDM system over PLC channel without needing any knowledge about the IN. It has been found that the computation of OBT depending on the accuracy of the signal PAPR estimate.

2.9 Summary of the Chapter

This chapter described the general history, networks characterization and the challenges of PLC. PLC is the technology that uses the existing PL grid for high-speed data transmission along with the electrical current. The structures and the physical properties of the PL channel reveal a

hostile environment for high-speed data transmission, as discussed in this chapter. However, in order to successfully deploy PLC, all challenges of the network topology need to be resolved.

Zimmermann and Dostert multipath model was presented in this chapter to model the channel transfer function of PLC channel, which depended on a few parameters. Generally, PLC can be classified into NB-PLC and BB-PLC. On the other hand, several additive NGNs are characterized and presented for the PLC channel in this chapter, such as CBN, NB noise, in addition to three types of impulsive noise. Among all the contaminated NGNs, the asynchronous IN was presented as the most dominant factor, which causes degradation in the BER performance due to high PSD that exceeds all the other types of noise. Moreover, the Nakagami-m distribution type model was demonstrated to model the background noise. The MCAIN model, the BGMIN model and simplified MCAIN model are considered in the rest of the chapter for modelling asynchronous impulsive noise. Furthermore, the OFDM multi-carrier modulation method over PL based communication has been presented in the presence of NGN.

Finally, this chapter provides overview of several state-of-the-art IN countering strategies in the time-domain. The amplitude clipping or blanking methods are mostly used over channels affected by IN to give significant performance improvements compared to a system without cancellation is applied.

Chapter 3

Forward Error Correction Codes and PLNC System

3.1 Introduction

Shannon's theorem in 1948 [92], states that it is possible to recover transmitted signal over a noisy channel correctly at the receiver at any rate smaller than the channel capacity, and the theory gives theoretical bounds on the performance of Forward Error Correction (FEC) coding [93]. Recently, none of the proposed codes were able to achieve performances close to Shannon limit until Berrou, Glavieux and Thitimajshima presented the iterative Turbo coding scheme in 1993 [94]. Three years later, MacKay and Neal [95, 96] rediscovered LDPC codes with iterative soft-decision decoding based on the belief propagation decoding algorithm to achieve performance very close to the Shannon limit [97] and better than TCs [98].

Generally, the design of reliable communication over a noisy channel involves trade-offs between the BER performance, transmitted signal power and system cost. FEC or channel coding is one of the efficient techniques to perform these requirements. There are two main categories of FEC codes, which are classified into block codes such as the BCH code, Reed-Solomon code and LDPC code, and convolutional codes such as TC. In block codes, information bits $\mathbf{d}$ of length k_c are encoded to codeword $\mathbf{c}$ of length n_c by adding extra bits of length r_c to allow the decoder to detect and correct random and burst errors encountered during the transmission through the channel. In convolutional codes, the input data stream is passing through a linear finite state shift register to generate a convolutional coded stream. TCs and LDPC codes achieves are able to achieve an excellent performance over PLC channels in the presence of impulse noise and high channel multipath selectivity with an appropriate complexity of decoding

in the hardware design [56, 99, 100].

3.2 Binary Low Density Parity Check codes

B-LDPC codes over Galois field 2, GF(2), or field 2, $\mathbb{F}_2$, are one of the most important linear block codes that were introduced firstly by Gallager in 1962 [101] and rediscovered by Mackay and Neal in 1996 [95]. The rate-$1/2$ B-LDPC code with random construction and for a block length of 10^7 bits achieves BER performance of 10^{-6} falls within 0.0045dB away from the Shannon capacity in the AWGN channel [102–104].

LDPC codes can be classified into regular (R) and irregular (IR) codes, in which, the latter type achieves a superior BER performance than the first type. Nowadays, Irregular-Binary-Low Density Parity Check (IR-B-LDPC) codes can efficiently operate close to many channels capacity, therefore, B-LDPC codes have been adopted as an error correcting codes for many standards such as a Digital Video Broadcasting - Satellite - Second Generation (DVB-S2) standard and the 10 Gigabit Ethernet [105, 106]. The B-LDPC codes can be constructed by using $(n_c - k_c) \times n_c$ sparse parity check matrix $\mathbf{H}$ with column weight w_c corresponding to the number of ones per column and row weight w_r corresponding to the number of ones per row, where n_c is the codeword length, k_c is the information length and $r_c = n_c - k_c$ is the parity check length. However, the size of $\mathbf{H}$ is usually very large compared to the number of non-zero elements in the code. Therefore, the sparse parity check matrix is said to have a low density. However, Regular-Binary-Low Density Parity Check (R-B-LDPC) code parameters $(n_c; r_c; w_c; w_r)$ have a constant w_c and w_r, while the IR type has a variable w_c and w_r [93]. In general, B-LDPC codes constructed using Irregular-Sparse Parity Check Matrix (IR-$\mathbf{H}$) have a better BER performance than that of Regular-Sparse Parity Check Matrix (R-$\mathbf{H}$) construction.

3.2.1 Tanner Graph Representation

A Factor Graph or Tanner Graph is a bipartite graph used to describe the sparse parity check matrix $\mathbf{H}$ of LDPC codes by utilizing two types of nodes: the variable nodes (v) and check nodes (c) which relate to columns and rows of $\mathbf{H}$, respectively. An edge exists between v and c if and only if the element connecting these two nodes in $\mathbf{H}$ is a non-zero element [107].

A cycle or a girth in the Tanner graph representation is defined as a loop starting and ending at the same node without entering the node more than once [108]. The minimum cycle or a girth in the B-LDPC code has a loop containing 4-cycles, which represent the parameter that mostly

degrades the BER performance for small size codes, because it affects the independence of the extrinsic information exchange between the variable nodes and check nodes in the iterative decoder [109]. However, cycles of length greater than 4 have less affect on the BER performance of the code [108]. We can detect 4-cycles in the Tanner graph when the ones produce a square in the matrix $\mathbf{H}$, as given in the following example

$$\mathbf{H} = \begin{bmatrix} \mathbf{1} & 0 & 0 & \mathbf{1} & 0 & 1 \\ 0 & \mathbf{1} & \mathbf{1} & 0 & 1 & 0 \\ 0 & \mathbf{1} & \mathbf{1} & 0 & 0 & 1 \\ \mathbf{1} & 0 & 0 & \mathbf{1} & 1 & 0 \end{bmatrix}. \tag{3.1}$$

In this example, we have two 4-cycles in the Factor Graph representation in the parity-check matrix $\mathbf{H}$, the first cycle is $v_1 \rightarrow c_1 \rightarrow v_4 \rightarrow c_4 \rightarrow v_1$ while the second cycle is $v_2 \rightarrow c_2 \rightarrow v_3 \rightarrow c_3 \rightarrow v_2$ as shown in Fig. 3.1 by the bold lines.

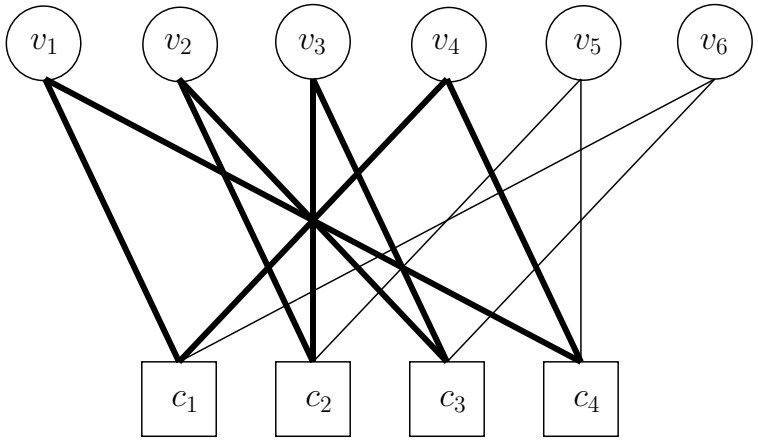

Figure 3.1: Factor Graph representation of $\mathbf{H}$ in (3.1).

Moreover, the number of edges in the cycle represents the cycle length, and the girth of the graph represents the smallest cycle size [108]. Therefore, due to the girth in $\mathbf{H}$, the decoding algorithm iterates many times until it converges to the correct code. Indeed, longer girths greater than 4 in Tanner graph have a slight effect on the performance of B-LDPC codes, thus, removing the girth 4 is required for reliable communication. A simple method for counting the number of $4, 6, 8$ and 10-cycles is presented in [109]. Generally, the construction of $\mathbf{H}$ can be done in two ways: random construction and algebraic construction [108]. Construction of $\mathbf{H}$ based on Finite-geometry reported in [110] ensures the Tanner graph do not contain cycles of length 4 with good minimum distance. The set of check bits connected to the coded bit can be denoted

as $\mathcal{M}_n = \{m : H_{mn} = 1\}$, and the set of coded bits that are connected to the parity check bit is denoted as $\mathcal{N}_m = \{n : H_{mn} = 1\}$. So from the $\mathbf{H}$ in (3.1), the parity checks c_1 and c_4 are connected to coded bit v_1 and can be expressed as $\mathcal{M}_1 = \{1, 4\}$. While the coded bits v_1, v_4 and v_6 are connected to parity check c_1 and can be expressed as $\mathcal{N}_1 = \{1, 4, 6\}$. Moreover, the set of $\mathcal{M}_n$ except the check bit m is denoted as $\mathcal{M}_n \backslash m$ and the set of $\mathcal{N}_m$ except the coded bit n is denoted as $\mathcal{N}_m \backslash n$. Therefore, $\mathcal{M}_1 \backslash 1 = \{4\}$ and $\mathcal{N}_1 \backslash 1 = \{4, 6\}$. We will utilize these notations when describing the sum-product decoding algorithm.

On the other hand, the Progressive Edge-Growth (PEG) algorithm proposed in [111] ensures no girth cycles of length four are generated in the Tanner graph. Hence, the BER performance will not degrade. The PEG algorithm is a powerful algorithm that can effectively construct for short or medium LDPC code length. The optimized symbol node degree distribution of ones in $\mathbf{H}$ that constructed using PEG for $\mathrm{rate} = 1/2$ B-LDPC code is given in Table 3.1, where the block length in binary representation is equal to nb [111].

Table 3.1: Optimized symbol node degree distribution.

Galois field	(n, m)	Symbol node degree distribution	Average symbol degree
$\mathbb{F}_2$	$(1008, 504)$	$0.47532x^2 + 0.279537x^3 + 0.0348672x^4 + 0.108891x^5 + 0.101385x^{15}$	3.994
$\mathbb{F}_8$	$(336, 168)$	$0.643772x^2 + 0.149719x^3 + 0.193001x^4 + 0.013508x^5$	2.5762
$\mathbb{F}_{16}$	$(252, 126)$	$0.772739x^2 + 0.102863x^3 + 0.113797x^4 + 0.010601x^5$	2.3623
$\mathbb{F}_{32}$	$(202, 101)$	$0.84884x^2 + 0.142034x^3 + 0.009126x^4$	2.1603
$\mathbb{F}_{64}$	$(168, 84)$	$0.94x^2 + 0.05x^3 + 0.01x^4$	2.07

3.2.2 B-LDPC Encoder

The sparse parity-check matrix $\mathbf{H}$ generated by the PEG algorithm can be expressed in systematic form as given by

$$\mathbf{H} = [\mathbf{P} \mid \mathbf{I}], \tag{3.2}$$

where $\mathbf{P}$ is the binary matrix of dimension $(n_c - k_c) \times k_c$ and $\mathbf{I}$ is an identity matrix of dimension $(n_c - k_c) \times (n_c - k_c)$. A systematic generator matrix $\mathbf{G}$ of block code can be constructed from $\mathbf{H}$ as

$$\mathbf{G} = [\mathbf{I} \mid \mathbf{P}^T], \tag{3.3}$$

where T denote the matrix transpose operation, the codeword $\mathbf{c}$ in the systematic form can be generated using

$$\mathbf{c} = \mathbf{dG}, \tag{3.4}$$

where $\mathbf{c} = [c_1, c_2, \ldots, c_{n_c}]$, $\mathbf{d} = [d_1, d_2, \ldots, d_{k_c}]$ denote the information message and the product between $\mathbf{d}$ and $\mathbf{G}$ can be achieved by multiplication the information bits $\mathbf{d}$ be each column of $\mathbf{G}$ bit by bit and then taken Modulo-2 addition [99].

3.2.3 Sum-Product Decoding Algorithm

The B-LDPC codes can be decoded the noisy codeword by utilizing the Message Passing Algorithm (MPA). This algorithm is based on the passing of messages along the edges of the Tanner graph during the decoding process. Mainly, the decoding algorithms can be classified into two algorithms depending on the messages passing through the Tanner graph. If the messages are binary/LLR values, these algorithms are called hard/soft decision decoding algorithms such as the Bit-Flipping Algorithm (BFA)/Sum-Product Decoding Algorithm (SPA), respectively [93]. The SPA that utilises the LLR values perform better than the hard decision decoding algorithm. Therefore, the SPA is used to reduce the decoding complexity with respect to the MPA [112]. However, if the sparse parity check matrix is cycle-free, the SPA achieves the Shannon-limit performance [96, 111, 112]. The SPA is presented in Algorithm 1 [102, 113, 114].

The LLRs in the initialization step of SPA for equiprobable inputs modulated by using Binary Phase Shift Keying (BPSK) modulation over the AWGN channel, can be computed from the received noisy bits y_k as

$$L(X_k) = \log \frac{p(Y_k|X_k = -1)}{p(Y_k|X_k = +1)} = \log \frac{e^{-\frac{(Y_k+1)^2}{2\sigma^2}}}{e^{-\frac{(Y_k-1)^2}{2\sigma^2}}} = \frac{[(Y_k - 1)^2 - (Y_k + 1)^2]}{2\sigma^2} = -\frac{2Y_k}{\sigma^2}, \tag{3.5}$$

where X_k, Y_k and σ^2 denotes the k-th bit of the transmitted codeword, the received codeword and the noise variance, respectively.

Algorithm 1: Sum-Product Algorithm (SPA)

Initialization:
$\text{Iteration} = 1,$
$\text{LLR}(b_k) = \log \frac{p(Y_k|X_k=0)}{p(Y_k|X_k=1)},$
$L(q_{n\to m}) = \text{LLR}(b_k),$
while $\mathbf{H}\hat{\mathbf{X}} \neq \mathbf{0}$ and iteration $\leq$ max iteration **do**
  Update checks to nodes: for each m**, and** $n \in \mathcal{N}(m)$**, compute**
  $L(r_{m\to n}) = 2\tanh^{-1}\left(\prod_{n'\in\mathcal{N}(m)\setminus n}\tanh\left(\frac{1}{2}L(q_{n'\to m})\right)\right),$
  Update nodes to checks: for each n**, and** $m \in \mathcal{M}(n)$**, compute**
  $L(q_{n\to m}) = \text{LLR}(b_k) + \sum_{m'\in\mathcal{M}(n)\setminus m} L(r_{m'\to n}),$
  For each k**, compute**
  $L(Q_k) = \text{LLR}(b_k) + \sum_{m'\in\mathcal{M}(n)} L(r_{m'\to n}),$
  Decision: $\hat{x}_k = \begin{cases} 0 & L(Q_k) < 0 \\ 1 & \textbf{Otherwise} \end{cases}$
  Iteration = Iteration+1,
end

3.2.4 Implementation of Logarithm Function

The logarithm function utilizes for LLR computations can be implemented in Field-Programmable Gate Array (FPGA) platforms by using two main methods. The first method utilizes the look-up table (LUT) based algorithms and, on the other, utilizes iterative methods. The first approach is faster than the second approach and beneficial for low precision, while it requires a high amount of memory in the LUT to achieve high accuracy. In this case, one operation needs to fetch the result of the logarithm from the LUT. Moreover, iterative algorithms are slower than the first approach but it is suitable for high precision due to utilizing Taylor's series expansion. Therefore, the number of operations needs to compute the logarithm will depend on Taylor's series size [115, 116]. According to Taylors series, $\log(x)$ can be expressed as $-\sum_{k=1}^{n}\frac{(-1)^k(-1+x)^k}{k}$ for $|-1+x|<1$. Thus, the number of arithmetic operations needed to compute $\log(x)$ based on Taylors series for $k = 1, 2, 3$ can be computed as given in Table 3.2

Table 3.2: Number of arithmetic operations needed for computing $\log(x)$

k	$\log(x)$	Addition	Subtraction	Multiplication	Division
1	$x-1$	0	1	0	0
2	$-\frac{x^2}{2}+2x-\frac{3}{2}$	1	2	2	2
3	$\frac{x^3}{3}-\frac{3x^2}{2}+3x-\frac{11}{6}$	1	2	5	3

3.3 EXIT Chart for B-LDPC Codes

The EXIT chart is a graphical tool that tracks the exchange of the mutual information between component decoders at each iteration [117], which analyses the convergence properties of iterative decoding, estimate the decoding thresholds of iterative code ensembles as well as the BER performance. In this section, we will briefly outline the EXIT charts for R-B-LDPC and IR-B-LDPC codes in the presence of Gaussian noise [118].

It is important to note that the variable node decoder VND and check node decoder CND corresponding to $\mathbf{H}$ are considered as two component blocks of B-LDPC decoder, respectively [118]. In this method, the *extrinsic* information curve of $\mathrm{VND}/\mathrm{CND}$ is plotted between the *a priori* information $I_{A,VND}/I_{A,CND}$ going into the $\mathrm{VND}/\mathrm{CND}$ in the x-axis against the *extrinsic* information of $I_{E,VND}/I_{E,CND}$ coming out of the $\mathrm{VND}/\mathrm{CND}$ in the y-axis, respectively. The decoding trajectory between the $I_{E,VND}$ and $I_{E,CND}$ curves gives the amount of information that is exchanged between the VND and CND in the iterative decoder as shown in Fig. 3.2

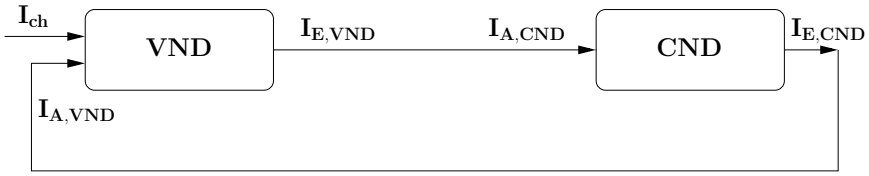

Figure 3.2: Block diagram of the B-LDPC iterative SPA decoder.

3.3.1 EXIT Curve of the VND

The output of VND of degree $d_v + 1$ for the variable node degree d_v can be expressed as

$$L_{n,out} = L_{ch} + \sum_{m \neq n} L_{m,in}, \tag{3.6}$$

where $L_{n,out}$ is the n-th *extrinsic* LLRs coming out of the VND, L_{ch} is the channel LLRs and the $L_{m,in}$ is the m-th *priori* LLRs going into the VND. Consider the channel LLR values in (3.5), the variance of the channel can be expressed as

$$\sigma_{ch}^2 = \frac{4}{\sigma^2} = 8R_c\frac{E_b}{N_0}, \tag{3.7}$$

where R_c, E_b and N_0 are the code rate, the energy per transmitted bit and the noise power, respectively. The *extrinsic* LLR, $L_{n,out}$, exhibits a Gaussian distribution with variance $\sigma^2 = \sigma_{ch}^2 + (d_v - 1)\sigma_a^2$, where σ_a^2 is the variance of the *a priori* LLRs. Now, the EXIT function $I_{E,VND}$ of the R-B-LDPC code can be expressed as

$$\begin{aligned} I_{E,VND} = J(\sigma) &= J\left(\sqrt{(d_v - 1)\left[J^{-1}(I_{A,VND})\right]^2 + \sigma_{ch}^2}\right) \\ &= J\left(\sqrt{(d_v - 1)\sigma_a^2 + \sigma_{ch}^2}\right), \end{aligned} \tag{3.8}$$

where $J^{-1}(\cdot)$ is the inverse function of $J(\cdot)$ with proper approximation given in [118]. Moreover, the mutual information $I(X, Y)$ for equally likely inputs x can be expressed as [119]

$$I(X, Y) = \frac{1}{2} \sum_{x=\pm 1} \int_{-\infty}^{+\infty} p(y|x) \log_2 \frac{p(y|x)}{p(y)} dy, \tag{3.9}$$

with

$$p(y) = \frac{1}{2}\left(p(y|x = +1) + p(y|x = -1)\right), \tag{3.10}$$

and

$$p(y|x = \pm 1) = \frac{1}{\sqrt{2\pi}\sigma} e^{-\frac{(y \pm 1)^2}{2\sigma^2}}. \tag{3.11}$$

The ensemble of the IR-B-LDPC codes can be characterized by the (variable/check) node degree distribution (d_v/d_c), respectively, and can be expressed by degree distribution polynomials as $\mathcal{V}(x) = \sum_{i=2}^{d_v} \mathcal{V}_i x^{i-1}$ and $\mathcal{K}(x) = \sum_{i=2}^{d_c} \mathcal{K}_i x^{i-1}$ where $\mathcal{V}_i$ and $\mathcal{K}_i$ represent the fraction of variables nodes and check nodes, respectively. The EXIT function $I_{E,VND}$ involving all d_v can be expressed as [118, 120]

$$I_{E,VND} = \sum_{d_v} \nu_{d_v} J\left(\sqrt{(d_v - 1)\left[J^{-1}(I_{A,VND})\right]^2 + \sigma_{ch}^2}\right). \tag{3.12}$$

3.3.2 EXIT Curve of the CND

Similarly, the EXIT function $I_{E,CND}$ for a R-B-LDPC code can be expressed as [118]

$$I_{E,CND} = 1 - J\left(\sqrt{(d_c - 1)\left[J^{-1}(1 - I_{A,CND})\right]^2}\right). \tag{3.13}$$

While for IR-B-LDPC codes, the EXIT function $I_{E,CND}$ involving all d_c can be expressed as

$$I_{E,CND} = \sum_{d_c} \kappa_{d_c} \left[1 - J\left(\sqrt{(d_c - 1)\left[J^{-1}(1 - I_{A,CND}) \right]^2} \right) \right]. \tag{3.14}$$

3.4 Non-Binary Low Density Parity Check codes

Recently, NB-LDPC codes are promising error correcting codes which have increasingly raised interested. The performance gain comes at the cost of an increase in the decoding complexity. NB-LDPC codes with high order Galois fields GF(q) or $\mathbb{F}_q$ have better BER performance than B-LDPC codes for the same block length in bits, especially over channels with noise bursts [121,122]. NB-LDPC codes are the class of linear block code introduced by Davey and Mackay over Galois field $\mathbb{F}_q := \{0, 1, \delta, \ldots, \delta^{q-2}\}$ for $q > 2^p$, where p is a positive number larger than 1 and δ is the root of the primitive polynomial that is used to define $\mathbb{F}_q$ [123, 124]. For example, the tables of addition and multiplication of NB-LDPC codes over Galois field $\mathbb{F}_4$ can be expressed as given in Table 3.3 and Table 3.4,respectively. Moreover, the elements of $\mathbb{F}_4$ can be constructed using the primitive polynomial $f(x) = x^2 + x + 1$ for the root δ of $f(x)$ as $\delta^2 = \delta + 1$ as given in Table 3.5

Table 3.3: Additions over $\mathbb{F}_4$

+	0	1	δ	δ^2
0	0	1	δ	δ^2
1	1	0	δ^2	δ
δ	δ	δ^2	0	1
δ^2	δ^2	δ	1	0

Table 3.4: Multiplications over $\mathbb{F}_4$

$\times$	0	1	δ	δ^2
0	0	0	0	0
1	0	1	δ	δ^2
δ	0	δ	δ^2	1
δ^2	0	δ^2	1	δ

Table 3.5: Construction of $\mathbb{F}_4$

Element in $\mathbb{F}_4$	Polynomial	Binary representation
0	0	00
1	1	01
δ	δ	10
δ^2	$\delta + 1$	11

NB-LDPC codes can achieve higher coding gain and outperforms the equivalent B-LDPC codes and all other states of the art codes on channels with noise burst [114, 123, 124], but with higher computational complexity. Different methods are proposed in [125] to construct the sparse parity check matrix of the non-binary LDPC codes using array dispersion technique. A NB-LDPC code over $\mathbb{F}_q$ can be constructed using $\mathbf{H} \in \mathbb{F}_q^{M \times N}$ as a set of code words $\mathcal{C} = \{c \in \mathbb{F}_q^{1 \times N} : \mathbf{H}\mathbf{c}^{\mathrm{T}} \overset{\mathbf{GF}}{=} \mathbf{0}\}$. However, we utilize the PEG algorithm with optimized symbol node degree distribution to construct $\mathbf{H}$ in this thesis as presented in Table 3.1. The sets of non-zero elements per row or column in $\mathbf{H}$ can be expressed as $\mathcal{N}_m = \{n : H_{mn} \neq 0\},\ \mathcal{N}_{mn} = \mathcal{N}_m \backslash \{n\}$ and $\mathcal{M}_n = \{m : H_{mn} \neq 0\},\ \mathcal{M}_{nm} = \mathcal{M}_n \backslash \{m\}$, respectively. The parity check elements for the check node $m \in \{1, 2, \ldots, M\}$ can be generated as

$$r_m = \sum_{n=1}^{N} H_{mn} c_n = \sum_{n \in \mathcal{N}_m} H_{mn} c_n \in \mathbb{F}_q. \tag{3.15}$$

An IR-NB-LDPC code can be constructed using a sparse parity check matrix $\mathbf{H}$ with $|\mathcal{M}_n| \neq$ constant and $|\mathcal{N}_m| \neq$ constant.

3.4.1 Signed Log Fast Fourier Transform Decoding Algorithm

The Tanner graph can be used to express the decoding process of NB-LDPC code with the message-passing decoding algorithm in an effective way, which has a similar representation to that described in B-LDPC code. In the Tanner graph, the variable nodes are connected to the check nodes for the corresponding non-zero value of $\mathbf{H}$ [124].

Particularly, NB-LDPC codes can be decoded either in the probability domain or logarithmic domain. The latter has the advantage of reducing the decoding complexity and numerical stability. Hence, allowing us to decode NB-LDPC codes over large Galois fields and to achieve near Shannon performance and closer to the channel capacity for many future applications. A log-domain decoder with frequency domain implementation, i.e. FFT-based check node processing reduces the complexity from $\mathcal{O}(q^2)$ to $\mathcal{O}(q \log\ q)$ [126]. The Signed Log Fast Fourier Transform Decoding Algorithm (SL-FFT) decoding algorithm exhibits lower decoding complexity compared to other known decoding algorithms, which transform multiplication operations to addition operations in the logarithmic domain. Hence, reducing the decoding complexity, hardware cost and more suitable for hardware implementation. Therefore, it is adopted in this study. The decoding procedure of the SL-FFT algorithm and the signed-log domain utilizes in this algorithm are illustrated in Algorithm 2 and Algorithm 3, respectively, [127, 128].

Algorithm 2: LOG-FFT Decoding Algorithm

Initialization:

$\text{Iteration} = 1,$

$F^a_{q,k} = \log\left(\frac{p(Y_k|X_k=\mathbf{C}(a+1))}{p(Y_k|X_k=\mathbf{C}(1))}\right),\ a \in \mathbb{F}_q\backslash\{0\},$

$R^a_{m,n} = \mathbf{0},$

$Q^a_{m,n} = F^a_{q,k},$

while $\mathbf{H}\hat{\mathbf{X}} \neq \mathbf{0}$ and iteration $\leq$ max iteration **do**

  Permute $Q_{m,n}$ **according to** $a = \mathbf{H}_{m,n} \in \mathbb{F}_q\backslash\{0\}$

  $\widetilde{Q}_{m,n} = \mathcal{P}_a(Q_{m,n}),\ \ \forall m, n$

  Transform to signed-log domain: $\widetilde{\varphi}_{m,n} = (\widetilde{\varphi}_{m,n}(s), \widetilde{\varphi}_{m,n}(r))$**, with**

  $\widetilde{\varphi}_{m,n}(s) = 1,\ \widetilde{\varphi}_{m,n}(r) = \widetilde{Q}_{m,n},\ \forall m, n$, where s and r are the sign and magnitude of $\widetilde{Q}_{m,n}$

  Transform to Fourier domain using Fast Walsh-Hadamard Transform:

  $\widetilde{\Phi}_{m,n} = \texttt{FWHT}(\widetilde{\varphi}_{m,n}),\ \ \forall m, n$

  Update check node messages:

  $\widetilde{\Theta}_{m,n}(s) = \prod_{\tilde{k}\in\mathcal{N}_m\backslash n} \widetilde{\Phi}_{m,\tilde{k}}(s),\ \forall m, n$

  $\widetilde{\Theta}_{m,n}(r) = \sum_{\tilde{k}\in\mathcal{N}_m\backslash n} \widetilde{\Phi}_{m,\tilde{k}}(r),\ \forall m, n$

  Take the Inverse Fourier Transform for check nodes:

  $\widetilde{\theta}_{m,n} = \texttt{IFWHT}(\widetilde{\Theta}_{m,n}),\ \ \forall m, n$

  Extracted the magnitude using signed-log domain:

  $\widetilde{R}_{m,n} = \widetilde{\theta}_{m,n}(r),\ \ \forall m, n$

  Inverse permutation of $\widetilde{R}_{m,n}$ **according to**

  $a = \mathbf{H}_{m,n} \in \mathbb{F}_q\backslash\{0\}$**,**

  $R_{m,n} = \mathcal{P}_a^{-1}(\widetilde{R}_{m,n}),\ \ \forall m, n$

  Update variable nodes:

  $Q_{m,n} = F^a_{q,k} + \sum_{\tilde{k}\in\mathcal{M}_n\backslash m} R_{\tilde{k},n} - \alpha_{m,n}$**,**

  $\alpha_{m,n} = \max_a Q_{m,n}$

  Tentative decoding:

  $\hat{X}_k = \arg\max_a F^a_{q,k} + \sum_{\tilde{k}\in\mathcal{M}_n} R_{k,n},\ \ \forall k$

  Iteration = Iteration+1,

end

Algorithm 3: Signed-Log Domain

$$z(s) = \begin{cases} x(s) & x(s) = y(s) \quad \textbf{or} \quad x(m) \geq y(m) \\ -x(s) & \textbf{otherwise,} \end{cases}$$

$$\gamma = \begin{cases} 1 & x(s) = y(s) \\ -1 & \textbf{otherwise,} \end{cases}$$

$$z(m) = \max^*[x(m),\ y(m)] + \log(1 + \gamma e^{-|x(m)-y(m)|})$$

The LLR equations over $\mathbb{F}_4$ utilizes the constellation mapping $\mathbf{C}$ in Fig. 5.3 over AWGN

channel can be computed as

$$F_{4,k}^{0} = \mathbf{0}, \tag{3.16}$$

$$F_{4,k}^{1} = \log\left(\frac{p(Y_k|X_k = \mathbf{C}(2))}{p(Y_k|X_k = \mathbf{C}(1))}\right) = \frac{2(Y_k^{\Im} - Y_k^{\Re})}{\sigma_w^2}, \tag{3.17}$$

$$F_{4,k}^{2} = \log\left(\frac{p(Y_k|X_k = \mathbf{C}(3))}{p(Y_k|X_k = \mathbf{C}(1))}\right) = \frac{2(Y_k^{\Re} + Y_k^{\Im})}{\sigma_w^2}, \tag{3.18}$$

$$F_{4,k}^{3} = \log\left(\frac{p(Y_k|X_k = \mathbf{C}(4))}{p(Y_k|X_k = \mathbf{C}(1))}\right) = \frac{4Y_k^{\Im}}{\sigma_w^2}. \tag{3.19}$$

3.5 Binary Turbo Codes

A TC is an error correcting scheme invented by Berrou et al. [94] in 1993, and they were found to have excellent coding gain, approaching to Shannon capacity by using the iterative soft decoding algorithm. The reliable performance of TCs has led to adopting it as an iterative decoder in many standards, such as the third generation (3G) of mobile communications [129], satellite broadcasting [130] and IEEE P1901 draft standards [15].

Generally, Non-Recursive Convolutional (NRC) codes and Recursive Systematic Convolutional (RSC) codes are two types of convolutional code, in which the RSC gives better performance than the NRC code, especially at low SNR [94]. The Parallel concatenation of RSC codes with an interleaver between them such as Long-Term Evolution (LTE) interleaver and "puncturing" stage are used to construct the TC or a Parallel Concatenated Convolutional Code (PCCC). In fact, the original information sequence is encoded twice in Turbo encoder, then the outputs from the two RSC are punctured and multiplexed. A turbo encoder is often described by its generator polynomials in octal notation described as $G = (1, g_2/g_1, g_2/g_1)$, where the optimal generators of TC are presented in [56]. For example, for the case of the TC constructed using two identical RSC with (7,5) RSC1 and (7,5) RSC2, the generator matrix of the turbo encoder can be expressed as $G = (1, 5/7, 5/7)$. The information sequence X_s is fed to the RSC1 encoder to generate the parity check bits X_{p_1}. On the other branch, the information sequence X_s is interleaved and then fed to the RSC2 encoder to generate the parity check bits X_{p_2}. Finally, the puncturing mechanism is used to achieve the desired code rate as shown in Fig. 3.3

3.5.1 Max-Log-MAP Decoding Algorithm

An iterative decoding algorithm known as Bahl, Cocke, Jelinek, and Raviv (BCJR) algorithm was proposed by Bahl et al. in 1974 [131]. This algorithm is an optimal decoding algorithm

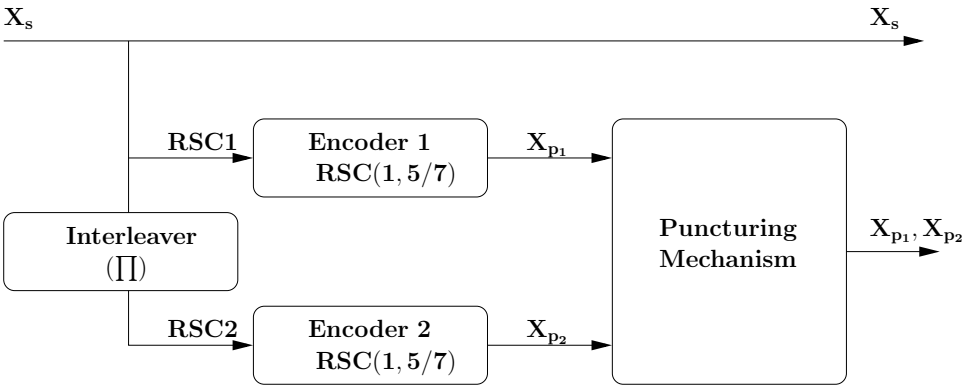

Figure 3.3: Turbo encoder implementation.

for maximizing A *Posteriori* Probability (APP) on the AWGN channel. The Turbo decoder utilizes two APP decoders corresponding to each RSC encoder in an iterative decoding algorithm, where each constituent RSC is decoded separately [132].

A Turbo decoder with the BCJR algorithm exhibits higher decoding complexity than Viterbi decoding algorithm. Therefore, a sub-optimal decoding algorithm has been used instead which is called the Max-Log-MAP [133,134]. This algorithm has been accepted for practical purposes to reduce the decoding complexity by converting the multiplication operations in MAP decoding algorithm to addition operations in the logarithmic domain, therefore, it is adopted in this thesis. The log forward/backward recursion formulas of the branch transition probabilities calculation of iterative Max-Log-MAP decoding algorithm is presented in Algorithm 4 which uses $\overset{*}{\max}$ operation defined in (5.13) [135].

Algorithm 4: Max-Log-MAP Algorithm

1 **Compute: branch metric γ_k^{LM}, forward recursion α_k^{LM} and backward recursion β_{k-1}^{LM} using Log-MAP decoding:**

$$\gamma_k^{LM}(s^{'}, s) = \frac{1}{2} L_c.y_{k,1}.u_k + \frac{1}{2}\sum_{v=2}^{n} L_c.y_{k,v}.x_{k,v} + \frac{1}{2} u_k.L(u_k),$$
$$\alpha_k^{LM}(s) = \max_{s'}^{*}\left(\gamma_k^{LM} + \alpha_{k-1}^{LM}\right),$$
$$\beta_{k-1}^{LM}(s^{'}) = \max_{s}^{*}\left(\gamma_k^{LM} + \beta_k^{LM}\right),$$

2 **Compute $\alpha_k^{MLM}, \beta_{k-1}^{MLM}$ and L using MAX-Log-MAP decoding:**

$$\alpha_k^{MLM}(s) = \max\left(\left[\gamma_{u_k=+1}^{LM}(s^{'}, s) + \alpha_{k-1}^{LM}(s^{'})\right], \left[\gamma_{u_k=-1}^{LM}(s^{'}, s) + \alpha_{k-1}^{LM}(s^{'})\right]\right),$$
$$\beta_{k-1}^{MLM}(s^{'}) = \max\left(\left[\gamma_{u_k=+1}^{LM}(s^{'}, s) + \beta_k^{LM}(s)\right], \left[\gamma_{u_k=-1}^{LM}(s^{'}, s) + \beta_k^{LM}(s)\right]\right),$$
$$L(\hat{u}_k) = \max_{u_k=+1}^{(s^{'},s)}\Bigg(\left[\gamma_k^{LM}(s^{'}, s) + \alpha_{k-1}^{MLM}(s) + \beta_k^{MLM}(s^{'})\right], \left[\gamma_k^{LM}(s^{'}, s) + \alpha_k^{MLM}(s) + \beta_k^{MLM}(s^{'})\right]\Bigg) - \max_{u_k=-1}^{(s^{'},s)}\Bigg(\left[\gamma_k^{LM}(s^{'}, s) + \alpha_{k-1}^{MLM}(s) + \beta_k^{MLM}(s^{'})\right], \left[\gamma_k^{LM}(s^{'}, s) + \alpha_k^{MLM}(s) + \beta_k^{MLM}(s^{'})\right]\Bigg),$$

3.5.2 EXIT Chart for Turbo Codes

The EXIT-chart method for TCs is approximately the same as that for LDPC codes. For PCCC, both decoders are directly connected to the *a priori* LLRs, so the the *extrinsic* information curves $\mathrm{I_{E_1}}$ and $\mathrm{I_{E_2}}$ for both decoders will depend on the values of $\frac{E_b}{N_0}$. However, The *extrinsic* output $\mathrm{I_{E_1}}/\mathrm{I_{E_2}}$ of the first/second decoder is used as *a priori* input to $\mathrm{I_{A_2}}/\mathrm{I_{A_1}}$ of the second/first decoder, then the *extrinsic* output $\mathrm{I_{E_2}}/\mathrm{I_{E_1}}$ of the second/first decoder is used as *a priori* input to $\mathrm{I_{A_1}}/\mathrm{I_{A_2}}$ of the first/second decoder and the same process is repeated [99, 117].

For each iteration, the extrinsic information vector $\mathrm{E_1}/\mathrm{E_2}$ at the first/second decoder output will be interleaved/deinterleaved to become the a priori information vector $\mathrm{A_1}/\mathrm{A_2}$ for the second/first decoder. The extrinsic information vector of both decoders can be expressed

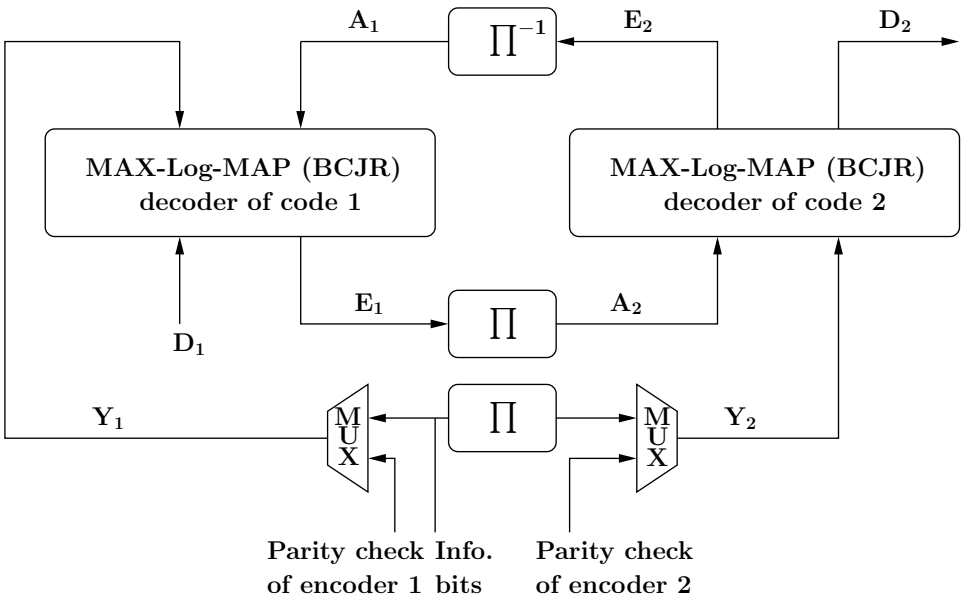

Figure 3.4: *A priori, extrinsic* and channel informations managed by a MAX-Log-MAP (BCJR) decoder.

as [99, 117]

$$E_1 = D_1 - A_1 - Y_1, \tag{3.20}$$

$$E_2 = D_2 - A_2 - Y_2, \tag{3.21}$$

where variables $E_1, D_1, A_1, Y_1, E_2, D_2, A_2, Y_2$ denote LLR values. The LLR values L_k of the received signal $Y_k = X_k + N_k$ over Gaussian noise with zero mean and variance σ^2 and for the transmitted BPSK symbols $X_k = \pm 1$ can be expressed as [99, 117]

$$L_k = \log \frac{p(Y_k|X_k = +1)}{p(Y_k|X_k = -1)} = \frac{2}{\sigma^2} Y_k = \frac{2}{\sigma^2}(X_k + N_k). \tag{3.22}$$

This can also be expressed in another form as

$$L_k = \mu_L x_k + N_L, \tag{3.23}$$

where μ_L and σ_L^2 are equal to $\frac{2}{\sigma^2}$ and $\frac{4}{\sigma^2}$, respectively, with $\mu_L = \frac{\sigma_L^2}{2}$. Thus, the *a priori* input A to the constituent decoder is modeled by a Gaussian distribution as

$$L_A = \mu_A x_k + N_A, \tag{3.24}$$

where N_A denotes the additive white Gaussian noise, therefore, the LLR values,L_A, can be computed based on Gaussian distributions with mean value $\mu_A = \frac{\sigma_A^2}{2}$ and variance σ_A^2. The conditional PDF belonging to the LLR value L_A can be expressed as

$$p_A(\xi|X=x) = \frac{1}{\sqrt{2\pi}\sigma_A} e^{-\frac{\left(\xi - \frac{\sigma_A^2}{2}x\right)^2}{2\sigma_A^2}}. \tag{3.25}$$

The mutual information $I_A = I(X;A)$ can be computed as [99, 117]

$$I_A = \frac{1}{2}\sum_{x=\pm 1}\int_{-\infty}^{+\infty} p_A(\xi|X=x)\log_2\left(\frac{2p_A(\xi|X=x)}{p_A(\xi|X=-1)+p_A(\xi|X=+1)}\right)d\xi, \tag{3.26}$$

where $0 \leq I_A \leq 1$ and $\sigma_a = J^{-1}(I_A)$. Following the same previous manner, I_E can be computed as

$$I_E = \frac{1}{2}\sum_{x=\pm 1}\int_{-\infty}^{+\infty} p_E(\xi|X=x)\log_2\left(\frac{2p_E(\xi|X=x)}{p_E(\xi|X=-1)+p_E(\xi|X=+1)}\right)d\xi, \tag{3.27}$$

where $0 \leq I_E \leq 1$. The extrinsic information transfer characteristics are defined as

$$I_E = T\left(I_A, \frac{E_b}{N_0}\right), \tag{3.28}$$

where the mutual information I_E is a function, $T(.)$, of the mutual information I_A and the $\frac{E_b}{N_0}$ value. Therefore, the EXIT curve needs to be plotted for each energy per bit to noise PSD ratio $\left(\frac{E_b}{N_0}\right)$ value.

3.5.3 Average Upper Bounds

The AUBs are used to analyze TCs at high SNR regions beyond simulation capabilities, where these AUBs are useful to predict the system performance and to determine the error floor region [136]. The AUB can be determined using the Input Redundancy Weight Enumerating Function (IRWEF) of the TC that constructed using two parallel convolutional codes. Firstly, the Conditional Weight Enumerating Function (CWEF) of each parallel convolutional codes can be expressed as $A_{im}^{C_1}(w,Z)$ and $A_{jl}^{C_2}(w,Z)$, which are derived from the transfer function of each parallel convolutional code. The normalized product of the CWEF can be computed as

$$A_{ij,ml}^{C_P}(w,Z) = \frac{A_{im}^{C_1}(w,Z)A_{jl}^{C_2}(w,Z)}{\binom{N}{w}}, \tag{3.29}$$

where $A^{C_i}(w, Z), i \in 1, 2$ is the CWEF of the parity check bits generated from the input words of weight w for the code C_i. Then, the IRWEF can be computed utilizing the normalized CWEF as

$$A^{C_P}(W, Z) = \sum_{w} W^w A^{C_P}_{ij,ml}(w, Z). \tag{3.30}$$

Finally, $A^{C_P}(W, Z)$ can be used to determine the union upper bound of the probability of error utilizing the maximum likelihood decoding as [56]

$$\begin{aligned} P_b &\leq \sum_{w=1}^{N} \frac{w}{N} W^w A^{C_P}(W, Z)\Big|_{W=Z=e^{-\frac{R_c E_b}{N_0}}} \\ &\approx \sum_{\nu} D_\nu P_\nu, \end{aligned} \tag{3.31}$$

and

$$D_\nu = \sum_{w=1}^{N} D_{w\nu} \frac{w}{N}, \tag{3.32}$$

where $D_{w\nu}$ is the number of code words that have a total weight ν for the input weight w. D_ν coefficients are tabulated in [136] for interleaver sizes of $100, 1000$ and 10000, respectively. The error probability of decoding the codeword $\mathbf{c}_2$ when transmitting the codeword $\mathbf{c}_1$ is defined as the the Pairwise Error Probability (PEP).The PEP or P_ν can be expressed over the AWGN channel as [136–138]

$$P_\nu = Q\left(\sqrt{2\nu R_c \frac{E_b}{N_0}}\right), \tag{3.33}$$

and over the Rayleigh fading channel as [136, 137]

$$P_\nu = q^\nu \sum_{k=0}^{\nu-1} \binom{\nu - 1 + k}{k} (1 - q)^k, \tag{3.34}$$

with

$$q = \frac{1}{2}\left(1 - \sqrt{\frac{\gamma_b R_c}{1 + \gamma_b R_c}}\right), \tag{3.35}$$

where E_b is the received energy per information bit, $\frac{N_0}{2}$ is the double-sided noise spectral density, $Q(x) = \frac{1}{\sqrt{2\pi}} \int_x^\infty e^{-\frac{z^2}{2}} dz$ and γ_b is the average $\frac{E_b}{N_0}$.

3.6 Complexity Analyses

The attention is now focusing on the complexity computations. The total number of maximization, addition, boxplus, multiplication and table look-up needed per one iteration for SPA, SL-FFT and Max-Log-MAP decoding algorithms are compared in table 3.6, where $n_c = 1008$, $k_c = 504$ and dv_i represented in table 3.1 for the case of SPA over $\mathbb{F}_2$. $n_c = 252$, $k_c = 126$, $q = 16$, $p = 4$ and d_v represented in table 3.1 for the case of SL-FFT over $\mathbb{F}_{16}$. $\mathcal{L} = 8$ is the number of states of TC in Max-Log-MAP algorithm for $G = (1, 5/7, 5/7)$ [127, 139–141].

Table 3.6: Complexity of different algorithms per one iteration

Algorithm	Maximization	Addition	Boxplus	Multiplication	Table look-up
SPA	0	$2\sum_{i=1}^{k_c} dv_i + 4(n_c - k_c) - 2$	$3\sum_{i=1}^{k_c} dv_i - 5$	0	0
SL-FFT	0	$n_c\bar{d}_v^2 q + (n_c - k_c)(\bar{d}_c^2 - 1)q$	0	0	$2(n_c - k_c)\bar{d}_c pq$
Max-Log-MAP	$5\mathcal{L} - 2$	$10\mathcal{L} - 2$	0	0	0

3.7 Other Near-Shannon Performance FEC Codes

Polar coding is a new technique stated in [142] based on the channel polarization method to achieve Shannon limits for large block length, and to be interesting contender for B-LDPC codes and NB-LDPC codes. Unfortunately, the performance of polar codes with short block length is not competitive to the performance of IR-B-LDPC codes and IR-NB-LDPC codes. This was in part due to weak minimum distance properties of these codes, the suboptimal nature of the standard successive cancellation algorithm and the decoder latency would increase linearly with the code length. Moreover, non-binary polar codes and binary polar codes constructed based on larger base matrix have not yet received much attention for practical purposes due to their high complexity.

On the other hand, the second type of TCs is the block turbo codes (BTCs) or turbo product code. The performance of TCs may be effected by the block size, interleaver design and code weight. The BER performance of the proposed convolutional (C)TCs outperform the BTCs in the waterfall region because it depends on the minimum code weight. While BTCs outperform CTCs at low SNR. Due to the hostile environment of the PLC channel, the high SNR are needed for reliable communication. Therefore, BTCs are not allowed in PLC channels [143].

3.8 Physical Layer Network Coding

A Two-way relay network (TWRN) [144] is a model that uses the relay node R to exchange information between two end nodes A and B. The relay and end nodes are operating in a half-duplex mode; i.e. the end nodes cannot transmit and receive at the same time. In a TWRN scheme, the information transmitted between end nodes A and B can take two, three or four time slots to exchange two packets in opposite directions [145, 146].

- In the four time slot transmission scheme: A sends the information message to R in the first time slot, then R forwards the information message to B in the second time slot with B remaining idle. Next, B sends the information message to R in the third time slot, and finally, R forwards the information message to A in the fourth time slot with A remaining idle. The Block diagram of two-way relaying systems with four time slots is shown in Fig. 3.5.

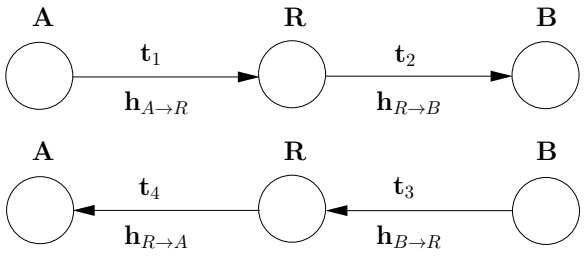

Figure 3.5: Two-way relaying systems with 4-time slot.

- In the three time slot transmission scheme: A sends the information message to R during the first time slot, while B sends the information message to R during the second time slot. Then R broadcasts the XOR-ed sum of the messages in the case of binary transmission to both A and B during the third time slot. The Block diagram of two-way relaying systems with three time slots is shown in Fig. 3.6.

- In the two time slot transmission scheme or PLNC, the first time slot or the Multiple Access (MA) stage, A and B send the information message simultaneously to R. While in the second time slot or the Broad Cast (BC) stage, the superimposed signals at the relay forwards the EX-OR sum of the messages in the case of binary transmission to both A and B. The block diagram of two-way relaying systems with two time slots is shown in Fig. 3.7.

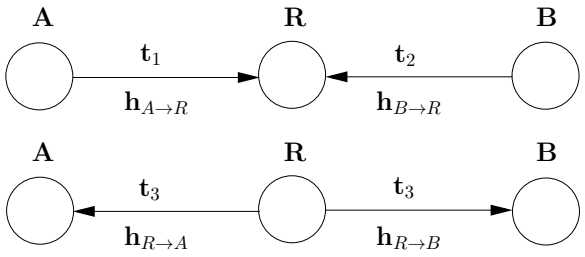

Figure 3.6: Two-way relaying systems with 3-time slot.

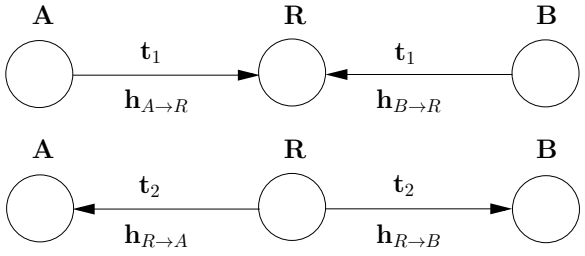

Figure 3.7: Two-way relaying systems with 2-time slot.

In PLNC, the relay assists the bidirectional communication between end nodes A and B. Therefore, one of the most important properties of PLNC is the use of two time slots to exchange the information and to achieve doubles capacity, i.e. increase the system throughput by 100% compared to the four time slot transmission scheme, but with lower sum-BER.

The two main relaying protocols are Denoise and Forward (DNF) and Amplify and Forward (AF) [147]. In the AF protocol, the relay simply forwards an amplified superimposed signal in the last time-slot to the destinations. This method suffers from noise amplification and low effective power which leads to BER degradation. While, in DNF protocol, the relay directly removes the noise from the superimposed signal, then re-transmits the noise free signal to the end nodes. Therefore, the DNF protocol has better BER performance than the AF protocol. Moreover, better BER performance can be achieved by using Decode and Forward (DF) protocol which is obtained by combing DNF protocol with error control coding [148].

On the other hand, different works have been proposed in the literature to improve the BER performance of PLNC systems, these research can be summarized as

- In [145], the performance of PLNC schemes over two, three and four time slots for a network consisting of two end nodes and a relay node has been investigated. It has been shown that the time slot plays a key factor between the data throughput and the BER performance of PLNC scheme. For example, when the time slot decreases, the data through-

put will increase but with more BER degradation and vice versa. Moreover, closed-form expressions have been derived for the outage probability, maximum sum rate and sum-BER. Monte-Carlo simulations have been investigated that the multiple relay nodes can significantly reduce the sum-BER.

- In [149], the modulation schemes optimized for PLNC system have been investigated. The design of QPSK modulation and network coding at the relay have been showed that the XOR network coding at the relay does not always offer the better mapping transmission for the BC stage, hence, the unconventional 5ary constellations can be achieved higher E2E data throughput for PLNC system under several conditions.

- In [150], the error performance of the uncoded BPSK for PLNC which consists of two end nodes and a relay node over Rayleigh fading channels has been analyzed. In this paper, both nodes have been worked in half-duplex mode. The ML detection metric for the superimposed signals at the relay has been approximated by adopting the max-log approximation. The tight upper/lower error bounds at the relay and E2E have been derived.

- In [151], the LBL-coded PLNC has been investigated. This paper shows that there is a compatible decoder that in-able to map the superimposed signal at the relay efficiently for the Repeat Accumulate code that used at the end nodes. For this reason, the belief propagation decoding algorithm of the Repeat Accumulate code has been a redesign for PLNC system. Simulation results show that the proposed scheme outperforms the conventional schemes in terms of BER with moderate scheme complexity.

- In [152], the design of modulation schemes for coded-PLNC have been investigated. The DNF protocol has been proposed for the coded-PLNC scheme, which consists MA stage and BC stage. Two approaches have been proposed regarding problems in DNF protocol in the MA stage. The first approach utilizes QPSK constellation at the BC stage, while the second one utilizes the unconventional 5ary modulations which optimized according to the Nakagami-Rice fading channels condition. Monte-Carlo simulation shows a big improvement in E2E throughput can be achieved over the used channel.

- In [153], the PLNC scheme has been used to increase the data throughput by 100% and 50% with respect to conventional transmission in wireless networks. It also shows a double capacity improvement can be achieved over than the traditional point to point

transmission and point to point network coding by using a relay node between two source nodes in proposed two-time slot PLNC scheme.

- In [154], the design of irregular repeat accumulate code has been proposed and analyzed for PLNC based on soft information computations. It is assumed the superimposed signal has synchronized and equal power at the relay. In this paper, the construction of irregular repeat accumulate code has been optimized based on the EXIT chart analysis for binary-input Gaussian PLNC scheme. Monte-Carlo simulation result shows the optimized code outperforms the conventional code over different scenarios of coding rate.

3.8.1 Multiple Access Stage

The DNF scheme consists of MA stage and BC stage. During MA stage, let A and B communicate with each other using OFDM system with BPSK modulation expressed as $X_A = \mathcal{M}(b^A)$ and $X_B = \mathcal{M}(b^B)$, respectively, where b^A and b^B represents the uncoded data symbols of 1-bit binary representation and $\mathcal{M}(.)$ represents the modulated data. The received superimposed signal in the first time slot at the relay R node in the frequency domain over the PLC channel can be expressed as

$$\begin{aligned} Y_R(t_1,k) &= H_{A\to R}(k)X_A(t_1,k) + H_{B\to R}(k)X_B(t_1,k) + W_R(k), \\ &\forall k = 0,1,2,\cdots,N-1, \end{aligned} \tag{3.36}$$

where $H_{A\to R}(k)$ and $H_{B\to R}(k)$ are the complex-valued channel coefficients in the frequency domain from A to R and from B to R, respectively, and W_R represents the complex Gaussian noise at the relay in the case of free impulsive noise. The relay R employs a mapping function based on the received superimposed signal Y_R to a new signal, expressed as $\hat{b}^R \equiv b^A \oplus b^B$ in the case of BPSK modulation. The modulation mapping at the end nodes A and B, the demodulation and modulation mapping at the R can be expressed as shown in Table 3.7 for noise free level. For the sake of simplicity, the index k will be removed from the equations inside the table.

The ML detection rule utilizing Table 3.7 can be expressed as [150]

Table 3.7: PLNC mapping in PLC channel.

Modulation mapping						Demodulation mapping		
b^A	b^B	$X_A(b^A)$	$X_B(b^B)$	$H_{A\to R}X_A(b^A)$	$H_{B\to R}X_B(b^B)$	Superimposed signal at R	Modulation mapping at R	
						$H_{A\to R}X_A(b^A)+H_{B\to R}X_B(b^B)$	$\hat{b}^R=b^A\oplus b^B$	X_R
0	0	-1	-1	$-H_{A\to R}$	$-H_{B\to R}$	$-H_{A\to R}-H_{B\to R}$	0	-1
0	1	-1	1	$-H_{A\to R}$	$H_{B\to R}$	$-H_{A\to R}+H_{B\to R}$	1	1
1	0	1	-1	$H_{A\to R}$	$-H_{B\to R}$	$H_{A\to R}-H_{B\to R}$	1	1
1	1	1	1	$H_{A\to R}$	$H_{B\to R}$	$H_{A\to R}+H_{B\to R}$	0	-1

$$\frac{\sum_{b^A\oplus b^B=0}\exp\left(-\frac{\left|Y_R-\left(H_{A\to R}X_A(b^A)+H_{B\to R}X_B(b^B)\right)\right|^2}{2\sigma_w^2}\right)}{\sum_{b^A\oplus b^B=1}\exp\left(-\frac{|Y_R-(H_{A\to R}X_A(b^A)+H_{B\to R}X_B(b^B))|^2}{2\sigma_w^2}\right)}\underset{\hat{b}^R=1}{\overset{\hat{b}^R=0}{\gtrless}}1, \tag{3.37}$$

and the relay makes the decision based on the received superimposed signal Y_R as $\hat{b}^R \equiv b^A \oplus b^B$. Moreover, the superimposed signal at the relay over the AWGN channels can be expressed as

$$\begin{aligned} Y_R(t_1,k) &= X_A(t_1,k)+X_B(t_1,k)+W_R(k),\\ &\forall k=0,1,2,\cdots,N-1. \end{aligned} \tag{3.38}$$

The modulation mapping at the end nodes A and B, the demodulation and modulation mapping at R are shown in Table 3.8.

Table 3.8: PLNC mapping in AWGN channel.

Modulation mapping				Demodulation mapping		
b^A	b^B	$X_A(b^A)$	$X_B(b^B)$	$X_A(b^A)+X_B(b^B)$	Modulation mapping at R	
					$\hat{b}^R=b^A\oplus b^B$	X_R
0	0	-1	-1	-2	0	-1
0	1	-1	1	0	1	1
1	0	1	-1	0	1	1
1	1	1	1	2	0	-1

The ML detection rule utilizing Table 3.8 can be expressed as

$$\frac{\sum_{b^A\oplus b^B=0}\exp\left(-\frac{\left|Y_R-\left(X_A(b^A)+X_B(b^B)\right)\right|^2}{2\sigma_w^2}\right)}{\sum_{b^A\oplus b^B=1}\exp\left(-\frac{|Y_R-(X_A(b^A)+X_B(b^B))|^2}{2\sigma_w^2}\right)}\underset{\hat{b}^R=1}{\overset{\hat{b}^R=0}{\gtrless}}1. \tag{3.39}$$

3.8.2 Broadcast Phase

During the broadcast or downlink phase, t_2, the relay broadcasts the modulated mapping signal $X_R \in \{-1, 1\}$ in the case of BPSK constellation depending on the detected bit $\hat{b}^R \in \{0, 1\}$ to both users A and B. The received signal $Y_D(t_2, k)$ over PLC channel can be expressed as

$$Y_D(t_2, k) = H_{R\to D}(k)X_R(t_2, k) + W_D(k), \tag{3.40}$$

where $D \in \{A, B\}$, $Y_D(t_2, k)$ is the received signal in the frequency domain at end nodes A and B, $H_{R\to D}(k)$ denote the complex-valued channel coefficients in the frequency domain from R to A and from R to B and $W_D(k)$ represents the AWGN at the end nodes in the case of free impulsive noise. The ML detection rule at the user A and B can be expressed as

$$\frac{\exp\left(-\frac{|Y_D+H_{R\to D}|^2}{2\sigma_w^2}\right)}{\exp\left(-\frac{|Y_D-H_{R\to D}|^2}{2\sigma_w^2}\right)} \underset{\hat{b}^D=1}{\overset{\hat{b}^D=0}{\gtrless}} 1. \tag{3.41}$$

Moreover, the received signal $Y_D(t_2, k)$ over the AWGN channels can be expressed as

$$Y_D(t_2, k) = X_R(t_2, k) + W_D(k). \tag{3.42}$$

The ML detection rule at the user A and B can be expressed as

$$\frac{\exp\left(-\frac{|Y_D+1|^2}{2\sigma_w^2}\right)}{\exp\left(-\frac{|Y_D-1|^2}{2\sigma_w^2}\right)} \underset{\hat{b}^D=1}{\overset{\hat{b}^D=0}{\gtrless}} 1. \tag{3.43}$$

Both users can detect the transmitted data from user A and B by EX-ORing the detected data with the user's own information data. From the fact that each end node knows its own message signal, indeed, the message from the user A can be detected at node B in free noise level as

$$\hat{b}^A = \hat{b}^B \oplus b^B, \tag{3.44}$$

and the message from user B can be detected at node A in free noise level as

$$\hat{b}^B = \hat{b}^A \oplus b^A. \tag{3.45}$$

3.9 Summary of the Chapter

In this chapter, different FEC codes are proposed to combat multipath effects over PLC channels and to mitigate the NGN. This chapter has also given the details of the construction of B-LDPC codes, NB-LDPC codes and TCs, in addition to the decoding algorithms such as SPA, SL-FFT and Max-Log-MAP which are used to decode these codes, respectively, which usually leads to significant BER improvement over PLC channel in the presence of IN. The proposed iterative decoders for OFDM schemes are inherently more robust to IN than iterative decoders for single carrier scheme. Moreover, to analyze the convergence behaviour of B-LDPC codes and TCs, EXIT charts analysis have been presented in detail. Furthermore, the AUB of TCs has been described to predict the system BER performance. On the other hand, PLNC has been proposed for PLC systems to achieve higher maximum sum rates and to exchange full E2E packet through the relay node when no connection available between two nodes.

Chapter 4

Uncoded OFDM Systems

4.1 Introduction

The Non-Gaussian nature of the noise over PLC channels leads to sub-optimal performance when using Gaussian distribution in the receiver detector. Therefore, in this chapter, novel exact noise PDFs at the ZF equalizer output in the presence of NGN have been derived in order to optimize the signal detection at the OFDM receiver. Thus, improving the performance of the coded systems in the next chapter. Therefore, the derived system has been analyzed based on deriving low complexity clipping and blanking thresholds with exact BER.

The BER performance of uncoded OFDM system over PLC channels impaired by different scenarios of NGN have been analysed and evaluated using Monte-Carlo simulation. The Nakagami-m and Middletons class A are two accurate models have utilized to represent the BI noise and the IN, respectively, over PL systems, therefore, both of them are adopted in this thesis. The Middletons class A model can also be simplified to Bernoulli-Gaussian mixture model to characterize the IN. The Bernoulli-Gaussian mixture model has a lower complexity in hardware implementations, therefore, it has been adopted in this chapter. Moreover, the performance of OFDM system has been improved by utilizing ML detectors based on the closed-form noise distributions at the ZF equalizer output. On the other hand, the non-linearity thresholds are usually obtained using Monte-Carlo simulation as BER cost function or by complex analytical expression formulas [69,72,80]. Therefore, low complexity threshold formulas for clipping and blanking IN mitigation methods have been derived in this chapter.

4.2 OFDM System over PLC Channels

The block of information bits $\mathbf{d} = \{d_0, d_1, \ldots, d_{k-1}\}$ for $d_k \in \{0, 1\}$ are first divided into groups of κ bits and then mapped unto to the 2^κ symbols of a M-ary QAM constellation, i.e. for a κ-tuple $\{b_m, b_{m+1}, \ldots b_{m+\kappa-1}\}$ of bits, the corresponding M-ary QAM symbol in the frequency domain can be expressed as $X_k = \mathbf{C}\left[\sum_{m=0}^{\kappa-1} 2^{\kappa-1-m} b_m\right]$, where $\mathbf{C} \in \mathbb{C}^{2^\kappa \times 1}$ is the Gray-encoded constellation vector. The complex base-band OFDM signal in the time domain can be implemented using an N-points IFFT as [155]

$$x_n = \frac{1}{\sqrt{N}} \sum_{k=0}^{N-1} X_k e^{j2\pi kn/N}, n = 0, 1, \cdots, N-1, \tag{4.1}$$

where N is the number of sub-carriers. To eliminate ISI between consecutive OFDM symbols in PLC channels, a time-domain CP of length N_{CP} samples which is designed to exceed the maximum PLC channel delay spread τ_L, is inserted at the beginning of each OFDM symbol by copying the last N_{CP} samples of the IFFT output $\mathbf{x}$ and appending them at the beginning of $\mathbf{x}$ to produce the transmitted symbol $\tilde{\mathbf{x}}$ of length $N_t = N + N_{CP}$ samples which can be expressed as $\tilde{\mathbf{x}} = [x_{N-N_{CP}}, x_{N-N_{CP}+1}, \ldots, x_{N-1}, x_0, x_1, \ldots, x_{N-1}]$. The OFDM symbol in the time domain is then spread through the PL channel. The frequency response (FR) of the PLC channel, $H(f)$, which is exhibiting L paths can be modelled by using Zimmermann and Dostert model as [8, 156]

$$H(f) = \sum_{i=1}^{L} \underbrace{g_i}_{\text{weighting}} \underbrace{e^{-(a_0+a_1 f^k)d_i}}_{\text{attenuation}} \underbrace{e^{-j2\pi f \frac{d_i}{v_p}}}_{\text{delay}}. \tag{4.2}$$

The validity of Zimmermann and Dostert model has been checked by the Alternative Transients Program-Electromagnetic Transients Program (ATP-EMTP) [156]. It has been found that the amplitude of the Zimmermann and Dostert model and that predicted by ATP-EMTP software are similar, while the time delay in the Zimmermann and Dostert model and ATP-EMTP software is different. Therefore, the time delay problem in Zimmermann and Dostert model has been resolved in the modified Zimmermann and Dostert model by removing the distance parameter d_i in the attenuation term to achieve matching results to the ATP-EMTP software [156]. The proposed discrete-time complex-baseband model of the OFDM transmission system over PLC channels is shown in the Fig. 4.1.

Under perfect synchronization and ISI compensation, the received signal $\tilde{y}_n$ in the time

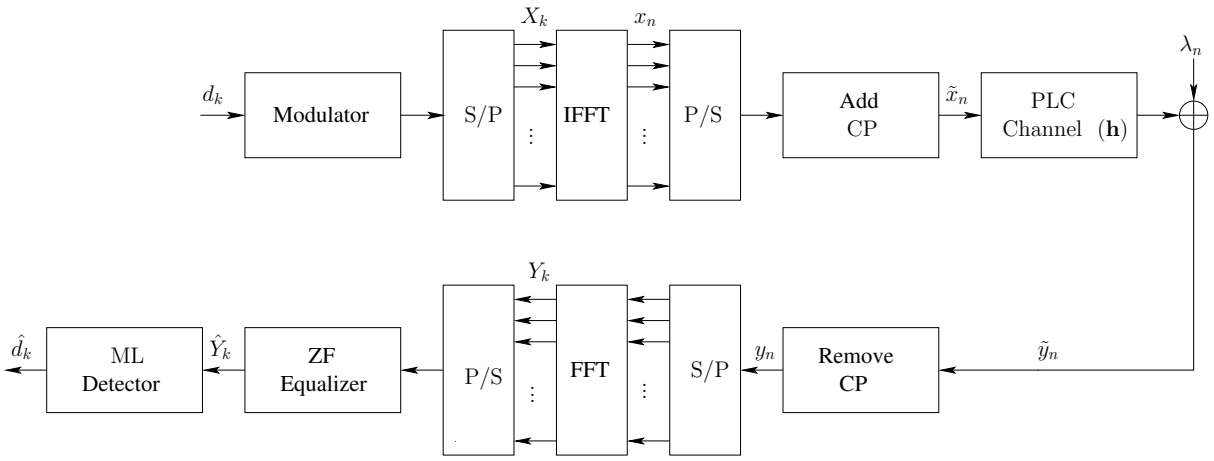

Figure 4.1: Block diagram of the proposed OFDM system over PLC channel.

domain can be expressed as:

$$\tilde{y}_n = \sum_{i=0}^{L-1} h_i \tilde{x}_{n-i} + \lambda_n, \;\; 0 \leq n \leq N + N_{CP} - 1, \tag{4.3}$$

where $\{h_i\}_{i=0}^{L-1}$ are the coefficients of the discrete impulse response of the multipath PLC channel in the time domain, L is the channel length and $\boldsymbol{\lambda} = [\lambda_0, \lambda_1, \ldots, \lambda_{N+N_{CP}-1}]$ denotes the total NGN samples in the time domain. The NGN samples include the Nakagami-m BI noise and IN modulated either by utilizing BGMIN model or the MCAIN model. Thus, λ_n can be expressed as $\lambda_n = b_n + i_n$, where b_n is the BI noise with the real and imaginary components expressed as $b_n^{\Re} = |\tilde{b}_n| \cos(\theta_n)$ and $b_n^{\Im} = |\tilde{b}_n| \sin(\theta_n)$, respectively, where $|\tilde{b}_n|$ expressed in (2.3) and i_n is the IN. The received complex signal after CP removal can be expressed as $\mathbf{y} = [y_0, y_1, \ldots, y_{N-1}]$. After performing the FFT operation for all sub-carriers $k = 0, 1, \ldots, N-1$, the received signal in the frequency domain can be expressed as

$$Y_k = \frac{1}{\sqrt{N}} \sum_{n=0}^{N-1} y_n e^{\frac{-j2\pi nk}{N}} = H_k X_k + \Lambda_k, \tag{4.4}$$

where H_k and X_k are the channel transfer function of the modified PLC channel for the k-th sub-carrier and the modulated symbols, respectively. Λ_k represents the FFT of the total NGN samples λ_n at the receiver expressed as

$$\Lambda_k = \frac{1}{\sqrt{N}} \sum_{n=0}^{N-1} \lambda_n e^{\frac{-j2\pi nk}{N}}. \tag{4.5}$$

The magnitude of the modified PLC channel $|H_k| = \sqrt{(H_k^{\Re})^2 + (H_k^{\Im})^2}$ exhibits a Rayleigh

distribution of two degrees of freedom, i.e. [156]

$$p_H(|H_k|) = \frac{|H_k|}{\sigma_h^2} e^{\left(\frac{-|H_k|^2}{2\sigma_h^2}\right)}, \;\; |H_k| \geq 0, \tag{4.6}$$

and the phase, $\phi_{H_k} = \tan^{-1}\left(\frac{H_k^{\Im}}{H_k^{\Re}}\right)$, is uniformly distributed as

$$p_\phi(\phi_{H_k}) = \frac{1}{2\pi} \quad \text{for} \quad -\pi \leq \phi_{H_k} < \pi, \tag{4.7}$$

where $H_k^{\Re}$ and $H_k^{\Im}$ are zero-mean statistically independent orthogonal Gaussian random variables (RVs) and their variances are $\sigma_h^2 = \frac{1}{2}$ per dimension. The simulation results are correctly investigated the magnitude of the channel in (4.2) has a Rayleigh distribution and the phase has a uniform distribution as shown in the Fig. 4.2.

The received data symbols can be recovered by using ZF equalizer after the N-point FFT operation in (4.4) as

$$\begin{aligned} C_k^{\text{ZF}} Y_k &= X_k + C_k^{\text{ZF}} \Lambda_k, \\ \frac{Y_k^{\Re} + jY_k^{\Im}}{H_k^{\Re} + jH_k^{\Im}} &= X_k^{\Re} + jX_k^{\Im} + \frac{\Lambda_k^{\Re} + j\Lambda_k^{\Im}}{H_k^{\Re} + jH_k^{\Im}}, \\ \hat{Y}_k^{\Re} + j\hat{Y}_k^{\Im} &= X_k^{\Re} + jX_k^{\Im} + \hat{Z}_k^{\Re} + j\hat{Z}_k^{\Im}, \end{aligned} \tag{4.8}$$

where $C_k^{\text{ZF}} = \frac{1}{H_k^{\Re} + jH_k^{\Im}}$ are the complex-valued of the ZF equalizer, $\hat{Y}_k^{\Re} + j\hat{Y}_k^{\Im} = C_k^{\text{ZF}} Y_k = \frac{Y_k^{\Re} + jY_k^{\Im}}{H_k^{\Re} + jH_k^{\Im}}$ are the complex-valued equalized received signal and $\hat{Z}_k^{\Re} + j\hat{Z}_k^{\Im} = C_k^{\text{ZF}} \Lambda_k = \frac{\Lambda_k^{\Re} + j\Lambda_k^{\Im}}{H_k^{\Re} + jH_k^{\Im}}$ are the complex-valued equalized NGN samples for the k-th sub-carrier.

4.3 Derivation of the Effective Noise Distributions at the ZF Equalizer Output

4.3.1 Distribution of the Impulsive Noise based on MCAIN Model

In the presence of complex IN modelled by MCAIN model, λ_n in (4.3) can be expressed as $\lambda_n^{\Re} = i_n^{\Re}$ and $\lambda_n^{\Im} = i_n^{\Im}$ representing the real and imaginary components of IN, respectively [5, 7]. The real, the imaginary and the joint distributions in the time domain can be expressed

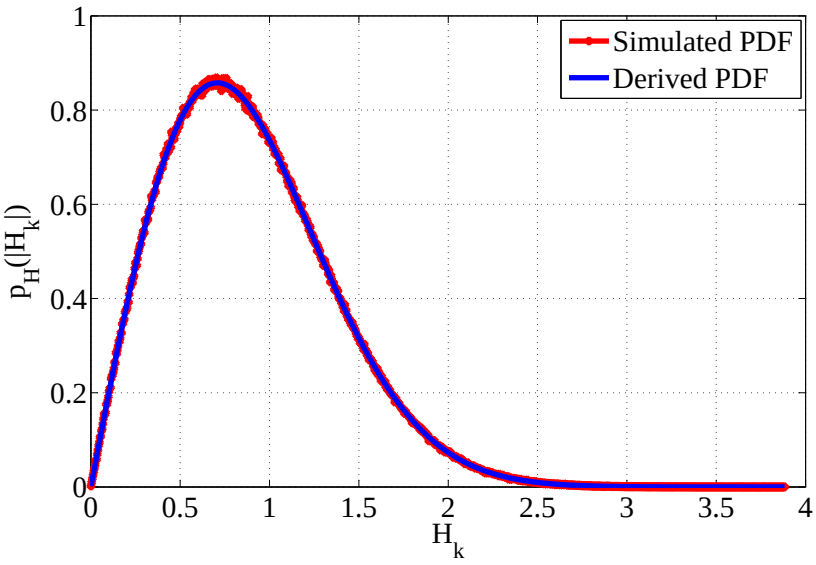

(a) Magnitude of the PLC channel in the frequency domain.

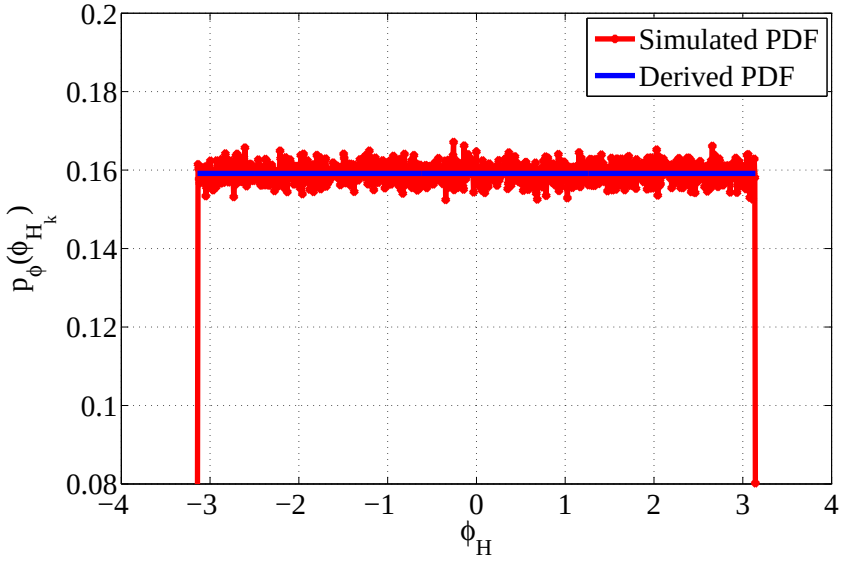

(b) Phase of the PLC channel in the frequency domain.

Figure 4.2: Magnitude and phase of the complex PLC channel.

as [5, 7, 50]

$$p_A(\lambda_n^{\Re}) = p_A(i_n^{\Re}) = \sum_{\ell=0}^{\infty} \frac{e^{-A}A^{\ell}}{\ell!} \frac{1}{\sqrt{2\pi\sigma_\ell^2}} e^{\left(-\frac{(i_n^{\Re})^2}{2\sigma_\ell^2}\right)},$$
$$p_A(\lambda_n^{\Im}) = p_A(i_n^{\Im}) = \sum_{\ell=0}^{\infty} \frac{e^{-A}A^{\ell}}{\ell!} \frac{1}{\sqrt{2\pi\sigma_\ell^2}} e^{\left(-\frac{(i_n^{\Im})^2}{2\sigma_\ell^2}\right)}, \tag{4.9}$$

$$p_A(\lambda_n^{\Re}, \lambda_n^{\Im}) = p_A(i_n^{\Re}, i_n^{\Im}) = \sum_{\ell=0}^{\infty} \frac{e^{-A}A^{\ell}}{\ell!} \frac{1}{2\pi\sigma_\ell^2} e^{\left(-\frac{(i_n^{\Re})^2}{2\sigma_\ell^2}\right)} e^{\left(-\frac{(i_n^{\Im})^2}{2\sigma_\ell^2}\right)}. \tag{4.10}$$

The FFT operation spreads the IN over multiple sub-carriers in (4.4). Hence, the noise on each sub-carrier exhibits a Gaussian distribution, which can be determined using a statistical approximation. According to the Central Limit Theorem (CLT) [157], the noise distribution of $p_\Lambda(\Lambda_k^r)$ in the frequency domain will be approaching a normal distribution [2], with mean $\mu_A = 0$ and variance σ_A^2, and $r = \{\Re, \Im\}$ represents the real and imaginary components, respectively. The noise variance can be computed per each dimension as

$$\begin{aligned}\mu_i^r = \mathbb{E}\{i_n^r\} &= \int_{-\infty}^{\infty} i_n^r p(i_n^r) di_n^r = \int_{-\infty}^{\infty} i_n^r \sum_{\ell=0}^{\infty} \frac{e^{-A}A^\ell}{\ell!} \frac{1}{\sqrt{2\pi\sigma_\ell^2}} e^{\left(-\frac{(i_n^r)^2}{2\sigma_\ell^2}\right)} di_n^r \\ &= \sum_{\ell=0}^{\infty} \frac{e^{-A}A^\ell}{\ell!} \int_{-\infty}^{\infty} \frac{i_n^r}{\sqrt{2\pi\sigma_\ell^2}} e^{\left(-\frac{(i_n^r)^2}{2\sigma_\ell^2}\right)} di_n^r = 0, \end{aligned} \tag{4.11}$$

$$\begin{aligned}\mathbb{E}\{(i_n^r)^2\} &= \int_{-\infty}^{\infty} (i_n^r)^2 p(i_n^r) di_n^r = \int_{-\infty}^{\infty} (i_n^r)^2 \sum_{\ell=0}^{\infty} \frac{e^{-A}A^\ell}{\ell!} \frac{1}{\sqrt{2\pi\sigma_\ell^2}} e^{\left(-\frac{(i_n^r)^2}{2\sigma_\ell^2}\right)} di_n^r \\ &= \sum_{\ell=0}^{\infty} \frac{e^{-A}A^\ell}{\ell!} \int_{-\infty}^{\infty} \frac{(i_n^r)^2}{\sqrt{2\pi\sigma_\ell^2}} e^{\left(-\frac{(i_n^r)^2}{2\sigma_\ell^2}\right)} di_n^r = \sum_{\ell=0}^{\infty} \frac{\sqrt{\pi} e^{-A}A^\ell (2\sigma_\ell^2)^{\frac{3}{2}}}{2\sqrt{2\pi}\ell!\sigma_\ell} \\ &= \sum_{\ell=0}^{\infty} \frac{e^{-A}A^\ell}{\ell!} \sigma_\ell^2 = \sum_{\ell=0}^{\infty} \frac{e^{-A}A^\ell}{\ell!} \sigma_w^2 \left(\frac{\ell}{A\rho} + 1\right), \end{aligned} \tag{4.12}$$

where $\mathbb{E}\{\cdot\}$ is the expectation value. Therefore, the variance σ_A^2 can be computed as

$$\sigma_A^2 = \mathbb{E}\{(i_n^r)^2\} - (\mathbb{E}\{i_n^r\})^2 = \sum_{\ell=0}^{\infty} \frac{e^{-A}A^\ell}{\ell!} \sigma_w^2 \left(\frac{\ell}{A\rho} + 1\right). \tag{4.13}$$

While for the case of simplified MCAIN model defined in (2.26), ℓ take values 0 and 1. The variance σ_A^2 can be computed as

$$\begin{aligned}\sigma_A^2 &= e^{-A}\sigma_w^2 + (1 - e^{-A})\sigma_w^2 \left(1 + \frac{1}{A\rho}\right) \\ &= \sigma_w^2 + (1 - e^{-A})\frac{\sigma_w^2}{A\rho}, \end{aligned} \tag{4.14}$$

where σ_w^2 is the AWGN variance, respectively. Therefore, the distribution of the real and imaginary components after FFT operation can be expressed as

$$p_\Lambda(\Lambda_k^{\Re}) = p_I(I_k^{\Re}) = \frac{1}{\sqrt{2\pi\sigma_A^2}} e^{\left(-\frac{(I_k^{\Re})^2}{2\sigma_A^2}\right)},$$
$$p_\Lambda(\Lambda_k^{\Im}) = p_I(I_k^{\Im}) = \frac{1}{\sqrt{2\pi\sigma_A^2}} e^{\left(-\frac{(I_k^{\Im})^2}{2\sigma_A^2}\right)}. \tag{4.15}$$

The covariance function between two vectors $I_k^{\Re}$ and $I_k^{\Im}$ can be defined for each pair of components as [158, 159]

$$\begin{aligned}\mathrm{cov}(I_k^{\Re}, I_k^{\Im}) &= \mathbb{E}\left\{(I_k^{\Re} - \mu_{I_k^{\Re}})(I_k^{\Im} - \mu_{I_k^{\Im}})\right\} \\ &= \mathbb{E}\{I_k^{\Re} I_k^{\Im}\} - \mathbb{E}\{I_k^{\Re}\}\mathbb{E}\{I_k^{\Im}\}. \end{aligned} \tag{4.16}$$

The expectation of $I_k^{\Re} I_k^{\Im}$ can be computed as

$$\begin{aligned} E\{I_k^{\Re} I_k^{\Im}\} &= \int_{-\infty}^{\infty}\int_{-\infty}^{\infty} I_k^{\Re} I_k^{\Im}\, p(I_k^{\Re}, I_k^{\Im})\, dI_k^{\Re} dI_k^{\Im} \\ &= \int_{-\infty}^{\infty}\int_{-\infty}^{\infty} \frac{I_k^{\Re} I_k^{\Im}}{2\pi\sigma_A^2} e^{\left(\frac{-(I_k^{\Re})^2-(I_k^{\Im})^2}{2\sigma_A^2}\right)}\, dI_k^{\Re} dI_k^{\Im} \\ &= \int_{-\infty}^{\infty} 0\, dI_k^{\Im} \\ &= 0, \end{aligned} \tag{4.17}$$

and

$$\begin{aligned} E\{I_k^{\Re}\} &= \int_{-\infty}^{\infty} I_k^{\Re}\, p(I_k^{\Re})\, dI_k^{\Re} \\ &= \int_{-\infty}^{\infty} \frac{I_k^{\Re}}{\sqrt{2\pi\sigma_A^2}} e^{\left(-\frac{(I_k^{\Re})^2}{2\sigma_A^2}\right)}\, dI_k^{\Re} = 0 \end{aligned} \tag{4.18}$$

$$\begin{aligned} E\{I_k^{\Im}\} &= \int_{-\infty}^{\infty} I_k^{\Im}\, p(I_k^{\Im})\, dI_k^{\Im} \\ &= \int_{-\infty}^{\infty} \frac{I_k^{\Im}}{\sqrt{2\pi\sigma_A^2}} e^{\left(-\frac{(I_k^{\Im})^2}{2\sigma_A^2}\right)}\, dI_k^{\Im} = 0, \end{aligned} \tag{4.19}$$

hence, the covariance can be determined using (4.16) as

$$\mathrm{cov}(I_k^{\Re}, I_k^{\Im}) = 0. \tag{4.20}$$

In this case, $I_k^{\Re}$ and $I_k^{\Im}$ are uncorrelated, i.e., their $\mathrm{cov}(I_k^{\Re}, I_k^{\Im})$ is zero, hence $I_k^{\Re}$ and $I_k^{\Im}$ are independent RVs [160]. Therefore, the joint probability $p_\Lambda(\Lambda_k^{\Re}, \Lambda_k^{\Im})$ can be expressed by the product of the individual probability, i.e,

$$p_\Lambda(\Lambda_k^{\Re}, \Lambda_k^{\Im}) = p_I(I_k^{\Re}, I_k^{\Im}) = \frac{1}{2\pi\sigma_A^2} e^{\left(-\frac{(I_k^{\Re})^2+(I_k^{\Im})^2}{2\sigma_A^2}\right)}. \tag{4.21}$$

Hence, the magnitude and phase of IN can be expressed as $|I_k| = \sqrt{(I_k^{\Re})^2 + (I_k^{\Im})^2}$ and $\phi_{I_k} = \tan^{-1}\left(\frac{I_k^{\Im}}{I_k^{\Re}}\right)$, respectively. The distribution of the $|I_k|$ and ϕ_{I_k} can be computed using the joint PDF $p(I_k^{\Re}, I_k^{\Im})$ for $I_k^{\Re} \leq X + dI_k^{\Re}$ and $I_k^{\Im} \leq Y + dI_k^{\Im}$ can be expressed as

$$p(I_k^{\Re} \leq X + dI_k^{\Re}, I_k^{\Im} \leq Y + dI_k^{\Im}) = \frac{1}{2\pi\sigma_A^2} e^{\left(-\frac{(I_k^{\Re})^2+(I_k^{\Im})^2}{2\sigma_A^2}\right)} dI_k^{\Re} dI_k^{\Im}. \tag{4.22}$$

The area $dI_k^{\Re} dI_k^{\Im}$ in the Cartesian co-ordinate is equal to the area $I_k dI_k d\phi_{I_k}$ in the Polar co-ordinate. Therefore

$$\begin{aligned} p(I_k^{\Re} \leq X + dI_k^{\Re}, I_k^{\Im} \leq Y + dI_k^{\Im}) &= p(I_k \leq Z + dI_k, \phi_{I_k} \leq \theta + d\phi_{I_k}) \\ &= \frac{1}{2\pi\sigma_A^2} e^{\left(-\frac{(I_k^{\Re})^2+(I_k^{\Im})^2}{2\sigma_A^2}\right)} I_k dI_k d\phi_{I_k} \\ &= \frac{I_k}{2\pi\sigma_A^2} e^{-\frac{I_k^2}{2\sigma_A^2}} dI_k d\phi_{I_k}, \end{aligned} \tag{4.23}$$

the joint PDF can be expressed as

$$p(I_k, \phi_{I_k}) = \frac{I_k}{2\pi\sigma_A^2} e^{-\frac{I_k^2}{2\sigma_A^2}}. \tag{4.24}$$

Therefore, the magnitude of the total NGN after FFT operation in (4.5) exhibits a Rayleigh distribution as $p_\Lambda(|\Lambda_k|) = p_I(|I_k|) = \frac{|I_k|}{\sigma_A^2} e^{\left(-\frac{|I_k|^2}{2\sigma_A^2}\right)}$ and the phase $\phi_{\Lambda_k} = \phi_{I_k} = \tan^{-1}\left(\frac{I_k^{\Im}}{I_k^{\Re}}\right)$ exhibits a uniform distribution in $[-\pi, \pi)$ as $p_\phi(\phi_{\Lambda_k}) = p_\phi(\phi_{I_k}) = \frac{1}{2\pi}$ as derived in (4.24). The simulation results presented in Fig. 4.3 have correctly investigated that the magnitude of the IN modelled using MCAIN model has a Rayleigh distribution and the phase has a uniform distribution in the frequency domain for different cases parameters of $A = 10^{-2}$ and $\rho = 10^{-3}, 10^{-2}, 10^{-1}$ at SNR=10 dB.

Hence, the complex noise samples at the ZF equalizer output in (4.8) can be expressed as

$$\hat{Z}_k = \hat{Z}_k^{\Re} + j\hat{Z}_k^{\Im} = \frac{\Lambda_k^{\Re} + j\Lambda_k^{\Im}}{H_k^{\Re} + jH_k^{\Im}} = \frac{|I_k| e^{j\phi_{I_k}}}{|H_k| e^{j\phi_{H_k}}} = |\chi_k| e^{j\left(\phi_{I_k} - \phi_{H_k}\right)}, \tag{4.25}$$

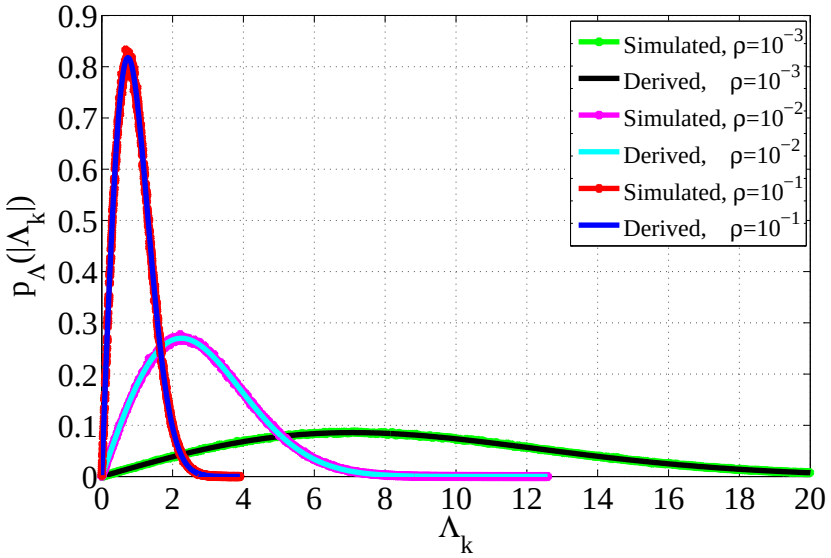

(a) Magnitude of the impulsive noise in the frequency domain.

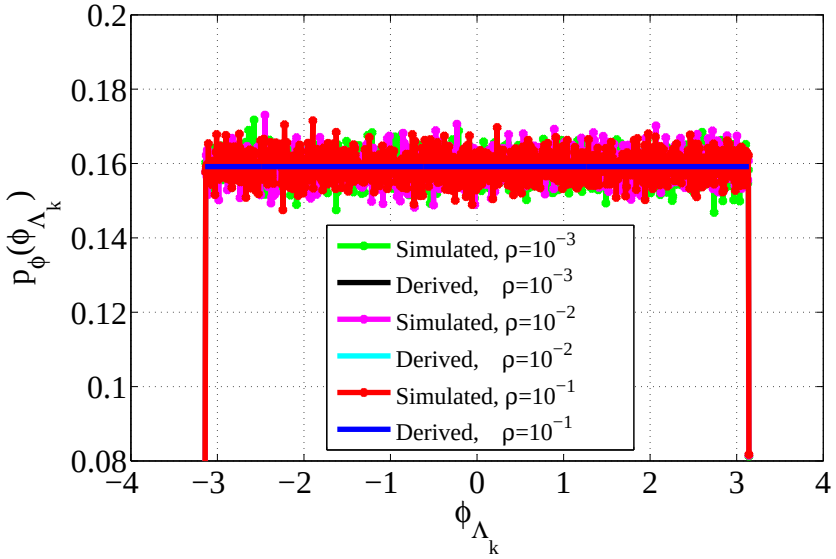

(b) Phase of the impulsive noise in the frequency domain.

Figure 4.3: Distribution of the magnitude and phase for the complex impulsive noise in the frequency domain modeled using MCAIN model with $A = 10^{-2}$ at SNR = 10 dB.

where $\phi_{t_k} = \phi_{I_k} - \phi_{H_k}$ and $\hat{Z}_k^{\Re} = |\chi_k| \cos(\phi_{t_k})$ and $\hat{Z}_k^{\Im} = |\chi_k| \sin(\phi_{t_k})$ are the total phase, the real and imaginary parts of the equalized noise samples, respectively. Indeed, the PDF of $|\chi_k| = \frac{|I_k|}{|H_k|}$ can be computed as a ratio of two RVs with Rayleigh distributions, where the joint PDF between I_k and H_k independent RVs can be expressed as [161]

$$p_{IH}(|I_k|, |H_k|) = p_I(|I_k|) p_H(|H_k|) = \frac{|I_k||H_k|}{\sigma_A^2 \sigma_h^2} e^{-\frac{|I_k|^2}{2\sigma_A^2} - \frac{|H_k|^2}{2\sigma_h^2}}, \tag{4.26}$$

letting $|\chi_k| = \frac{|I_k|}{|H_k|}$ and substituting $|I_k| = |\chi_k||H_k|$ in (4.26), we get

$$p_{IH}(|\chi_k||H_k|, |H_k|) = \frac{|\chi_k||H_k|^2}{\sigma_A^2\sigma_h^2} e^{-|H_k|^2\left(\frac{\sigma_h^2|\chi_k|^2+\sigma_A^2}{2\sigma_A^2\sigma_h^2}\right)}, \tag{4.27}$$

we have utilized the computational knowledge engine[1] to determine the PDF of $|\chi_k|$ using the division of two RVs formula [161], yield

$$\begin{aligned} p_{\chi_k}(\chi_k) &= \int_0^\infty |H_k| p_{IH}(|\chi_k||H_k|, |H_k|) dH_k \\ &= \int_0^\infty \frac{|\chi_k||H_k|^3}{\sigma_A^2\sigma_h^2} e^{-|H_k|^2\left(\frac{\sigma_h^2|\chi_k|^2+\sigma_A^2}{2\sigma_A^2\sigma_h^2}\right)} dH_k \\ &= \frac{2\sigma_h^2\sigma_A^2|\chi_k|}{(\sigma_h^2|\chi_k|^2+\sigma_A^2)^2}, \quad \text{for } \Re\left(\frac{\sigma_h^2|\chi_k|^2+\sigma_A^2}{2\sigma_A^2\sigma_h^2}\right) > 0. \end{aligned} \tag{4.28}$$

As mentioned above, the total phase ϕ_{t_k} has uniform distribution as $p_\phi(\phi_{t_k}) = \frac{1}{2\pi}$. Thus, the conditional PDF, $p_Z(\hat{Z}_k^{\Re}|\phi_{t_k})$, of the real part for the equalized NGN, $\hat{Z}_k^{\Re} = |\chi_k|\cos(\phi_{t_k})$, can be expressed as

$$\begin{aligned} p_Z(\hat{Z}_k^{\Re}|\phi_{t_k}) &= \frac{1}{|\cos(\phi_{t_k})|} p(|\chi_k|)\Big|_{|\chi_k|=\hat{Z}_k^{\Re}/\cos(\phi_{t_k})} \\ &= \frac{1}{|\cos^2(\phi_{t_k})|} \frac{2\sigma_h^2\sigma_A^2\hat{Z}_k^{\Re}}{(\sigma_h^2|\frac{\hat{Z}_k^{\Re}}{\cos(\phi_{t_k})}|^2+\sigma_A^2)^2}, \end{aligned} \tag{4.29}$$

and the joint PDF, $p_{Z,\phi}(\hat{Z}_k^{\Re}, \phi_{t_k})$, can be expressed as

$$\begin{aligned} p_{Z,\phi}(\hat{Z}_k^{\Re}, \phi_{t_k}) &= p_Z(\hat{Z}_k^{\Re}|\phi_{t_k}) p_\phi(\phi_{t_k}) \\ &= \frac{1}{2\pi} \frac{1}{|\cos^2(\phi_{t_k})|} \frac{2\sigma_h^2\sigma_A^2\hat{Z}_k^{\Re}}{\left(\sigma_h^2|\frac{\hat{Z}_k^{\Re}}{\cos(\phi_{t_k})}|^2+\sigma_A^2\right)^2}. \end{aligned} \tag{4.30}$$

Hence, the PDF $p_Z(\hat{Z}_k^{\Re})$, of the effective noise samples at the ZF equalizer output can be computed as

$$\begin{aligned} p_Z(\hat{Z}_k^{\Re}) &= \int_{-\pi}^{\pi} p_{Z,\phi}(\hat{Z}_k^{\Re}, \phi_{t_k}) d\phi_{t_k} \\ &= 4\int_0^{\pi/2} \frac{1}{\pi|\cos^2(\phi_{t_k})|} \frac{\sigma_h^2\sigma_A^2\hat{Z}_k^{\Re}}{\left(\sigma_h^2|\frac{\hat{Z}_k^{\Re}}{\cos(\phi_{t_k})}|^2+\sigma_A^2\right)^2} d\phi_{t_k}, \end{aligned} \tag{4.31}$$

[1] https://www.wolframalpha.com

letting $\cos^2(\phi_{t_k}) = t$ gives $d\phi_{t_k} = -\frac{dt}{2\sqrt{t}\sqrt{1-t}}$, then

$$p_Z(\hat{Z}_k^{\Re}) = 2\int_0^1 \frac{\sigma_h^2\sigma_A^2\hat{Z}_k^{\Re}\sqrt{t}}{\pi\sqrt{1-t}(\sigma_h^2|\hat{Z}_k^{\Re}|^2 + \sigma_A^2 t)^2}dt, \tag{4.32}$$

utilizing the computational knowledge engine[1], we get

$$p_Z(\hat{Z}_k^{\Re}) = \frac{\sigma_A^2\sigma_h}{2\left(\sigma_h^2|\hat{Z}_k^{\Re}|^2 + \sigma_A^2\right)^{\frac{3}{2}}}. \tag{4.33}$$

Moreover, the PDF of the equalized NGN for the imaginary part in the case of MCAIN model can be obtained by utilizing, $\hat{Z}_k^{\Re} = |\chi_k|\sin(\phi_{t_k})$, and following similar derivation steps in (4.29)-(4.33), yields

$$p_Z(\hat{Z}_k^{\Im}) = \frac{\sigma_A^2\sigma_h}{2\left(\sigma_h^2|\hat{Z}_k^{\Im}|^2 + \sigma_A^2\right)^{\frac{3}{2}}}. \tag{4.34}$$

4.3.2 Distribution of the Impulsive Noise based on BGMIN Model

In the presence of complex IN modelled by BGMIN model, λ_n in (4.3) can be expressed as $\lambda_n^{\Re} = i_n^{\Re}$ and $\lambda_n^{\Im} = i_n^{\Im}$, where $i_n^{\Re}$ and $i_n^{\Im}$ are the real and imaginary components, respectively, which represents a mixture of impulsive noise and background Gaussian noise due to thermal effects in the electronics in the time domain. Their PDFs can be expressed as a sum of two Gaussian PDFs [4]. The real part, the imaginary part and the joint distribution in the time domain can be expressed as [4]

$$\begin{aligned} p(\lambda_n^{\Re}) = p(i_n^{\Re}) &= (1-\alpha)\mathcal{N}(i_n^{\Re}, 0, \sigma_w^2) + \alpha\mathcal{N}(i_n^{\Re}, 0, \sigma_w^2 + \sigma_i^2), \\ p(\lambda_n^{\Im}) = p(i_n^{\Im}) &= (1-\alpha)\mathcal{N}(i_n^{\Im}, 0, \sigma_w^2) + \alpha\mathcal{N}(i_n^{\Im}, 0, \sigma_w^2 + \sigma_i^2), \end{aligned} \tag{4.35}$$

$$\begin{aligned} p(\lambda_n^{\Re}, \lambda_n^{\Im}) = p(i_n^{\Re}, i_n^{\Im}) =& (1-\alpha)\mathcal{N}(i_n^{\Re}, 0, \sigma_w^2)\mathcal{N}(i_n^{\Im}, 0, \sigma_w^2) + \\ & \alpha\mathcal{N}(i_n^{\Re}, 0, \sigma_w^2 + \sigma_i^2)\mathcal{N}(i_n^{\Im}, 0, \sigma_w^2 + \sigma_i^2), \end{aligned} \tag{4.36}$$

where $0 < \alpha < 1$ is the probability of impulse occurrence, σ_w^2 and σ_i^2 are the AWGN and IN noise variances, respectively, and $\mathcal{N}(i_n^r, \mu, \sigma^2) = \frac{1}{\sqrt{2\pi}\sigma}e^{-\frac{(i_n^r-\mu)^2}{2\sigma^2}}$. The FFT operation will spread the effect of the IN on each subcarrier in (4.4) converting its PDF to a Gaussian distribution. Thus, the PDF of the real and imaginary parts in (4.35) after the FFT operation can be expressed

as [4, 155]

$$p_{\Lambda}(\Lambda_k^r) = p_I(I_k^r) = \sum_{n=0}^{N} \binom{N}{n} \alpha^n (1-\alpha)^{N-n} \mathcal{N}(I_k^r, 0, \sigma_n^2), \tag{4.37}$$

and the joint PDF in (4.36) as

$$p_{\Lambda}(\Lambda_k^{\Re}, \Lambda_k^{\Im}) = p_I(I_k^{\Re}, I_k^{\Im}) = \sum_{n=0}^{N} \binom{N}{n} \alpha^n (1-\alpha)^{N-n} \mathcal{N}(I_k^{\Re}, 0, \sigma_n^2) \mathcal{N}(I_k^{\Im}, 0, \sigma_n^2), \tag{4.38}$$

where $\sigma_n^2 = \sigma_w^2 + \frac{n\sigma_i^2}{N}$ and $\binom{N}{n} = \frac{N!}{(N-n)!n!}$. Following similar derivation steps in (4.15)-(4.24), it is easy to show that the magnitude of the IN after FFT operation in (4.5), $|\Lambda_k| = |I_k| = \sqrt{(I_k^{\Re})^2 + (I_k^{\Im})^2}$, exhibits weighted sum of Rayleigh distributions expressed as

$$p_{\Lambda}(|\Lambda_k|) = p_I(|I_k|) = \sum_{n=0}^{N} \binom{N}{n} \alpha^n (1-\alpha)^{N-n} \frac{|I_k|}{\sigma_n^2} e^{-\frac{|I_k|^2}{2\sigma_n^2}}, \tag{4.39}$$

and its phase $\phi_{I_k} = \tan^{-1}\left(\frac{I_k^{\Im}}{I_k^{\Re}}\right)$ exhibits a uniform distribution in $[-\pi, \pi)$ as $p_{\phi}(\phi_{I_k}) = \frac{1}{2\pi}$.

The simulation results presented in Fig. 4.4 have correctly investigated the magnitude of the IN that modeled as a Bernoulli-Gaussian random process using BGMIN model has a Rayleigh distribution and the phase has a uniform distribution in the frequency domain for different cases parameters of $\alpha = 0.3, 0.1, 0.01$ and $\tilde{\rho} = 100$ at SNR=10 dB.

Thus, the PDF of the effective complex noise samples at the ZF output in (4.8) can be expressed as

$$\hat{Z}_k = \hat{Z}_k^{\Re} + j\hat{Z}_k^{\Im} = \frac{\Lambda_k^{\Re} + j\Lambda_k^{\Im}}{H_k^{\Re} + jH_k^{\Im}} = \sum_{n=0}^{N} \binom{N}{n} \alpha^n (1-\alpha)^{N-n} \frac{|I_k| e^{j\phi_{I_k}}}{|H_k| e^{j\phi_{H_k}}} = |\chi_k| e^{j\phi_{t_k}}, \tag{4.40}$$

the PDF of $|\chi_k| = \frac{|I_k|}{|H_k|}$ can be computed as a ratio of two independent RVs with Rayleigh distribution, where the joint PDF between I_k and H_k can be expressed as [161]

$$p_{IH}(|I_k|, |H_k|) = p_I(|I_k|) p_H(|H_k|) = \sum_{n=0}^{N} \binom{N}{n} \alpha^n (1-\alpha)^{N-n} \frac{|I_k||H_k|}{\sigma_n^2 \sigma_h^2} e^{-\frac{|I_k|^2}{2\sigma_n^2} - \frac{|H_k|^2}{2\sigma_h^2}}, \tag{4.41}$$

assuming $|\chi_k| = \frac{|I_k|}{|H_k|}$ and substituting $|I_k| = |\chi_k||H_k|$ in (4.41), yields

$$p_{IH}(|\chi_k||H_k|, |H_k|) = \sum_{n=0}^{N} \binom{N}{n} \alpha^n (1-\alpha)^{N-n} \frac{|\chi_k||H_k|^2}{\sigma_n^2 \sigma_h^2} e^{-|H_k|^2 \left(\frac{\sigma_h^2 |\chi_k|^2 + \sigma_n^2}{2\sigma_n^2 \sigma_h^2}\right)}, \tag{4.42}$$

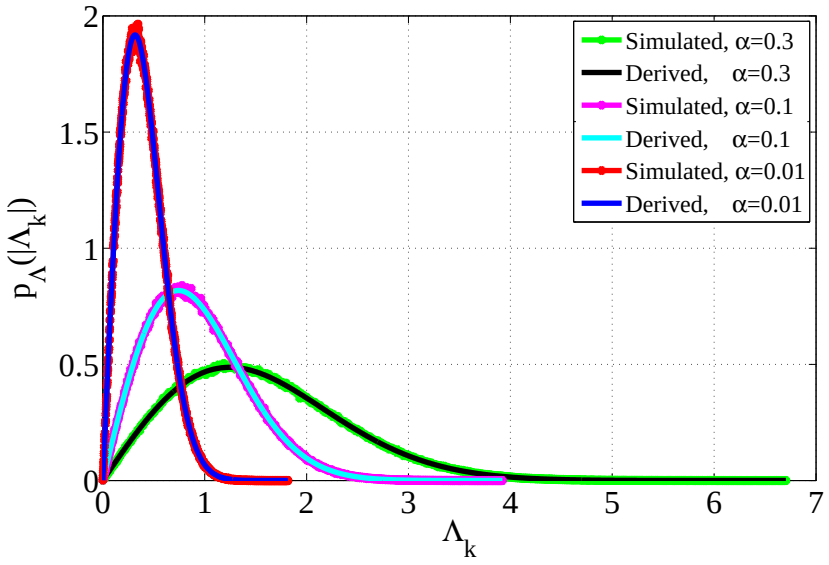

(a) Magnitude of the non-Gaussian Noise in the frequency domain.

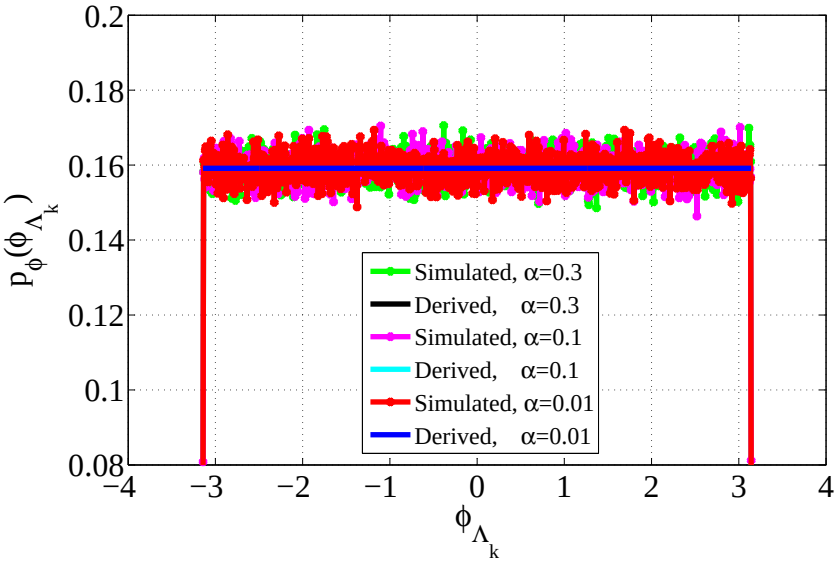

(b) Phase of the non-Gaussian Noise in the frequency domain.

Figure 4.4: Distribution of the magnitude and phase for the complex impulsive noise in the frequency domain modeled using BGMIN model with $\tilde{\rho} = 100$ at SNR = 10 dB.

we have utilized the computational knowledge engine[1] to determine the PDF of $|\chi_k|$ using the

[1] https://www.wolframalpha.com

division of two RVs formula [161], yield

$$\begin{aligned} p_{\chi_k}(|\chi_k|) &= \int_0^\infty |H_k| p_{IH}(|\chi_k||H_k|, |H_k|) dH_k \\ &= \int_0^\infty \sum_{n=0}^{N} \binom{N}{n} \alpha^n (1-\alpha)^{N-n} \frac{|\chi_k||H_k|^3}{\sigma_n^2 \sigma_h^2} e^{-|H_k|^2 \left(\frac{\sigma_h^2 |\chi_k|^2 + \sigma_n^2}{2\sigma_n^2 \sigma_h^2}\right)} dH_k \\ &= \sum_{n=0}^{N} \binom{N}{n} \alpha^n (1-\alpha)^{N-n} \frac{2\sigma_h^2 \sigma_n^2 |\chi_k|}{(\sigma_h^2 |\chi_k|^2 + \sigma_n^2)^2}, \quad \text{for } \Re\left(\frac{\sigma_h^2 |\chi_k|^2 + \sigma_n^2}{2\sigma_n^2 \sigma_h^2}\right) > 0. \end{aligned} \tag{4.43}$$

As mentioned above, the total phase ϕ_{t_k} has uniform distribution as $p_\phi(\phi_{t_k}) = \frac{1}{2\pi}$. Thus, the conditional PDF, $p_Z(\hat{Z}_k^{\Re}|\phi_{t_k})$, of the real part of the equalized NGN samples, $\hat{Z}_k^{\Re} = |\chi_k| \cos(\phi_{t_k})$, can be expressed as

$$\begin{aligned} p_Z(\hat{Z}_k^{\Re}|\phi_{t_k}) &= \sum_{n=0}^{N} \binom{N}{n} \alpha^n (1-\alpha)^{N-n} \frac{1}{|\cos(\phi_{t_k})|} p(|\chi_k|) \Big|_{|\chi_k| = \hat{Z}_k^{\Re}/\cos(\phi_{t_k})} \\ &= \sum_{n=0}^{N} \binom{N}{n} \alpha^n (1-\alpha)^{N-n} \frac{1}{|\cos^2(\phi_{t_k})|} \frac{2\sigma_h^2 \sigma_n^2 \hat{Z}_k^{\Re}}{(\sigma_h^2 |\frac{\hat{Z}_k^{\Re}}{\cos(\phi_{t_k})}|^2 + \sigma_n^2)^2}, \end{aligned} \tag{4.44}$$

and the joint PDF, $p_{Z,\phi}(\hat{Z}_k^{\Re}, \phi_{t_k})$, can be expressed as

$$\begin{aligned} p_{Z,\phi}(\hat{Z}_k^{\Re}, \phi_{t_k}) &= \sum_{n=0}^{N} \binom{N}{n} \alpha^n (1-\alpha)^{N-n} p_Z(\hat{Z}_k^{\Re}|\phi_{t_k}) p_\phi(\phi_{t_k}) \\ &= \sum_{n=0}^{N} \binom{N}{n} \alpha^n (1-\alpha)^{N-n} \frac{1}{2\pi} \frac{1}{|\cos^2(\phi_{t_k})|} \frac{2\sigma_h^2 \sigma_n^2 \hat{Z}_k^{\Re}}{\left(\sigma_h^2 |\frac{\hat{Z}_k^{\Re}}{\cos(\phi_{t_k})}|^2 + \sigma_n^2\right)^2}. \end{aligned} \tag{4.45}$$

Hence, the PDF $p(\hat{Z}_k^{\Re})$, of the effective noise samples at the ZF equalizer output can be computed as

$$\begin{aligned} p_Z(\hat{Z}_k^{\Re}) &= \int_{-\pi}^{\pi} p_{Z,\phi}(\hat{Z}_k^{\Re}, \phi_{t_k}) d\phi_{t_k} \\ &= 4 \int_0^{\pi/2} \sum_{n=0}^{N} \binom{N}{n} \alpha^n (1-\alpha)^{N-n} \frac{1}{\pi |\cos^2(\phi_{t_k})|} \frac{\sigma_h^2 \sigma_n^2 \hat{Z}_k^{\Re}}{\left(\sigma_h^2 |\frac{\hat{Z}_k^{\Re}}{\cos(\phi_{t_k})}|^2 + \sigma_n^2\right)^2} d\phi_{t_k}, \end{aligned} \tag{4.46}$$

letting $\cos^2(\phi_{t_k}) = t$ gives $d\phi_{t_k} = -\frac{dt}{2\sqrt{t}\sqrt{1-t}}$, then

$$p_Z(\hat{Z}_k^{\Re}) = 2 \int_0^1 \sum_{n=0}^{N} \binom{N}{n} \alpha^n (1-\alpha)^{N-n} \frac{\sigma_h^2 \sigma_n^2 \hat{Z}_k^{\Re} \sqrt{t}}{\pi \sqrt{1-t} (\sigma_h^2 |\hat{Z}_k^{\Re}|^2 + \sigma_n^2 t)^2} dt, \tag{4.47}$$

utilizing the computational knowledge engine[1], we get

$$p_Z(\hat{Z}_k^{\Re}) = \sum_{n=0}^{N} \binom{N}{n} \alpha^n (1-\alpha)^{N-n} \frac{\sigma_n^2 \sigma_h}{2\left(\sigma_h^2 |\hat{Z}_k^{\Re}|^2 + \sigma_n^2\right)^{\frac{3}{2}}}. \tag{4.48}$$

Moreover, the PDF of the equalized NGN samples for the imaginary part in the case of BGMIN model can be obtained form, $\hat{Z}_k^{\Im} = |\chi_k| \sin(\phi_{t_k})$, and following similar derivation steps in (4.44)-(4.48), we obtain

$$p_Z(\hat{Z}_k^{\Im}) = \sum_{n=0}^{N} \binom{N}{n} \alpha^n (1-\alpha)^{N-n} \frac{\sigma_n^2 \sigma_h}{2\left(\sigma_h^2 |\hat{Z}_k^{\Im}|^2 + \sigma_n^2\right)^{\frac{3}{2}}}, \tag{4.49}$$

where the Stirlings logarithmic factorial approximation method is used to compute the large factorials in (4.48) and (4.49) expressed as [162]

$$\log(f!) = \left(f + \frac{1}{2}\right) \log(f) - f + \frac{1}{2} \log(2\pi). \tag{4.50}$$

4.3.3 Distribution of the BI Noise based on the Nakagami-m Model

In the presence of Nakagami-m BI noise, the real and imaginary components of λ_n in (4.3) can be expressed as $\lambda_n^{\Re} = b_n^{\Re} = |\tilde{b}_n| \cos(\theta_n)$ and $\lambda_n^{\Im} = b_n^{\Im} = |\tilde{b}_n| \sin(\theta_n)$, respectively. Practically, the envelope $|\tilde{b}_n|$ of BI noise in the time-domain follows the Nakagami-m distribution and it can be expressed as [2]

$$p(\tilde{b}_n) = \frac{2\tilde{b}_n^{2m-1}}{\Gamma(m)} \left(\frac{m}{\Omega}\right)^m e^{-\left(\frac{m\tilde{b}_n^2}{\Omega}\right)}, \tilde{b}_n \geq 0 \tag{4.51}$$

where $m = (\mathbb{E}\{\tilde{b}_n^2\})^2 / \mathbb{E}\{(\tilde{b}_n^2 - \mathbb{E}\{\tilde{b}_n^2\})^2\}$ is the Nakagami-m parameter, $\Omega = \mathbb{E}\{\tilde{b}_n^2\}$ is the mean power of the RV $\tilde{b}_n$, $\Gamma(\cdot)$ is the Gamma function, and $\mathbb{E}\{\cdot\}$ is the expectation value. Moreover, the phase θ_n is uniformly distributed in $[-\pi, \pi)$. Thus, the conditional probability distribution of the real and imaginary parts can be expressed as [2]

$$p_\lambda(\lambda_n^r | \theta_n) = p_b(b_n^r | \theta_n) = \frac{2(b_n^r)^{2m-1}}{\Gamma(m)(\Delta^r)^{2m}} \left(\frac{m}{\Omega}\right)^m e^{\left(\frac{-m \times (b_n^r)^2}{\Omega \times (\Delta^r)^2}\right)}, \tag{4.52}$$

where $\{\Delta^{\Re}, \Delta^{\Im}\} = \{\cos(\theta_n), \sin(\theta_n)\}$, respectively. The closed-form expressions of the real part distribution and the imaginary part distribution utilizing (4.52) for $0 < m < 1$, $m \neq \frac{1}{2}$ and $-\infty < \lambda_n^r < \infty$, can be expressed as [3]

$$p_\lambda(\lambda_n^r) = p_b(b_n^r) = \frac{e^{-\frac{m\times(b_n^r)^2}{\Omega}}}{\sqrt{\pi}\Gamma(m)}\sqrt{\frac{m}{\Omega}}\left[\frac{\Gamma(\frac{1}{2}-m)}{\Gamma(1-m)}\left(\frac{m\times(b_n^r)^2}{\Omega}\right)^{m-\frac{1}{2}} {}_1F_1\left(\frac{1}{2},\frac{1}{2}+m,\frac{m\times(b_n^r)^2}{\Omega}\right)+\right.$$
$$\left.\frac{\Gamma(m-\frac{1}{2})}{\sqrt{\pi}} {}_1F_1\left(1-m,\frac{3}{2}-m,\frac{m\times(b_n^r)^2}{\Omega}\right)\right], \tag{4.53}$$

and for $m=\frac{1}{2}$ as

$$p_\lambda(\lambda_n^r) = p_b(b_n^r) = \frac{1}{\pi}\sqrt{\frac{1}{2\pi\Omega}}e^{-\frac{(b_n^r)^2}{4\Omega}}K_0\left(\frac{(b_n^r)^2}{4\Omega}\right), \tag{4.54}$$

where $r=\{\Re,\Im\}$ denotes the real and imaginary components, respectively, where ${}_1F_1(a;b;z)$ is the confluent hypergeometric function and $K_0(\cdot)$ is the modified Bessel function of the second kind of order zero expressed as given in (2.12) and (2.13), respectively.

After performing the FFT operation in (4.4), the distribution of Nakagami-m BI noise samples in (4.53) and (4.54) will be changed and can be determined using statistical approximation. According to the CLT, the PDF of the real and imaginary parts of BI noise, $p_\lambda(\lambda_n^r)$, after performing the FFT operation will be approaching the normal distribution [2], i.e. $p_B(B_k^r) = \mathcal{N}(B_k^r,\mu_b,\sigma_b^2) = \frac{1}{\sqrt{2\pi}\sigma_b}\exp\left(-\frac{(B_k^r-\mu_b)^2}{2\sigma_b^2}\right)$ with mean $\mu_b=0$ and the variance σ_b^2. In this case, σ_b^2 can be computed from either (4.53) or (4.54), which gives equal variance. For simplicity, σ_b^2 can be computed from (4.54) as

$$\begin{aligned}\sigma_b^2 &= \mathbb{E}\{(\lambda_n^r)^2\} - (\mathbb{E}\{\lambda_n^r\})^2\\ &= \mathbb{E}\{(b_n^r)^2\} - (\mathbb{E}\{b_n^r\})^2.\end{aligned} \tag{4.55}$$

The expectation value $\mathbb{E}\{(b_n^r)^2\}$ in (4.55) can be computed as

$$\begin{aligned}\mathbb{E}\{(b_n^r)^2\} &= \int_{-\infty}^{+\infty}(b_n^r)^2 p_b(b_n^r)db_n^r\\ &= \int_{-\infty}^{+\infty}\frac{1}{\pi}\sqrt{\frac{1}{2\pi\Omega}}(b_n^r)^2 e^{-\frac{(b_n^r)^2}{4\Omega}}K_0\left(\frac{(b_n^r)^2}{4\Omega}\right)db_n^r,\end{aligned} \tag{4.56}$$

letting $(b_n^r)^2 = x$, we get $b_n^r = \sqrt{x}$ and $db_n^r = \frac{dx}{2\sqrt{x}}$. Hence

$$\mathbb{E}\{x\} = \frac{1}{\pi}\sqrt{\frac{1}{2\pi\Omega}}\int_0^{+\infty}\sqrt{x}e^{-\frac{x}{4\Omega}}K_0\left(\frac{x}{4\Omega}\right)dx, \tag{4.57}$$

utilizing the integralion formula in [45, Eq.(6.621,3)], $\mathbb{E}\{x\}$ can be computed when assuming

$\mu = \frac{3}{2}, \alpha = \frac{1}{4\Omega}, v = 0$ and $\beta = \frac{1}{4\Omega}$ as

$$\mathbb{E}\{x\} = \frac{2\Omega}{\pi}\left(\Gamma\left(\frac{3}{2}\right)\right)^2 {}_2F_1\left(\frac{3}{2}, \frac{1}{2}, 2, 0\right). \tag{4.58}$$

Moreover, the mean value $\mu = \mathbb{E}\{(b_n^r)\}$ in (4.55) can be computed as

$$\begin{aligned}\mathbb{E}\{(b_n^r)\} &= \int_{-\infty}^{+\infty} b_n^r p_b(b_n^r) db_n^r \\ &= \int_{-\infty}^{+\infty} \frac{1}{\pi}\sqrt{\frac{1}{2\pi\Omega}} b_n^r e^{-\frac{(b_n^r)^2}{4\Omega}} K_0\left(\frac{(b_n^r)^2}{4\Omega}\right) db_n^r,\end{aligned} \tag{4.59}$$

assuming $(b_n^r)^2 = x$, we get $b_n^r = \sqrt{x}$ and $db_n^r = \frac{dx}{2\sqrt{x}}$. Hence

$$\mathbb{E}\{\sqrt{x}\} = \frac{1}{2\pi}\sqrt{\frac{1}{2\pi\Omega}}\left[\int_{-\infty}^{0} e^{-\frac{x}{4\Omega}} K_0\left(\frac{x}{4\Omega}\right) dx + \int_{0}^{+\infty} e^{-\frac{x}{4\Omega}} K_0\left(\frac{x}{4\Omega}\right) dx\right], \tag{4.60}$$

utilizing the integral formula in [45, Eq.(6.621,3)], $\mathbb{E}\{\sqrt{x}\}$ can be computed when assuming $\mu = 1, \alpha = \frac{1}{4\Omega}, v = 0$ and $\beta = \frac{1}{4\Omega}$ as

$$\begin{aligned}\mathbb{E}\{\sqrt{x}\} = \frac{1}{2\pi}\sqrt{\frac{1}{2\pi\Omega}}\Bigg[&-\frac{\sqrt{\pi}}{\left(\frac{1}{4\Omega}+\frac{1}{4\Omega}\right)}\frac{\left(\Gamma(1)\right)^2}{\Gamma\left(\frac{3}{2}\right)} {}_2F_1\left(1, \frac{1}{2}, \frac{3}{2}, 0\right) + \\ &\frac{\sqrt{\pi}}{\left(\frac{1}{4\Omega}+\frac{1}{4\Omega}\right)}\frac{\left(\Gamma(1)\right)^2}{\Gamma\left(\frac{3}{2}\right)} {}_2F_1\left(1, \frac{1}{2}, \frac{3}{2}, 0\right)\Bigg] = 0.\end{aligned} \tag{4.61}$$

Therefore, the variance can be expressed as

$$\sigma_b^2 = \mathbb{E}\{x\} - (\mathbb{E}\{\sqrt{x}\})^2 = \mathbb{E}\{x\} - 0 = \frac{\Omega}{2} {}_2F_1\left(\frac{3}{2}, \frac{1}{2}, 2, 0\right), \tag{4.62}$$

where σ_b^2 depends on the mean power of the RV $\tilde{b}_n$ as $\Omega = \mathbb{E}\{\tilde{b}_n^2\}$ and ${}_2F_1(a, b; c; z)$ is the Gauss hypergeometric function expressed as in [45, Eq.(9.14)].

The joint PDF between the real and imaginary components in the frequency domain can be expressed as $p_B(B_k^{\Re}, B_k^{\Im}) = p_B(B_k^{\Re}) p_B(B_k^{\Im}) = \mathcal{N}(B_k^{\Re}, 0, \sigma_b^2)\mathcal{N}(B_k^{\Im}, 0, \sigma_b^2)$. Therefore, the magnitude $|B_k| = \sqrt{(B_k^{\Re})^2 + (B_k^{\Im})^2}$ follows a Rayleigh distribution expressed as

$$p_B(|B_k|) = \frac{|B_k|}{\sigma_b^2} e^{-\frac{|B_k|^2}{2\sigma_b^2}}, \tag{4.63}$$

and its phase $\phi_{B_k} = \tan^{-1}\left(\frac{B_k^{\Im}}{B_k^{\Re}}\right)$ exhibits a uniform distribution in $[-\pi, \pi)$ expressed as

$$p_{\phi}(\phi_{B_k}) = \frac{1}{2\pi}. \tag{4.64}$$

The simulation results in Fig. 4.5 have correctly investigated that the magnitude of the BI noise has a Rayleigh distribution and the phase has a uniform distribution in the frequency domain.

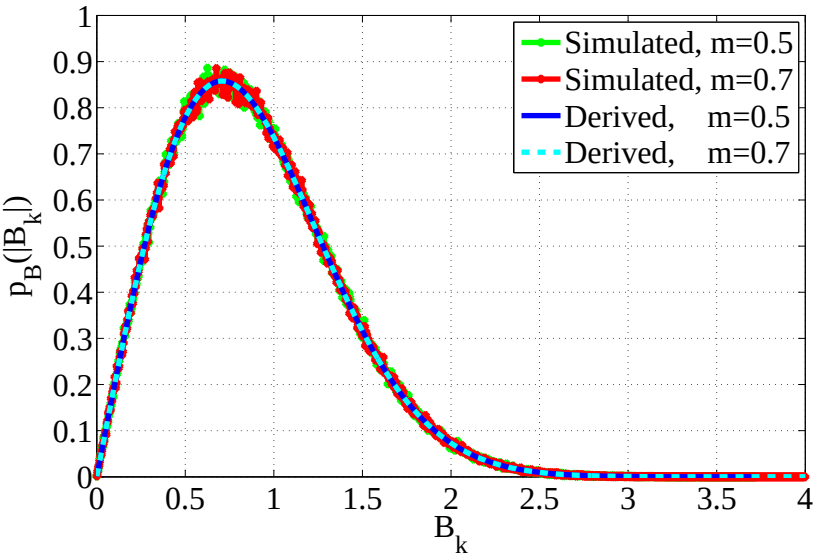

(a) Magnitude of the Nakagami-m backgroung noise in the frequency domain.

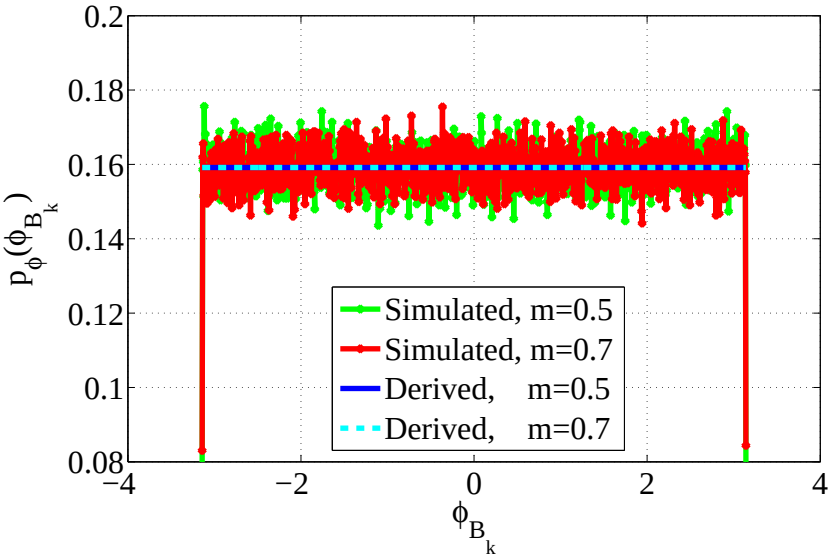

(b) Phase of the Nakagami-m background noise in the frequency domain.

Figure 4.5: Magnitude and phase of the Nakagami-m background noise in the frequency domain with $m = 0.5$ and $m = 0.7$ in the frequency domain at SNR = 10 dB.

Hence, the complex-valued noise samples after the ZF equalizer in (4.8) can be expressed as

$$\hat{Z}_k = \hat{Z}_k^{\Re} + j\hat{Z}_k^{\Im} = \frac{|B_k|e^{j\phi_{B_k}}}{|H_k|e^{j\phi_{H_k}}} = |\chi_k|e^{j\left(\phi_{B_k}-\phi_{H_k}\right)}. \tag{4.65}$$

Following the same derivation steps in (4.26)-(4.32), the real and imaginary parts distribution at the ZF equalizer output can be expressed as

$$p_Z(\hat{Z}_k^{\Re}) = \frac{\sigma_b^2\sigma_h}{2\left(\sigma_h^2|\hat{Z}_k^{\Re}|^2+\sigma_b^2\right)^{\frac{3}{2}}}, \tag{4.66}$$

$$p_Z(\hat{Z}_k^{\Im}) = \frac{\sigma_b^2\sigma_h}{2\left(\sigma_h^2|\hat{Z}_k^{\Im}|^2+\sigma_b^2\right)^{\frac{3}{2}}}. \tag{4.67}$$

4.3.4 Distribution of the Combined BI Noise and Impulsive Noise based on MCAIN Model

In the presence of the combined BI noise and MCAIN, the real and imaginary components of the total NGN samples in (4.3) can be expressed as $\lambda_n^{\Re} = b_n^{\Re} + i_n^{\Re} = \left(|\tilde{b}_n|\cos(\theta_n) + i_n^{\Re}\right)$ and $\lambda_n^{\Im} = b_n^{\Im} + i_n^{\Im} = \left(|\tilde{b}_n|\sin(\theta_n) + i_n^{\Im}\right)$, respectively. The complex-valued noise samples after the FFT operation in (4.4) can be computed by utilizing the sum of two RVs as $\Lambda_k = \Lambda_k^{\Re} + j\Lambda_k^{\Im} = (B_k^{\Re} + I_k^{\Re}) + j(B_k^{\Im} + I_k^{\Im})$ [161]. It is more convenient to compute the real and imaginary distributions using the characteristic function. The characteristic function in the frequency domain can be computed by taking the Fourier transform of $p_B(B_k^{\Re})$ as [158]

$$\Psi_B^{\Re}(w) = \mathcal{F}_t\left[\frac{1}{\sqrt{2\pi}\sigma_b}e^{-\frac{(B_k^{\Re})^2}{2\sigma_b^2}}\right] = e^{-\frac{w^2\sigma_b^2}{2}}, \tag{4.68}$$

and the characteristic function of $p(I_k^{\Re})$ can be computed as

$$\Psi_I^{\Re}(w) = \mathcal{F}_t\left[\frac{1}{\sqrt{2\pi}\sigma_A}e^{-\frac{(I_k^{\Re})^2}{2\sigma_A^2}}\right] = e^{-\frac{w^2\sigma_A^2}{2}}, \tag{4.69}$$

Thus, the real distribution of sum two random variables can be computed using the convolution of two distributions in the probabilistic domain. Thus, the convolution in the probabilistic domain corresponds to product of their characteristic functions in the frequency domain as

$$\Psi_B^{\Re}(w)\Psi_I^{\Re}(w) = e^{-\frac{w^2\sigma_b^2}{2}}e^{-\frac{w^2\sigma_A^2}{2}} = e^{-\frac{w^2(\sigma_b^2+\sigma_A^2)}{2}}. \tag{4.70}$$

Hence, the distribution that describes the combined noise samples after FFT operation can be obtained by taking inverse Fourier transform of (4.70) as

$$p_{\Lambda}(\Lambda_k^{\Re}) = \mathcal{F}_t^{-1}\left[e^{-\frac{w^2(\sigma_b^2+\sigma_A^2)}{2}}\right] = \frac{1}{\sqrt{2\pi(\sigma_b^2+\sigma_A^2)}} e^{-\frac{(\Lambda_k^{\Re})^2}{2(\sigma_b^2+\sigma_A^2)}} = p_{\Lambda}(\Lambda_k^{\Im}). \tag{4.71}$$

It can be easily shown that the magnitude of the combined noise, $|\Lambda_k| = \sqrt{(\Lambda_k^{\Re})^2 + (\Lambda_k^{\Im})^2}$ exhibits a Rayleigh distribution as $p_{\Lambda}(|\Lambda_k|) = \frac{|\Lambda_k|}{\sigma_b^2+\sigma_A^2} e^{\left(-\frac{|\Lambda_k|^2}{2(\sigma_b^2+\sigma_A^2)}\right)}$ and the phase $\phi_{\Lambda_k} = \tan^{-1}\left(\frac{\Lambda_k^{\Im}}{\Lambda_k^{\Re}}\right)$ exhibits a uniform distribution in $[-\pi, \pi)$, i.e. $p_{\phi}(\phi_{\Lambda_k}) = \frac{1}{2\pi}$. Thus, the effective noise samples after the ZF equalizer can computed by substituting $|\Lambda_k|e^{j\phi_{\Lambda_k}}$ instead of $|I_k|e^{j\phi_{I_k}}$ in (4.25) and following similar derivation steps as described in (4.26)-(4.32). The real and imaginary distributions of the equalized noise samples can be expressed as

$$p_Z(\hat{Z}_k^{\Re}) = \frac{(\sigma_b^2+\sigma_A^2)\sigma_h}{2\left(\sigma_h^2|\hat{Z}_k^{\Re}|^2 + \sigma_b^2 + \sigma_A^2\right)^{\frac{3}{2}}}, \tag{4.72}$$

$$p_Z(\hat{Z}_k^{\Im}) = \frac{(\sigma_b^2+\sigma_A^2)\sigma_h}{2\left(\sigma_h^2|\hat{Z}_k^{\Im}|^2 + \sigma_b^2 + \sigma_A^2\right)^{\frac{3}{2}}}. \tag{4.73}$$

4.3.5 Distribution of the Combined BI Noise and Impulsive Noise based on BGNIN Model

In the presence of the combined BI noise and BGMIN, the real and imaginary components of the overall NGN samples in (4.3) can be expressed as $\lambda_n^{\Re} = b_n^{\Re} + i_n^{\Re} = \left(\tilde{b}_n\cos(\theta_n) + i_n^{\Re}\right)$ and $\lambda_n^{\Im} = b_n^{\Im} + i_n^{\Im} = \left(\tilde{b}_n\sin(\theta_n) + i_n^{\Im}\right)$, respectively. The complex-valued noise samples after FFT operation in (4.4) can be expressed as $\Lambda_k = \Lambda_k^{\Re} + j\Lambda_k^{\Im} = (B_k^{\Re} + I_k^{\Re}) + j(B_k^{\Im} + I_k^{\Im})$ [161]. Hence, the joint PDF of the real and imaginary parts, $p(B_k^r, I_k^r)$ can be expressed as

$$p_{B,I}(B_k^r, I_k^r) = p_B(B_k^r)p_I(I_k^r) = \sum_{n=0}^{N}\binom{N}{n}\alpha^n(1-\alpha)^{N-n}\frac{1}{2\pi\sigma_b\sigma_n}e^{-\frac{(B_k^r)^2}{2\sigma_b^2}-\frac{(I_k^r)^2}{2\sigma_n^2}}. \tag{4.74}$$

Assuming $\Lambda_k^r = B_k^r + I_k^r$ and substituting $I_k^r = \Lambda_k^r - B_k^r$ in (4.74), the $p(\Lambda_k^r)$ can be computed as

$$p_{\Lambda}(\Lambda_k^r) = \int_{-\infty}^{\infty}\sum_{n=0}^{N}\binom{N}{n}\alpha^n(1-\alpha)^{N-n}\frac{e^{-\frac{|\Lambda_k^r|^2}{2\sigma_n^2}}}{2\pi\sigma_b\sigma_n}e^{-(B_k^r)^2\left(\frac{1}{2\sigma_b^2}+\frac{1}{2\sigma_n^2}\right)+B_k^r\frac{|\Lambda_k^r|}{\sigma_n^2}}dB_k^r. \tag{4.75}$$

Comparing (4.75) with the integral formula in [45, Eq.$(3.462, 2.^8)$], the distribution of the combined noise samples after the FFT operation can be obtained as

$$p_{\Lambda}(\Lambda_k^r) = \sum_{n=0}^{N} \binom{N}{n} \alpha^n (1-\alpha)^{N-n} \frac{e^{-\frac{(\Lambda_k^r)^2}{2(\sigma_b^2+\sigma_n^2)}}}{\sqrt{2\pi(\sigma_b^2+\sigma_n^2)}}. \tag{4.76}$$

Hence, the PDF of the magnitude of Λ_k, can be described by a weighted sum of Rayleigh PDFs as

$$p_{\Lambda}(|\Lambda_k|) = \sum_{n=0}^{N} \binom{N}{n} \alpha^n (1-\alpha)^{N-n} \frac{|\Lambda_k|}{\sigma_b^2+\sigma_n^2} e^{-\frac{|\Lambda_k|^2}{2(\sigma_b^2+\sigma_n^2)}}, \tag{4.77}$$

and its phase can be described by a uniform distribution as $p_{\phi}(\phi_{\Lambda_k}) = \frac{1}{2\pi}$. Thus, the effective noise samples after the ZF equalizer can computed by substituting $|\Lambda_k|e^{j\phi_{\Lambda_k}}$ instead of $|I_k|e^{j\phi_{I_k}}$ in (4.25) and following similar derivation steps as described in (4.26)-(4.32). The real and imaginary distributions of the equalized noise samples can be expressed as obtain

$$p_Z(\hat{Z}_k^{\Re}) = \sum_{n=0}^{N} \binom{N}{n} \alpha^n (1-\alpha)^{N-n} \frac{\sigma_h(\sigma_b^2+\sigma_n^2)}{2\big(\sigma_h^2|\hat{Z}_k^{\Re}|^2 + (\sigma_b^2+\sigma_n^2)\big)^{\frac{3}{2}}}, \tag{4.78}$$

$$p_Z(\hat{Z}_k^{\Im}) = \sum_{n=0}^{N} \binom{N}{n} \alpha^n (1-\alpha)^{N-n} \frac{\sigma_h(\sigma_b^2+\sigma_n^2)}{2\big(\sigma_h^2|\hat{Z}_k^{\Im}|^2 + (\sigma_b^2+\sigma_n^2)\big)^{\frac{3}{2}}}. \tag{4.79}$$

4.4 Maximum Likelihood Detectors and BER Derivations

4.4.1 ML Detectors based on the Derived PDFs

The focus now is on deriving the likelihood based on ML detector as in [56] for the uncoded OFDM system at the ZF equalizer output over PLC channels. The ML detectors are derived in the presence of MCAIN, BGMIN, Nakagami-m BI noise and their combinations utilizing M-ary square QAM constellation. The number of points in the constellation diagram can be expressed as $M = 2^{\delta \text{ bits}}$ over the alphabet size $\{\mathbf{C} = \pm(2\delta-1)d \pm j(2\delta-1)d\}$, where $\delta \in \{1, \cdots, \frac{\sqrt{M}}{2}\}$. The General form of the equalized received noise distributions utilizing M-QAM constellation of the real and imaginary parts for the case of MCAIN in (4.33)-(4.34), BI noise in (4.66)-(4.67) and their combination in (4.72)-(4.73) can be written as

$$p_Z(\hat{Y}_k^r|X_k) = \sum_{X_k \in \mathbf{C}_n^r} \frac{\sigma_\beta^2 \sigma_h}{2\left(\sigma_h^2|\hat{Y}_k^r - X_k|^2 + \sigma_\beta^2\right)^{\frac{3}{2}}}, \ \forall k = 0, 1, \cdots \frac{N-1}{\log_2(M)}, \tag{4.80}$$

where $\sigma_\beta^2 = \sigma_A^2$ in the case of the MCAIN model, $\sigma_\beta^2 = \sigma_b^2$ in the case of the Nakakami-m BI noise and $\sigma_\beta^2 = \sigma_b^2 + \sigma_A^2$ in the case of their combination. By utilizing the PDF in (4.80), the ML detector for the real and imaginary parts of received signal can be expressed as

$$\sum_{X_k \in \mathbf{C}_n^r(0)} \frac{\sigma_\beta^2 \sigma_h}{2\left(\sigma_h^2 |\hat{Y}_k^r - X_k|^2 + \sigma_\beta^2\right)^{\frac{3}{2}}} \underset{1}{\overset{0}{\gtrless}} \sum_{X_k \in \mathbf{C}_n^r(1)} \frac{\sigma_\beta^2 \sigma_h}{2\left(\sigma_h^2 |\hat{Y}_k^r - X_k|^2 + \sigma_\beta^2\right)^{\frac{3}{2}}}, \tag{4.81}$$

where the $\mathbf{C}^r(0)$ and $\mathbf{C}^r(1)$ denotes the signal subset of all possible equiprobable symbols of X_k whose n-th bit is either 0 or 1 in the real and imaginary components. After simplifying (4.81), the ML detector can be expressed as

$$\frac{\sum_{X_k \in \mathbf{C}_n^r(0)} \frac{1}{\left(\sigma_h^2 |\hat{Y}_k^r - X_k|^2 + \sigma_\beta^2\right)^{\frac{3}{2}}}}{\sum_{X_k \in \mathbf{C}_n^r(1)} \frac{1}{\left(\sigma_h^2 |\hat{Y}_k^r - X_k|^2 + \sigma_\beta^2\right)^{\frac{3}{2}}}} \underset{1}{\overset{0}{\gtrless}} 1. \tag{4.82}$$

Moreover, the general form of the conditional equalized received samples utilizing M-QAM constellation of the real and imaginary parts for the case of BGMIN in (4.48)-(4.49) and the combination of BI noise and BGMIN in (4.78)-(4.79) can be written as

$$p_Z(\hat{Y}_k^r | X_k) = \sum_{X_k \in \mathbf{C}_n^r} \sum_{n=0}^{N} \binom{N}{n} \alpha^n (1-\alpha)^{N-n} \frac{\sigma_\beta^2 \sigma_h}{2\left(\sigma_h^2 |\hat{Y}_k^r - X_k|^2 + \sigma_\beta^2\right)^{\frac{3}{2}}},$$
$$\forall k = 0, 1, \cdots \frac{N-1}{\log_2(M)}, \tag{4.83}$$

where $\sigma_\beta^2 = \sigma_n^2$ and $\sigma_\beta^2 = \sigma_b^2 + \sigma_n^2$ for the cases of BGMIN and the combined BI noise and BGMIN, respectively. The ML detector for the real and imaginary parts of received signal can be expressed as

$$\frac{\sum_{X_k \in \mathbf{C}_n^r(0)} \sum_{n=0}^{N} \binom{N}{n} \alpha^n (1-\alpha)^{N-n} \frac{\sigma_\beta^2}{\left(\sigma_h^2 |\hat{Y}_k^r - X_k|^2 + \sigma_\beta^2\right)^{\frac{3}{2}}}}{\sum_{X_k \in \mathbf{C}_n^r(1)} \sum_{n=0}^{N} \binom{N}{n} \alpha^n (1-\alpha)^{N-n} \frac{\sigma_\beta^2}{\left(\sigma_h^2 |\hat{Y}_k^r - X_k|^2 + \sigma_\beta^2\right)^{\frac{3}{2}}}} \underset{1}{\overset{0}{\gtrless}} 1. \tag{4.84}$$

While the sub-optimal demodulator based on Gaussian distribution can be expressed as [56]

$$\frac{\sum_{X_k \in \mathbf{C}_n^r(0)} e^{-\left(\frac{|\hat{Y}_k^r - X_k|^2}{\sigma_w^2}\right)}}{\sum_{X_k \in \mathbf{C}_n^r(1)} e^{-\left(\frac{|\hat{Y}_k^r - X_k|^2}{\sigma_w^2}\right)}} \underset{1}{\overset{0}{\gtrless}} 1. \tag{4.85}$$

4.4.2 BER Derivations over PLC Channel in the Presence of NGN

We proceed now to compute the Symbol Error Rate (SER) and BER based on derived PDFs. The General equalized received noise samples for the real and imaginary parts for the case of MCAIN (4.33)-(4.34) with $\sigma_\beta^2 = \sigma_A^2$, BI noise (4.66)-(4.67) with $\sigma_\beta^2 = \sigma_b^2$ and their combination (4.72)-(4.73) with $\sigma_\beta^2 = \sigma_b^2 + \sigma_A^2$ can be written as

$$p_Z(Z_k^r) = \frac{\sigma_\beta^2 \sigma_h}{2\left(\sigma_h^2 |Z_k^r|^2 + \sigma_\beta^2\right)^{\frac{3}{2}}}. \tag{4.86}$$

The SER can be derived using the Cumulative Distribution Function (CDF) of the the equalized noise samples at the ZF equalizer output as

$$\begin{aligned} F_Z(z) = P(Z \leq z) &= \int_{-\infty}^{z} p_z(u)du \\ &= \int_{-\infty}^{z} \left[\frac{\sigma_\beta^2 \sigma_h}{2(\sigma_h^2 u^2 + \sigma_\beta^2)^{3/2}}\right] du = \left[\frac{\sigma_h u}{2(\sigma_h^2 u^2 + \sigma_\beta^2)^{1/2}}\right]_{u=-\infty}^{z} \\ &= \left[\frac{\sigma_h z}{2(\sigma_h^2 z^2 + \sigma_\beta^2)^{1/2}} - \lim_{u\to-\infty} \frac{\sigma_h u}{2(\sigma_h^2 u^2 + \sigma_\beta^2)^{1/2}}\right] \\ &= \left[\frac{\sigma_h z}{2(\sigma_h^2 z^2 + \sigma_\beta^2)^{1/2}} + \frac{1}{2}\right], \end{aligned} \tag{4.87}$$

therefore, the probability of error for the real and imaginary parts utilizing 4-QAM constellation for the OFDM system over PLC channels can be expressed as

$$\begin{aligned} p_s^r(4-\text{QAM}) = F_Z(0) = P(Z \leq 0) &= \left[\frac{\sigma_h(0 - \sqrt{E_b})}{2(\sigma_h^2(0 - \sqrt{E_b})^2 + \sigma_\beta^2)^{1/2}} + \frac{1}{2}\right] \\ &= \frac{1}{2}\left[1 - \sqrt{\frac{\sigma_h^2 E_b}{\sigma_h^2 E_b + \sigma_\beta^2}}\right] = \frac{1}{2}\left[1 - \sqrt{\frac{\psi}{\psi+1}}\right], \end{aligned} \tag{4.88}$$

where $\psi = \frac{\sigma_h^2 E_b}{\sigma_\beta^2}$. Therefore, the SER can be computed as [56]

$$p_s(4-\text{QAM}) = 1 - [1 - p_s^r(4-\text{QAM})]^2 \approx \left[1 - \sqrt{\frac{\psi}{\psi+1}}\right]. \tag{4.89}$$

and the BER can be computed as

$$p_b(4-\text{QAM}) = \frac{p_s(4-\text{QAM})}{\log_2(M)} = \frac{p_s(4-\text{QAM})}{\log_2(4)} = \frac{1}{2}\left[1 - \sqrt{\frac{\psi}{\psi+1}}\right]. \tag{4.90}$$

Thus, the SER of the M-ary QAM signal for $M >> 4$ can be derived using the SER of the $\sqrt{M}$-ary Pulse Amplitude Modulation ($\sqrt{M}$-PAM) as [56]

$$p_s^{\sqrt{M}-\mathrm{PAM}} = \left(1 - \frac{1}{\sqrt{M}}\right)(1 - \Psi), \tag{4.91}$$

where $\Psi = \sqrt{\frac{K\psi}{K\psi+1}}$, $K = \frac{3\log_2(M)}{2(M-1)}$ and E_b is the energy per transmitted bit. The SER of the M-ary QAM signal can be derived as [56]

$$p_s^{M-\mathrm{QAM}} = 1 - \left(1 - p_s^{\sqrt{M}-\mathrm{PAM}}\right)^2 = 2P_s^{\sqrt{M}-\mathrm{PAM}} - \left(P_s^{\sqrt{M}-\mathrm{PAM}}\right)^2, \tag{4.92}$$

the exact solution of (4.92) can be expressed as given in [159] as

$$p_s^{M-\mathrm{QAM}} = 2\left(1 - \frac{1}{\sqrt{M}}\right)(1 - \Psi) - \left(1 - \frac{1}{\sqrt{M}}\right)^2 \left[1 - \frac{4}{\pi}\Psi \ \tan^{-1}\left(\frac{1}{\Psi}\right)\right]. \tag{4.93}$$

Therefore, the general expression formula that describes the tight approximation of BER can be expressed as

$$p_b^{M-\mathrm{QAM}} \approx \frac{p_s^{M-\mathrm{QAM}}}{\log_2(M)}. \tag{4.94}$$

Moreover, the general form of the conditional equalized received samples utilizing M-QAM constellation of the real and imaginary parts for the case of BGMIN (4.48)-(4.49) with $\sigma_\beta^2 = \sigma_n^2$ and the combination of BI noise and BGMIN (4.78)-(4.79) with $\sigma_\beta^2 = \sigma_b^2 + \sigma_n^2$ can be written as

$$p_Z(Z_k^r) = \sum_{n=0}^{N} \binom{N}{n} \alpha^n (1-\alpha)^{N-n} \frac{\sigma_\beta^2 \sigma_h}{2\left(\sigma_h^2 |Z_k^r|^2 + \sigma_\beta^2\right)^{\frac{3}{2}}}. \tag{4.95}$$

Following the similar derivation steps (4.87)-(4.91). The SER of the $\sqrt{M}$-PAM can be expressed as

$$p_s^{\sqrt{M}-\mathrm{PAM}} = \left(1 - \frac{1}{\sqrt{M}}\right) \sum_{n=0}^{N} \binom{N}{n} \alpha^n (1-\alpha)^{N-n} (1 - \Psi). \tag{4.96}$$

Therefore, the tight approximation of the BER in different scenarios of BGMIN and the combination between BI noise and BGMIN over PLC channel utilizing M-ary QAM constellation can be computed by substituting (4.96) in (4.92) and the outcome in (4.94) with the help of (4.50) for computing large factorials.

4.5 Threshold Optimization for Conventional OFDM System

In order to reduce the high power of the IN in the time domain for the conventional receiver, blanking or clipping non-linearity methods can be applied before the OFDM demodulator, replacing the incoming signal, $\tilde{y}_n$ in (4.3), by the zero values or the threshold values when the received signal magnitudes exceed the blanking threshold or clipping threshold, respectively. The improved conventional discrete-time complex-baseband model of the OFDM transmission system over PLC channels is shown in the Fig. 4.6 as

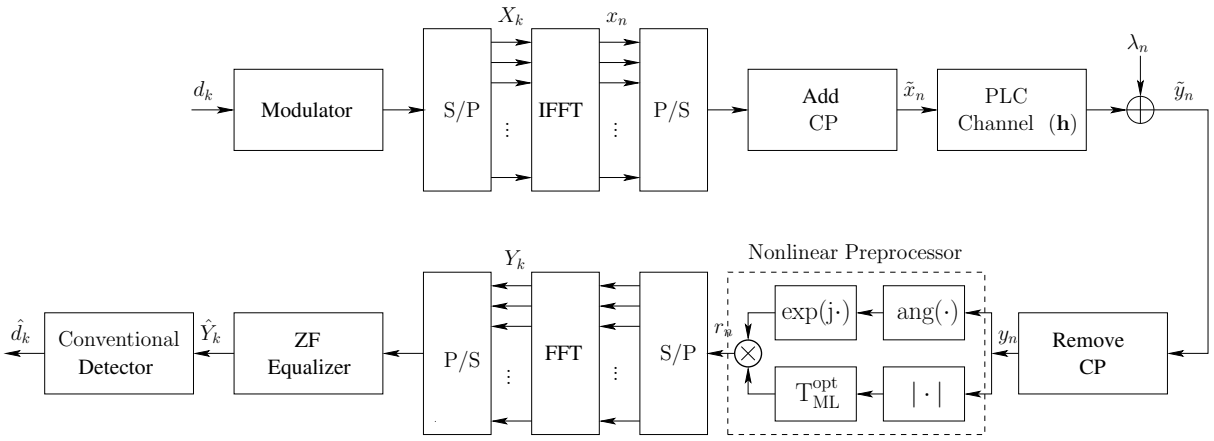

Figure 4.6: Block diagram of the conventional OFDM system over PLC channel.

Hence, the blanker output and the clipper output can be expressed as [69, 72, 80, 81]

$$r_n = \begin{cases} \tilde{y}_n, & |\tilde{y}_n| \leq T_{ML}^{opt} \\ 0, & \text{otherwise} \end{cases}, \quad n = 0, 1, \cdots, N-1,$$

$$r_n = \begin{cases} \tilde{y}_n, & |\tilde{y}_n| \leq T_{ML}^{opt} \\ T_{ML}^{opt} e^{j \arg \tilde{y}_n}, & \text{otherwise} \end{cases}, \quad n = 0, 1, \cdots, N-1. \tag{4.97}$$

4.5.1 MCAIN Model and the Combination of BI Noise and MCAIN Model

The real and imaginary distributions of the MCAIN model in (4.9) can be expressed as a mixture of two Gaussian PDF's, each PDF with zero mean but with different variances as presented in the simplified model in (2.26). For complex noise, the magnitude of the simplified form exhibits a mixture of two Rayleigh PDF's as

$$p(|i_n|) = \frac{e^{-A}|i_n|}{\sigma_w^2} e^{-\frac{|i_n|^2}{2\sigma_w^2}} + \frac{(1-e^{-A})|i_n|}{\zeta^2} e^{-\frac{|i_n|^2}{2\zeta^2}}, \tag{4.98}$$

where $\zeta^2 = \sigma_w^2\left(1+\frac{1}{A\rho}\right)$. For large number of orthogonal sub-carriers N, the transmitted signal x_n in (4.1) will follow the Gaussian distribution as $\mathcal{N}(x_n, 0, \sigma_x^2)$. Hence, the complex received signal $\tilde{y}_n$ in (4.3) will follow the distribution of (4.98) as

$$p(|\tilde{y}_n|) = \frac{e^{-A}|\tilde{y}_n|}{\sigma_1^2} e^{-\frac{|\tilde{y}_n|^2}{2\sigma_1^2}} + \frac{(1-e^{-A})|\tilde{y}_n|}{\sigma_2^2} e^{-\frac{|\tilde{y}_n|^2}{2\sigma_2^2}}, \tag{4.99}$$

where $(1-e^{-A})$ is the probability of impulsive occurrence, σ_1^2 denotes the variance of the received signal in the case of free impulsive and σ_2^2 denotes the variance of the received signal in the case of impact impulsive. The decision rule using the ML criterion [56] based on combination criterion can be expressed as

$$\mathrm{ML} = \begin{cases} \tilde{y}_n \in X_1, & \text{if} \quad \dfrac{\frac{|\tilde{y}_n|}{\sigma_1^2} e^{-\frac{|\tilde{y}_n|^2}{2\sigma_1^2}}}{\frac{|\tilde{y}_n|}{\sigma_2^2} e^{-\frac{|\tilde{y}_n|^2}{2\sigma_2^2}}} \geq 1 \\ \tilde{y}_n \in X_2, & \text{elsewhere} \end{cases}. \tag{4.100}$$

The decision rule is exactly equivalent to

$$\mathrm{ML} = \begin{cases} \tilde{y}_n \in X_1, & \text{if} \quad \tilde{y}_n \leq T_{ML}^{opt} \\ \tilde{y}_n \in X_2, & \text{elsewhere} \end{cases}, \tag{4.101}$$

where T_{ML}^{opt} is the ML criterion threshold which satisfies the following condition

$$\frac{|T_{ML}^{opt}|}{\sigma_1^2} e^{-\frac{|T_{ML}^{opt}|^2}{2\sigma_1^2}} = \frac{|T_{ML}^{opt}|}{\sigma_2^2} e^{-\frac{|T_{ML}^{opt}|^2}{2\sigma_2^2}}, \tag{4.102}$$

we can simplify the (4.102) as

$$\begin{aligned} \frac{\sigma_2^2}{\sigma_1^2} &= e^{-\frac{|T_{ML}^{opt}|^2}{2\sigma_2^2} + \frac{|T_{ML}^{opt}|^2}{2\sigma_1^2}}, \\ \frac{\sigma_2^2}{\sigma_1^2} &= e^{|T_{ML}^{opt}|^2\left(\frac{\sigma_2^2-\sigma_1^2}{2\sigma_2^2\sigma_1^2}\right)}, \\ |T_{ML}^{opt}|^2 &= \frac{2\sigma_2^2\sigma_1^2}{\sigma_2^2-\sigma_1^2}\ln\left(\frac{\sigma_2^2}{\sigma_1^2}\right), \\ |T_{ML}^{opt}| &= \sqrt{\frac{2\sigma_2^2\sigma_1^2}{\sigma_2^2-\sigma_1^2}\ln\left(\frac{\sigma_2^2}{\sigma_1^2}\right)}. \end{aligned} \tag{4.103}$$

Thus, in the case of complex MCAIN only, σ_1^2 and σ_2^2 can be expressed as $\sigma_1^2 = \frac{\mathbb{E}\{|h|^2\}\mathbb{E}\{|x|^2\}}{2}+\sigma_w^2$ and $\sigma_2^2 = \frac{\mathbb{E}\{|h|^2\}\mathbb{E}\{|x|^2\}}{2} + \zeta^2$. The simplification of the first term $\frac{2\sigma_2^2\sigma_1^2}{\sigma_2^2-\sigma_1^2}$ can be expressed as

$$\begin{aligned}
\frac{2\sigma_2^2\sigma_1^2}{\sigma_2^2-\sigma_1^2} &= \frac{2\left(\frac{\mathbb{E}\{|h|^2\}\mathbb{E}\{|x|^2\}}{2}+\zeta^2\right)\left(\frac{\mathbb{E}\{|h|^2\}\mathbb{E}\{|x|^2\}}{2}+\sigma_w^2\right)}{\left(\frac{\mathbb{E}\{|h|^2\}\mathbb{E}\{|x|^2\}}{2}+\zeta^2\right)-\left(\frac{\mathbb{E}\{|h|^2\}\mathbb{E}\{|x|^2\}}{2}+\sigma_w^2\right)}, \\
&= \frac{2\left(\frac{\mathbb{E}\{|h|^2\}\mathbb{E}\{|x|^2\}}{2}+\sigma_w^2\left(1+\frac{1}{A\rho}\right)\right)\left(\frac{\mathbb{E}\{|h|^2\}\mathbb{E}\{|x|^2\}}{2}+\sigma_w^2\right)}{\frac{\sigma_w^2}{A\rho}}, \\
&= 2A\rho\left(\frac{\mathbb{E}\{|h|^2\}\mathbb{E}\{|x|^2\}}{2\sigma_w^2}+\frac{1}{A\rho}+1\right)\sigma_w^2\left(\frac{\mathbb{E}\{|h|^2\}\mathbb{E}\{|x|^2\}}{2\sigma_w^2}+1\right), \\
&= 2A\rho\sigma_w^2\left(\mathrm{SNR}+\frac{1}{A\rho}+1\right)(\mathrm{SNR}+1), \qquad (4.104)
\end{aligned}$$

where the $\mathrm{SNR} = \frac{\mathbb{E}\{|h|^2\}\mathbb{E}\{|x|^2\}}{2\sigma_w^2}$. Moreover, the simplification of the second term $\ln\left(\frac{\sigma_2^2}{\sigma_1^2}\right)$ can be expressed as

$$\begin{aligned}
\ln\left(\frac{\sigma_2^2}{\sigma_1^2}\right) &= \ln\left(\frac{\frac{\mathbb{E}\{|h|^2\}\mathbb{E}\{|x|^2\}}{2}+\sigma_w^2\left(1+\frac{1}{A\rho}\right)}{\frac{\mathbb{E}\{|h|^2\}\mathbb{E}\{|x|^2\}}{2}+\sigma_w^2}\right), \\
&= \ln\left(1+\frac{\frac{\sigma_w^2}{A\rho}}{\frac{\mathbb{E}\{|h|^2\}\mathbb{E}\{|x|^2\}}{2}+\sigma_w^2}\right), \\
&= \ln\left(1+\frac{1}{A\rho\left(\frac{\mathbb{E}\{|h|^2\}\mathbb{E}\{|x|^2\}}{2\sigma_w^2}+1\right)}\right), \\
&= \ln\left(1+\frac{1}{A\rho\left(\mathrm{SNR}+1\right)}\right). \qquad (4.105)
\end{aligned}$$

Therefore, the optimal threshold in the presence of MCAIN model can be computed by utilizing (4.103) as

$$|T_{ML}^{opt}| = \sqrt{2A\rho\sigma_w^2\left(\mathrm{SNR}+\frac{1}{A\rho}+1\right)(\mathrm{SNR}+1)\ln\left(1+\frac{1}{A\rho\left(\mathrm{SNR}+1\right)}\right)}. \qquad (4.106)$$

In order to compute the threshold in the presence of BI noise and MCAIN model. The closed form distribution of the real part of combined BI noise and MCAIN model $\lambda_n^{\Re}$ conditioned on θ_n in the time domain has been derived in [163] as

$$p(\lambda_n^{\Re}|\theta_n) = \frac{2^{1.5-m}\Gamma(2m)}{\Gamma(m)\Gamma(m+0.5)}\left(\frac{m}{\Omega\cos^2(\theta_n)}\right)^m \sum_{\ell=0}^{\infty}\frac{e^{-A}A^k e^{\left(-\frac{(\lambda_n^{\Re})^2}{2\sigma_\ell^2}\right)}}{\ell!\sigma_\ell(c^{\Re}(\theta_n))^m}{}_1F_1\left(m;\frac{1}{2};\frac{(\lambda_n^{\Re})^2}{2\sigma_\ell^4 c^{\Re}(\theta_n)}\right), \qquad (4.107)$$

where $c^{\Re}(\theta_n) = \left(\frac{2m}{\Omega\cos^2(\theta_n)} + \frac{1}{\sigma_\ell^2}\right)$. Therefore, following similar derivation steps in [163], the distribution of the imaginary part of combined BI noise and MCAIN model $\lambda_n^{\Im}$ conditioned on θ_n in the time domain can be derived as

$$p(\lambda_n^{\Im}|\theta_n) = \frac{2^{1.5-m}\Gamma(2m)}{\Gamma(m)\Gamma(m+0.5)}\left(\frac{m}{\Omega\sin^2(\theta_n)}\right)^m \sum_{\ell=0}^{\infty}\frac{e^{-A}A^k e^{\left(-\frac{(\lambda_n^{\Im})^2}{2\sigma_\ell^2}\right)}}{\ell!\sigma_\ell(c^{\Im}(\theta_n))^m}{}_1F_1\left(m;\frac{1}{2};\frac{(\lambda_n^{\Im})^2}{2\sigma_\ell^4 c^{\Im}(\theta_n)}\right), \tag{4.108}$$

where $c^{\Im}(\theta_n) = \left(\frac{2m}{\Omega\sin^2(\theta_n)} + \frac{1}{\sigma_\ell^2}\right)$. Due to the high complexity of the distributions of the combined BN and IN modelled by using MCAIN model in (4.107) and(4.108), the noise distribution in (4.98) can be utilized instead of (4.107) and(4.108). Therefore, σ_1^2 and σ_2^2 can be expressed as $\sigma_1^2 = \frac{\mathbb{E}\{|h|^2\}\mathbb{E}\{|x|^2\}}{2} + \sigma_b^2 + \sigma_w^2$ and $\sigma_2^2 = \frac{\mathbb{E}\{|h|^2\}\mathbb{E}\{|x|^2\}}{2} + \sigma_b^2 + \zeta^2$, respectively. The threshold can be computed by utilizing (4.103) and after some simplifications yields

$$|T_{ML}| = \sqrt{2A\rho\sigma_w^2\left(\mathrm{SNR} + \frac{\sigma_b^2}{\sigma_w^2} + \frac{1}{A\rho} + 1\right)\left(\mathrm{SNR} + \frac{\sigma_b^2}{\sigma_w^2} + 1\right)\ln\left(\frac{1}{A\rho\left(\mathrm{SNR} + \frac{\sigma_b^2}{\sigma_w^2} + 1\right)} + 1\right)}. \tag{4.109}$$

4.5.2 BGMIN Model and the Combination of BI Noise and BGMIN Model

The real and imaginary parts distribution of the BGMIN model in the time domain can be expressed as (2.23) as

$$p(\lambda_n^r) = \frac{(1-\alpha)}{\sqrt{2\pi\sigma_w^2}}e^{-\frac{(\lambda_n^r)^2}{2\sigma_w^2}} + \frac{\alpha}{\sqrt{2\pi(\sigma_w^2+\sigma_i^2)}}e^{-\frac{(\lambda_n^r)^2}{2(\sigma_w^2+\sigma_i^2)}}. \tag{4.110}$$

While the distribution of complex noise samples can be expressed as two Rayleigh PDFs mixture model as

$$p(|\lambda_n|) = \frac{(1-\alpha)|\lambda_n|}{\sigma_w^2}e^{-\frac{|\lambda_n|^2}{2\sigma_w^2}} + \frac{\alpha|\lambda_n|}{\sigma_w^2+\sigma_i^2}e^{-\frac{|\lambda_n|^2}{2(\sigma_w^2+\sigma_i^2)}}. \tag{4.111}$$

Following similar derivation steps (4.99)-(4.103). Assuming $\sigma_1^2 = \frac{\mathbb{E}\{|h|^2\}\mathbb{E}\{|x|^2\}}{2} + \sigma_w^2$ and $\sigma_2^2 = \frac{\mathbb{E}\{|h|^2\}\mathbb{E}\{|x|^2\}}{2} + \sigma_w^2 + \sigma_i^2$ in the case of complex BGMIN. After substituting σ_1^2 and σ_2^2 in (4.103). The optimal threshold after some simplifications yields

$$|T_{ML}^{opt}| = \sqrt{2\sigma_w^2\left(\mathrm{SNR}+1\right)\left(\frac{\mathrm{SNR}+1}{\tilde{\rho}}+1\right)\ln\left(1+\frac{\tilde{\rho}}{\mathrm{SNR}+1}\right)}. \tag{4.112}$$

In order to compute the threshold in the case of combined BI noise and BGMIN model, the probability distribution of the real and imaginary parts conditioned on θ_n can be used to find the closed form distribution. The BI noise distribution in (4.52) can be used instead of using (4.53)-(4.54) to combine with the distribution of the BGMIN in (4.35) and is recalled in a simplified expression in (4.113)

$$p(\lambda_n^r) = p(i_n^r) = (1-\alpha)\mathcal{N}(i_n^r, 0, \sigma_w^2) + \alpha\mathcal{N}(i_n^r, 0, \sigma_w^2 + \sigma_i^2) = \sum_{\ell=1}^{2} \frac{p_\ell}{\sqrt{2\pi}\sigma_\ell} e^{-\frac{(i_n^r)^2}{2\sigma_\ell^2}}, \quad (4.113)$$

where $p_1 = 1-\alpha, p_2 = \alpha, \sigma_1^2 = \sigma_w^2$ and $\sigma_2^2 = \sigma_w^2 + \sigma_i^2$. Therefore, the distribution of sum two independent RVs, b_n^r conditioned θ_n in (4.52) and λ_n^r in (4.113) can be computed as a convolution between two PDFs. Therefore, the joint distribution can be expressed as

$$p_{bi}(b_n^r, i_n^r|\theta_n) = \sum_{\ell=1}^{2} \frac{2p_\ell \times \left(\frac{m}{\Omega}\right)^m}{\sqrt{2\pi}\Gamma(m)(\Delta^r)^{2m}\sigma_\ell} (b_n^r)^{2m-1} e^{-\frac{m\times(b_n^r)^2}{\Omega\times(\Delta^r)^2}} e^{-\frac{(i_n^r)^2}{2\sigma_\ell^2}}. \quad (4.114)$$

For simplicity, letting $c_1 = \frac{2p_\ell \times \left(\frac{m}{\Omega}\right)^m}{\sqrt{2\pi}\Gamma(m)(\Delta^r)^{2m}\sigma_\ell}$, $c_2 = \frac{m}{\Omega\times(\Delta^r)^2}$ and $c_3 = \frac{1}{2\sigma_\ell^2}$. The new RV denotes z_n^r which is express the sum of b_n^r and i_n^r as $z_n^r = b_n^r + i_n^r$. Substituting $i_n^r = z_n^r - b_n^r$ in (4.114) yields

$$p_z(b_n^r, z_n^r - b_n^r|\theta_n) = \sum_{\ell=1}^{2} c_1 \times (b_n^r)^{2m-1} e^{-c_2\times(b_n^r)^2} e^{-c_3\times(z_n^r - b_n^r)^2}. \quad (4.115)$$

The conditional distribution of $p_z(z_n^r|\theta_n)$ can be computed as

$$p_z(z_n^r|\theta_n) = \sum_{\ell=1}^{2} \int_{-\infty}^{\infty} c_1 e^{-c_3\times(z_n^r)^2} (b_n^r)^{2m-1} e^{-(c_2+c_3)\times(b_n^r)^2 + 2c_3 z_n^r b_n^r} db_n^r. \quad (4.116)$$

Splitting the integral in to two integrals and then utilizing the integral form [45, Eq.(3.462.1)] with $v = 2m$, $\beta = c_2 + c_3$, and $\gamma = 2c_3 z_n^r$ or $\gamma = -2c_3 z_n^r$ as the case may be. Thus

$$
\begin{aligned}
p_z(z_n^r|\theta_n) =& \sum_{\ell=1}^{2} c_1 e^{-c_3\times(z_n^r)^2} \left(2(c_2+c_3)\right)^{-m} \Gamma(2m) e^{\frac{4c_3^2\times(z_n^r)^2}{8(c_2+c_3)}} \times \\
& \left[D_{-2m}\left(\frac{2c_3 z_n^r}{\sqrt{2(c_2+c_3)}}\right) + D_{-2m}\left(\frac{-2c_3 z_n^r}{\sqrt{2(c_2+c_3)}}\right)\right] \\
=& \sum_{\ell=1}^{2} c_1 e^{-c_3\times(z_n^r)^2} \left(2(c_2+c_3)\right)^{-m} \Gamma(2m) e^{\frac{c_3^2\times(z_n^r)^2}{2(c_2+c_3)}} \times \\
& 2^{-m} e^{-\frac{c_3^2\times(z_n^r)^2}{2(c_2+c_3)}} \left[\frac{2\sqrt{\pi}}{\Gamma(m+\frac{1}{2})}\Phi\left(m,\frac{1}{2},\frac{2c_3^2\times(z_n^r)^2}{(c_2+c_3)}\right)\right],
\end{aligned} \tag{4.117}
$$

where $D_p(.)$ is the parabolic cylinder function defined in [45, Eq.(9.240)]. Utilizing $\Phi(a,c;x) = {}_1F_1(\alpha;\gamma;x)$, the real and imaginary distributions after some simplifications yields

$$
\begin{aligned}
p_z(z_n^{\Re}|\theta_n) =& \sum_{\ell=1}^{2} \frac{2^{1.5-2m} p_\ell \times \Gamma(2m)}{\sigma_\ell \Gamma(m)\Gamma(m+\frac{1}{2})\left(\frac{m}{\Omega\cos^2(\theta_n)}+\frac{1}{2\sigma_\ell^2}\right)^m} \left(\frac{m}{\Omega\cos^2(\theta_n)}\right)^m e^{-\frac{(z_n^{\Re})^2}{2\sigma_\ell^2}} \times \\
& {}_1F_1\left(m,\frac{1}{2},\frac{(z_n^{\Re})^2}{2\sigma_\ell^4\times\left(\frac{m}{\Omega\cos^2(\theta_n)}+\frac{1}{2\sigma_\ell^2}\right)}\right).
\end{aligned} \tag{4.118}
$$

$$
\begin{aligned}
p_z(z_n^{\Im}|\theta_n) =& \sum_{\ell=1}^{2} \frac{2^{1.5-2m} p_\ell \times \Gamma(2m)}{\sigma_\ell \Gamma(m)\Gamma(m+\frac{1}{2})\left(\frac{m}{\Omega\sin^2(\theta_n)}+\frac{1}{2\sigma_\ell^2}\right)^m} \left(\frac{m}{\Omega\sin^2(\theta_n)}\right)^m e^{-\frac{(z_n^{\Im})^2}{2\sigma_\ell^2}} \times \\
& {}_1F_1\left(m,\frac{1}{2},\frac{(z_n^{\Im})^2}{2\sigma_\ell^4\times\left(\frac{m}{\Omega\sin^2(\theta_n)}+\frac{1}{2\sigma_\ell^2}\right)}\right).
\end{aligned} \tag{4.119}
$$

The joint PDF of the real part can be expressed as

$$
\begin{aligned}
p_{Z,\theta}(z_k^{\Re},\theta_n) =& p_z(z_n^{\Re}|\theta_n)p_\theta(\theta_n) \\
=& \sum_{\ell=1}^{2} \frac{2^{0.5-2m} p_\ell \times \Gamma(2m)}{\pi\sigma_\ell \Gamma(m)\Gamma(m+\frac{1}{2})\left(\frac{m}{\Omega\cos^2(\theta_n)}+\frac{1}{2\sigma_\ell^2}\right)^m} \left(\frac{m}{\Omega\cos^2(\theta_n)}\right)^m e^{-\frac{(z_n^{\Re})^2}{2\sigma_\ell^2}} \times \\
& {}_1F_1\left(m,\frac{1}{2},\frac{(z_n^{\Re})^2}{2\sigma_\ell^4\times\left(\frac{m}{\Omega\cos^2(\theta_n)}+\frac{1}{2\sigma_\ell^2}\right)}\right).
\end{aligned} \tag{4.120}
$$

Hence, the PDF of the real part can be computed as

$$
\begin{aligned}
p_Z(z_k^{\Re}) &= \int_{-\pi}^{\pi} p_{Z,\theta}(z_k^{\Re}, \theta_n) d\theta_n \\
&= 4 \int_0^{\pi/2} \sum_{\ell=1}^{2} \frac{2^{0.5-2m} p_\ell \times \Gamma(2m)}{\pi \Gamma(m) \Gamma(m+\frac{1}{2}) \sigma_\ell \times \left(\frac{m}{\Omega \cos^2(\theta_n)} + \frac{1}{2\sigma_\ell^2} \right)^m} \left(\frac{m}{\Omega \cos^2(\theta_n)} \right)^m e^{-\frac{(z_n^{\Re})^2}{2\sigma_\ell^2}} \times \\
&\quad {}_1F_1 \left(m, \frac{1}{2}, \frac{(z_n^{\Re})^2}{2\sigma_\ell^4 \times \left(\frac{m}{\Omega \cos^2(\theta_n)} + \frac{1}{2\sigma_\ell^2} \right)} \right) d\theta_n. \qquad (4.121)
\end{aligned}
$$

No closed-form expression for this integral is available in the literature, hence, the noise distribution in (4.111) can be utilized instead of (4.121). The variances σ_1^2 and σ_2^2 can be expressed as $\sigma_1^2 = \frac{\mathbb{E}\{|h|^2\}\mathbb{E}\{|x|^2\}}{2} + \sigma_b^2 + \sigma_w^2$ and $\sigma_2^2 = \frac{\mathbb{E}\{|h|^2\}\mathbb{E}\{|x|^2\}}{2} + \sigma_b^2 + \sigma_w^2 + \sigma_i^2$, respectively. The threshold can be computed by utilizing (4.103) and after some simplifications yields

$$
|T_{ML}| = \sqrt{2\sigma_w^2 \left(\mathrm{SNR} + \frac{\sigma_b^2}{\sigma_w^2} + 1 \right) \left(\frac{\mathrm{SNR}+1}{\tilde{\rho}} + \frac{\sigma_b^2}{\tilde{\rho}\sigma_w^2} + 1 \right) \ln \left(1 + \frac{\tilde{\rho}}{\mathrm{SNR} + \frac{\sigma_b^2}{\sigma_w^2} + 1} \right)}. \qquad (4.122)
$$

4.6 Simulation Results

4.6.1 Investigation of the PDFs

In this Section, the exact fitting of the derived distributions have been investigated by using Monte-Carlo simulation. A comparison between the histogram plot of the real and imaginary parts for the equalized received signal and theoretical noise PDFs are shown in the Fig. 4.7-Fig.4.11. The histogram are plotted in the presence of different scenarios of MCAIN, BGMIN, BI noise, combined MCAIN and BI noise and finally combined BGMIN and BI noise over 15-path PLC channel, where the channel parameters are listed in Table 4.1 [8].

The simulation parameters are set as: $m = 0.5$ and $m = 0.7$ in the case of the BI noise, $A = 10^{-2}$ and $\rho = 10^{-1}, 10^{-2}, 10^{-3}$ in the case of MCAIN model and $\alpha = 0.3, 0.1, 0.01$ and $\tilde{\rho} = 100$ in the case of BGMIN model. It is worth noting that the derivations of theoretical, closed-form PDFs exhibit close matching with their corresponding empirically obtained distributions using Monte-Carlo simulation. The Mean Squared Error (MSE) is used to compute the closing value between empirical and theoretical derived PDFs, which can be evaluated for the real and imaginary components as $\mathrm{MSE}^r = \frac{1}{N} \sum_{k=0}^{N-1} (\hat{Z}_k^r - Z_k^r)^2$.

Table 4.1: Parameters of the 15-path model.

Attenuation parameters					
$k = 1$		$a_0 = 0$		$a_1 = 7.8 \times 10^{-10}$	
Path-parameters					
i	g_i	$d_i(m)$	i	g_i	$d_i(m)$
1	0.029	90	9	0.071	411
2	0.043	102	10	-0.035	490
3	0.103	113	11	0.065	567
4	-0.058	143	12	-0.055	740
5	-0.045	148	13	0.042	960
6	-0.040	200	14	-0.059	1130
7	0.038	260	15	0.049	1250
8	-0.038	322			

Fig. 4.7 (a)-(b) demonstrates the histogram plot for real and imaginary parts utilizing derived distributions in (4.33) and (4.34), respectively, in the presence of IN modelled by using MCAIN model compared with Gaussian distribution as a reference distribution when substituting $\sigma_A^2 = \sigma_w^2$ in (4.33) and (4.34). It is worth noting that the closed-form derived PDFs exhibit close matching with their corresponding empirically obtained distributions for real and imaginary components using Monte-Carlo. Moreover, the Gaussian distribution has high level due to low σ_w^2 compared to σ_A^2. It can conclude that due to orthogonality, the real and imaginary components of the noise exhibit identical statistical behaviours. The MSEs are presented for both components in Table. 4.2.

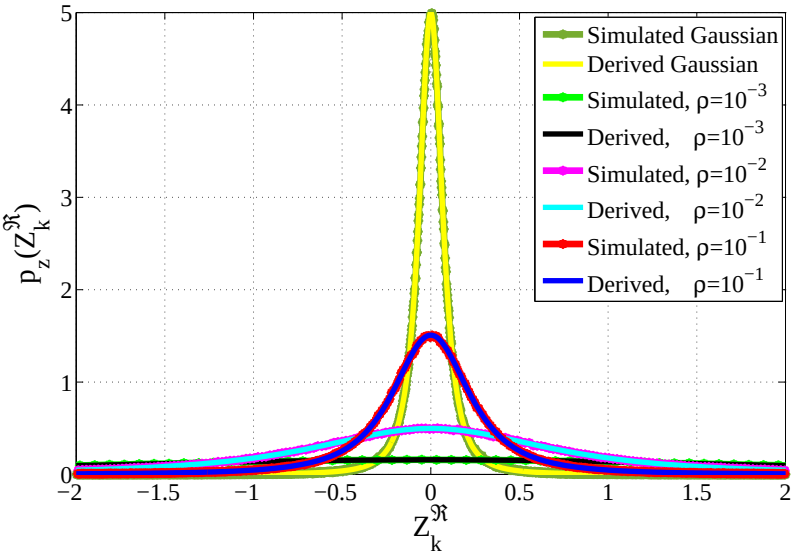

(a) Real part of the MCAIN.

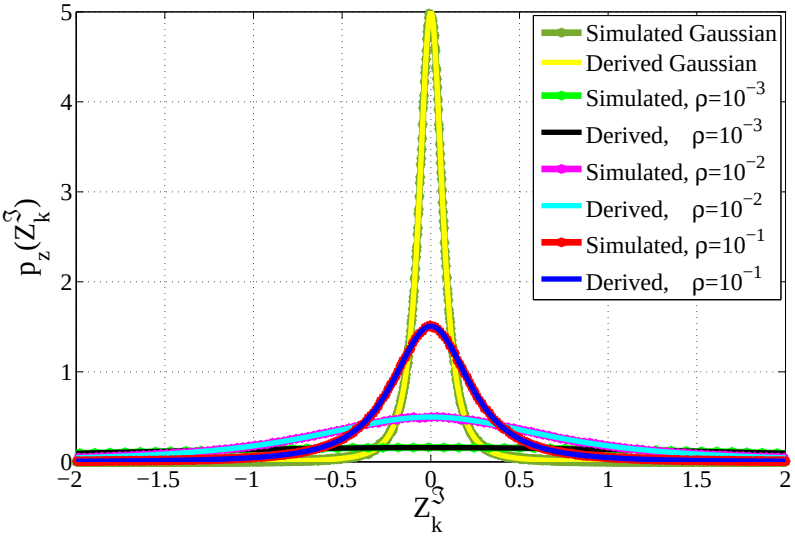

(b) Imaginary part of the MCAIN.

Figure 4.7: hanged Histogram plot at the ZF equalizer output in the presence of IN modelled by MCAIN with $A = 10^{-2}$ over 15-path PLC channel at SNR = 20 dB.

Table 4.2: MSE of MCAIN with $A = 10^{-2}$ at the ZF equalizer output over 15-path PLC channel.

MCAIN	Real part	Imaginary part
$\rho = 10^{-3}$	4.5561×10^{-13}	2.3456×10^{-12}
$\rho = 10^{-2}$	8.7281×10^{-11}	5.9811×10^{-12}
$\rho = 10^{-1}$	7.7514×10^{-10}	1.2252×10^{-10}

Fig. 4.8 (a)-(b) demonstrates the histogram plot for real and imaginary parts utilizing derived distributions in (4.48) and (4.49), respectively, in the presence of BGMIN model. The closed-

form PDFs exhibit close matching with their corresponding empirically obtained distribution for real and imaginary components using Monte-Carlo. Moreover, the Gaussian distribution has high level due to low σ_w^2 compared to σ_N^2. Furthermore, the real and imaginary components of the noise exhibit identical statistical behaviours. The MSEs are presented for real and imaginary components in Table. 4.3.

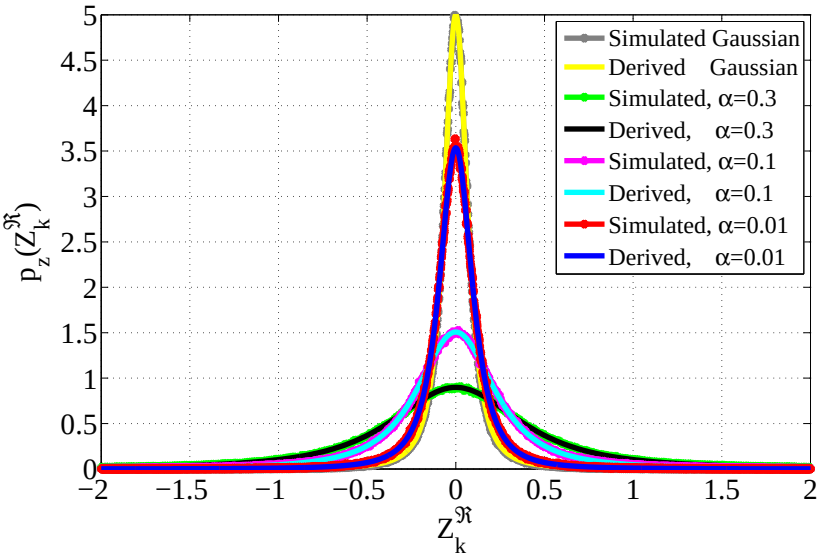

(a) Real part of the BGMIN.

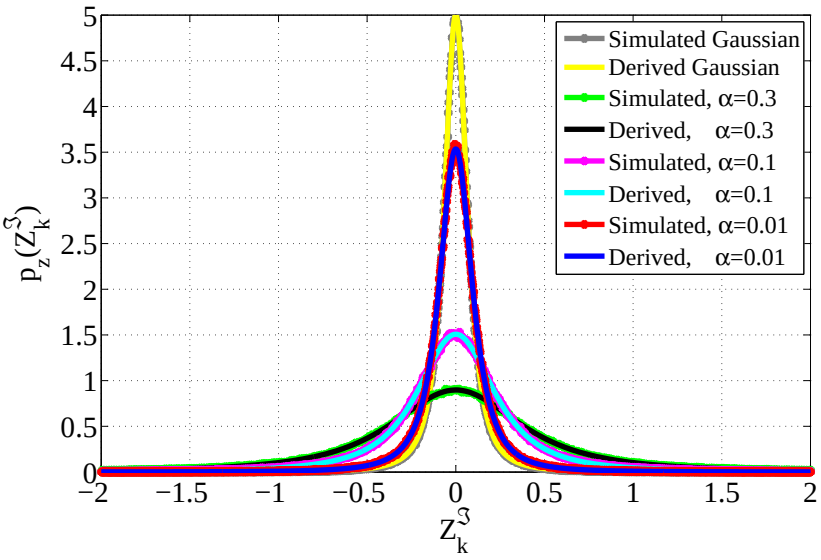

(b) Imaginary part of the BGMIN.

Figure 4.8: Histogram plot of at the ZF equalizer output in the presence of IN modelled by BGMIN with $\tilde{\rho} = 100$ over 15-path PLC channel at SNR = 20 dB.

Table 4.3: MSE of BGMIN with $\tilde{\rho} = 100$ at the ZF equalizer output over 15-path PLC channel.

BGMIN	Real part	Imaginary part
$\alpha = 0.3$	8.4397×10^{-13}	4.3556×10^{-12}
$\alpha = 0.1$	1.7281×10^{-11}	7.1681×10^{-10}
$\alpha = 0.01$	7.7574×10^{-11}	3.2352×10^{-12}

Fig. 4.9 (a)-(b) demonstrates the histogram plot of real and imaginary parts utilizing derived distributions in (4.66) and (4.67), respectively, in the presence of Nakagami-m BI noise. The closed-form PDFs exhibit close matching with their corresponding empirically obtained distributions using Monte-Carlo. Moreover, the Gaussian distribution has high level due to low σ_w^2 compared to σ_b^2. Furthermore, the real and imaginary components of the noise exhibit identical statistical behaviours. The MSEs are presented for real and imaginary components in Table. 4.4. Thus, both components have identical statistical behaviours.

Table 4.4: MSE of BI noise at the ZF equalizer output over 15-path PLC channel.

Nakagami-m	Real part	Imaginary part
$m = 0.5$	2.5811×10^{-11}	4.8317×10^{-12}
$m = 0.7$	1.1169×10^{-10}	5.8948×10^{-11}

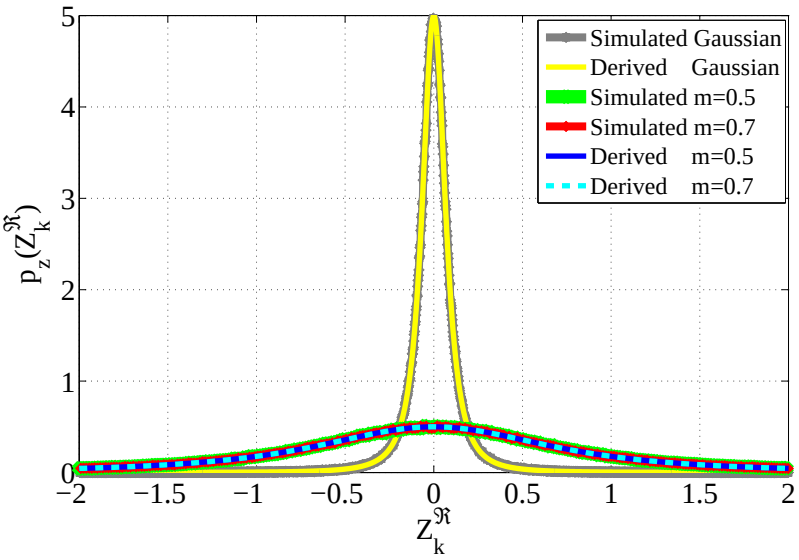

(a) Real part of the BI noise.

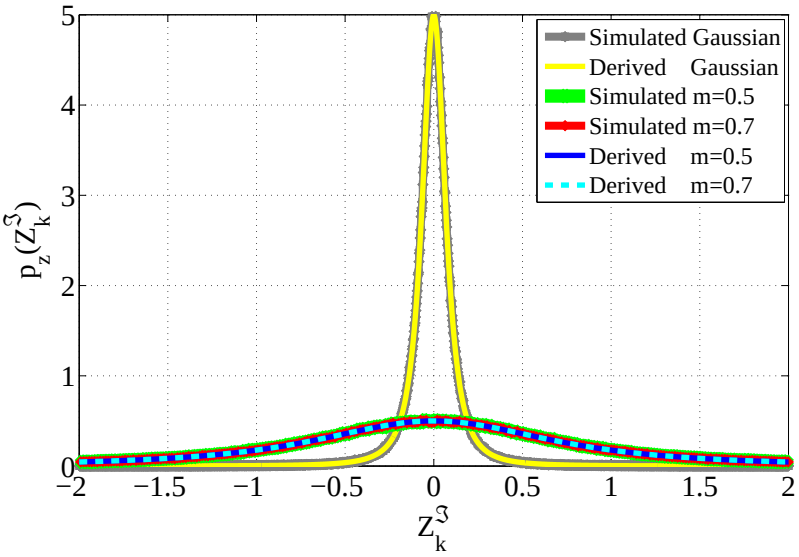

(b) Imaginary part of the BI noise.

Figure 4.9: Histogram plot at the ZF equalizer output in the presence of Nakagami-m BI noise with $\Omega = 1$ over 15-path PLC channel.

Fig. 4.10 (a)-(b) demonstrates the histogram plot of real and imaginary components utilizing derived distributions in (4.72) and (4.73), respectively, in the presence of combined Nakagami-m BI noise and MCAIN model. The closed-form PDFs exhibit close matching with their corresponding empirically obtained distributions using Monte-Carlo. Moreover, the Gaussian distribution has high level due to low σ_w^2 compared to $\sigma_b^2 + \sigma_A^2$. Furthermore, the real and imaginary components of the noise exhibit identical statistical behaviours. The MSEs are presented for real and imaginary components in Table. 4.5. Thus, both components have identical statistical behaviours.

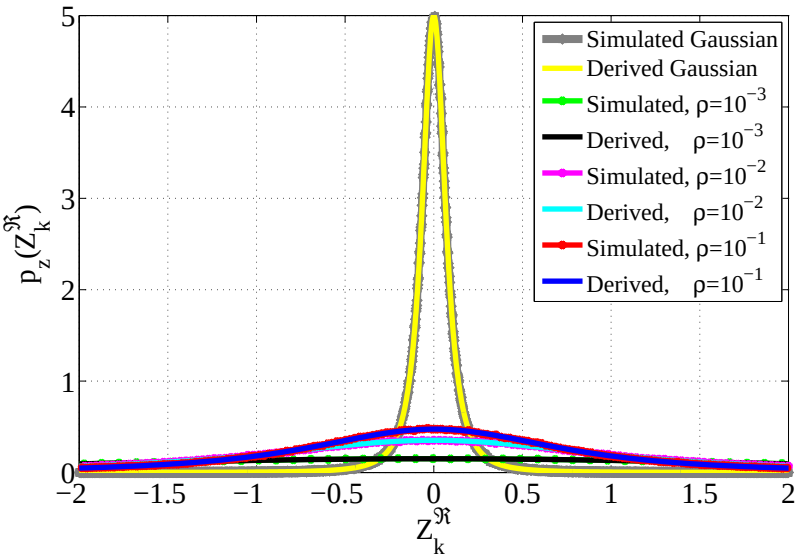

(a) Real part of the combined BI noise and MCAIN.

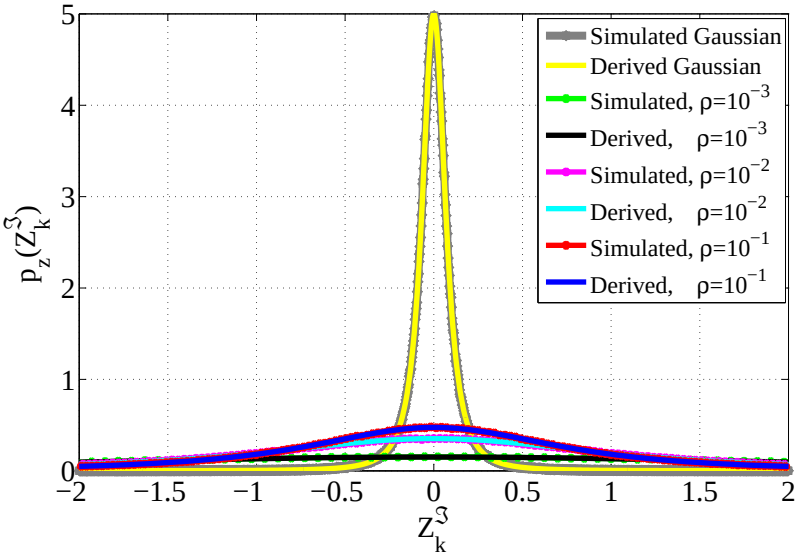

(b) Imaginary part of the combined BI noise and MCAIN.

Figure 4.10: Histogram plot at the ZF equalizer output in the presence of combined Nakagami-m BI noise with $m = 0.7$ and MCAIN with $A = 10^{-2}$ over 15-path PLC channel at SNR = 20 dB.

Table 4.5: MSE of combined BI noise with $m = 0.7$ and MCAIN with $A = 10^{-2}$ at the ZF equalizer output over 15-path PLC channel.

BI noise and MCAIN	Real part	Imaginary part
$\rho = 10^{-3}$	8.4823×10^{-10}	4.9977×10^{-10}
$\rho = 10^{-2}$	8.1702×10^{-11}	5.0091×10^{-12}
$\rho = 10^{-1}$	3.1567×10^{-11}	6.6759×10^{-10}

Fig. 4.11 (a)-(b) demonstrates the histogram plot of real and imaginary components utilizing derived distributions in (4.78) and (4.79), respectively, in the presence of combined Nakagami-

m BI noise and BGMIN model. The closed-form PDFs exhibit close matching with their corresponding empirically obtained distributions with MSEs are presented for real and imaginary components in Table. 4.6. Thus, both components have identical statistical behaviours.

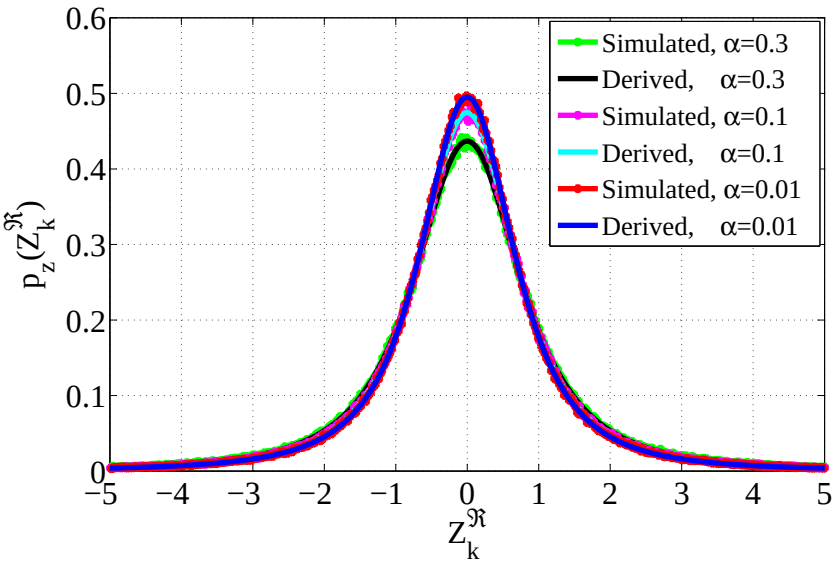

(a) Real part of combined BI noise and BGMIN.

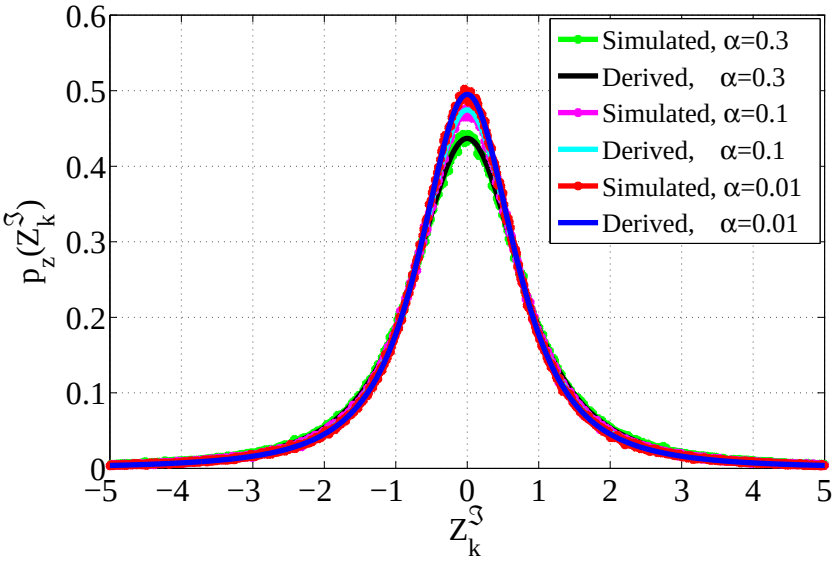

(b) Imaginary part of combined BI noise and BGMIN.

Figure 4.11: Histogram plot at the ZF equalizer output in the presence of combined Nakagami-m BI noise with $m = 0.7$ and BGMIN with $\tilde{\rho} = 100$ over 15-path PLC channel at SNR = 20 dB.

Table 4.6: MSE of the combined BI noise with $m = 0.7$ and BGMIN with $\tilde{\rho} = 100$ at the ZF equalizer output over 15-path PLC channel.

BI noise and BGMIN	Real part	Imaginary part
$\alpha = 0.3$	3.3432×10^{-11}	5.9981×10^{-11}
$\alpha = 0.1$	3.4456×10^{-10}	7.8223×10^{-11}
$\alpha = 0.01$	4.8234×10^{-12}	2.5567×10^{-11}

4.6.2 BER Simulations

In order to assess the performance of the derived PDFs for the OFDM system over PLC channel in the presence of NGN. The ML detector in (4.82) is used for the case of BI noise, MCAIN and their combination, and in (4.84) is used for BGMIN and combined BI noise and BGMIN. The simulation parameters were set as follows, the number of sub-carriers was set as N=1024 and the constellation size was set as 256-QAM and 1024-QAM. The BER performances are investigated over modified Zimmermann model with 15-path PLC channel presented in Table 4.1. The system performance is compared against the conventional OFDM system, in which the blanking and clipping non-linearity IN mitigation methods in the time domain and the sub-optimal detector based on the Gaussian distribution in (4.85) are utilized.

The Fig. 4.12 demonstrates the BER performance of the OFDM system in the presence of Nakagami-m BI noise utilizing the derived ML detector in (4.82) with $\sigma_\beta^2 = \sigma_b^2$ for $m = 0.7$ and 0.5. It can be seen from the figure that the BER performance is approximately unaffected by changing the value of m associated to Nakagami distribution. This is due to the fact that the BI noise after the FFT operation will appear in the frequency domain as a Gaussian noise; i.e. the BER performance will depend on the average noise power as seen by the sub-carriers.

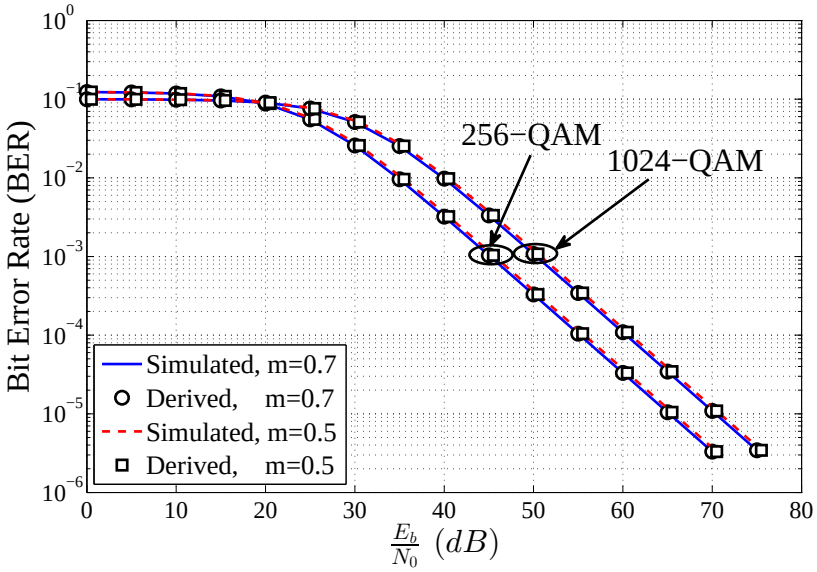

Figure 4.12: Performance of 256-QAM versus 1024-QAM for the OFDM system over 15-path PLC channel in the presence of Nakagami-m BI noise.

In Fig. 4.13, the BER performance of four different systems have been compared. The proposed OFDM system utilizes the derived PDFs has been compared with the conventional OFDM system without any IN cancellation methods at the receiver and with the conventional OFDM system utilizes the derived threshold in (4.122) with clipping and blanking methods.

The systems performance are compared in the presence of combined BI noise with $m = 0.7$ and BGMIN model with $\alpha = 0.3, 0.1, 0.01$ for $\tilde{\rho} = 100$. It can be seen from the figures that the performance of the systems is degraded more than the case of BI noise only with severe power loss in terms of $\frac{E_b}{N_0}$ when the IN parameters are increased. Also, the parameters of α and $\tilde{\rho}$ play a key role in the systems performance. For example, when α is increased, the BER performance degrades for all systems. Moreover, in all scenarios of combined noise, the derived receiver which utilizes the exact noise distribution at the ZF equalizer output with ML detector computation in (4.84) outperforms the conventional receivers that utilize blanking threshold or clipping threshold (4.122) with ML detector based on the Gaussian distribution in (4.85). Furthermore, the conventional receiver utilizing clipping or blanking non-linearity method at the receiver can lead to significant BER improvements. While the conventional receiver without using clipping or blanking non-linearity method suffers from error floors at high SNRs. In this case, the error floor beginning at $\frac{E_b}{N_0} = 60$ dB due to using a constant value of $\tilde{\rho} = 100$. In addition to the increase in the constellation size from 256-QAM to 1024-QAM leads to more degradation in the BER performance.

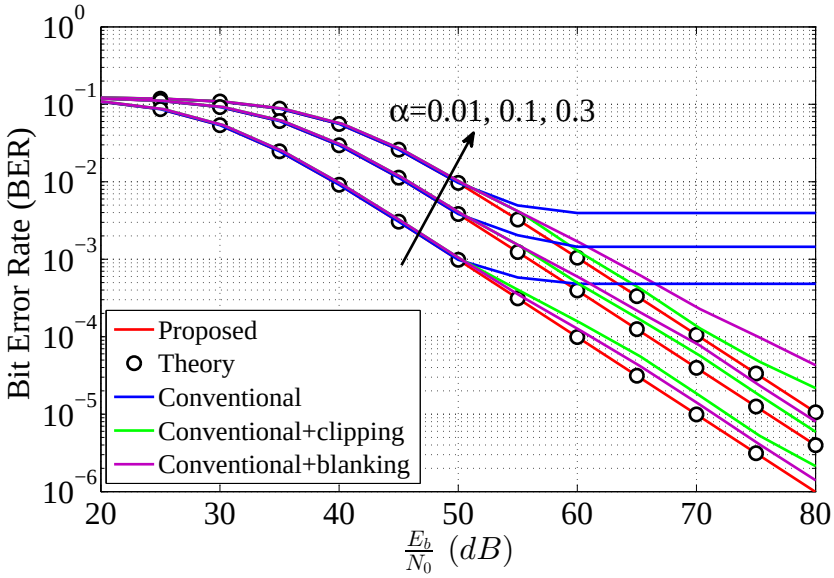

(a) 256-QAM modulation.

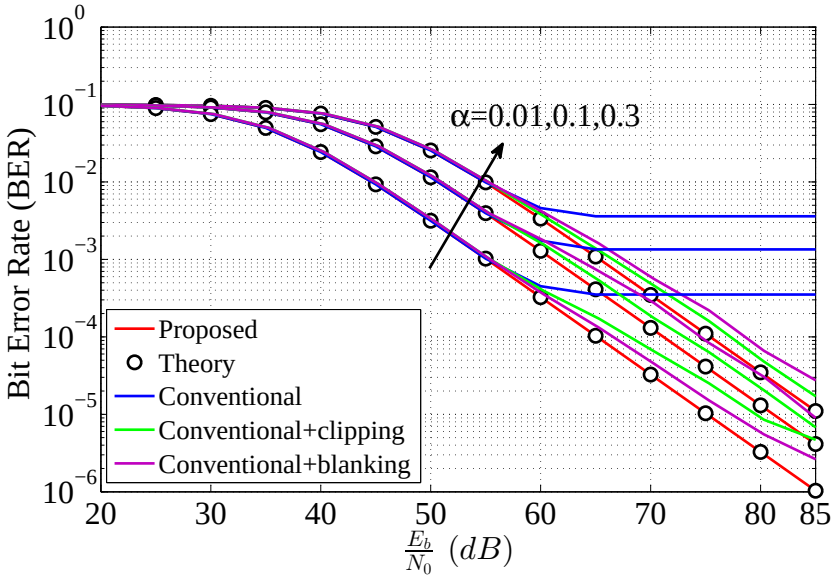

(b) 1024-QAM modulation.

Figure 4.13: Performance of 256-QAM and 1024-QAM modulation OFDM systems over 15-path PLC channel in the presence of combined Nakagami-m BI noise with $m = 0.7$ and IN modelled by BGMIN model with $\tilde{\rho} = 100$.

The Fig. 4.14 demonstrates the BER performance of the proposed derived OFDM system versus the conventional OFDM system with and without any treatment at the receiver. The systems performance are compared in the presence of combined BI noise with $m = 0.7$ and IN modelled using MCAIN model with $\rho = 10^{-1}, 10^{-2}, 10^{-3}$ and $A = 10^{-2}$ for $\ell = 0 - 100$. It can be seen from the figures that the performance of all systems is degraded more than the case of BI noise only and in the case of combined BI noise and BGMIN model with severe power loss. Also, the parameters A and ρ play a key role in the BER performance degradation of the systems. For example, when ρ decreases the BER performance degrades

for all systems. Moreover, the derived receiver utilizing the ML detector computed in (4.82) outperforms the conventional receivers that utilize the threshold in (4.109) with ML detector based on the Gaussian distribution in (4.85) in all scenarios of combined noise. Furthermore, the conventional receiver utilizing clipping or blanking non-linearity method at the receiver can lead to significant BER improvements compared to the conventional system without treatment. While the conventional receiver without using clipping or blanking non-linearity method suffers from error floors at high SNRs. In this case, the error floor begins at $\frac{E_b}{N_0} = 60$ dB due to using a constant value of $A = 0.01$ which leads to the same impact in all cases. Moreover, the high values of $\frac{E_b}{N_0}$ are due to using 256-QAM or 1024-QAM. In this case, each symbol error will cause 8-bit or 10-bit errors, respectively. Indeed, for reliable communication, the $\frac{E_b}{N_0}$ increases to achieve lower BER, where $\frac{E_b}{N_0}$ can be computed using (5.4) and the effective $\frac{E_b}{N_i}$ which takes into consideration the average impulsive noise can be computed using (5.5).

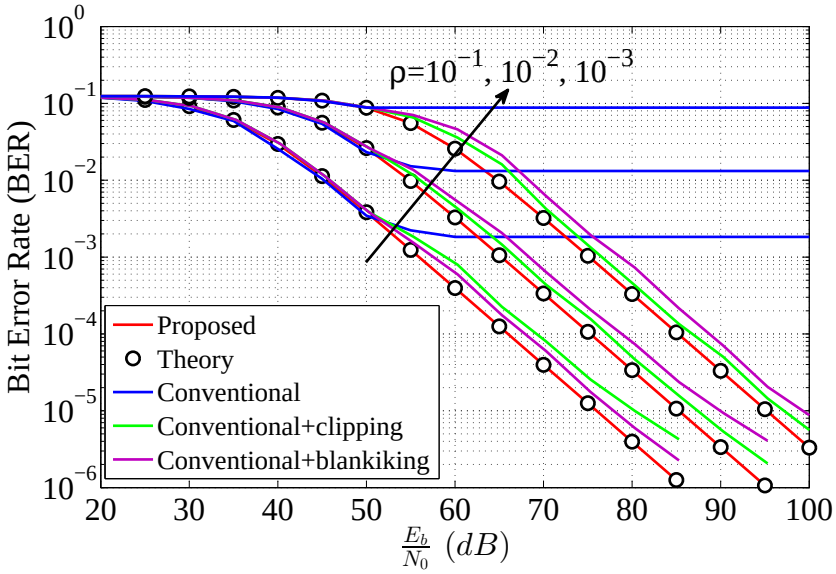

(a) 256-QAM modulation.

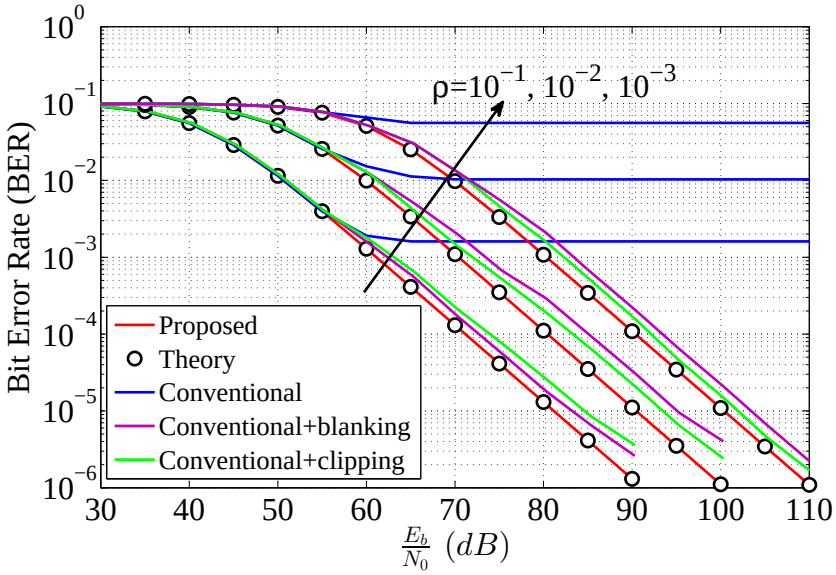

(b) 1024-QAM modulation.

Figure 4.14: Performance of 256-QAM and 1024-QAM modulation OFDM systems over 15-path PLC channel in the presence of combined Nakagami-m BI noise with $m = 0.7$ and IN modelled by MCAIN model with $A = 0.01$.

4.7 Summary of the Chapter

In this chapter, the noise sample distributions at the ZF equalizer output have been derived for different scenarios of Nakagami-m BI noise and IN modelled either by BGMIN model or MCAIN model. These PDFs are utilized to improve the performance of OFDM systems over PLC channel. Moreover, a generalized analytical expression of the optimal ML detector and the average BER based on derived PDFs have been derived. Furthermore, in this chapter, an optimization of the clipping and blanking thresholds have been derived at low complexity. The

performances of the uncoded system are improved by utilizing optimal noise distributions at the ZF equalizer output impaired by different scenarios of NGN over PLC channels. While the derived clipping and the blanking threshold have been shown useless for conventional OFDM systems and leading to significant BER improvements.

Chapter 5

Coded OFDM Systems

5.1 Introduction

The NGN impacts over PLC channel lead to BER performance degradation when utilizing a detector based on Gaussian distribution. Therefore, the derived noise distributions at the ZF equalizer output in the previous chapter are utilized to compute the optimal LLRs of soft decoders, and to improve the BER performance for different proposed coded OFDM systems over PLC channel in the presence of different scenarios of Nakagami-m BI noise and IN modelled either by using BGMIN model or MCAIN model. The performance of proposed coded OFDM systems is compared against coded conventional OFDM system and uncoded system to investigate the improvement amount in Coding Gain (CG) that can be achieved by utilizing the derived PDFs.

In this chapter, the performances of B-LDPC, NB-LDPC and TC utilizing 4-QAM and 16-QAM OFDM system has been improved over multipath PLC channel. The SPA is proposed to decode the B-LDPC code, while the SL-FFT decoding algorithm is proposed to decode the NB-LDPC code and the Max-Log-MAP decoding algorithm is proposed to decode the TC. The sparse parity check matrices $\mathbf{H}$ of B-LDPC code and NB-LDPC code have been constructed using progressive edge growth (PEG) algorithm whilst the TC has been constructed using two identical RSC codes. All decoders utilize the novel derived LLR values based on ED over PLC channel in the presence of NGN.

5.2 Coded OFDM System over PLC Channels

B-LDPC code and NB-LDPC code belong to class of linear block codes originally proposed by Gallager [101] and by Davey and Mackay [123], respectively. The LDPC codes can be classified into R and IR codes, in which, the latter type achieve a superior BER performance than the first type. The IR-LDPC code can be constructed by $\mathbf{H}$ of size $(n_c - k_c) \times n_c$ with variable column weight, w_c, and the row weight, w_r, respectively [114], where n_c and k_c are the codeword length and the information length, respectively.

The block-diagram of the B/NB-LDPC-COFDM system is shown in Fig. 5.1.

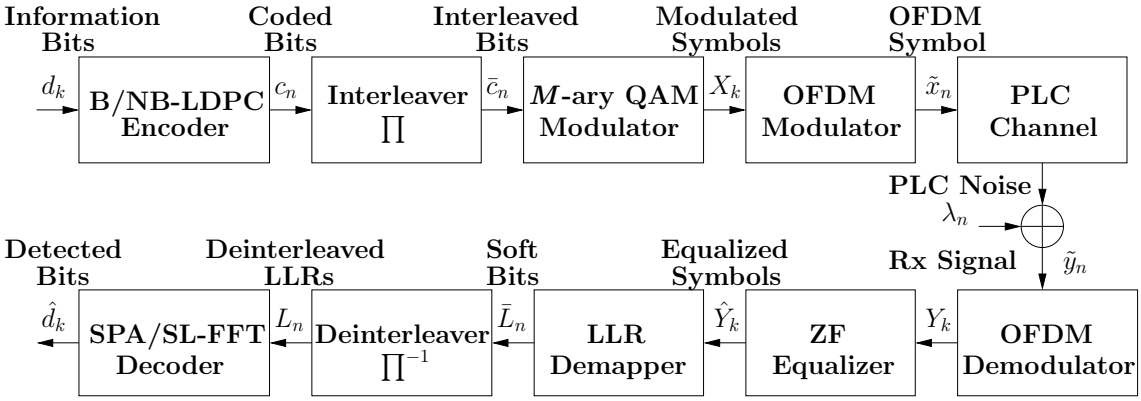

Figure 5.1: Block diagram of the M-ary QAM B/NB-LDPC-COFDM system over multipath PLC channel.

The block of information $\mathbf{d} = \{d_0, d_1, \ldots, d_{k_c-1}\}$ of length k (bits/digits) is encoded into codeword $\mathbf{c} = \{c_0, c_1, \ldots, c_{n_c-1}\}$ of length n_c (bits/digits) using the B/NB-LDPC encoder, respectively. Typically, random block interleaver is employed to scrambling the codeword in different order $\mathbf{c}$ (bits/digits) to $\bar{\mathbf{c}} = \prod(\mathbf{c})$. Subsequently, the codeword digits $\bar{\mathbf{c}}$ in the case of NB-LDPC codes are first converted to binary bits. Then for both encoder, the interleaved binary bits are grouped into groups of κ bits and then mapped unto to the 2^κ symbols of an M-ary QAM constellation, the corresponding QAM symbol for κ-tuple $\{c_m, c_{m+1}, \ldots c_{m+\kappa-1}\}$ bits can be computed as $X_k = \mathbf{C}[\sum_{m=0}^{\kappa-1} 2^{\kappa-1-m} c_m]$, where $\kappa = \log_2(M)$ and $\mathbf{C} \in \mathbb{C}^{2^\kappa \times 1}$ is the Gray-encoded constellation vector.

On the other hand, TC was invented by Berrou et al. in 1993 [94], as an error control coding for approaching the Shannon capacity performance through using iterative soft decoding algorithm. The basic block-diagram of the T-COFDM system is shown in Fig. 5.2

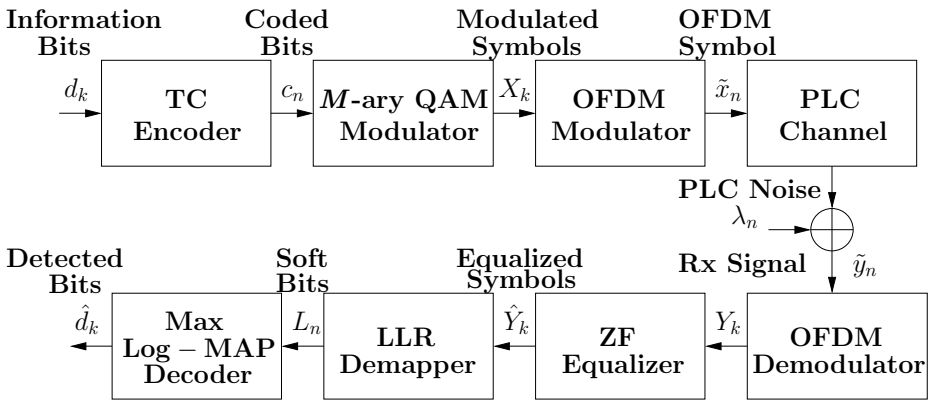

Figure 5.2: Block diagram of the T-COFDM system over PLC channel using M-ary QAM constellation.

The TC can be constructed using parallel concatenation of NRC codes or RSC codes with Long-Term Evolution (LTE) interleaver between them and "puncturing" stage, in which the TC based on RSC outperform the NRC [94]. The TC has been constructed using two identical RSC using generator matrix expressed as $G = (1, 5/7, 5/7)$ as shown in Fig. 3.3. The information sequence $\mathbf{d} = \{d_0, d_1, \ldots, d_{k_c-1}\}$ is fed to the RSC1 encoder to generate the parity check bits X_{p_1}. While on the other branch, the information sequence $\mathbf{d}$ is interleaved using LTE interleaver and then fed to the RSC2 encoder to generate the parity check bits X_{p_2}. Finally, the puncturing mechanism is used to achieve the encoded bits $\mathbf{c}$ for the desired code rate. Subsequently, the bits of the codeword $\mathbf{c}$ are then grouped into groups of κ bits and then mapped unto to the 2^κ symbols of an M-ary QAM constellation.

In addition, the complex base-band COFDM symbol in the time domain for all utilizing codes can be generated by taking IFFT for the modulated symbols as given in (4.1), then the COFDM symbol is transmitted over PLC channel. Under perfect time synchronization between the transmitter and the receiver, the received complex signal after CP removal and FFT operation can be expressed as given in Chapter 4 in (4.4) whose definition is recalled in (5.1)

$$Y_k = \frac{1}{\sqrt{N}} \sum_{n=0}^{N-1} y_n e^{\frac{-j2\pi nk}{N}} = H_k X_k + \Lambda_k. \tag{5.1}$$

According to the CLT, the distribution of the real and imaginary components of the total NGN, $p_\Lambda(\Lambda_k^r)$, will be approaching to Gaussian distribution, which can be expressed as

$$p_\Lambda(\Lambda_k^r) = p_I(I_k^r) = \frac{1}{\sqrt{2\pi}\sigma_\beta} e^{-\frac{(I_k^r)^2}{2\sigma_\beta^2}}, \tag{5.2}$$

where $\sigma_\beta^2 = \sigma_A^2$ in (4.13) for the case of the MCAIN model, $\sigma_\beta^2 = \sigma_b^2$ in (4.62) for the case

of the Nakakami-m BI noise, $\sigma_\beta^2 = \sigma_b^2 + \sigma_A^2$ for the case of combined Nakakami-m BI noise and MCAIN model, $\sigma_\beta^2 = \sigma_n^2$ for the case of BGMIN model and $\sigma_\beta^2 = \sigma_b^2 + \sigma_n^2$ for the case of combined BI noise and BGMIN model. For large number of sub-carriers, σ_n^2 for the case of BGMIN model can be expressed as σ_N^2 and can be computed as [58]

$$\sigma_N^2 = (1-\alpha)\sigma_w^2 + \alpha(\sigma_w^2 + \sigma_i^2) = \sigma_w^2 + \alpha\sigma_i^2 = \sigma_w^2(1+\alpha\tilde{\rho}), \tag{5.3}$$

where σ_w^2 and σ_i^2 are the AWGN and IN variances for coded systems which can be computed by

$$\text{SNR} = 10\log_{10}\left(\frac{E_b}{2\sigma_w^2 R_c}\right), \tag{5.4}$$

$$\text{SINR} = 10\log_{10}\left(\frac{E_b}{2\sigma_i^2 R_c}\right), \tag{5.5}$$

where SNR, SINR and R_c are the signal to noise ratio, signal to impulsive noise ratio and the coding rate, respectively. Moreover, $\tilde{\rho} = \frac{\sigma_i^2}{\sigma_w^2}$ and $\rho = \frac{\sigma_w^2}{\sigma_i^2}$ are the IGNPR for the case of BGMIN model and the GINPR for the case of MCAIN model, respectively.

Consequently, the complex NGN in (5.1) can be expressed as $Y_k - H_k X_k = \Lambda_k$. Therefore, the $p(Y_k|H_k, X_k)$ will follow the noise distribution in (5.2) and can be expressed as

$$p(Y_k|H_k, X_k) = \frac{1}{\sqrt{2\pi}\sigma_\beta} e^{-\frac{|Y_k - H_k X_k|^2}{2\sigma_\beta^2}}. \tag{5.6}$$

Hence, the attention has been now changing to compute the LLRs based on the Gaussian distribution in (5.6) for coded systems in the next section in this chapter.

5.3 LLR Computations Based on Euclidean Distance

5.3.1 Binary LDPC Codes

The modified LLRs for B-LDPC codes over PLC channels in the presence of NGN can be computed as

$$\mathrm{LLR}(b_k(m)) = \log \frac{p(Y_k|H_k, X_k=-1)}{p(Y_k|H_k, X_k=+1)} = \log \frac{\sum_{X_k \in \mathbf{C}_m^r(0)} e^{-\frac{|Y_k+H_k|^2}{2\sigma_\beta^2}}}{\sum_{X_k \in \mathbf{C}_m^r(1)} e^{-\frac{|Y_k-H_k|^2}{2\sigma_\beta^2}}},$$
$$m = 0, \cdots, \kappa-1 \ \text{ and } \ k = 0, 1, \ldots, \frac{N-1}{\kappa}, \tag{5.7}$$

where $\mathbf{C}_m^r(0)$ and $\mathbf{C}_m^r(1)$ denote the signal subset of all possible equiprobable symbols of X_k being 0 or 1, respectively. The $\mathrm{LLR}(b_k(0)), \ldots, \mathrm{LLR}(b_k(\kappa-1))$ can be computed corresponding to the M-QAM Gray constellation mapping $\mathbf{C} \in \mathbb{C}^{2^\kappa \times 1}$ for each $b_k(0), \ldots, b_k(\kappa-1)$ where $\kappa = \log_2(M)$ is the number of bits that representing one symbol in the constellation map. For example, the LLR equations corresponding to the 4-QAM constellation diagram in Fig. (5.3) can be computed as

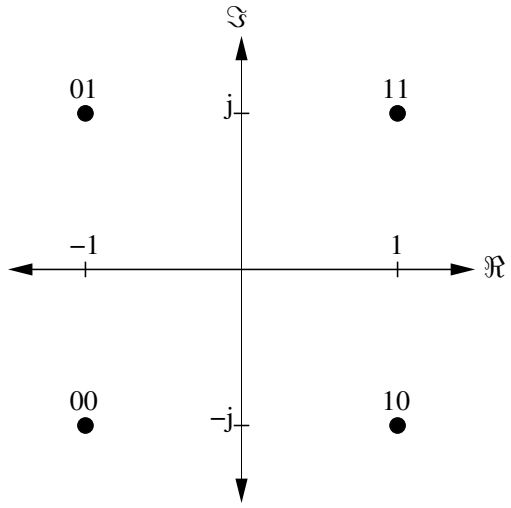

Figure 5.3: 4-QAM constellation.

$$\mathrm{LLR}(b_k(0)) = \log \frac{e^{-\frac{|Y_k+H_k|^2}{2\sigma_\beta^2}}}{e^{-\frac{|Y_k-H_k|^2}{2\sigma_\beta^2}}} = -\frac{2}{\sigma_\beta^2}\Re\{Y_k H_k^*\}, \tag{5.8}$$

$$\mathrm{LLR}(b_k(1)) = \log \frac{e^{-\frac{|Y_k+jH_k|^2}{2\sigma_\beta^2}}}{e^{-\frac{|Y_k-jH_k|^2}{2\sigma_\beta^2}}} = \frac{2}{\sigma_\beta^2}\Im\{Y_k^* H_k\}. \tag{5.9}$$

Moreover, the LLR equations corresponding to the 16-QAM constellation map in Fig. (5.4) can be computed as

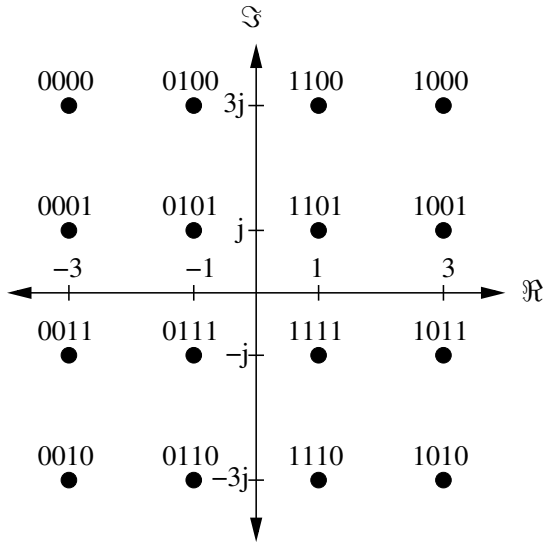

Figure 5.4: 16-QAM constellation.

$$\mathrm{LLR}(b_k(0)) = \log \frac{e^{-\frac{|Y_k+3H_k|^2}{2\sigma_\beta^2}} + e^{-\frac{|Y_k+H_k|^2}{2\sigma_\beta^2}}}{e^{-\frac{|Y_k-H_k|^2}{2\sigma_\beta^2}} + e^{-\frac{|Y_k-3H_k|^2}{2\sigma_\beta^2}}} \approx \log \frac{e^{-\frac{|Y_k+H_k|^2}{2\sigma_\beta^2}}}{e^{-\frac{|Y_k-H_k|^2}{2\sigma_\beta^2}}} = -\frac{2}{\sigma_\beta^2}\Re\{Y_k H_k^*\}, \tag{5.10}$$

$$\mathrm{LLR}(b_k(1)) = \log \frac{e^{-\frac{|Y_k+3H_k|^2}{2\sigma_\beta^2}} + e^{-\frac{|Y_k-3H_k|^2}{2\sigma_\beta^2}}}{e^{-\frac{|Y_k+H_k|^2}{2\sigma_\beta^2}} + e^{-\frac{|Y_k-H_k|^2}{2\sigma_\beta^2}}}, \tag{5.11}$$

the LLR of the second bit can be simplified by computing the LLR for each different neighbor bits as

$$\begin{aligned}
\mathrm{Eq.}(1) &= \log \frac{e^{-\frac{|Y_k+3H_k|^2}{2\sigma_\beta^2}}}{e^{-\frac{|Y_k+H_k|^2}{2\sigma_\beta^2}}} = -\frac{2}{\sigma_\beta^2}\left(\Re\{Y_k H_k^*\} + 2|H_k|^2\right), \\
\mathrm{Eq.}(2) &= \log \frac{e^{-\frac{|Y_k-3H_k|^2}{2\sigma_\beta^2}}}{e^{-\frac{|Y_k-H_k|^2}{2\sigma_\beta^2}}} = \frac{2}{\sigma_\beta^2}\left(\Re\{Y_k H_k^*\} - 2|H_k|^2\right),
\end{aligned} \tag{5.12}$$

then, the $\mathrm{LLR}(b_k(1))$ can be computed by utilizing the $\overset{*}{\max}$ operations (Jacobian logarithm) which is defined as [135]

$$\overset{*}{\max}(x, y) = \max(x, y) + \log(1 + e^{-|x-y|}), \tag{5.13}$$

therefore

$$\mathrm{LLR}(b_k(1)) = \overset{*}{\max}(\mathrm{Eq.}(1), \mathrm{Eq.}(2)). \tag{5.14}$$

$$\mathrm{LLR}(b_k(2)) = \log \frac{e^{-\frac{|Y_k - jH_k|^2}{2\sigma_\beta^2}} + e^{-\frac{|Y_k - 3jH_k|^2}{2\sigma_\beta^2}}}{e^{-\frac{|Y_k + 3jH_k|^2}{2\sigma_\beta^2}} + e^{-\frac{|Y_k + jH_k|^2}{2\sigma_\beta^2}}} \approx \log \frac{e^{-\frac{|Y_k - jH_k|^2}{2\sigma_\beta^2}}}{e^{-\frac{|Y_k + jH_k|^2}{2\sigma_\beta^2}}} = \frac{2}{\sigma_\beta^2} \Im\{Y_k H_k^*\}, \tag{5.15}$$

$$\mathrm{LLR}(b_k(3)) = \log \frac{e^{-\frac{|Y_k + 3jH_k|^2}{2\sigma_\beta^2}} + e^{-\frac{|Y_k - 3jH_k|^2}{2\sigma_\beta^2}}}{e^{-\frac{|Y_k + jH_k|^2}{2\sigma_\beta^2}} + e^{-\frac{|Y_k - jH_k|^2}{2\sigma_\beta^2}}},$$

$$\mathrm{Eq.}(1) = \log \frac{e^{-\frac{|Y_k + 3jH_k|^2}{2\sigma_\beta^2}}}{e^{-\frac{|Y_k + jH_k|^2}{2\sigma_\beta^2}}} = \frac{2}{\sigma_\beta^2} \left(\Im\{Y_k^* H_k\} - 2|H_k|^2 \right),$$

$$\mathrm{Eq.}(2) = \log \frac{e^{-\frac{|Y_k - 3jH_k|^2}{2\sigma_\beta^2}}}{e^{-\frac{|Y_k - jH_k|^2}{2\sigma_\beta^2}}} = -\frac{2}{\sigma_\beta^2} \left(\Im\{Y_k^* H_k\} + 2|H_k|^2 \right),$$

$$\mathrm{LLR}(b_k(3)) = \overset{*}{\max}(\mathrm{Eq.}(1), \mathrm{Eq.}(2)). \tag{5.16}$$

5.3.2 Non-binary LDPC Codes

The modified LLR equations for the NB-LDPC codes over PLC channel in the presence of NGN can be derived as

$$F_{q,k}^a = \log \left(\frac{e^{-\frac{|Y_k - H_k X_k|^2}{2\sigma_\beta^2}} | X_k = a}{e^{-\frac{|Y_k - H_k X_k|^2}{2\sigma_\beta^2}} | X_k = 0} \right), \ a \in \mathbb{F}_q \backslash \{0\}. \tag{5.17}$$

The modified LLRs for the 4-QAM constellation points in the Fig. 5.3 can be derived as

$$F_{4,k}^{0} = \log\left(\frac{e^{-\frac{|Y_k-(-1-j)H_k|^2}{2\sigma_\beta^2}}}{e^{-\frac{|Y_k-(-1-j)H_k|^2}{2\sigma_\beta^2}}}\right) = \mathbf{0}, \tag{5.18}$$

$$F_{4,k}^{1} = \log\left(\frac{e^{-\frac{|Y_k-(-1+j)H_k|^2}{2\sigma_\beta^2}}}{e^{-\frac{|Y_k-(-1-j)H_k|^2}{2\sigma_\beta^2}}}\right) = \frac{2}{\sigma_\beta^2}\Im\{Y_k H_k^*\}, \tag{5.19}$$

$$F_{4,k}^{2} = \log\left(\frac{e^{-\frac{|Y_k-(1-j)H_k|^2}{2\sigma_\beta^2}}}{e^{-\frac{|Y_k-(-1-j)H_k|^2}{2\sigma_\beta^2}}}\right) = \frac{2}{\sigma_\beta^2}\Re\{Y_k H_k^*\}, \tag{5.20}$$

$$F_{4,k}^{3} = \log\left(\frac{e^{-\frac{|Y_k-(1+j)H_k|^2}{2\sigma_\beta^2}}}{e^{-\frac{|Y_k-(-1-j)H_k|^2}{2\sigma_\beta^2}}}\right) = \frac{2}{\sigma_\beta^2}\left(\Re\{Y_k H_k^*\} + \Im\{Y_k H_k^*\}\right). \tag{5.21}$$

Furthermore, the modified LLRs for the 16-QAM constellation points in the Fig. 5.4 can derived as

$$F_{16,k}^{0} = \log\left(\frac{e^{-\frac{|Y_k-(-3+3j)H_k|^2}{2\sigma_\beta^2}}}{e^{-\frac{|Y_k-(-3+3j)H_k|^2}{2\sigma_\beta^2}}}\right) = \mathbf{0}, \tag{5.22}$$

$$F_{16,k}^{1} = \log\left(\frac{e^{-\frac{|Y_k-(-3+3j)H_k|^2}{2\sigma_\beta^2}}}{e^{-\frac{|Y_k-(-3+j)H_k|^2}{2\sigma_\beta^2}}}\right) = \frac{2}{\sigma_\beta^2}\left(\Im\{Y_k^* H_k\} + 2|H_k|^2\right), \tag{5.23}$$

$$F_{16,k}^{2} = \log\left(\frac{e^{-\frac{|Y_k-(-3-3j)H_k|^2}{2\sigma_\beta^2}}}{e^{-\frac{|Y_k-(-3+j)H_k|^2}{2\sigma_\beta^2}}}\right) = \frac{6}{\sigma_\beta^2}\Im\{Y_k^* H_k\}, \tag{5.24}$$

$$F_{16,k}^{3} = \log\left(\frac{e^{-\frac{|Y_k-(-3-j)H_k|^2}{2\sigma_\beta^2}}}{e^{-\frac{|Y_k-(-3+j)H_k|^2}{2\sigma_\beta^2}}}\right) = \frac{4}{\sigma_\beta^2}\left(\Im\{Y_k^* H_k\} + |H_k|^2\right), \tag{5.25}$$

$$F_{16,k}^{4} = \log\left(\frac{e^{-\frac{|Y_k-(-1+3j)H_k|^2}{2\sigma_\beta^2}}}{e^{-\frac{|Y_k-(-3+j)H_k|^2}{2\sigma_\beta^2}}}\right) = \frac{2}{\sigma_\beta^2}\left(\Re\{Y_k^* H_k\} + 2|H_k|^2\right), \tag{5.26}$$

$$F_{16,k}^{5} = \log\left(\frac{e^{-\frac{|Y_k-(-1+j)H_k|^2}{2\sigma_\beta^2}}}{e^{-\frac{|Y_k-(-3+j)H_k|^2}{2\sigma_\beta^2}}}\right) = \frac{2}{\sigma_\beta^2}\left(\Re\{Y_k^* H_k\} + \Im\{Y_k^* H_k\} + 4|H_k|^2\right), \tag{5.27}$$

$$F_{16,k}^{6} = \log\left(\frac{e^{-\frac{|Y_k-(-1-3j)H_k|^2}{2\sigma_\beta^2}}}{e^{-\frac{|Y_k-(-3+j)H_k|^2}{2\sigma_\beta^2}}}\right) = \frac{2}{\sigma_\beta^2}\left(\Re\{Y_k^* H_k\} + 3\Im\{Y_k^* H_k\} + 2|H_k|^2\right), \tag{5.28}$$

$$F_{16,k}^{7} = \log\left(\frac{e^{-\frac{|Y_k-(-1-j)H_k|^2}{2\sigma_\beta^2}}}{e^{-\frac{|Y_k-(-3+j)H_k|^2}{2\sigma_\beta^2}}}\right) = \frac{2}{\sigma_\beta^2}\left(\Re\{Y_k^* H_k\} + 2\Im\{Y_k^* H_k\} + 4|H_k|^2\right), \tag{5.29}$$

$$F_{16,k}^{8} = \log\left(\frac{e^{-\frac{|Y_k-(3+3j)H_k|^2}{2\sigma_\beta^2}}}{e^{-\frac{|Y_k-(-3+j)H_k|^2}{2\sigma_\beta^2}}}\right) = \frac{6}{\sigma_\beta^2}\Re\{Y_k^* H_k\}, \tag{5.30}$$

$$F_{16,k}^{9} = \log\left(\frac{e^{-\frac{|Y_k-(3+j)H_k|^2}{2\sigma_\beta^2}}}{e^{-\frac{|Y_k-(-3+j)H_k|^2}{2\sigma_\beta^2}}}\right) = \frac{2}{\sigma_\beta^2}\left(3\Re\{Y_k^* H_k\} + \Im\{Y_k^* H_k\} + 2|H_k|^2\right), \tag{5.31}$$

$$F_{16,k}^{10} = \log\left(\frac{e^{-\frac{|Y_k-(3-3j)H_k|^2}{2\sigma_\beta^2}}}{e^{-\frac{|Y_k-(-3+j)H_k|^2}{2\sigma_\beta^2}}}\right) = \frac{6}{\sigma_\beta^2}\left(\Re\{Y_k^* H_k\} + \Im\{Y_k^* H_k\}\right), \tag{5.32}$$

$$F_{16,k}^{11} = \log\left(\frac{e^{-\frac{|Y_k-(3-j)H_k|^2}{2\sigma_\beta^2}}}{e^{-\frac{|Y_k-(-3+j)H_k|^2}{2\sigma_\beta^2}}}\right) = \frac{2}{\sigma_\beta^2}\left(3\Re\{Y_k^*H_k\} + 2\Im\{Y_k^*H_k\} + 2|H_k|^2\right), \tag{5.33}$$

$$F_{16,k}^{12} = \log\left(\frac{e^{-\frac{|Y_k-(1+3j)H_k|^2}{2\sigma_\beta^2}}}{e^{-\frac{|Y_k-(-3+j)H_k|^2}{2\sigma_\beta^2}}}\right) = \frac{4}{\sigma_\beta^2}\left(\Re\{Y_k^*H_k\} + |H_k|^2\right), \tag{5.34}$$

$$F_{16,k}^{13} = \log\left(\frac{e^{-\frac{|Y_k-(1+j)H_k|^2}{2\sigma_\beta^2}}}{e^{-\frac{|Y_k-(-3+j)H_k|^2}{2\sigma_\beta^2}}}\right) = \frac{2}{\sigma_\beta^2}\left(2\Re\{Y_k^*H_k\} + \Im\{Y_k^*H_k\} + 4|H_k|^2\right), \tag{5.35}$$

$$F_{16,k}^{14} = \log\left(\frac{e^{-\frac{|Y_k-(1-3j)H_k|^2}{2\sigma_\beta^2}}}{e^{-\frac{|Y_k-(-3+j)H_k|^2}{2\sigma_\beta^2}}}\right) = \frac{2}{\sigma_\beta^2}\left(2\Re\{Y_k^*H_k\} + 3\Im\{Y_k^*H_k\} + 2|H_k|^2\right), \tag{5.36}$$

$$F_{16,k}^{15} = \log\left(\frac{e^{-\frac{|Y_k-(1-j)H_k|^2}{2\sigma_\beta^2}}}{e^{-\frac{|Y_k-(-3+j)H_k|^2}{2\sigma_\beta^2}}}\right) = \frac{4}{\sigma_\beta^2}\left(\Re\{Y_k^*H_k\} + \Im\{Y_k^*H_k\} + 2|H_k|^2\right), \tag{5.37}$$

It is worth highlighting that there is no information loss when the number of modulation levels M is equal to Galois field $\mathbb{F}_q$ and the channel LLRs are directly passed to the decoder as shown in Table. 5.1 in the 5-th column. While in the case of $q > M$ and M divides q, the symbols over $\mathbb{F}_q$ can be generated by the sum of the LLRs of the demodulated symbols as shown in Table. 5.1 in the 6-th column for the primitive polynomial $f(\alpha) = \alpha^4 + \alpha + 1$ over $\mathbb{F}_{16}$.

5.3.3 Binary Turbo Codes

The modified LLR equations for TCs over PLC channel in the presence of NGN can be computed as

$$\mathrm{LLR}(b_k(m)) = \log\frac{p(Y_k|H_k, X_k=+1)}{p(Y_k|H_k, X_k=-1)} = -\log\frac{\sum_{X_k\in\mathbf{C}_m^r(0)} e^{-\frac{|Y_k+H_k|^2}{2\sigma_\beta^2}}}{\sum_{X_k\in\mathbf{C}_m^r(1)} e^{-\frac{|Y_k-H_k|^2}{2\sigma_\beta^2}}},$$
$$m = 0, \cdots, \kappa-1 \ \text{ and } \ k = 0, 1, \ldots, \frac{N-1}{\kappa}. \tag{5.38}$$

Therefore, the LLR equations of TC are similar to the LLR equations of B-LDPC code multiplied by a negative sign.

Table 5.1: Primitive polynomial over $\mathbb{F}_{16}$ and LLR computations.

i	$\mathbb{F}_{16}$	Polynomial in α	Binary	LLRs for 16QAM	LLRs for 4QAM
0	0	0	0000	$F_{16,k}^{0}$	$F_{4,k}^{0}+F_{4,k}^{0}$
1	1	1	0001	$F_{16,k}^{1}$	$F_{4,k}^{0}+F_{4,k}^{1}$
2	α	α	0010	$F_{16,k}^{2}$	$F_{4,k}^{0}+F_{4,k}^{2}$
3	α^2	α^2	0100	$F_{16,k}^{3}$	$F_{4,k}^{1}+F_{4,k}^{0}$
4	α^3	α^3	1000	$F_{16,k}^{4}$	$F_{4,k}^{2}+F_{4,k}^{0}$
5	α^4	$\alpha+1$	0011	$F_{16,k}^{5}$	$F_{4,k}^{0}+F_{4,k}^{3}$
6	α^5	$\alpha^2+\alpha$	0110	$F_{16,k}^{6}$	$F_{4,k}^{1}+F_{4,k}^{2}$
7	α^6	$\alpha^3+\alpha^2$	1100	$F_{16,k}^{7}$	$F_{4,k}^{3}+F_{4,k}^{0}$
8	α^7	$\alpha^3+\alpha+1$	1011	$F_{16,k}^{8}$	$F_{4,k}^{2}+F_{4,k}^{3}$
9	α^8	α^2+1	1001	$F_{16,k}^{9}$	$F_{4,k}^{2}+F_{4,k}^{1}$
10	α^9	$\alpha^3+\alpha$	1010	$F_{16,k}^{10}$	$F_{4,k}^{2}+F_{4,k}^{2}$
11	α^{10}	$\alpha^2+\alpha+1$	0111	$F_{16,k}^{11}$	$F_{4,k}^{1}+F_{4,k}^{3}$
12	α^{11}	$\alpha^3+\alpha^2+\alpha$	1110	$F_{16,k}^{12}$	$F_{4,k}^{3}+F_{4,k}^{2}$
13	α^{12}	$\alpha^3+\alpha^2+\alpha+1$	1111	$F_{16,k}^{13}$	$F_{4,k}^{3}+F_{4,k}^{3}$
14	α^{13}	$\alpha^3+\alpha^2+1$	1101	$F_{16,k}^{14}$	$F_{4,k}^{3}+F_{4,k}^{1}$
15	α^{14}	α^3+1	1001	$F_{16,k}^{15}$	$F_{4,k}^{2}+F_{4,k}^{1}$

5.4 LLR Computations Based on the Derived PDFs at the ZF Equalizer Output

The complex received signal in (5.1) can be recovered by utilizing ZF equalizer after the N-point FFT operation expressed as

$$\hat{Y}_k^{\Re}+j\hat{Y}_k^{\Im}=\frac{Y_k^{\Re}+jY_k^{\Im}}{H_k^{\Re}+jH_k^{\Im}}=X_k^{\Re}+jX_k^{\Im}+\frac{\Lambda_k^{\Re}+j\Lambda_k^{\Im}}{H_k^{\Re}+jH_k^{\Im}}. \tag{5.39}$$

Therefore, the attention is now channging to compute the LLRs based on the derived noise PDFs at the ZF equalizer output in Chapter 4.

5.4.1 Binary LDPC Codes

The performance B-LDPC codes utilizing SPA decoding algorithm can be improved by computing the exact LLRs based on the optimal derived noise distributions at the ZF equalizer output. Thus, the modified initial LLRs can be computed over PLC channel in the presence of MCAIN

model, Nakakami-m BI noise, combined Nakakami-m BI noise and MCAIN model, BGMIN model and the combined Nakakami-m BI noise and BGMIN model by utilizing $\sigma_\beta^2 = \sigma_A^2$ in (4.13), $\sigma_\beta^2 = \sigma_b^2$ in (4.62), $\sigma_\beta^2 = \sigma_b^2 + \sigma_A^2$, $\sigma_\beta^2 = \sigma_N^2$ in (5.3) and $\sigma_\beta^2 = \sigma_b^2 + \sigma_N^2$ as

$$\mathrm{LLR}(b_k(m)) = \log \frac{\sum_{X_k \in \mathbf{C}_m^r(0)} p(\hat{Y}_k^r | X_k)}{\sum_{X_k \in \mathbf{C}_m^r(1)} p(\hat{Y}_k^r | X_k)} = \log \frac{\sum_{X_k \in \mathbf{C}_m^r(0)} \frac{1}{\left(\sigma_h^2 |\hat{Y}_k^r - X_k|^2 + \sigma_\beta^2\right)^{\frac{3}{2}}}}{\sum_{X_k \in \mathbf{C}_m^r(1)} \frac{1}{\left(\sigma_h^2 |\hat{Y}_k^r - X_k|^2 + \sigma_\beta^2\right)^{\frac{3}{2}}}},$$
$$m = 0, \cdots, \kappa - 1 \ \text{ and } \ k = 0, 1, \ldots, \frac{N-1}{\kappa}. \tag{5.40}$$

While the sub-optimal LLRs can be computed based on Gaussian distribution as [56]

$$\mathrm{LLR}(b_k(m)) = \log \frac{\sum_{X_k \in \mathbf{C}_m^r(0)} e^{-\left(\frac{|\hat{Y}_k^r - X_k|^2}{\sigma_w^2}\right)}}{\sum_{X_k \in \mathbf{C}_m^r(1)} e^{-\left(\frac{|\hat{Y}_k^r - X_k|^2}{\sigma_w^2}\right)}}, \ \ m = 0, \cdots, \kappa - 1 \ \text{ and } \ k = 0, 1, \ldots, \frac{N-1}{\kappa}. \tag{5.41}$$

where the $\mathbf{C}_m^r(0)$ and $\mathbf{C}_m^r(1)$ represents the signal subset of all possible equiprobable symbols of X_k whose m-th bit is either 0 or 1 in the real and imaginary components.

5.4.2 Non-binary LDPC Codes

The performance NB-LDPC codes utilizing SL-FFT iterative decoding algorithm can be improved by computing the exact LLRs based on optimal derived noise distributions at the ZF equalizer output. Thus, the modified initial LLRs can be derived as

$$\begin{aligned} F_{q,k}^a &= \log \frac{p(\hat{Y}_k | X_k = \mathbf{C}(a+1))}{p(\hat{Y}_k | X_k = \mathbf{C}(1))} \\ &= \log \frac{\frac{1}{\left(\sigma_h^2 |\hat{Y}_k - \mathbf{C}(a+1)|^2 + \sigma_\beta^2\right)^{\frac{3}{2}}}}{\frac{1}{\left(\sigma_h^2 |\hat{Y}_k - \mathbf{C}(1)|^2 + \sigma_\beta^2\right)^{\frac{3}{2}}}}, \ a \in \mathbb{F}_q \backslash \{0\}. \end{aligned} \tag{5.42}$$

While the sub-optimal LLRs can be computed based on Gaussian distribution as

$$F_k^a = \log \frac{e^{-\left(\frac{|\hat{Y}_k - \mathbf{C}(a+1)|^2}{\sigma_w^2}\right)}}{e^{-\left(\frac{|\hat{Y}_k - \mathbf{C}(1)|^2}{\sigma_w^2}\right)}}, \ a \in \mathbb{F}_q \backslash \{0\}. \tag{5.43}$$

5.4.3 Binary Turbo Codes

The performance TCs utilizing the Max-Log-MAP iterative decoding algorithm can be improved by computing the exact LLRs based on the optimal derived noise distributions at the ZF equalizer output. Thus, The modified LLRs can be computed as

$$\begin{aligned}\mathrm{LLR}(b_k(m)) &= \log \frac{\sum_{X_k \in \mathbf{C}_m^r(1)} p(\hat{Y}_k^r | X_k)}{\sum_{X_k \in \mathbf{C}_m^r(0)} p(\hat{Y}_k^r | X_k)} = -\log \frac{\sum_{X_k \in \mathbf{C}_m^r(0)} p(\hat{Y}_k^r | X_k)}{\sum_{X_k \in \mathbf{C}_m^r(1)} p(\hat{Y}_k^r | X_k)} \\ &= -\log \frac{\sum_{X_k \in \mathbf{C}_m^r(0)} \frac{1}{\left(\sigma_h^2 |\hat{Y}_k^r - X_k|^2 + \sigma_\beta^2\right)^{\frac{3}{2}}}}{\sum_{X_k \in \mathbf{C}_m^r(1)} \frac{1}{\left(\sigma_h^2 |\hat{Y}_k^r - X_k|^2 + \sigma_\beta^2\right)^{\frac{3}{2}}}}, \\ m &= 0, \cdots, \kappa - 1 \ \text{ and } \ k = 0, 1, \ldots, \frac{N-1}{\kappa}. \end{aligned} \tag{5.44}$$

While the sub-optimal LLRs can be computed based on Gaussian distribution as [56]

$$\begin{aligned}\mathrm{LLR}(b_k(m)) &= -\log \frac{\sum_{X_k \in \mathbf{C}_m^r(0)} e^{-\left(\frac{|\hat{Y}_k^r - X_k|^2}{\sigma_w^2}\right)}}{\sum_{X_k \in \mathbf{C}_m^r(1)} e^{-\left(\frac{|\hat{Y}_k^r - X_k|^2}{\sigma_w^2}\right)}}, \\ m &= 0, \cdots, \kappa - 1 \ \text{ and } \ k = 0, 1, \ldots, \frac{N-1}{\kappa}. \end{aligned} \tag{5.45}$$

5.5 Iterative Decoding Algorithms

5.5.1 B-LDPC Codes

The B-LDPC codes are the class of linear block code that can be constructed using $\mathbf{H}$ of dimensions $m_c \times n_c$. The IR-B-LDPC codes with sum-product algorithm (SPA) can be approaching to the Shannon capacity of the AWGN channel within 0.0045 dB using large block length [102, 114]. The latency introduced by long block codes can be solved using the PEG algorithm proposed in [111]. The PEG ensures the extrinsic information in the iterative SPA decoder is unaffected and no girth cycles of length four are generated in the Tanner graph. Therefore, it can be closing to the Shannon capacity with short block length [111]. The optimal bit node degree distribution of ones in the sparse parity check matrix $\mathbf{H}$ of rate $R_c = 1/2$ B-LDPC code with codeword length $n_c = 1008$ can be expressed as given in Table 3.1 [111] as

$$\mathbb{F}_2 = 0.47532x^2 + 0.279537x^3 + 0.0348672x^4 + 0.108891x^5 + 0.101385x^{15} \tag{5.46}$$

The iterative SPA has been presented in Algorithm 1 in Chapter 3 [102, 114]. This algorithm can be used to decode the B-LDPC codes by utilizing the LLR derivation equations in (5.8)-(5.16) in the case of LLRs computed based on ED and (5.40) based on derived PDFs at the ZF equalizer output in Chapter 4.

5.5.2 NB-LDPC Codes

The Non-binary LDPC (NB-LDPC) codes are class of linear block codes that first proposed by Davey and Mackay [123] for Galois field $\mathbb{F}_q$ extended from the binary extension field of order $q = 2^p$. The NB-LDPC codes outperform B-LDPC codes and requiring less number of iterations for similar block length in binary bits representation and code rate especially on channels with noise bursts [114, 123], but involve higher computational complexity. In practice, NB-LDPC codes are decoded in either the probability domain or logarithmic domain. The latter has the advantage of reduced complexity and numerical stability and more suitable for hardware design. Therefore, the SL-FFT decoding algorithm based on Hadamard matrix has been utilized in this chapter due to exhibits lower decoding complexity compared to the others decoding algorithms. The optimal symbol node degree distribution of the non-zero elements in $\mathbf{H}$ over $\mathbb{F}_{16}$ for rate $R_c = 1/2$ NB-LDPC code for code length $n_c = 252$ can be expressed as given in Table 3.1 [111] as

$$\mathbb{F}_{16} = 0.772739x^2 + 0.102863x^3 + 0.113797x^4 + 0.010601x^5. \tag{5.47}$$

The SL-FFT is presented in the Algorithm 2 and Algorithm 3 [127, 128]. These algorithms can be used to decode NB-LDPC codes incorporating the LLR derivations in (5.18)-(5.37) in the case of LLRs computed based on ED and (5.42) based on derived PDFs at the ZF equalizer output in Chapter 4.

5.5.3 Binary Turbo Codes

The TC has been invented by Berrou et al. [94] as an error correcting scheme for approaching the Shannon capacity by using an iterative soft decoding algorithm. The iterative Max-Log-MAP decoding algorithm has been invited to decode the TC by [133, 134] to reduce the decoding complexity in practical purposes by converting the multiplication operations in MAP decoding algorithm to addition operations in the logarithmic domain. The log forward/backward recursion formulas of the branch transition probabilities calculation in the Max-Log-MAP decoding algorithm is shown in Algorithm 4, is used to decode the TC incorporating the LLR derivations by utilizing (5.38) in the case of LLRs computed based on ED, which yields the same equations in (5.8) - (5.16) multiplied by a negative sign and (5.44) based on derived PDFs at the ZF equalizer output in Chapter 4. The MAX-Log-MAP decoding algorithm is presented in Algorithm refMaxLogMAP which uses $\overset{*}{\max}$ operation defined in (5.13).

5.6 EXIT Chart Analysis over PLC Channels in the Presence of NGN

5.6.1 EXIT Chart for B-LDPC Codes

The EXIT chart analysis was first introduced in [118] to analyze the convergence behaviour of an iterative decoding, which can be achieved by observing the mutual information exchange between the variable node processors (VNPs) and check node processors (CNPs) that work cooperatively and iteratively to make the bit decisions in the iterative LDPC decoder [117, 118] as shown in Fig. 3.2. The channel L-values at the receiver based on the received discrete time signal in (5.1) with BPSK modulation over PLC in the presence of NGN can be computed by utilizing the distribution in (5.6) as

$$\begin{aligned} L_k^{ch} &= \log \frac{p(Y_k|H_k, X_k=-1)}{p(Y_k|H_k, X_k=+1)} = \log \frac{e^{-\frac{|Y_k+H_k|^2}{2\sigma_\beta^2}}}{e^{-\frac{|Y_k-H_k|^2}{2\sigma_\beta^2}}} \\ &= -\frac{2}{\sigma_\beta^2}\Re\{H_k^* Y_k\} \\ &= -\frac{2}{\sigma_\beta^2}\Re\{H_k^2 X_k + H_k^* \Lambda_k\} \\ &= -\left[\frac{2|H_k|^2}{\sigma_\beta^2} X_k + \frac{\Re\{2H_k^*\Lambda_k\}}{\sigma_\beta^2}\right]. \end{aligned} \tag{5.48}$$

As a result, the L_k^{ch} has a conditional mean $\mu_{ch} = \frac{2|H_k|^2}{\sigma_\beta^2} = \frac{2(2\sigma_h^2)^2}{\sigma_\beta^2} = \frac{2}{\sigma_\beta^2}$ and a variance $\sigma_{ch}^2 = \frac{4|H_k|^2}{\sigma_\beta^2} = \frac{4(2\sigma_h)^2}{\sigma_\beta^2} = \frac{4}{\sigma_\beta^2}$, we note that $\mu_{ch} = \frac{\sigma_{ch}^2}{2}$ [118] where $\sigma_\beta^2 = \sigma_A^2$ in (4.13), $\sigma_\beta^2 = \sigma_b^2$ in (4.62), $\sigma_\beta^2 = \sigma_b^2 + \sigma_A^2$, $\sigma_\beta^2 = \sigma_N^2$ in (5.3) and $\sigma_\beta^2 = \sigma_b^2 + \sigma_N^2$. Therefore, the extrinsic density functions at the decoder output in the case of Rayleigh channel distribution have similar shapes to those of the Gaussian channel distribution [117, 118], and the EXIT characteristics can be computed by using the similar derived equations as presented in Chapter 3 section 3.3 [117, 118]. Also, very good agreement of transfer characteristics and simulated decoding trajectories between Rayleigh channel and AWGN channel has been found in [117, 118].

The EXIT functions $I_{E,VND}$ and $I_{E,CND}$ of the R-B-LDPC code can be expressed as

$$I_{E,VND} = J(\sigma) = J\left(\sqrt{(d_v - 1)\left[J^{-1}(I_{A,VND})\right]^2 + \sigma_{ch}^2}\right), \tag{5.49}$$

$$I_{E,CND} = 1 - J\left(\sqrt{(d_c - 1)\left[J^{-1}(1 - I_{A,CND})\right]^2}\right), \tag{5.50}$$

and the EXIT functions $I_{E,VND}$ and $I_{E,CND}$ of IR-B-LDPC codes involving all variable nodes d_v and all check nodes d_c can be expressed as [118, 120]:

$$I_{E,VND} = \sum_{d_v} \nu_{d_v} J\left(\sqrt{(d_v - 1)\left[J^{-1}(I_{A,VND})\right]^2 + \sigma_{ch}^2}\right), \tag{5.51}$$

$$I_{E,CND} = \sum_{d_c} \kappa_{d_c} \left[1 - J\left(\sqrt{(d_c - 1)\left[J^{-1}(1 - I_{A,CND})\right]^2}\right)\right], \tag{5.52}$$

where ν_{d_v} and κ_{d_c} represent the fraction of variables nodes and check nodes, respectively. $J(\cdot)$ represent the mutual information between the transmitted modulated bit X_k and the channel L-value expressed as $I(X_k, L_k^{ch})$ and $J^{-1}(\cdot)$ is the inverse function of $J(\cdot)$. The proper computer implementations of $J(\cdot)$ and $J^{-1}(\cdot)$ are given in [118].

5.6.2 Exit Chart for Turbo Codes

The EXIT-chart method for TCs is approximately the same as that for LDPC codes. The LLR values, L_k^{ch}, of TC codes can be computed using in (5.38) [99,117]. The L_k^{ch}, for a given a $priori$ information content value I_A in the case of Rayleigh channel distribution have similar shapes to those of the Gaussian channel distribution [117, 118], and therefore, it can be computed by using similar derived equations presented in Chapter 3 section 3.5.2 [117]. Therefore, I_A has a Gaussian distribution of mean $\mu_A = \frac{\sigma_\beta^2}{2}$ and the variance $\sigma_\beta^2 = (J^{-1}(I_A))^2$. Hence, the

conditional PDF of the L_A can be expressed as

$$p_A(\xi|X=x) = \frac{1}{\sqrt{2\pi}\sigma_\beta} e^{-\frac{\left(\xi - \frac{\sigma_\beta^2}{2}x\right)^2}{2\sigma_\beta^2}}, \tag{5.53}$$

where $\sigma_\beta^2 = \sigma_A^2$ in (4.13), $\sigma_\beta^2 = \sigma_b^2$ in (4.62), $\sigma_\beta^2 = \sigma_b^2 + \sigma_A^2$, $\sigma_\beta^2 = \sigma_N^2$ in (5.3) and $\sigma_\beta^2 = \sigma_b^2 + \sigma_N^2$. The mutual information $I_A = I(X;A)$ can be computed as [99, 117] as

$$I_A = \frac{1}{2}\sum_{x=\pm 1}\int_{-\infty}^{+\infty} p_A(\xi|X=x)\log_2\left(\frac{2p_A(\xi|X=x)}{p_A(\xi|X=-1)+p_A(\xi|X=+1)}\right)d\xi, \tag{5.54}$$

where $0 \leq I_A \leq 1$. Following the similar previous manner, I_E can be computed as

$$I_E = \frac{1}{2}\sum_{x=\pm 1}\int_{-\infty}^{+\infty} p_E(\xi|X=x)\log_2\left(\frac{2p_E(\xi|X=x)}{p_E(\xi|X=-1)+p_E(\xi|X=+1)}\right)d\xi, \tag{5.55}$$

where $0 \leq I_E \leq 1$.

5.7 Average Upper Bounds for Turbo Code

The SER of M-ary QAM signal can be expressed as derived in (4.92) as

$$p_s^{M-\mathrm{QAM}} = 1 - \left(1 - p_s^{\sqrt{M}-\mathrm{PAM}}\right)^2 = 2P_s^{\sqrt{M}-\mathrm{PAM}} - \left(P_s^{\sqrt{M}-\mathrm{PAM}}\right)^2, \tag{5.56}$$

where $\Psi = \sqrt{\frac{K\psi}{K\psi+1}}$, $K = \frac{3\log_2(M)}{2(M-1)}$, $\psi = \frac{E_b\sigma_h^2}{\sigma_\beta^2}$, and E_b is the energy per transmitted bit. The AUBs of TC are used to determine the bound performance in the high SNR and beyond the simulation capabilities. In order to evaluate the AUB for the fully-interleaved PLC channel, the PEP, P_ν, has the form [56]

$$P_\nu = \left(P_s^{M-\mathrm{QAM}}\right)^\nu \sum_{k=0}^{\nu-1}\binom{\nu-1+k}{k}\left(1-P_s^{M-\mathrm{QAM}}\right)^k, \tag{5.57}$$

and the union (average) symbol upper bound can be expressed as [136]

$$P_{s,AUB}^{M-\mathrm{QAM}} = \sum_\nu D(\nu)P_\nu, \tag{5.58}$$

and the union (average) bit upper bound can be expressed as

$$P_{b,AUB}^{M-\mathrm{QAM}} = \frac{P_{s,AUB}^{M-\mathrm{QAM}}}{\log_2(M)}, \tag{5.59}$$

where $D(\nu)$ coefficients are tabulated in [136] for interleaver sizes of $100, 1000$ and 10000, respectively. Moreover, the AUB of TC for fully-interleaved PLC channels can be expressed for different options as follows [138]

- Option 1:

  The exact solution of [138, Eq.(17)] can be computed by utilizing the computational Wolframalpha knowledge engine as

  $$P_2(\nu) \leq \left(\frac{E_s}{N_o}\right)^{-\nu} \frac{1}{\pi} \int_0^{\pi/2} [\sin\phi]^{2\nu}\, d\phi = \frac{\Gamma(\nu+\frac{1}{2})}{2\sqrt{\pi}\Gamma(\nu+1)} \left(\frac{E_s}{N_o}\right)^{-\nu}. \tag{5.60}$$

  Hence, the $P_s^{\sqrt{M}-\mathrm{PAM}}$ can be computed as

  $$P_s^{\sqrt{M}-\mathrm{PAM}} = 2\left(1-\frac{1}{\sqrt{M}}\right) P_2(\nu) = \left(1-\frac{1}{\sqrt{M}}\right) \frac{\Gamma(\nu+\frac{1}{2})}{\sqrt{\pi}\Gamma(\nu+1)} [K\psi]^{-\nu}, \tag{5.61}$$

  the SER of M-ary QAM signal, $P_s^{M-\mathrm{QAM}}$, can be computed by substituting (5.61) in (5.56). Then, the symbol AUB can be expressed as

  $$P_{s,AUB}^{M-\mathrm{QAM}} \approx \sum_{\nu} D(\nu) P_s^{M-\mathrm{QAM}}, \tag{5.62}$$

  followed by (5.59) for computing the bit AUB, $P_{b,AUB}^{M-\mathrm{QAM}}$.

- Option 2:

  Another option for upper bounding $P_2(\nu)$ can be expressed as given in [138, Eq.(21)] as

  $$P_2(\nu) \leq \frac{1}{2}\left[\frac{1}{1+\frac{E_s}{N_0}}\right]^{\nu}. \tag{5.63}$$

  The $P_s^{\sqrt{M}-\mathrm{PAM}}$ can be computed by utilizing (5.63) as

  $$P_s^{\sqrt{M}-\mathrm{PAM}} = \left(1-\frac{1}{\sqrt{M}}\right)\left[\frac{1}{1+K\psi}\right]^{\nu}, \tag{5.64}$$

  followed by similar steps used in Option 1 to compute the $P_{s,AUB}^{M-\mathrm{QAM}}$ in (5.62) and (5.59) for computing the bit AUB, $P_{b,AUB}^{M-\mathrm{QAM}}$.

- Option 3:

  Another option for upper bounding $P_2(\nu)$ can be expressed as given in [138, Eq.(24)] as

$$P_2(\nu) \leq \frac{1}{2}\left(1-\sqrt{\frac{\frac{E_s}{N_0}}{1+\frac{E_s}{N_0}}}\right)\left[\frac{1}{1+\frac{E_s}{N_0}}\right]^{\nu-1}. \tag{5.65}$$

  The $P_s^{\sqrt{M}-\mathrm{PAM}}$ can be computed by utilizing (5.65) as

$$P_s^{\sqrt{M}-\mathrm{PAM}} = \left(1-\frac{1}{\sqrt{M}}\right)\left[1-\sqrt{\frac{K\psi}{1+K\psi}}\right]\left[\frac{1}{1+K\psi}\right]^{\nu-1}, \tag{5.66}$$

  followed by similar steps used in Option 1 to compute $P_{s,AUB}^{M-\mathrm{QAM}}$ in (5.62) and (5.59) for computing the bit AUB, $P_{b,AUB}^{M-\mathrm{QAM}}$.

5.8 Simulation Results

5.8.1 Performance of Coded-OFDM Systems Using LLR Computed based on Euclidean Distance

In this section, the IR-B-LDPC code and IR-NB-LDPC code have been constructed for similar code rate and block length in binary bit representation. The performance of $(1008, 504)$ IR-B-LDPC code over $\mathbb{F}_2$ which has been constructed by using (5.46) utilizing the iterative SPA decoding algorithm presented in Algorithm 1 in Chapter 3, is compared to the performance of $(252, 126)$ IR-NB-LDPC code over $\mathbb{F}_{16}$ which has been constructed by using (5.47) utilizing the iterative SL-FFT decoding algorithm illustrated in Algorithm 2 and Algorithm 3 in Chapter 3. The performance of both decoders has been compared against to the rate-$1/2$, $(1, 5/7, 5/7)$ TC with the Max-Log-MAP decoding algorithm presented in Algorithm 4 in Chapter 3. The rate-$1/2$ TC is generated from rate-$1/3$ TC by puncturing the parity bits of both RSC encoder and systematic bits. Additionally, the three systems performance are compared with respect to the uncoded OFDM system that utilizes the ML detector in (4.82) in the case BI noise and combined BI noise and MCAIN model and (4.84) in the case of combined BI noise and BGMIN model, while the theoretical tight BER has been computed based on (4.94). The maximum number of decoding iterations is set to 50 in all decoders with random interleaver. Moreover, 4-QAM and 16-QAM constellations are utilized for N=1024 sub-carriers per OFDM symbol for CP= 256 samples. The performances are evaluated over modified multipath PLC channel with 15-path,

where the channel parameters are listed in Table 4.1 [8].

Fig. 5.5-a demonstrates the BER performance of the proposed IR-NB-LDPC-COFDM system compared with IR-B-LDPC-COFDM system, T-COFDM system and uncoded OFDM systems, respectively, by utilizing 4-QAM constellation, over 15-path PLC channel in the presence of Nakagami-m BI noise with $m = 0.7$, combined BI noise and MCAIN with $m = 0.7$, $A = 0.01$, $\rho = 0.01$, $\ell = 100$ and with the combined BI noise and BGMIN with $m = 0.7$, $\alpha = 0.1$, $\tilde{\rho} = 100$. Both IN models implying the IN power is 100 times stronger than the Gaussian noise power. The proposed derived LLRs in (5.8)-(5.9) in the case of IR-B-LDPC code, (5.18)-(5.21) in the case of IR-NB-LDPC code and (5.38) in the case of TC are utilized. It can be seen from the figure that the performance of IR-NB-LDPC code outperforms both decoders in all scenarios of NGN. The IR-NB-LDPC, IR-B-LDPC and TCs can improve the BER performance efficiently and saving in $\frac{E_b}{N_0}$ required to achieve a given BER. For example, the IR-NB-LDPC, IR-B-LDPC and TCs can achieve coding gains (CGs) approximately of 46.5 dB, 45.5 dB and 45 dB in the case of Nakagami-m BI noise, and 45 dB, 44 dB and 43.5 dB in the case of combined BI noise and BGMIN noise and 44.5 dB, 42.5 dB and 41 dB in the case of combined BI noise and MCAIN noise with respect to uncoded OFDM system, respectively, at $P_e = 10^{-5}$.

Moreover, Fig. 5.5-b presents the performances of the three coded OFDM systems and uncoded OFDM system by utilizing 16-QAM constellation in the presence of the same previous NGN parameters. The proposed LLRs have been calculated using (5.10)-(5.16) in the case of IR-B-LDPC code, (5.22)- (5.37) in the case of IR-NB-LDPC code and (5.38) in the case of TC are utilized. The achieved CGs of IR-NB-LDPC, IR-B-LDPC and TCs are approximately of 49 dB, 48 dB and 46.5 dB in the case of Nakagami-m BI noise and 47 dB, 46 dB and 45 dB in the case of combined BI noise and BGMIN noise and 46.5 dB, 44.5 dB and 42.5 dB in the case of combined BI noise and MCAIN noise with respect to the uncoded OFDM system, respectively, at $P_e = 10^{-5}$.

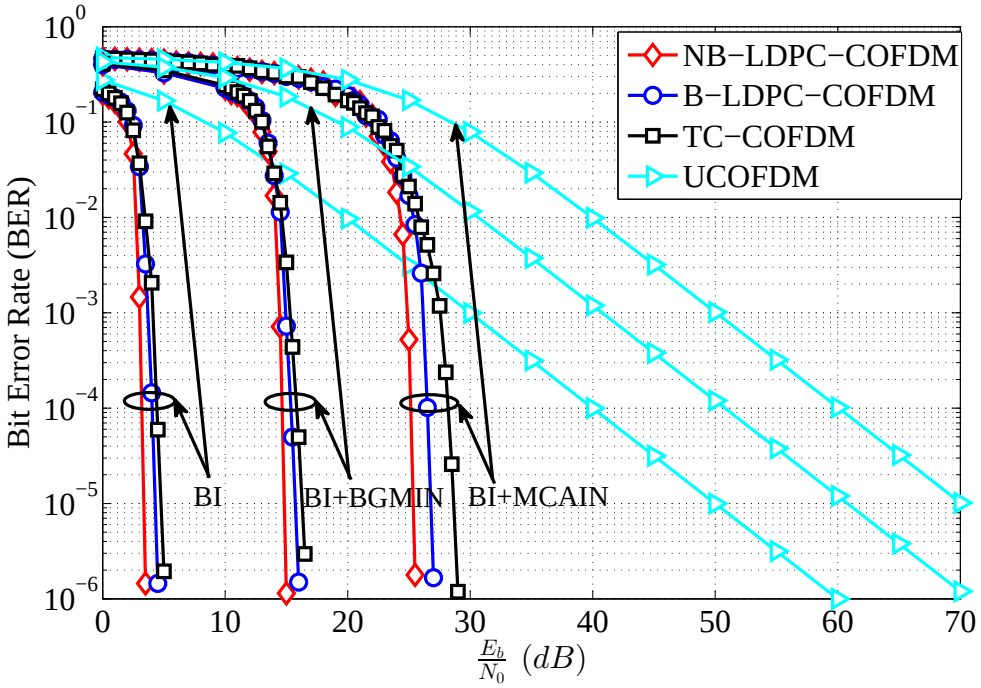

(a) 4-QAM.

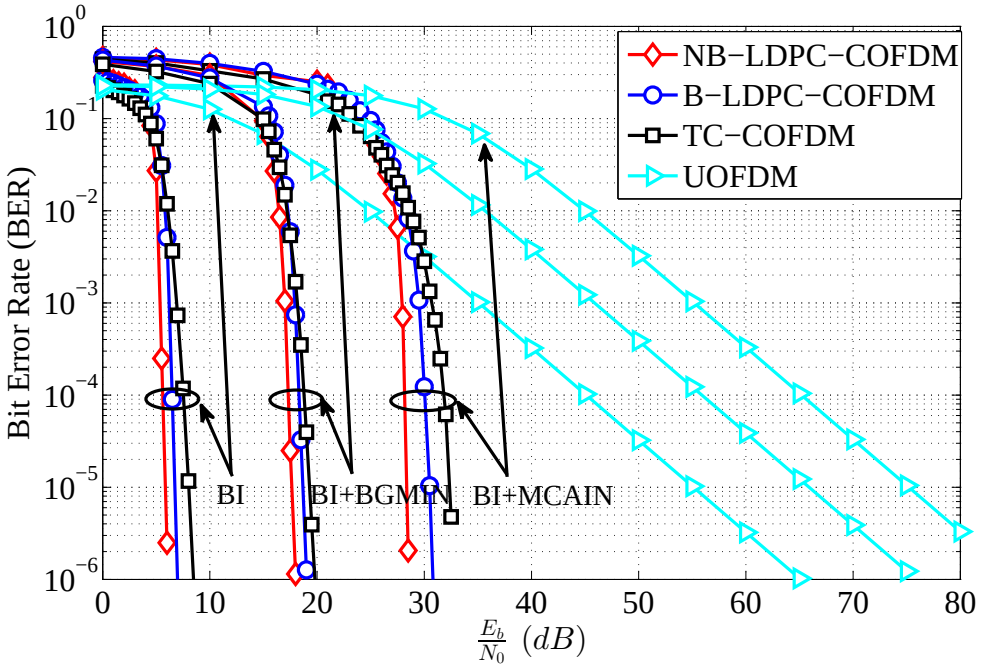

(b) 16-QAM.

Figure 5.5: BER performance comparison of IR-NB-LDPC, IR-B-LDPC and TC for COFDM system over PLC channel in the presence of NGN.

To analyze the iterative LDPC decoder and Turbo decoder, the density evolution (DE) technique was proposed in [164, 165] to compute the asymptotic performance of iterative decoders. Therefore, DE is performed to find the threshold SNRs of different receivers to predict the waterfall performance region of short iterative codes, and to design good codes have a perfor-

mance close to Shannon limit. An alternative method called EXIT chart has been proposed in this chapter to visualize the exchange of extrinsic information between consecutive decoders for the LDPC decoder and Turbo decoder and to find the decoding threshold SNR.

5.8.2 Performance of Coded-OFDM Systems Using LLR Computed based on Derived PDFs at the ZF equalizer Output

5.8.2.1 IR-B/NB-LDPC-COFDM System Versus Conventional IR-B-LDPC-COFDM System

In order to assess the performance of the IR-B/NB-LDPC-COFDM systems over the PLC channel contaminated by different scenarios of BI noise and IN, the derived PDFs at the ZF equalizer output in Chapter 4 are utilized. The simulation parameters were set as follows, the number of sub-carriers is set as N =4096, modulated using 4096-QAM constellation for a rate-$1/2$ IR-B-LDPC code over $\mathbb{F}_2$ and IR-NB-LDPC code over $\mathbb{F}_{16}$ decoded by the SPA and SL-FFT algorithms, respectively. The number of iterations is set 50 at each decoder. The PLC is modelled by the modified Zimmermann model with 15-taps channel in the presence of individual and combined Nakagami-m BI noise and IN modelled by BGMIN model. Both systems are compared against the conventional IR-B-LDPC-COFDM system, in which the blanking non-linearity IN mitigation method in (2.31) is utilize based on the derived threshold in (4.122), and the LLRs have been computed based on the Gaussian distribution (5.41). Additionally, the three systems are compared with respect to the uncoded OFDM system that utilizes the ML detector in (4.84) and for the frequency bandwidth of 22.4 MHz as utilized for HomePlug AV [1]. The theoretical tight BER of uncoded OFDM system has been computed based on (4.94).

Fig. 5.6-a and Fig. 5.6-b demonstrates the BER performance of IR-B-LDPC-COFDM and IR-NB-LDPC-COFDM systems, respectively, utilizing the derived PDFs in the presence of Nakagami-m BI noise only with $m = 0.7$ and 0.5, in which the LLRs are computed by utilizing (5.40) after substituting $\sigma_\beta^2 = \sigma_b^2$. The performance of both systems is compared to the conventional IR-B-LDPC-COFDM system and uncoded OFDM system, respectively. It can be seen from both figures that the BER performance is approximately unaffected by changing the values of m associated to Nakagami-m distribution. This is due to the fact that the BI noise after the FFT operation will appear in the frequency domain as a Gaussian noise; i.e. the BER performance will depend on the average noise power as seen by the sub-carriers. Additionally, in all parameters of BI noise, the derived LLRs of IR-B-LDPC-COFDM outperforms the conventional IR-B-LDPC-COFDM for all $\frac{E_b}{N_0}$ values and achieved CGs approximately 30 dB

and 20 dB, respectively, at $\mathrm{BER} = 10^{-5}$. While the derived LLRs of IR-NB-LDPC-COFDM outperforms the conventional IR-B-LDPC-COFDM and can achieve CGs approximately 34 dB and 20 dB, respectively, at $\mathrm{BER} = 10^{-5}$.

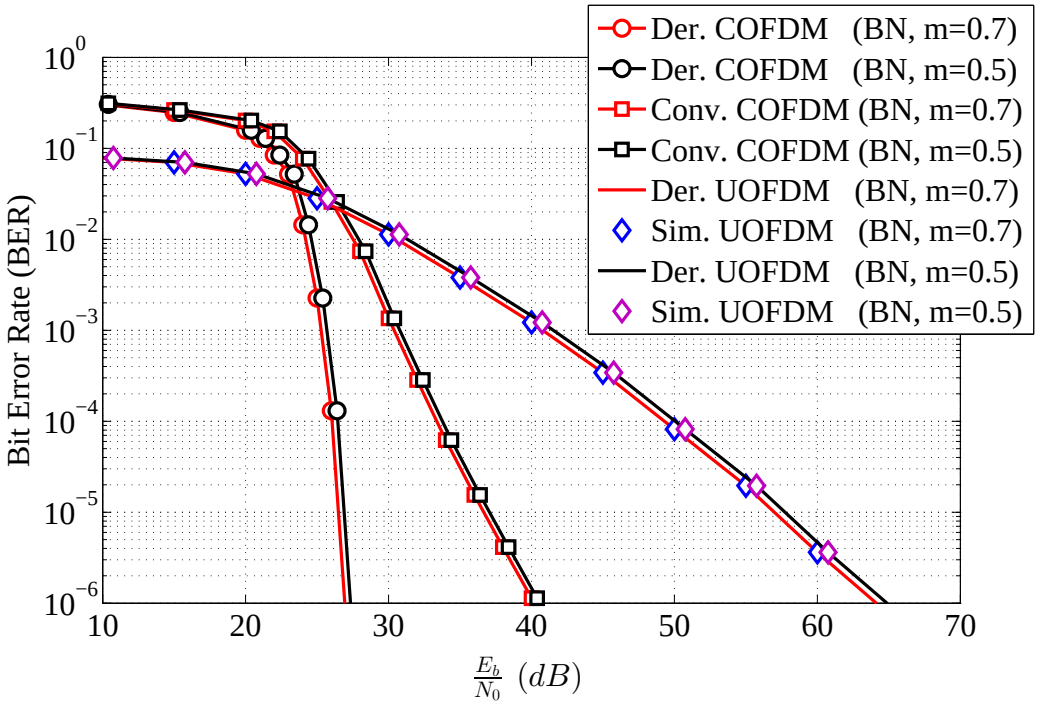

(a) B-LDPC code.

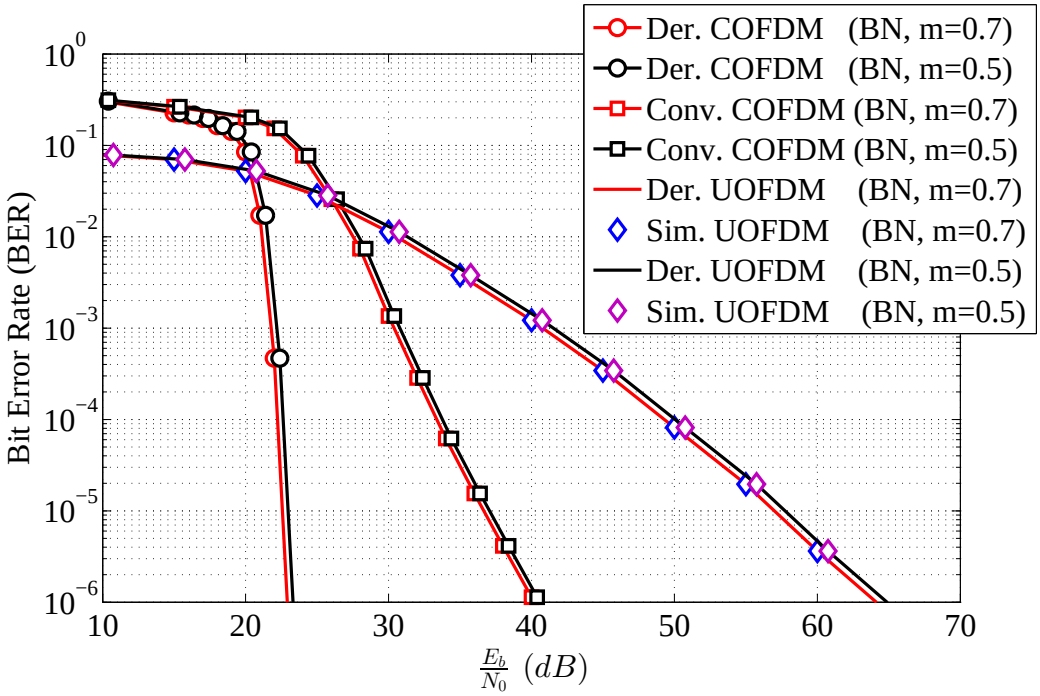

(b) NB-LDPC code over $\mathbb{F}_{16}$.

Figure 5.6: Performance of the derived versus conventional IR-LDPC-COFDM and uncoded OFDM system utilizing 4096-QAM over PLC in the presence of Nakagami-m BI noise.

Fig. 5.7-a and Fig. 5.7-b demonstrates the BER performance of IR-B-LDPC-COFDM and IR-NB-LDPC-COFDM systems, in which the obtained LLRs are computed by utilizing (5.40) and (5.42) after substituting $\sigma_{\beta}^2 = \sigma_b^2 + \sigma_N^2$, respectively, where σ_b^2 and σ_N^2 can be computed by using (4.62) and (5.3), respectively, in the presence of combined Nakagami-m BI noise with $m = 0.7$ and IN modelled by using BGMIN model with $\alpha = 0.1, 0.3$ and for constant $\tilde{\rho} = 100$. Additionally, the performance of IR-B-LDPC-COFDM system and IR-NB-LDPC-COFDM system have been compared against the conventional IR-B-LDPC-COFDM system and uncoded OFDM system that utilized the ML detector in (4.84). Moreover, the theoretical tight BER has been computed based on (4.94) for the uncoded OFDM system. It can be noted from the both figures that the obtained BER performance degrades further compared to the case of BI noise only, and as α increases the BER performance degrades. Moreover, the derived systems is very robust against the combined noise even with high impact of combined BI noise and BGMIN and outperforms the conventional receiver due to optimal computation of the initial LLRs of SPA and SL-FFT decoders. In practice, the utilization of IR-B-LDPC and IR-NB-LDPC codes will reduce the requirement $\frac{E_b}{N_0}$ of 80 dB in the case of uncoded systems with $\alpha = 0.3$ to 43 dB and 38 dB, respectively, at a $\mathrm{BER} = 5 \times 10^{-6}$, which is achievable with readily available receiver sensitivity of approximately 90 dBm. However, this requirement is further relaxed for milder multipath channels and lower levels of BI noise. Furthermore, at a BER of 10^{-5}, the B-LDPC-COFDM system outperforms the conventional IR-B-LDPC-COFDM system by approximately 12.5 and 13.5 dB and outperforms the uncoded OFDM system by approximately 34 and 34.5 dB for $\alpha = 0.1, 0.3$, respectively. While the IR-NB-LDPC-COFDM system outperforms the conventional IR-B-LDPC-COFDM system by approximately 18 and 19 dB and outperforms the uncoded OFDM system by approximately 40 and 39 dB for $\alpha = 0.1, 0.3$, respectively.

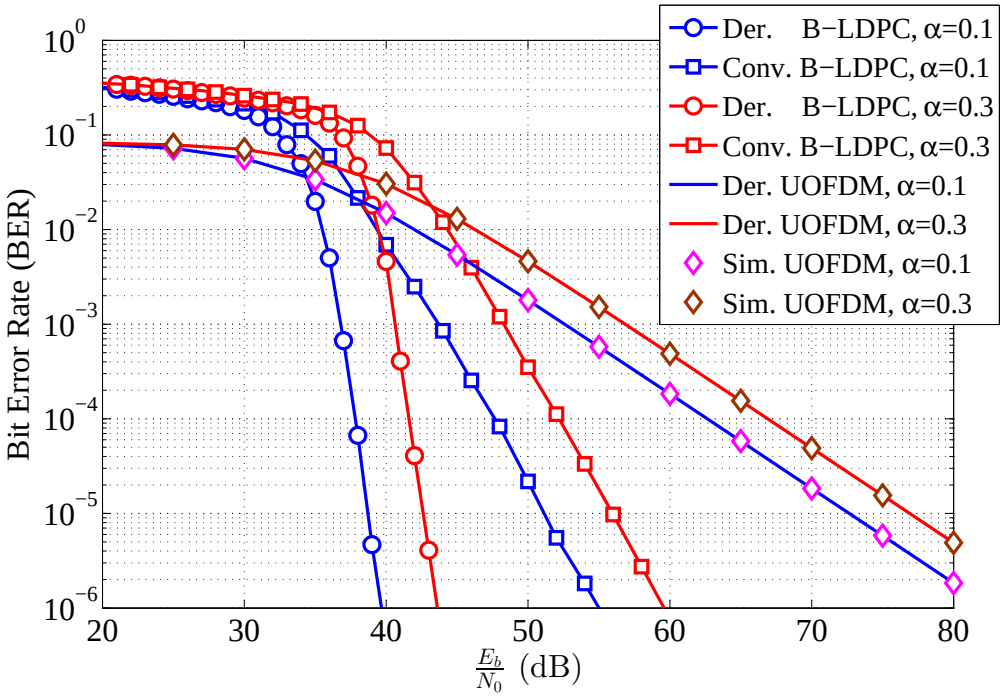

(a) B-LDPC code.

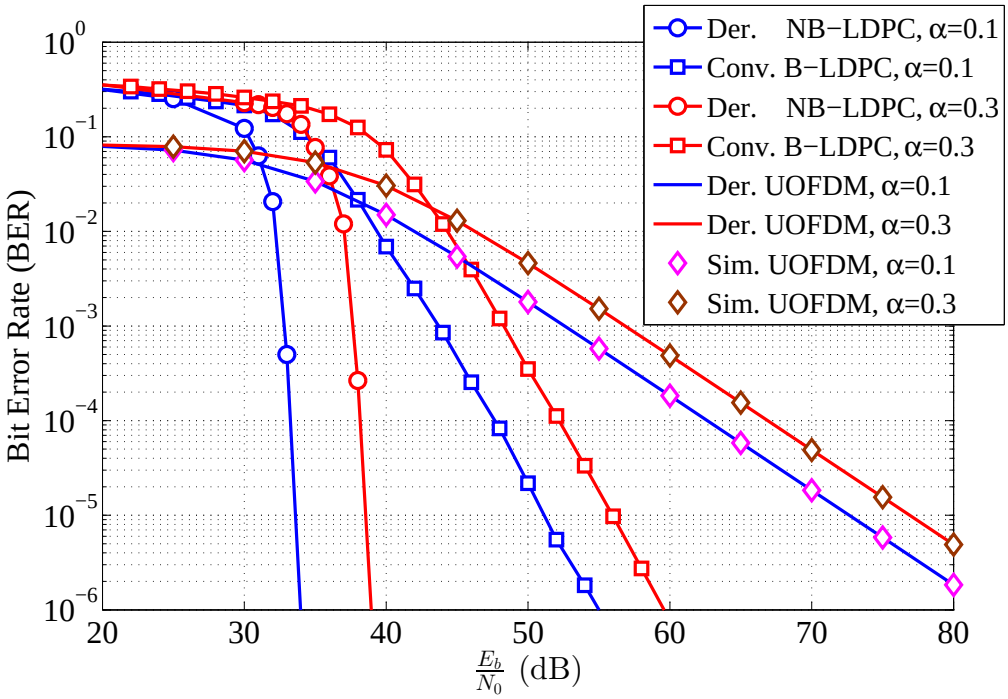

(b) NB-LDPC code.

Figure 5.7: Performance of the derived and conventional of IR-LDPC-COFDM versus uncoded OFDM system utilizing 4096-QAM over PLC in the presence of combined BI noise with $m = 0.7$ and BGMIN for $\tilde{\rho} = 100$ and α is changed.

Fig. 5.8-a and Fig. 5.8-b demonstrates the BER performance of IR-B-LDPC-COFDM and IR-NB-LDPC-COFDM systems, in the presence of combined Nakagami-m BI noise with $m = 0.7$ and BGMIN with constant $\alpha = 0.1$ and $\tilde{\rho} = 10^2, 10^3$ versus the conventional IR-B-LDPC-COFDM system. It can be seen from both figures that the increasing $\tilde{\rho}$ results in more significant

BER performance degradation than increasing α. Additionally, at a BER of 10^{-5}, the derived IR-B-LDPC-COFDM system outperforms the conventional IR-B-LDPC-COFDM system by approximately 12 and 10 dB and outperforms the uncoded OFDM receiver by approximately 34 and 33.5 dB for $\tilde{\rho} = 10^2, 10^3$, respectively. While the derived IR-NB-LDPC-COFDM system outperforms the conventional IR-B-LDPC-COFDM system by approximately 17 and 16 dB and outperforms the uncoded OFDM receiver by approximately 39 and 39 dB for $\tilde{\rho} = 10^2, 10^3$, respectively.

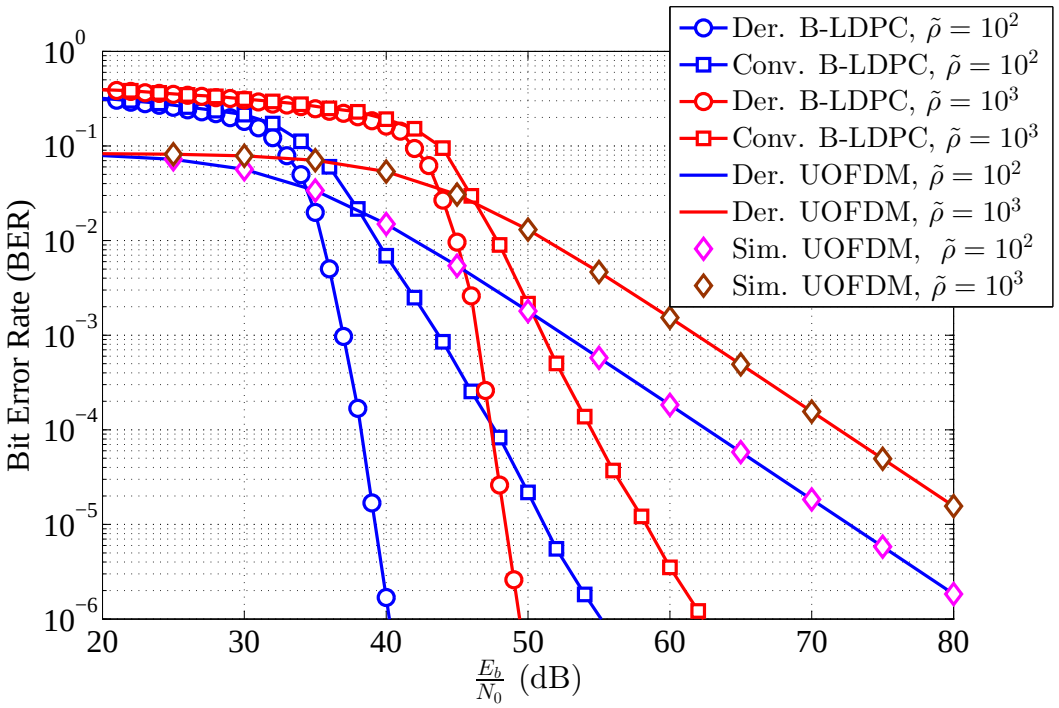

(a) B-LDPC code.

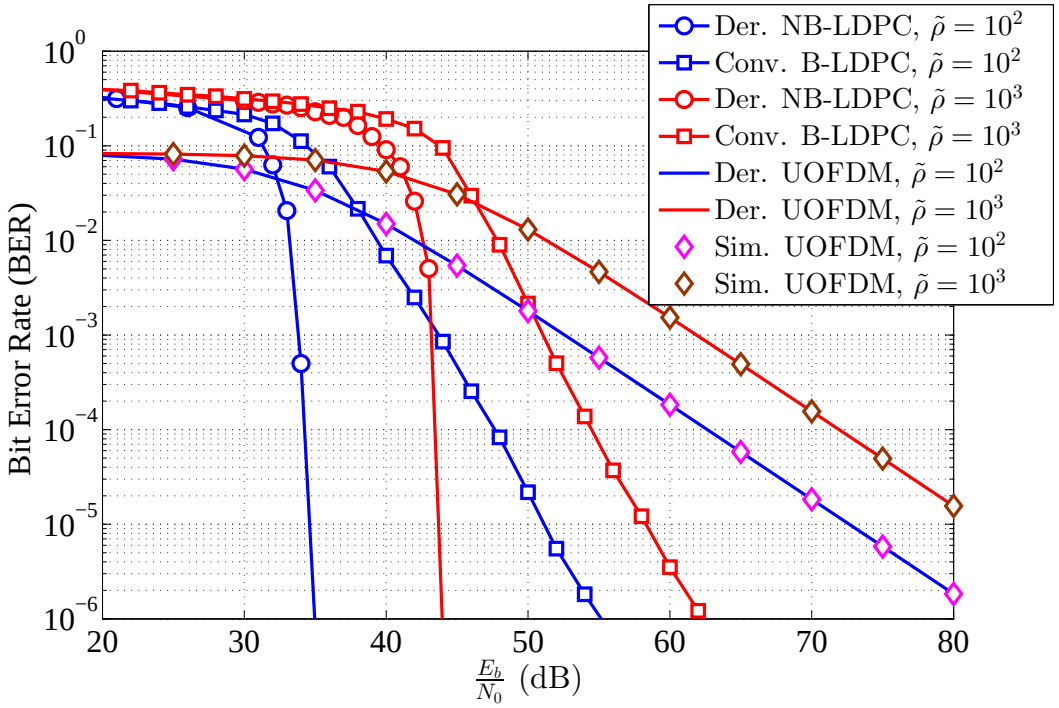

(b) NB-LDPC code.

Figure 5.8: Performance of the derived and conventional IR-LDPC-COFDM versus uncoded OFDM system utilizing 4096-QAM over PLC in the presence of combined BI noise with $m = 0.7$ and BGMIN for $\alpha = 0.1$ and $\tilde{\rho}$ is changed.

It is proceed now to compare the data throughput of both IR-B-LDPC-COFDM and IR-NB-LDPC-COFDM systems in the presence of BI noise with $m = 0.7$ and BGMIN with $\alpha = 0.1$ and $\tilde{\rho} = 100$. To achieve a BER of 10^{-5} by utilizing a 4096-QAM constellation, the derived IR-B-LDPC-COFDM system needs an $\frac{E_b}{N_0}$ of approximately 39 dB. In contrast, for the conventional

IR-B-LDPC-COFDM system to achieve the same performance an additional margin of 12.5 dB of SNR is required as shown in Fig. 5.7-(a) with blue lines. To compare the data throughput of both systems, the comparison needs to be performed at the same BER and $\frac{E_b}{N_0}$. Therefore, the conventional IR-B-LDPC-COFDM system needs to reduce the constellation size from 4096 to 512-QAM to achieve a BER level of 10^{-5} at a $\frac{E_b}{N_0}$ of approximately 39 dB, as in the derived system. This comparison is shown in Fig. 5.9. The resulting data throughput of the derived and conventional systems can be then computed as 256 Mbps and 145 Mbps, respectively, as shown in Table 5.2. Thus, the derived IR-B-LDPC-COFDM system offers a 111 Mbps higher data throughput than the conventional system.

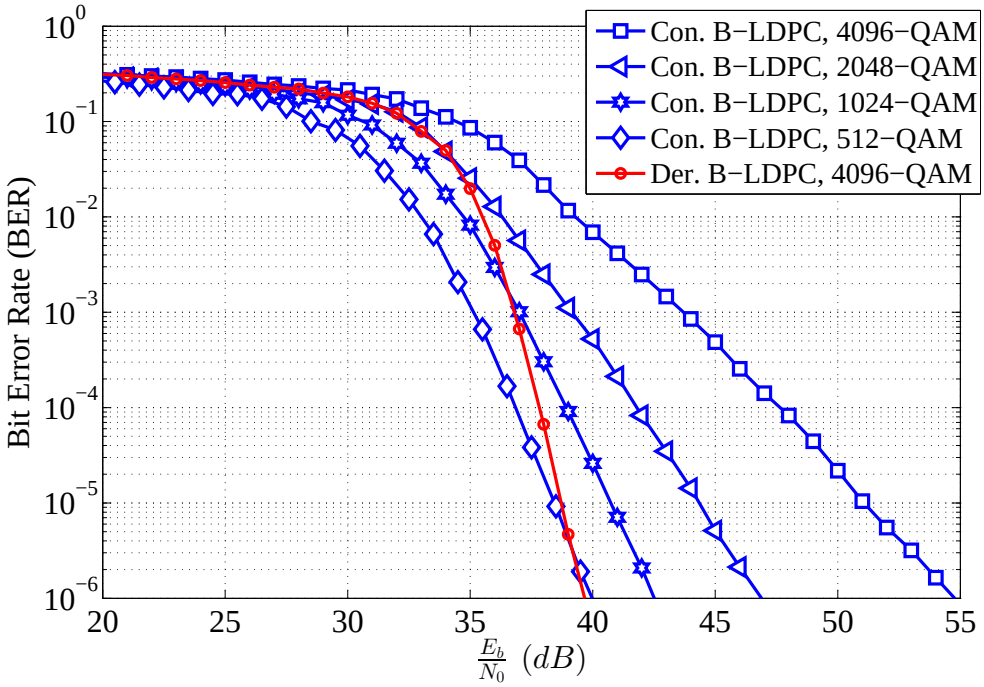

Figure 5.9: Proposed IR-B-LDPC-COFDM utilizing 4096-QAM versus conventional IR-B-LDPC-COFDM utilizing 4096, 2048, 1024 and 512-QAM constellations over PLC in the presence of combined BI noise and BGMIN.

Moreover, the data throughput of IR-NB-LDPC-COFDM system compared to conventional IR-B-LDPC-COFDM system at BER of 10^{-5} by utilizing a 4096-QAM constellation, the derived IR-NB-LDPC-COFDM system needs an $\frac{E_b}{N_0}$ of approximately 33 dB as shown in Fig. 5.7-(b) with blue lines. Therefore, the conventional IR-B-LDPC-COFDM system needs to reduce the constellation size from 4096 to 128-QAM to achieve a BER level of 10^{-5} at a $\frac{E_b}{N_0}$ of approximately 33 dB. This comparison is shown in Fig. 5.10. The resulting data throughput of the derived IR-NB-LDPC-COFDM over $\mathbb{F}_{16}$ and conventional IR-B-LDPC-COFDM systems can be then computed as 256 Mega symbols per second (Msps)=256 Mb/s $\times \log_2(16)$ b/s=1 Giga bits per second (Gbps) and 61 Mbps, respectively, as shown in Table 5.2. Thus, the derived IR-NB-LDPC-COFDM system offers a 963 Mbps higher data throughput than the conventional system.

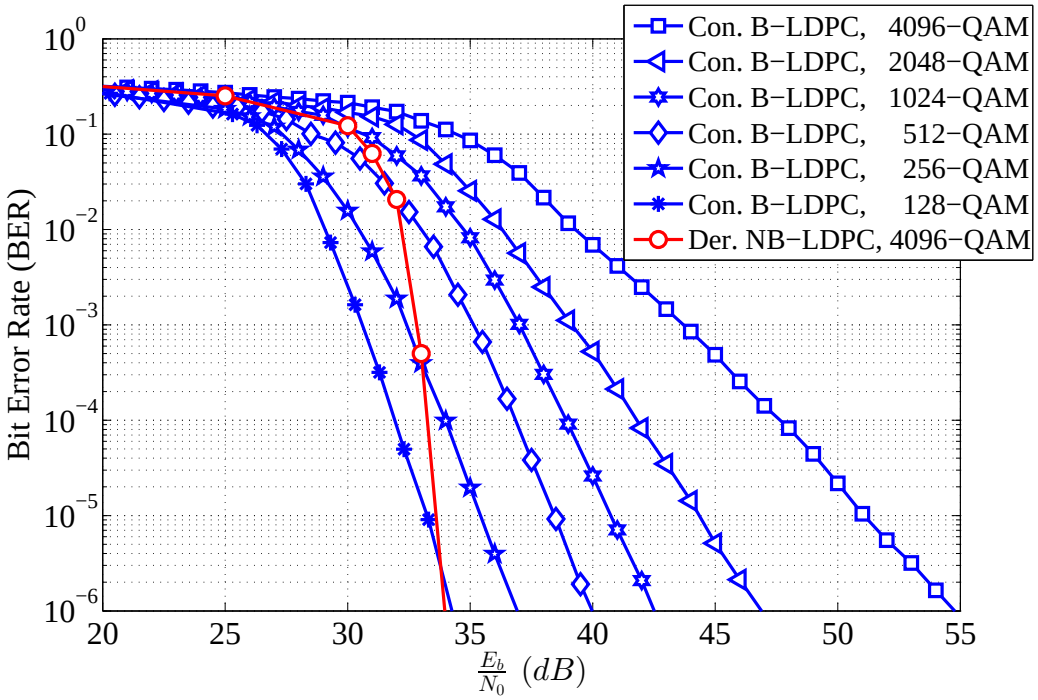

Figure 5.10: Proposed IR-NB-LDPC-COFDM utilizing 4096-QAM versus conventional IR-B-LDPC-COFDM utilizing 4096, 2048, 1024, 512, 256 and 128-QAM constellations over PLC in the presence of combined BI noise and BGMIN.

Table 5.2: Data throughput comparison at BER level of 10^{-5}.

System parameters	Proposed system	512-QAM Conventional	128-QAM Conventional
Bandwidth (BW)	22.4 MHz	22.4 MHz	22.4 MHz
IFFT length	4096	512	128
Subcarriers (N)	4096	512	128
Subcarrier spacing(Δ_f) = $\frac{\text{BW}}{\text{IFFT length}}$	5.4688 kHz	43.75 kHz	175 kHz
IFFT period = $\frac{1}{\Delta_f}$	182.86 μs	22.857 μs	5.7143 μs
CP period $> \frac{d_{max}}{v_p} = \frac{1250}{1.5\times10^8}$	8.93 μs	8.93 μs	8.93 μs
OFDM period (T) = IFFT period+CP	191.79 μs	31.787 μs	14.644 μs
M-ary QAM	4096-QAM	512-QAM	128-QAM
Maximum data rate = $\frac{N\log_2(M)}{T}$	256 Mbps for BLDPC 256 Msps for NBLDPC	145 Mbps	61 Mbps

5.8.2.2 Performance of T-COFDM System Versus Conventional T-COFDM System

In order to assess the performance of the proposed T-COFDM system over the PLC channel for different scenarios of BI noise and IN modelled by using MCAIN model, the derived PDFs at the ZF equalizer output in Chapter 4 are utilized. The simulation parameters were set as follows, the number of sub-carriers was set as N=1024 and the constellation size was set as 8192-QAM. The rate-1/3 TC constructed using the generator $(1, 5/7, 5/7)_8$ with the help of the derived $D(v)$ coefficients in [136] are utilized for AUBs computation. The BER performances are investigated over a modified Zimmermann model for 15-path. The system performance is compared against the conventional T-COFDM system and the uncoded system.

Fig. 5.11 illustrates the comparison between theoretical AUB bounds and Monte Carlo simulation results in the presence of BI noise with $m = 0.7$. The LLRs are computed utilizing (5.44) based on the exact noise PDFs in (4.66) and (4.67) for the real and imaginary parts, respectively, and compared with the conventional system utilizing clipping non-linearity IN mitigation method (2.32) and LLRs computed based on the Gaussian distribution (5.45). The proposed T-COFDM and conventional T-COFDM systems performance are compared to the uncoded OFDM system that utilizes the ML detector in (4.82) with $\sigma_\beta^2 = \sigma_b^2$. It can be seen from the figure that the theoretical BER derived in (4.93) and (4.94) for uncoded system gives close matching with Monte-Carlo simulation results. Moreover, the derived receiver outperforms the conventional receiver by 4.75 dB at SER=10^{-5} and gives about 34.4 dB CG compared to 29.65 dB in the case of the conventional T-COFDM system. Furthermore, the AUB has correctly predicted the system performance and gives closely matching to the derived system performance.

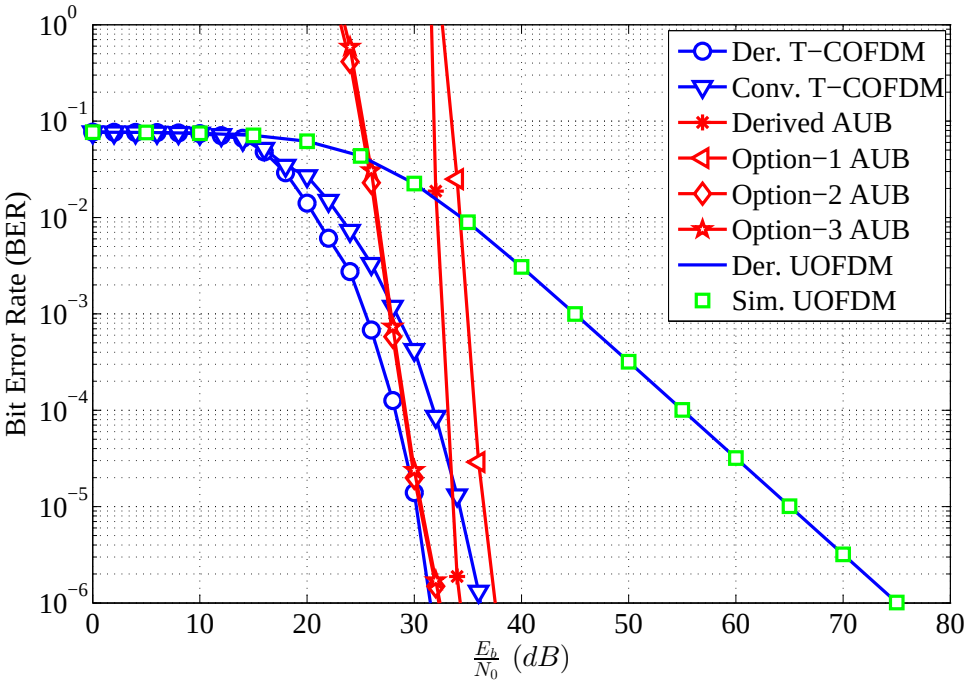

Figure 5.11: Performance of 8192-QAM T-COFDM over 15-PLC in the presence of Nakagami-m BI noise with $m = 0.7$.

Fig. 5.12-a, shows the BER performance results of the derived T-COFDM system versus the conventional T-COFDM system in the presence of combined BI noise and IN modelled by MCAIN model, utilizing LLRs computed in(5.44) based on the derived PDF in (4.72) and (4.73) for the real and imaginary parts, respectively. The conventional T-COFDM system utilizes the clipping IN mitigation based on the derived clipping threshold (4.109) and LLRs computed based on the Gaussian distribution (5.45). The IN parameters are taken as $m = 0.7$, $\ell = 0-100$, for constant $A = 10^{-2}$ and changing ρ as $\rho = 10^{-1}, 10^{-3}$. It can be seen from the figure that the BER performance of both systems are worse than the case of BI noise only and the performance depends on changing ρ. However, when ρ decreases, σ_A^2 in (4.13) will increase, which implies that the noise variance $\sigma_\beta^2 = \sigma_b^2 + \sigma_A^2$ becomes stronger, therefore, the performance becomes worse. Moreover, the performance of the derived receiver is more robust against the combined noise than the conventional T-COFDM system with AUBs closely match to the proposed T-COFDM simulation results. On the other hand, the coding gain for both systems has been compared to the uncoded OFDM system that utilized (4.82), gives $33.1, 28.5$ dB and $33.4, 29$ dB for $\rho = 10^{-1}, 10^{-3}$ in the case of derived and conventional T-COFDM systems, respectively, at BER=10^{-5}.

Fig. 5.12-b shows the BER performance result of the derived and conventional T-COFDM systems in the presence of combined BI noise and IN modelled by MCAIN model. The noise parameters are set as $m = 0.7$, $\ell = 0 - 100$, for changing $A = 10^{-1}, 10^{-2}$ and constant

$\rho = 10^{-1}$. It can be seen from the figure that, the BER performance approximately unchanged when changing the average number of impulses A, because when noise sources ℓ increases, A^{ℓ} will approach to zero and that leads to unchanged in the variance σ_A^2 in (4.13) and hence in σ_β^2. Thus, the system performance is unchanged.

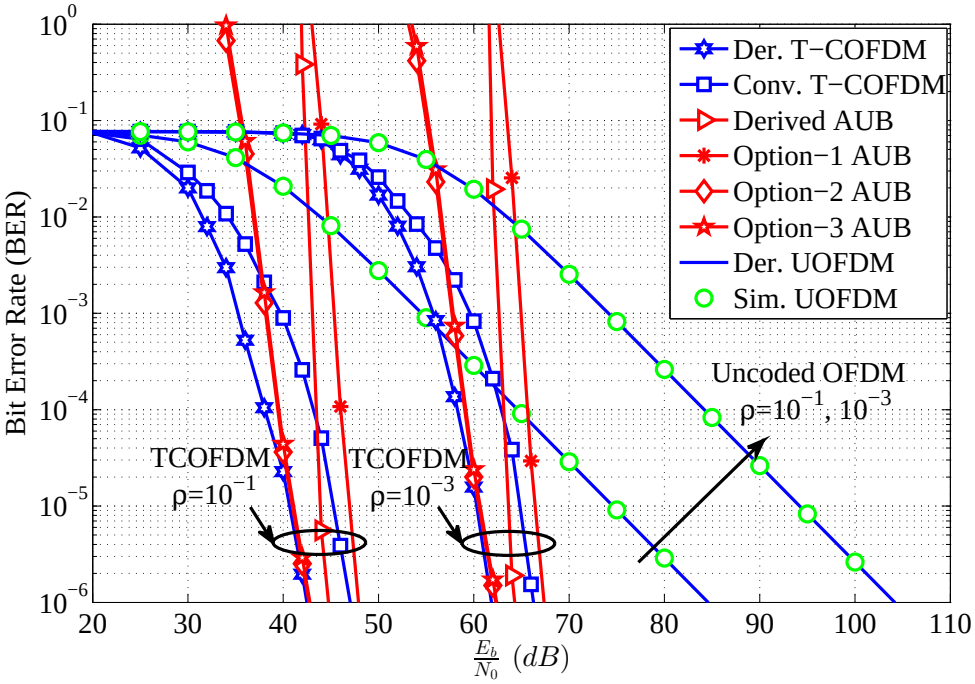

(a) Combined BI noise and IN for $A = 10^{-2}$ and $\rho = 10^{-1}, 10^{-3}$.

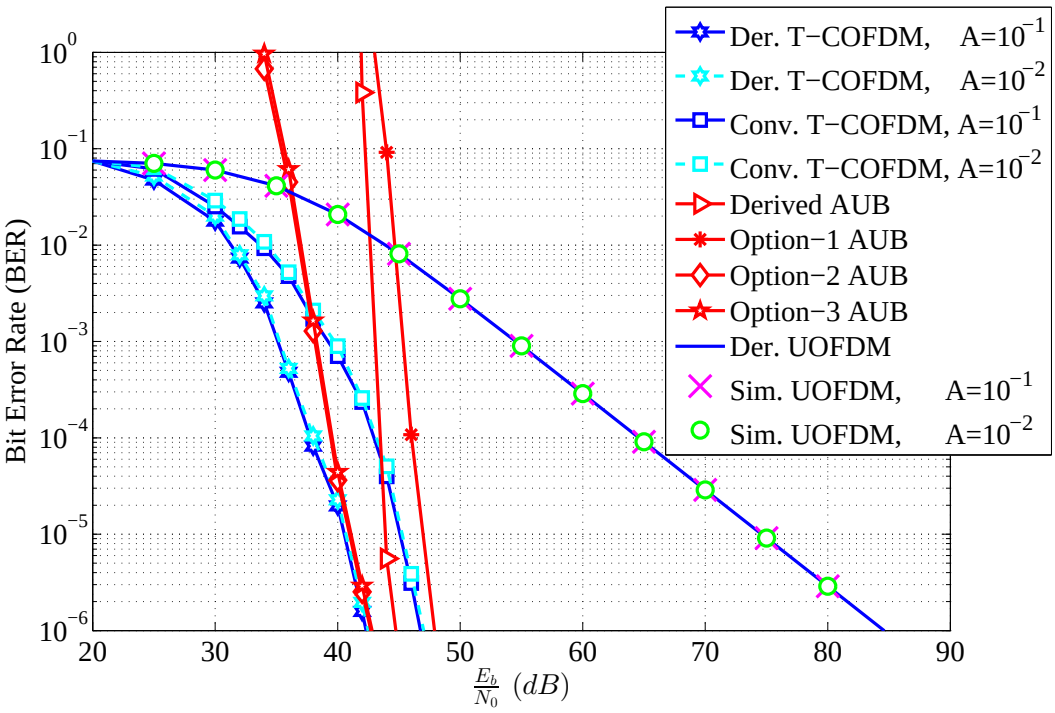

(b) Combined BI noise and IN for $A = 10^{-1}, 10^{-2}$ and $\rho = 10^{-1}$.

Figure 5.12: Performance of 8192-QAM T-COFDM over 15-PLC in the presence of combined of BI noise and MCAIN model.

5.9 Exit Chart

The Exit chart simulation represents the actual decoding trajectories which can be used to determine the number of iterations requires to converge. The simulation trajectories are presented for $(1008, 504)$ IR-B-LDPC code constructed by utilizing optimal bit node degree distribution of ones in (5.46) versus $(1, 5/7, 5/7)$ TC constructed using two identical RSCs at different values of $\frac{E_b}{N_0}$ for 4-QAM OFDM system over 15-path PLC channel in the presence of NGN. Different scenarios of NGN are simulated, theses include Nakagami-m BI noise, combined Nakagami-m BI noise and IN modelled either by MCAIN model of BGMIN model.

Fig. 5.13 shows the trajectories of IR-B-LDPC code versus TC at $\frac{E_b}{N_0}$= 2 dB and 3 dB in the presence of Nakagami-m BI noise with $m = 0.7$. At $\frac{E_b}{N_0}$=2 dB, the I_E of Turbo decoder has been intersected at low I_A with high probability. However, the intersection behavior before or at mutual information of 1 can give the probabilistic convergence behavior of the iterative decoding algorithm. Therefore, the BER performance of TC will degrade. While the $I_{E,VND}$ and $I_{E,CND}$ of LDPC decoder will not intersect with $I_{A,VND}$ and $I_{A,CND}$ values and need 22 iterations to converge to mutual information of 1, which results improved in the BER performance. While when the $\frac{E_b}{N_0}$ increased to 3 dB, the probability of intersecting for TC will decrease and the performance of both decoders will converge to mutual information of 1 with 14 and 8 iterations for LDPC and TC, respectively.

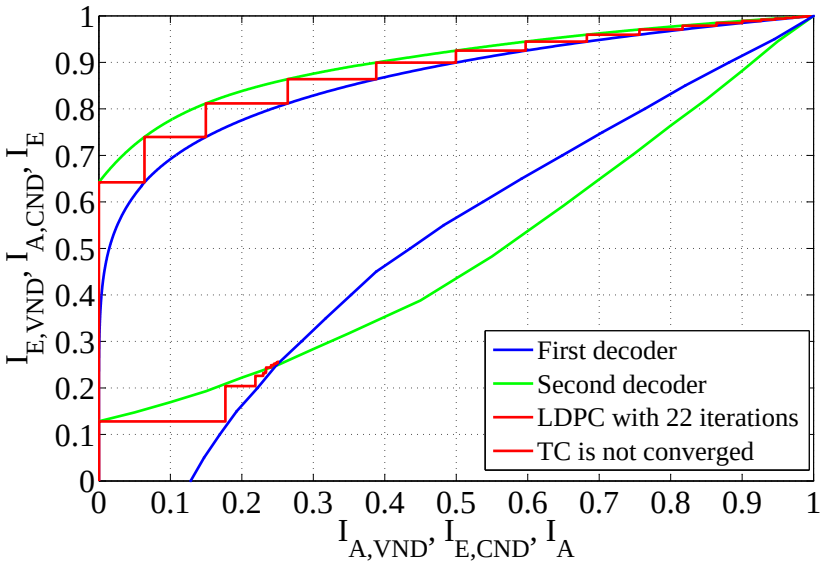

(a) $\frac{E_b}{N_0}$= 2dB.

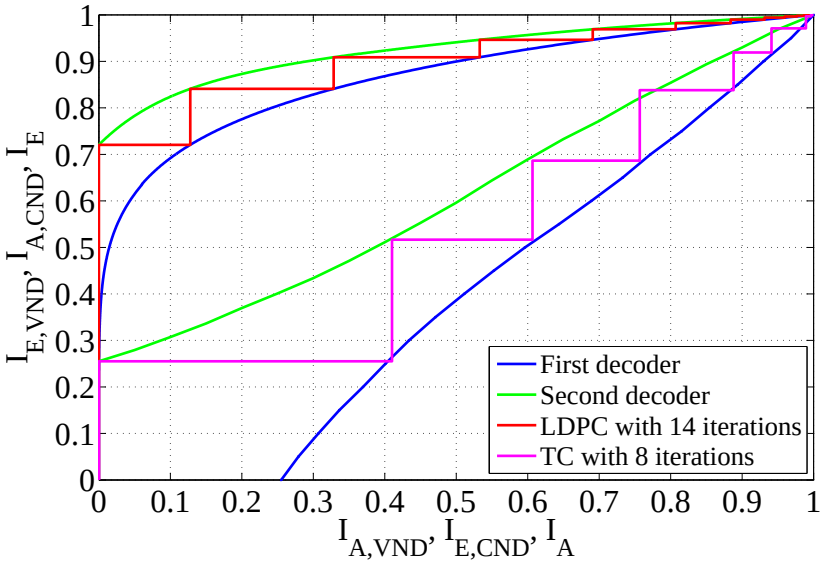

(b) $\frac{E_b}{N_0}$= 3dB.

Figure 5.13: Exit chart of $(1008, 504)$ IR-B-LDPC code versus $(1, 5/7, 5/7)$ TC for QAM modulation OFDM system over 15-path PLC channel in the presence of Nakagami-m BI noise with $m = 0.7$.

Fig. 5.14 shows trajectories of IR-B-LDPC code versus TC at $\frac{E_b}{N_0}$= 15 dB and 17 dB in the presence of combined Nakagami-m BI noise with $m = 0.7$ and IN modelled by MCAIN model with $A = 0.01$ and $\rho = 0.1$. It can be clearly seen that at $\frac{E_b}{N_0}$= 15 dB, the TC fails to converge while the LDPC code converges to a mutual information of 1 with 9 iterations. When the $\frac{E_b}{N_0}$ increases to 17 dB, the Exit curves of both decoder have a wider tunnel, which means that the system has a faster convergence to the mutual information of 1. Therefore, the $\frac{E_b}{N_0}$ present as important factor for convergence. Hence, the IR-B-LDPC code needs 5 iterations

for convergence while the TC needs 2 more iterations, i.e. 7 iterations to converge the mutual information of 1.

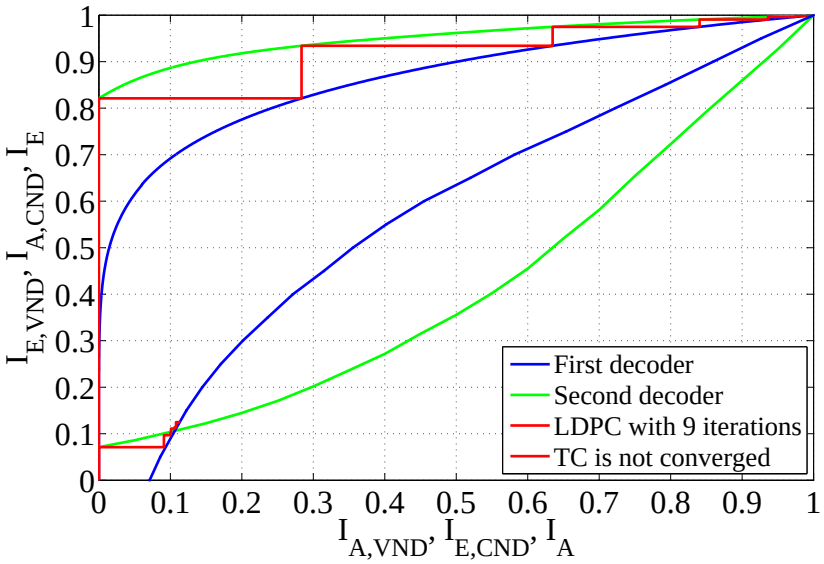

(a) $\frac{E_b}{N_0}$= 15dB.

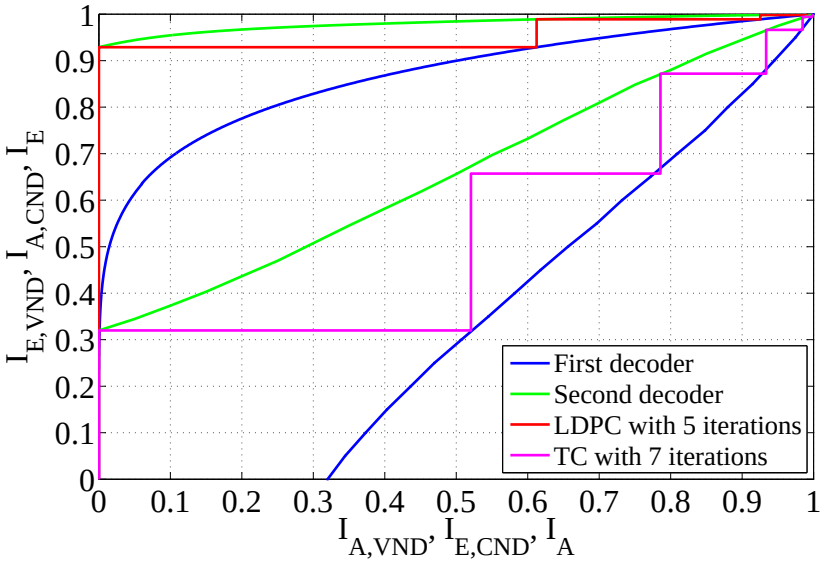

(b) $\frac{E_b}{N_0}$= 17dB.

Figure 5.14: Exit chart of $(1008, 504)$ IR-B-LDPC code versus $(1, 5/7, 5/7)$ TC for QAM modulation OFDM system over 15-path PLC channel in the presence combined Nakagami-m BI noise with $m = 0.7$ and MCAIN model with $A = 0.01$ and $\rho = 0.1$.

Fig. 5.15 shows trajectories of IR-B-LDPC code versus TC at $\frac{E_b}{N_0}$= 10 dB and 11 dB in the presence of combined Nakagami-m BI noise with $m = 0.7$ and IN modelled by using BGMIN model with $\alpha = 0.1$ and $\tilde{\rho} = 10$. It can be clearly seen that the IR-B-LDPC code needs lower $\frac{E_b}{N_0}$ and lower iterations than the TC to converge the mutual information of 1. It can be conclude that the performance of IR-B-LDPC code outperform the TC over PLC in the presence of different

scenarios of NGN. Therefore, the number of iterations at a certain $\frac{E_b}{N_0}$ can help the designers to determine the early stopping criterion based on EXIT chart over different scenarios of NGN.

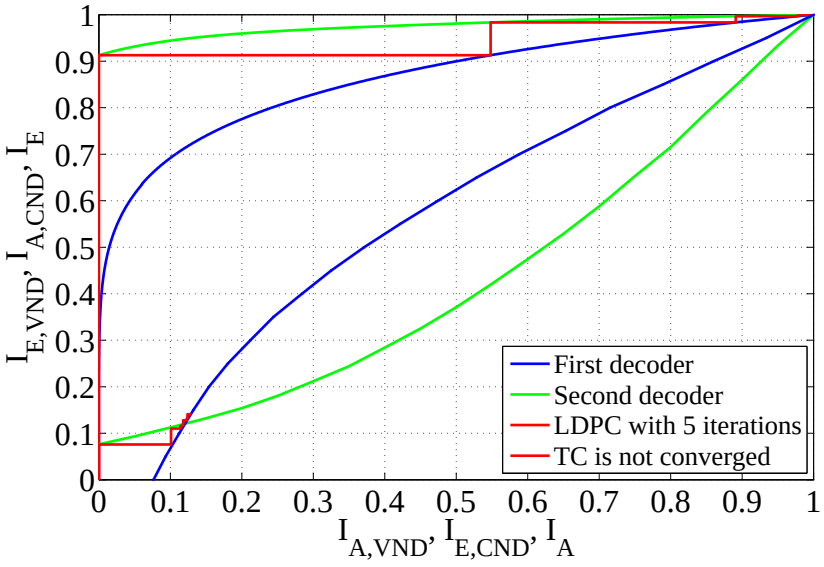

(a) $\frac{E_b}{N_0}$= 10dB.

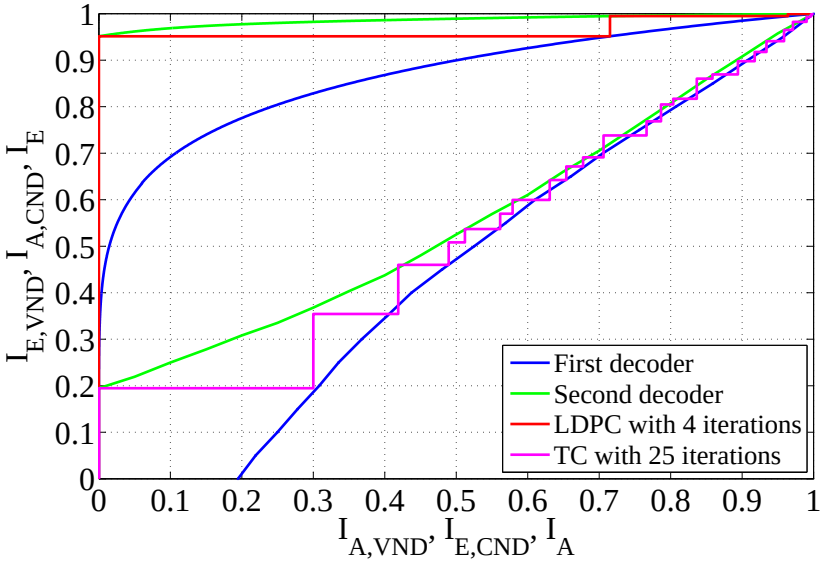

(b) $\frac{E_b}{N_0}$= 11dB.

Figure 5.15: Exit chart of $(1008, 504)$ IR-B-LDPC code versus $(1, 5/7, 5/7)$ TC for QAM modulation OFDM system over 15-path PLC channel in the presence of combined Nakagami-m BI noise with $m = 0.7$ and BGMIN model with $\alpha = 0.1$ and $\tilde{\rho} = 10$.

5.10 Summary of the Chapter

The LLRs in this chapter have been computed for IR-B/NB-LDPC codes and TC based on two methods, the first method is based on the noise distribution that utilizes the ED computations.

While in the second method is based on the derived noise distributions at the ZF equalizer output in Chapter 4.

The BER performance of the IR-B-LDPC-COFDM, IR-NB-LDPC-COFDM and T-COFDM systems has been significantly improved by using LLR computations based on ED as initials for SPA/SL-FFT/Max-Log-MAP decoders, respectively. Moreover, the optimum construction of sparse parity check matrix $\mathbf{H}$ has been used to construct the IR-B/NB-LDPC codes, while two parallel RSC codes have been used to construct the TC. The performances are simulated for similar block length in bits and coding rate over 15-path PLC channel. It is evident from the results that the derived IR-NB-LDPC codes over $\mathbb{F}_{16}$ outperform the derived IR-B-LDPC code over $\mathbb{F}_2$ and TC in all cases of NGN for all $\frac{E_b}{N_0}$ values. Additionally, the derived receivers requiring fewer iterations to achieve convergence in EXIT chart analysis.

Moreover, the performance of the IR-B/NB-LDPC-COFDM systems has been improved by computing the optimum LLRs based on the derived noise distributions at the ZF equalizer output. Monte-Carlo simulations show that the performance of the IR-B/NB-LDPC-COFDM systems with 4096-QAM constellation with LLRs computed based on derived noise distributions at the ZF equalizer output outperforms the conventional B-LDPC-COFDM system that utilized blanking IN mitigation method and LLRs computed based on the Gaussian distribution, in the presence of different NGN scenarios. Additionally, the derived IR-B-LDPC-COFDM system and IR-NB-LDPC-COFDM system offers 111 Mbps and 963 Mbps, respectively, higher data throughput than the conventional IR-B-LDPC-COFDM system for the same $\frac{E_b}{N_0}$ and BER level.

Furthermore, the performance of T-COFDM has been improved by utilizing the LLRs computed based on derived noise distributions at the ZF equalizer output. The derived receiver has been verified by using Monte-Carlo simulations utilizing 8192-QAM. Monte-Carlo simulation results show that the T-COFDM system that utilizing derived noise PDFs outperform the conventional T-COFDM system utilizing clipping IN mitigation method based on ML derived threshold and LLRs computed based on the Gaussian distribution. Moreover, the derived average upper-bounds are bounded within less than 1 dB from the proposed derived T-COFDM system over different scenarios of BI noise and IN modelled by using MCAIN model.

Chapter 6

Coded Versus Uncoded PLNC-OFDM Systems

6.1 Introduction

PLNC can be utilized to exchange information between two users (devices) using an intermediate relay (hub) node in two-time slots when no direct link is available between them. To this end, sophisticated relaying methods have been designed for the relay, such as DNF and DF protocols, to outperform the AF protocol.

In this chapter, the IR-B-LDPC code, IR-NB-LDPC code and TC are utilized at the relay node and at the end nodes to perform Like By Link-Coded Orthogonal Frequency Division Multiplexing-Physical Layer Network Coding (LBL-COFDM-PLNC) over multipath PLC channels in the presence of NGN. A novel detection scheme has been introduced that transforms the transmit signal constellation based on the frequency-domain channel coefficients to optimize detection at the relay and to improve the BER performance of LBL-COFDM-PLNC by utilizing novel derived noise distributions at the relay and at the end nodes. The closed-form expressions of the BER at the relay, relay to end nodes and E2E nodes have been derived, in addition to deriving the E2E-AUB. Monte Carlo simulation results closely verify the validity of the derived analytical expressions and reveal that the COFDM-PLNC systems utilize LLRs computed from on the exact derived noise distributions outperform the conventional system in different noise scenarios. The IN cancellation thresholds that are utilized in blanking and clipping methods in non-linear processor have been derived.

6.2 OFDM-PLNC System Model

This chapter considers a two-time slot COFDM-PLNC system to achieve higher maximum sum-rates, as shown in Fig. 6.1, which comprises two end nodes (A, B) and a relay node (R). A and B complete a full E2E packet exchange through R in two main phases as no direct link is present, namely the MA phase and BC phase. During the MA phase, each node A and B are operates in half duplex mode, i.e., A and B can not transmit and receive simultaneously. A and B transmit their information packets $\mathbf{d}^A = \{d_0, d_1, \ldots, d_{k_c-1}\}$ and $\mathbf{d}^B = \{d_0, d_1, \ldots, d_{k_c-1}\}$ of length k_c bits/digits, at the same time in the first interval, t_1. The information packets $\mathbf{d}^A$ and $\mathbf{d}^B$ are encoded by using IR-B-LDPC code and IR-NB-LDPC code, to generate the codewords $\mathbf{c}^A = \{c_0, c_1, \ldots, c_{n_c-1}\}$ and $\mathbf{c}^B = \{c_0, c_1, \ldots, c_{n_c-1}\}$ of length n_c bits/digits. Then, the random block interleaver is employed to interleaved the codewords $\mathbf{c}^A$ and $\mathbf{c}^B$ to $\bar{\mathbf{c}}^A = \prod(\mathbf{c}^A)$ and $\bar{\mathbf{c}}^B = \prod(\mathbf{c}^B)$. The interleaved codewords $\bar{\mathbf{c}}^A$ and $\bar{\mathbf{c}}^B$ in the case of IR-NB-LDPC codes are first converted to binary bits. Afterwards, the $\bar{\mathbf{c}}^A$ and $\bar{\mathbf{c}}^B$ are 4-QAM modulated to $\mathbf{X}^A = \mathcal{M}\{\bar{\mathbf{c}}^A\} = \mathbf{C}^{4QAM}[2\bar{\mathbf{c}}_1^A + \bar{\mathbf{c}}_0^A]$ and $\mathbf{X}^B = \mathcal{M}\{\bar{\mathbf{c}}^B\} = \mathbf{C}^{4QAM}[2\bar{\mathbf{c}}_1^B + \bar{\mathbf{c}}_0^B]$, respectively, utilizing the 4-QAM constellation mapping in Fig. 5.3. While in the case of TC, the information packets $\mathbf{d}^A$ and $\mathbf{d}^B$ in bits are encoded to $\bar{\mathbf{c}}^A$ and $\bar{\mathbf{c}}^B$ of length n_c bits by utilizing two RSC encoder with the LTE interleaver and puncturing mechanism to achieve the the desired code rate. Subsequently, $\bar{\mathbf{c}}^A$ and $\bar{\mathbf{c}}^B$ are 4-QAM modulated to $\mathbf{X}^A = \mathcal{M}\{\bar{\mathbf{c}}^A\}$ and $\mathbf{X}^B = \mathcal{M}\{\bar{\mathbf{c}}^B\}$, respectively.

The complex base-band COFDM symbol in the time domain $\mathbf{x}^A$ and $\mathbf{x}^B$ can be generated by taking the IFFT for the modulated symbols $\mathbf{X}^A$ and $\mathbf{X}^B$, respectively, then the $\tilde{\mathbf{x}}^A$ and $\tilde{\mathbf{x}}^B$ are produced by adding the CP and transmitted to the relay, R, simultaneously. The transmitted packets are distorted by two multipath frequency-selective PLC channels with impulse responses $\{h_{A\to R}\}_{l=0}^{L_1-1}$ and $\{h_{B\to R}\}_{l=0}^{L_2-1}$, respectively, where L_1 and L_2 are the numbers of multipath arrivals in each PLC channel in the presence of NGN. It is assumed that the forward and reverse channels are identical, i.e. $\{h_{A\to R}\}_{l=0}^{L_1-1} = \{h_{R\to A}\}_{l=0}^{L_1-1}$ and $\{h_{B\to R}\}_{l=0}^{L_2-1} = \{h_{R\to B}\}_{l=0}^{L_2-1}$.

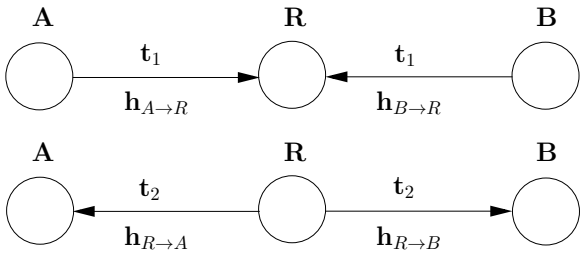

Figure 6.1: Two-way relaying systems with 2-time slot.

Under perfect synchronization, the received superimposed signal at the relay in the time domain at the first time interval, $y_R(t_1, n)$ can be expressed as

$$\tilde{y}_R(t_1, n) = \sum_{l=0}^{L_1-1} h_{A\to R}(l)\tilde{\mathbf{x}}^A(t_1, n-l) + \sum_{l=0}^{L_2-1} h_{B\to R}(l)\tilde{\mathbf{x}}^B(t_1, n-l) + \lambda_R(n),$$
$$n = 0, 1, \cdots, N + N_{CP} - 1. \tag{6.1}$$

where N is the number of orthogonal sub-carriers, $\tilde{\mathbf{x}}^A(t_1, n)$ and $\tilde{\mathbf{x}}^B(t_1, n)$ are the modulated COFDM symbols of the A and B nodes, respectively, and $\lambda_R(n) = b_n + i_n$ is the total NGN component in the time domain, where b_n is the Nakagami-m BI noise with the real and imaginary noise components expressed as $b_n^{\Re} = |\tilde{b}_n| \cos(\theta_n)$ and $b_n^{\Im} = |\tilde{b}_n| \sin(\theta_n)$, respectively, and i_n is the IN modelled either by BGMIN model or MCAIN model. Hence, the received signal at the relay after CP removal can be expressed as $\mathbf{y} = \{y_0, y_1, \cdots, y_{N-1}\}$. After performing the FFT operations, the superimposed signal at the relay in the frequency domain can be expressed as

$$Y_R(t_1, k) = H_{A\to R}(k)X_A(t_1, k) + H_{B\to R}(k)X_B(t_1, k) + \Lambda_R(k), \tag{6.2}$$
$$k = 0, 1, 2, \cdots, N-1,$$

where $H_{A\to R}(k)$ and $H_{B\to R}(k)$ are the complex-valued CFR of the multipath PLC channels, $\Lambda_R(k) = \frac{1}{\sqrt{N}} \sum_{n=0}^{N-1} \lambda_R(n) \exp\left(\frac{-j2\pi nk}{N}\right)$ is the FFT of the total uplink NGN samples, $\lambda_R(n)$, at the relay in (6.1).

6.2.1 New Relay (Hub) Mapping

It is assumed that the channel coefficients $H_{A\to R}(k)$ and $H_{B\to R}(k)$ are known at the relay. The received samples $Y_R(t_1, k)$ of (6.2) are equalized independently using zero-forcing equalizers,

i.e. $\mathrm{ZFE}_R^A(k) = \frac{1}{2H_{A\to R}(k)}$ and $\mathrm{ZFE}_R^B(k) = \frac{1}{2H_{B\to R}(k)}$ and the results are added together resulting in

$$\begin{aligned}\hat{Y}_R(t_1,k) =& \frac{Y_R(t_1,k)}{2H_{A\to R}(k)} + \frac{Y_R(t_1,k)}{2H_{B\to R}(k)} \\ =& \frac{X_A(t_1,k)}{2}\left[1+\frac{H_{A\to R}(k)}{H_{B\to R}(k)}\right] + \frac{X_B(t_1,k)}{2}\left[1+\frac{H_{B\to R}(k)}{H_{A\to R}(k)}\right] \\ &+ \frac{1}{2}\left[\frac{\Lambda_R(k)}{H_{A\to R}(k)} + \frac{\Lambda_R(k)}{H_{B\to R}(k)}\right], \quad k=0,\cdots,N-1, \end{aligned} \tag{6.3}$$

where the total equalized superimposed NGN samples at the relay can be expressed as

$$\hat{Z}_R(k) = \frac{1}{2}\left[\frac{\Lambda_R(k)}{H_{A\to R}(k)} + \frac{\Lambda_R(k)}{H_{B\to R}(k)}\right]. \tag{6.4}$$

Assuming that $S_1(k) = \frac{1}{2}\left[1+\frac{H_{A\to R}(k)}{H_{B\to R}(k)}\right]$ and $S_2(k) = \frac{1}{2}\left[1+\frac{H_{B\to R}(k)}{H_{A\to R}(k)}\right]$, the equalized superimposed signal $\hat{Y}_R(t_1,k)$ in (6.3) for a noise free level can be expressed as

$$\hat{Y}_R(t_1,k) = X_A(t_1,k)S_1(k) + X_B(t_1,k)S_2(k). \tag{6.5}$$

The the Gray constellation $\mathbf{C}^{4QAM}$ in Fig. 5.3 has been utilized to generate the denoise mapping in Table 6.1 over PLC channels and AWGN channels. It is worth mentioning that the index k will be removed from the equations inside the table for simplicity.

For instance, assuming the k-th sub-carrier index of $H_{A\to R}(k)$ and $H_{B\to R}(k)$ have complex values $-0.4686 - j0.2725$ and $1.0984 - j0.2779$, respectively. Therefore, the value of $S_1(k) = \frac{1}{2}\left[1+\frac{-0.4686-j0.2725}{1.0984-j0.2779}\right] = 0.329 - j0.1673$ and the value of $S_2(k) = \frac{1}{2}\left[1+\frac{1.0984-j0.2779}{-0.4686-j0.2725}\right] = -0.247 + j0.7309$. After substituting the values of $S_1(k)$ and $S_2(k)$ in the 6-th column in Table 6.1, the PLNC constellation mapping, C_i, for $i = 0, 1, \cdots, 15$ over PLC channels are shown in Fig. 6.2 by red circles. Moreover, the PLNC constellation mapping, C_i, over AWGN channels can be plotted by letting $H_A(k) = H_B(k) = 1$ in (6.3), which are lead to $S_1(k) = 1$, $S_2(k) = 1$. After substituting values of $S_1(k)$ and $S_2(k)$ in the 7-th column in Table 6.1. The PLNC constellation mapping, C_i, in AWGN channels are plotted in Fig.6.2 by blue squares.

The relay transforms the equalized superimposed signal $\hat{Y}_R(t_1,k)$ by utilizing the new denoise mapping using LLR computations in (6.57) for B-LDPC code, in (6.58) for NB-LDPC code and in (6.59) for TC. Then deinterleaved and decoded.

Table 6.1: PLNC with new mapping on PLC channels.

$\bar{\mathbf{c}}_1^A\bar{\mathbf{c}}_0^A$	$\frac{X_A S_1}{\sqrt{E_b}}$	$\bar{\mathbf{c}}_1^B\bar{\mathbf{c}}_0^B$	$\frac{X_B S_2}{\sqrt{E_b}}$	$b_1^R b_0^R$	$\hat{Y}_R(t_1,k)$ over PLC	$\hat{Y}_R(t_1,k)$ over AWGN
00	$(-1-j)S_1$	00	$(-1-j)S_2$	00	$C_0=(-1-j)S_1+(-1-j)S_2$	$C_0=-2-j2$
00	$(-1-j)S_1$	01	$(-1+j)S_2$	01	$C_1=(-1-j)S_1+(-1+j)S_2$	$C_1=-2$
00	$(-1-j)S_1$	10	$(1-j)S_2$	10	$C_2=(-1-j)S_1+(1-j)S_2$	$C_2=-j2$
00	$(-1-j)S_1$	11	$(1+j)S_2$	11	$C_3=(-1-j)S_1+(1+j)S_2$	$C_3=0$
01	$(-1+j)S_1$	00	$(-1-j)S_2$	01	$C_4=(-1+j)S_1+(-1-j)S_2$	$C_4=-2$
01	$(-1+j)S_1$	01	$(-1+j)S_2$	00	$C_5=(-1+j)S_1+(-1+j)S_2$	$C_5=-2+j2$
01	$(-1+j)S_1$	10	$(1-j)S_2$	11	$C_6=(-1+j)S_1+(1-j)S_2$	$C_6=0$
01	$(-1+j)S_1$	11	$(1+j)S_2$	10	$C_7=(-1+j)S_1+(1+j)S_2$	$C_7=j2$
10	$(1-j)S_1$	00	$(-1-j)S_2$	10	$C_8=(1-j)S_1+(-1-j)S_2$	$C_8=-j2$
10	$(1-j)S_1$	01	$(-1+j)S_2$	11	$C_9=(1-j)S_1+(-1+j)S_2$	$C_9=0$
10	$(1-j)S_1$	10	$(1-j)S_2$	00	$C_{10}=(1-j)S_1+(1-j)S_2$	$C_{10}=2-j2$
10	$(1-j)S_1$	11	$(1+j)S_2$	01	$C_{11}=(1-j)S_1+(1+j)S_2$	$C_{11}=2$
11	$(1+j)S_1$	00	$(-1-j)S_2$	11	$C_{12}=(1+j)S_1+(-1-j)S_2$	$C_{12}=0$
11	$(1+j)S_1$	01	$(-1+j)S_2$	10	$C_{13}=(1+j)S_1+(-1+j)S_2$	$C_{13}=j2$
11	$(1+j)S_1$	10	$(1-j)S_2$	01	$C_{14}=(1+j)S_1+(1-j)S_2$	$C_{14}=2$
11	$(1+j)S_1$	11	$(1+j)S_2$	00	$C_{15}=(1+j)S_1+(1+j)S_2$	$C_{15}=2+j2$

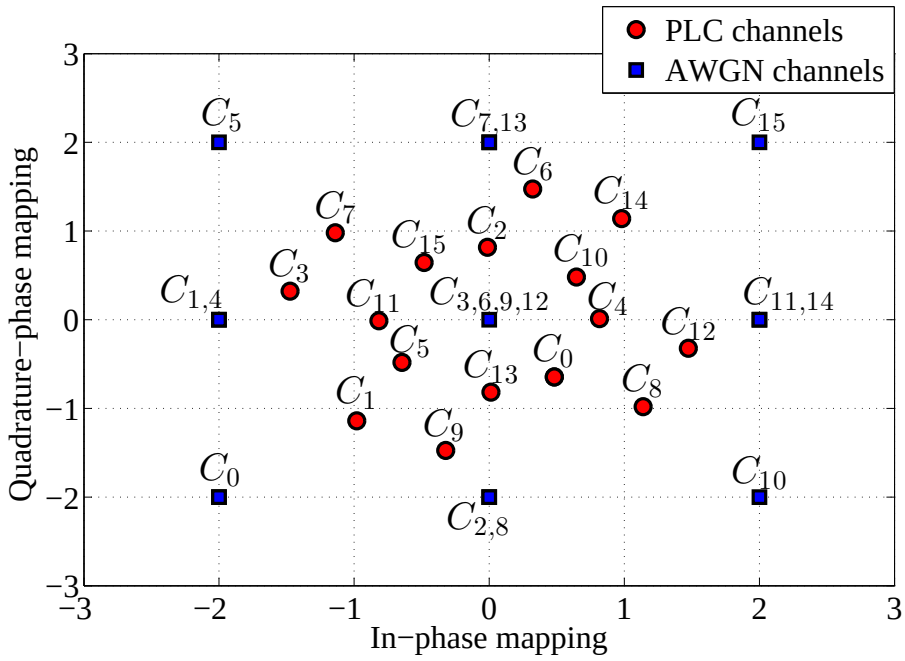

Figure 6.2: PLNC constellation mapping for k-th subcarrier index with complex valued PLC channel gains $H_A(k) = -0.4686 - j0.2725$ and $H_B(k) = 1.0984 - j0.2779$,and Eb = 1 compared with AWGN channels.

6.2.2 Broadcast Stage

The decoded signal at the relay is firstly encoded and then interleaved. Next, the 4-QAM modulated and the complex baseband OFDM symbol are generated for transmitting to the end

nodes A and B. The received signal during the broadcast or downlink phase, t_2, at both nodes after removing the CP and FFT operations by assuming perfect synchronization and perfect knowledge of the CFR for the k-th FFT sub-carrier, $H_{R\to D}(k)$, can be expressed as

$$Y_D(t_2,k) = H_{R\to D}(k)X_R(t_2,k) + \Lambda_D(k), \quad k = 0,1,\cdots,N-1, \tag{6.6}$$

where $D \in \{A,B\}$, $Y_D(t_2,k)$ is the received signal in the frequency domain at end nodes A and B, respectively, $X_R(t_2,k)$ is the modulated symbol at the relay and $\Lambda_D(k)$ represents the FFT of the noise samples $\lambda_D(n)$ at the end nodes expressed as $\Lambda_D(k) = \frac{1}{\sqrt{N}}\sum_{n=0}^{N-1}\lambda_D(n)\exp\left(\frac{-j2\pi nk}{N}\right)$. Hence, the received data symbols can be recovered at the end nodes using $\mathrm{ZFE}_D(k) = \frac{1}{H_{R\to D}(k)}$. The equalized k-th complex received symbol in (6.6) can be expressed as

$$\hat{Y}_D(t_2,k) = \frac{Y_D(t_2,k)}{H_{R\to D}(k)} = X_R(t_2,k) + \frac{\Lambda_D(k)}{H_{R\to D}(k)}, \tag{6.7}$$

where the total equalized NGN at the end nodes A and B can be expressed as

$$\hat{Z}_D(k) = \frac{\Lambda_D(k)}{H_{R\to D}(k)}. \tag{6.8}$$

Further, the LLR values are computed based on Chapter 5, deinterleaved and decoded. Then, both users can detect the transmitted data by EX-ORing the detected data with the user's own information data $\hat{\mathbf{d}}^A$ and $\hat{\mathbf{d}}^B$ as given in (3.44) and (3.45), respectively.

6.3 Derivation of the Noise PDFs

The BER performance of COFDM-PLNC system depends on the information received in the BC stage and mainly depends on the decision process at the R during the MA stage. Therefore, the key of optimization depends on the denoise process at the R node and at the end nodes, which depends on the distribution of the equalized noise for the proposed method at the R and at the end nodes.

6.3.1 At the Relay Node

The distribution of all types of the NGN samples in the frequency domain after the FFT operation at the relay can be expressed as given in (5.2) and is recalled in (6.9) as

$$p(\Lambda_R^r(k)) = \frac{1}{\sqrt{2\pi}\sigma_\beta} e^{-\frac{(\Lambda_R^r(k))^2}{2\sigma_\beta^2}}, \tag{6.9}$$

where $r = \{\Re, \Im\}$. Therefore, the distribution of the real part at the relay in (6.4) without the scaled $\frac{1}{2}$ can be obtained using the characteristic functions of their PDFs or by the convolution between two PDFs yields

$$p(\varrho^{\Re}) = \frac{4\sqrt{\pi}\sigma_h\sigma_\beta^2}{\Gamma(3.5)(\sigma_h|\varrho^{\Re}| + \sqrt{2}\sigma_\beta)^3} \, {}_2F_1\left(3, \frac{1}{2}; 3\frac{1}{2}; \frac{\sigma_h|\varrho^{\Re}| - \sqrt{2}\sigma_\beta}{\sigma_h|\varrho^{\Re}| + \sqrt{2}\sigma_\beta}\right). \tag{6.10}$$

Therefore, the real part of the distribution at the relay, $p(Z^{\Re})$, can be computed by using the scaled formula of the RV $\varrho^{\Re}$ as $Z^{\Re} = \frac{\varrho^{\Re}}{2}$ in (6.4). The $p\left(\frac{\varrho^{\Re}}{2}\right)$ can be computed using $Z^{\Re} = a\varrho^{\Re} + b$, where $a = \frac{1}{2}$ and $b = 0$, hence $p(Z^{\Re}) = \frac{1}{|a|}p_\varrho\left(\frac{Z^{\Re}-b}{a}\right)$ can be expressed as [161]

$$p(\hat{Z}_R^{\Re}(k)) = \frac{8\sqrt{\pi}\sigma_h\sigma_\beta^2}{\Gamma(3.5)(\sigma_h|2\hat{Z}_R^{\Re}(k)| + \sqrt{2}\sigma_\beta)^3} \, {}_2F_1\left(3, \frac{1}{2}; 3\frac{1}{2}; \frac{\sigma_h|2\hat{Z}_R^{\Re}(k)| - \sqrt{2}\sigma_\beta}{\sigma_h|2\hat{Z}_R^{\Re}(k)| + \sqrt{2}\sigma_\beta}\right). \tag{6.11}$$

It is worth noting that the PDF of the imaginary part at the relay, $p(Z^{\Im})$, is equal to the PDF of the real part $p(Z^{\Re})$ as

$$p(\hat{Z}_R^{\Im}(k)) = \frac{8\sqrt{\pi}\sigma_h\sigma_\beta^2}{\Gamma(3.5)(\sigma_h|2\hat{Z}_R^{\Im}(k)| + \sqrt{2}\sigma_\beta)^3} \, {}_2F_1\left(3, \frac{1}{2}; 3\frac{1}{2}; \frac{\sigma_h|2\hat{Z}_R^{\Im}(k)| - \sqrt{2}\sigma_\beta}{\sigma_h|2\hat{Z}_R^{\Im}(k)| + \sqrt{2}\sigma_\beta}\right), \tag{6.12}$$

where ${}_2F_1([a, b]; c; z)$ is the Gaussian hypergeometric function expressed as a series in [45, 9.100] as

$${}_2F_1(a, b; c; z) = \sum_{n=0}^{\infty} \frac{(a)_n(b)_n}{(c)_n} \frac{z^n}{n!}, \tag{6.13}$$

where a, b and c, are real-valued constants and $(q)_0 = 1$ and $(q)_n = q(q+1)\cdots(q+n-1)$ for $n > 0$. The distribution of $p(\hat{Z}_R^r(k))$ can be computed by changing the value of σ_β^2 corresponding to different scenarios of NGN over PLC channel.

6.3.2 At the Downlink

The distributions of the equalized NGN samples at the end nodes in (6.8) can be derived by following similar derivation steps in (4.25)-(4.34) for the case of MCAIN, (4.40)-(4.49) for the case of BGMIN, (4.65)-(4.67) for the case of Nakagami-m BI noise, (4.72)-(4.73) for the case of combined Nakagami-m BI noise and IN modelled by using MCAIN model, (4.74)-(4.79) for the case of combined Nakagami-m BI noise and IN modelled by using BGMIN model. The general equalized received noise samples can be expressed as in (4.86) and is recalled in (6.14)

$$p_{\hat{Z}}(\hat{Z}_D^r(k)) = \frac{\sigma_\beta^2 \sigma_h}{2\left(\sigma_h^2 |\hat{Z}_D^r(k)|^2 + \sigma_\beta^2\right)^{\frac{3}{2}}}, \tag{6.14}$$

where $\sigma_\beta^2 = \sigma_A^2$ in the case of the MCAIN model computed by (4.13), $\sigma_\beta^2 = \sigma_b^2$ in the case of the Nakakami-m BI noise computed by (4.62), $\sigma_\beta^2 = \sigma_b^2 + \sigma_A^2$ in the case of combined BI noise and MCAIN model, $\sigma_\beta^2 = \sigma_N^2$ in the case of BGMIN computed by (5.3) and $\sigma_\beta^2 = \sigma_b^2 + \sigma_N^2$ in the case of combined BI noise and BGMIN.

6.4 E2E-BER Computation

Assuming both users A and B transmit $\sqrt{\mathrm{E_b}}(1+j)$, the probability of error receiving $C_{15} = 2 + 2j$ at the relay over AWGN channels in presence of IN shown in Fig. 6.2 can be computed as [161]

$$\begin{aligned} P_e(C_{15}) &= P_e(x < \sqrt{E_b}, y < \sqrt{E_b}) \\ &= F_x^{C_{15}}(\sqrt{E_b}) + F_y^{C_{15}}(\sqrt{E_b}) - F_x^{C_{15}}(\sqrt{E_b}) F_y^{C_{15}}(\sqrt{E_b}). \end{aligned} \tag{6.15}$$

Due to symmetry, the marginal probabilities for the real and imaginary components are equal and can be computed using (6.9) as

$$\begin{aligned} F_x^{C_{15}}(\sqrt{E_b}) &= F_y^{C_{15}}(\sqrt{E_b}) \\ &= \int_{-\infty}^{\sqrt{E_b}} \frac{1}{\sqrt{2\pi}\sigma_\beta} \exp\left(-\frac{|\Lambda_R^r - 2\sqrt{E_b}|^2}{2\sigma_\beta^2}\right) d\Lambda_R^r. \end{aligned} \tag{6.16}$$

By substituting $\frac{(u^r)^2}{2} = \frac{|\Lambda_R^r - 2\sqrt{E_b}|^2}{2\sigma_\beta^2}$, u^r can be computed as $u^r = \frac{|\Lambda_R^r - 2\sqrt{E_b}|}{\sigma_\beta}$ and $du^r = \frac{d\Lambda_R^r}{\sigma_\beta}$. The upper integration limit can be expressed as $u^r|_{\Lambda_R^r = \sqrt{E_b}} = \frac{-\sqrt{E_b}}{\sigma_\beta} = -\sqrt{2\gamma_b}$, where $\gamma_b = \frac{\mathrm{E_b}}{2\sigma_\beta^2}$ is

the signal to noise ratio per bit. $P_e(C_{15})$ can rewrite as

$$F_x^{C_{15}}(\sqrt{E_b}) = F_y^{C_{15}}(\sqrt{E_b}) \\ = \int_{-\infty}^{-\sqrt{2\gamma_b}} \frac{1}{\sqrt{2\pi}} \exp\left(-\frac{u^2}{2}\right) du^r = Q\left(\sqrt{2\gamma_b}\right), \tag{6.17}$$

where Q(.) is the Q-function, defined as

$$Q(x) = \frac{1}{\sqrt{2\pi}} \int_x^{\infty} e^{-\frac{u}{2}} du. \tag{6.18}$$

Using (6.15) and (6.17), the probability of error associated with C_{15} is given as

$$P_e(C_{15}) = 2Q(\sqrt{2\gamma_b}) - Q^2(\sqrt{2\gamma_b}) \approx 2Q(\sqrt{2\gamma_b}), \quad \text{for } \gamma_b >> 0. \tag{6.19}$$

Due to the constellation symmetry, the error probability of C_{15} is equal to error probability of C_0, C_5 and C_{10} in Fig. 6.2. Following a similar approach, we can compute the probability of error receiving C_3 as

$$P_e(C_3) = 1 - \frac{1}{2\pi\sigma_\beta^2} \int_{-\sqrt{E_b}}^{\sqrt{E_b}} \int_{-\sqrt{E_b}}^{\sqrt{E_b}} \exp\left(-\frac{x^2+y^2}{2\sigma_\beta^2}\right) dxdy \\ = 1 - \left(F_x^{C_3}(\sqrt{E_b}) - F_x^{C_3}(-\sqrt{E_b})\right)^2. \tag{6.20}$$

The identities are exploiting $F_x^{C_3}(\sqrt{E_b}) = F_y^{C_3}(\sqrt{E_b})$ and $F_x^{C_3}(-\sqrt{E_b}) = F_y^{C_3}(-\sqrt{E_b})$, due to the symmetry around the origin of their marginal PDFs. Furthermore, by introducing $F_x^{C_3}(\sqrt{E_b}) = 1 - F_x^{C_3}(-\sqrt{E_b})$ in (6.20) yields

$$P_e(C_3) = 4F_x^{C_3}(-\sqrt{E_b}) - 4F_x^{C_3}(-\sqrt{E_b}). \tag{6.21}$$

It can be easily shown that $F_x^{C_3}(-\sqrt{E_b}) = Q(\sqrt{2\gamma_b})$ and substituting in (6.21) yields

$$P_e(C_3) = 4Q(\sqrt{2\gamma_b}) - 4Q^2(\sqrt{2\gamma_b}) \approx 4Q(\sqrt{2\gamma_b}), \quad \text{for } \gamma_b >> 0. \tag{6.22}$$

Due to the constellation symmetry, the error probability of C_3 is equal to error probability of C_6, C_9 and C_{12}. Similarly, the probabilities of error for C_1, C_2, C_4, C_7, C_8, C_{11}, C_{13} and C_{14}

are equal and can be computed as

$$P_e(C_1) = 3Q(\sqrt{2\gamma_b}) - 2Q^2(\sqrt{2\gamma_b}) \approx 3Q(\sqrt{2\gamma_b}), \quad \text{for } \gamma_b >> 0. \tag{6.23}$$

By exploiting the symmetry of the constellation points, the total symbol error probability at the relay can be expressed as

$$\begin{aligned} P_s(R) &= 4P(C_{15})P_e(C_{15}) + 4P(C_1)P_e(C_1) + P(C_3)P_e(C_3) \\ &= \frac{4}{16} \times 2Q(\sqrt{2\gamma_b}) + \frac{8}{16} \times 3Q(\sqrt{2\gamma_b}) + \frac{4}{16} \times 4Q(\sqrt{2\gamma_b}) \\ &= 3Q(\sqrt{2\gamma}) = \frac{3}{2}\text{erfc}(\sqrt{\gamma}), \end{aligned} \tag{6.24}$$

where $\text{erfc}(.)$ is the complementary error function, defined as

$$\text{erfc}(x) = \frac{2}{\sqrt{\pi}} \int_x^{\infty} e^{-t^2} dt. \tag{6.25}$$

Therefore, the BER at the relay over AWGN channel can be computed using (4.94) as

$$P_b(R) = \frac{P_s(R)}{\log_2(4)} = \frac{P_s(R)}{2} = \frac{3}{4}\text{erfc}(\sqrt{\gamma_b}). \tag{6.26}$$

The average SNR per bit, γ_b, due to the effect of the multipath PLC channel can be expressed as $\gamma_b = \mathbb{E}(h^2)\frac{E_b}{2\sigma_\beta^2}$, where $\mathbb{E}(h^2)$ is the average of h^2 [56]. Hence, the channel h exhibit a Rayleigh distribution, h^2 has a chi-squared probability distribution with two degrees of freedom, the distribution of the SNR can be expressed as $p(\gamma_b) = \frac{1}{\bar{\gamma}_b} \exp(-\frac{\gamma_b}{\bar{\gamma}_b})$. Therefore, γ_b in the presence two uplink multipath PLC channels can be expressed as $\gamma_b = (|H_{A\to R}|^2 + |H_{B\to R}|^2)\frac{E_b}{2\sigma_\beta^2}$. Since both channel have the same energy, the effective γ_b can be expressed as $\gamma_b = 2\mathbb{E}(h^2)\frac{E_b}{2\sigma_\beta^2}$. Thus, the pdf of γ_b can be expressed as

$$p(\gamma_b) = \frac{2}{\bar{\gamma}_b} \exp(-\frac{\gamma_b}{\bar{\gamma}_b}). \tag{6.27}$$

The average probability of error at the relay over PLC channels can be computed as

$$\begin{aligned} P_b(R) &= \int_0^\infty P_b(R)P(\gamma_b)d\gamma_b \\ &= \int_0^\infty \frac{3}{2\bar{\gamma}_b}\text{erfc}(\sqrt{\gamma_b})\exp(-\frac{\gamma_b}{\bar{\gamma}_b})d\gamma_b \\ &= \frac{3}{2}\left[1-\sqrt{\frac{\psi}{\psi+1}}\right], \end{aligned} \tag{6.28}$$

where $\psi = \frac{\sigma_h^2 E_b}{\sigma_\beta^2}$. Moreover, the probability of error for the real and imaginary components at the end nodes given that the relay transmits $\sqrt{\mathrm{E_b}}(-1-j)$ can be computed by utilizing (6.14) as

$$P_s^r(D) = \int_{\sqrt{E_b}}^\infty p(\hat{Z}_D^r(k))dZ_D^r(k) = \int_{\sqrt{E_b}}^\infty \frac{\sigma_\beta^2\sigma_h}{2\left(\sigma_h^2|\hat{Z}_D^r(k)|^2+\sigma_\beta^2\right)^{\frac{3}{2}}}dZ_D^r(k) = \frac{1}{2}\left[1-\sqrt{\frac{\psi}{\psi+1}}\right]. \tag{6.29}$$

Therefore, the probability of symbol error at the end nodes A or B over the PLC channel can be computed using (6.29) as

$$\begin{aligned} P_s(D) &= 1-[1-P_s^{\Re}(D)]^2 \\ &\approx \left[1-\sqrt{\frac{\psi}{\psi+1}}\right]. \end{aligned} \tag{6.30}$$

Hence, the BER at the end nodes can be computed utilizing (4.94) as

$$P_b(D) = \frac{P_s(D)}{2} = \frac{1}{2}\left[1-\sqrt{\frac{\psi}{\psi+1}}\right]. \tag{6.31}$$

Note that the transmitted symbol from A and B suffers two detection errors at the MA stage and at the BC stage. In order to calculate the E2E-BER, two different scenarios are used which are valid at moderate to high SNR, such that some of the bits that are detected without/with errors at the relay will be detected with/without errors at the end nodes, respectively. Then, the E2E instantaneous BER at the end node D denote as $P_b(E2E-D)$ for the uncoded OFDM-PLNC system becomes

$$P_b(E2E-D) = (1-P_b(R))P_b(D) + (1-P_b(D))P_b(R). \tag{6.32}$$

Averaging $P_b(E2E-A)$ and $P_b(E2E-B)$ gives the E2E-BER as

$$P_b(E2E) = \frac{1}{2}\left(P_b(E2E-A) + P_b(E2E-B)\right) = P_b(E2E-D). \tag{6.33}$$

6.5 AUBs of Turbo Code

The exact BER can not be computed for coded systems with an iterative decoding algorithm. Therefore, the AUB of TC can be used to bound the performance at high SNRs and beyond simulation capabilities. The PEP at the relay, $P_v(R)$, and end nodes, $P_v(D)$, can be used to compute the AUB by utilizing the $P_b(R)$ in (6.28) and $P_b(D)$ in (6.31), respectively. The PEP for 4-QAM constellation can be computed as [56]

$$P_v(R) = P_b^v(R)\sum_{k=0}^{v-1}\binom{v-1+k}{k}(1-P_b(R))^k, \tag{6.34}$$

$$P_v(D) = P_b^v(D)\sum_{k=0}^{v-1}\binom{v-1+k}{k}(1-P_b(D))^k. \tag{6.35}$$

The AUB at the relay node and at the end nodes can be expressed as

$$P_b^{\mathrm{AUB}}(R) = \sum_v D(v)P_v(R), \tag{6.36}$$

$$P_b^{\mathrm{AUB}}(D) = \sum_v D(v)P_v(D), \tag{6.37}$$

where the coefficients $D(v)$ are tabulated in [136] for interleaver sizes of $100, 1000$ and 10000, respectively. Hence, the E2E-AUB can be computed as

$$P_b^{\mathrm{AUB}}(E2E) \approx (1-P_b^{\mathrm{AUB}}(R))P_b^{\mathrm{AUB}}(D) + (1-P_b^{\mathrm{AUB}}(D))P_b^{\mathrm{AUB}}(R). \tag{6.38}$$

6.6 Threshold Optimization for OFDM-PLNC System

6.6.1 MCAIN Model and the Combination of BI Noise and MCAIN Model

For large number of orthogonal sub-carriers N, the complex received signal $\tilde{y}_R(t_1,n)$ in (6.1) will follow the distribution of (4.98) as

$$p(|\tilde{y}_R(t_1,n)|) = \frac{e^{-A}|\tilde{y}_R(t_1,n)|}{\sigma_1^2}e^{-\frac{|\tilde{y}_R(t_1,n)|^2}{2\sigma_1^2}} + \frac{(1-e^{-A})|\tilde{y}_R(t_1,n)|}{\sigma_2^2}e^{-\frac{|\tilde{y}_R(t_1,n)|^2}{2\sigma_2^2}}, \tag{6.39}$$

where σ_1^2 denotes the variance of the received signal in the case of free impulsive and σ_2^2 denotes the variance of the received signal in the case of impact impulsive. Following similar derivation steps (4.100)-(4.103). The derived threshold in (4.103) is utilized and is recalled in (6.40)

$$|T_{ML}^{opt}| = \sqrt{\frac{2\sigma_2^2\sigma_1^2}{\sigma_2^2 - \sigma_1^2} \ln\left(\frac{\sigma_2^2}{\sigma_1^2}\right)}. \tag{6.40}$$

However, in the case of complex MCAIN only, the simplified MCAIN has been utilized as given in (2.26). The σ_1^2 and σ_2^2 can be expressed based on the complex received signal $\tilde{y}_R(t_1, n)$ in (6.1) as

$$\sigma_1^2 = \frac{\mathbb{E}\{|h_A|^2\}\mathbb{E}\{|x_A|^2\}}{2} + \frac{\mathbb{E}\{|h_B|^2\}\mathbb{E}\{|x_B|^2\}}{2} + \sigma_w^2, \tag{6.41}$$

$$\sigma_2^2 = \frac{\mathbb{E}\{|h_A|^2\}\mathbb{E}\{|x_A|^2\}}{2} + \frac{\mathbb{E}\{|h_B|^2\}\mathbb{E}\{|x_B|^2\}}{2} + \zeta^2, \tag{6.42}$$

where $\zeta^2 = \sigma_w^2\left(1 + \frac{1}{A\rho}\right)$. The simplification of the first term $\frac{2\sigma_2^2\sigma_1^2}{\sigma_2^2-\sigma_1^2}$ can be expressed as

$$\begin{aligned}
\frac{2\sigma_2^2\sigma_1^2}{\sigma_2^2 - \sigma_1^2} &= \frac{2A\rho}{\sigma_w^2}\Bigg[\left(\frac{\mathbb{E}\{|h_A|^2\}\mathbb{E}\{|x_A|^2\}}{2} + \frac{\mathbb{E}\{|h_B|^2\}\mathbb{E}\{|x_B|^2\}}{2} + \sigma_w^2\left(1 + \frac{1}{A\rho}\right)\right) \times \\
&\quad \left(\frac{\mathbb{E}\{|h_A|^2\}\mathbb{E}\{|x_A|^2\}}{2} + \frac{\mathbb{E}\{|h_B|^2\}\mathbb{E}\{|x_B|^2\}}{2} + \sigma_w^2\right)\Bigg] \\
&= \frac{2A\rho}{\sigma_w^2}\Bigg[\sigma_w^2\left(\frac{\mathbb{E}\{|h_A|^2\}\mathbb{E}\{|x_A|^2\}}{2\sigma_w^2} + \frac{\mathbb{E}\{|h_B|^2\}\mathbb{E}\{|x_B|^2\}}{2\sigma_w^2} + \left(1 + \frac{1}{A\rho}\right)\right) \times \\
&\quad \sigma_w^2\left(\frac{\mathbb{E}\{|h_A|^2\}\mathbb{E}\{|x_A|^2\}}{2\sigma_w^2} + \frac{\mathbb{E}\{|h_B|^2\}\mathbb{E}\{|x_B|^2\}}{2\sigma_w^2} + 1\right)\Bigg] \\
&= 2A\rho\sigma_w^2\left(2\mathrm{SNR} + \frac{1}{A\rho} + 1\right)(2\mathrm{SNR} + 1)\,.
\end{aligned} \tag{6.43}$$

where $\mathrm{SNR} = \frac{\mathbb{E}\{|h_A|^2\}\mathbb{E}\{|x_A|^2\}}{2\sigma_w^2} = \frac{\mathbb{E}\{|h_B|^2\}\mathbb{E}\{|x_B|^2\}}{2\sigma_w^2}$. Moreover, the simplification of the second term $\ln\left(\frac{\sigma_2^2}{\sigma_1^2}\right)$ can be expressed as

$$\begin{aligned}
\ln\left(\frac{\sigma_2^2}{\sigma_1^2}\right) &= \ln\left(\frac{\frac{\mathbb{E}\{|h_A|^2\}\mathbb{E}\{|x_A|^2\}}{2} + \frac{\mathbb{E}\{|h_B|^2\}\mathbb{E}\{|x_B|^2\}}{2} + \sigma_w^2\left(1 + \frac{1}{A\rho}\right)}{\frac{\mathbb{E}\{|h_A|^2\}\mathbb{E}\{|x_A|^2\}}{2} + \frac{\mathbb{E}\{|h_B|^2\}\mathbb{E}\{|x_B|^2\}}{2} + \sigma_w^2}\right), \\
&= \ln\left(1 + \frac{1}{A\rho\left(\frac{\mathbb{E}\{|h_A|^2\}\mathbb{E}\{|x_A|^2\}}{2\sigma_w^2} + \frac{\mathbb{E}\{|h_B|^2\}\mathbb{E}\{|x_B|^2\}}{2\sigma_w^2} + 1\right)}\right), \\
&= \ln\left(1 + \frac{1}{A\rho\,(2\mathrm{SNR} + 1)}\right).
\end{aligned} \tag{6.44}$$

Therefore, the optimal threshold can be computed by utilizing (6.40) as

$$|T_{ML}^{opt}| = \sqrt{2A\rho\sigma_w^2\left(2\mathrm{SNR}+\frac{1}{A\rho}+1\right)(2\mathrm{SNR}+1)\ln\left(1+\frac{1}{A\rho\,(2\mathrm{SNR}+1)}\right)}. \tag{6.45}$$

While, in case of complex combined BI noise and MCAIN, let

$$\sigma_1^2 = \frac{\mathbb{E}\{|h_A|^2\}\mathbb{E}\{|x_A|^2\}}{2}+\frac{\mathbb{E}\{|h_B|^2\}\mathbb{E}\{|x_B|^2\}}{2}+\sigma_b^2+\sigma_w^2, \tag{6.46}$$

$$\sigma_2^2 = \frac{\mathbb{E}\{|h_A|^2\}\mathbb{E}\{|x_A|^2\}}{2}+\frac{\mathbb{E}\{|h_B|^2\}\mathbb{E}\{|x_B|^2\}}{2}+\sigma_b^2+\zeta^2. \tag{6.47}$$

The threshold can be computed by utilizing (6.40) and after some simplifications yields

$$|T_{ML}| = \sqrt{2A\rho\sigma_w^2\left(2\mathrm{SNR}+\frac{\sigma_b^2}{\sigma_w^2}+\frac{1}{A\rho}+1\right)\left(2\mathrm{SNR}+\frac{\sigma_b^2}{\sigma_w^2}+1\right)}\times \sqrt{\ln\left(1+\frac{1}{A\rho\left(2\mathrm{SNR}+\frac{\sigma_b^2}{\sigma_w^2}+1\right)}\right)}. \tag{6.48}$$

6.6.2 BGMIN Model and the Combination of BI Noise and BGMIN Model

In the case of complex BGMIN only, assume

$$\sigma_1^2 = \frac{\mathbb{E}\{|h_A|^2\}\mathbb{E}\{|x_A|^2\}}{2}+\frac{\mathbb{E}\{|h_B|^2\}\mathbb{E}\{|x_B|^2\}}{2}+\sigma_w^2, \tag{6.49}$$

$$\sigma_2^2 = \frac{\mathbb{E}\{|h_A|^2\}\mathbb{E}\{|x_A|^2\}}{2}+\frac{\mathbb{E}\{|h_B|^2\}\mathbb{E}\{|x_B|^2\}}{2}+\sigma_w^2(1+\tilde{\rho}), \tag{6.50}$$

where $\tilde{\rho}=\frac{\sigma_i^2}{\sigma_w^2}$. After substituting σ_1^2 and σ_2^2 in (6.40), the optimal threshold after some simplifications yields

$$|T_{ML}| = \sqrt{2\sigma_w^2\,(2\mathrm{SNR}+1)\left(\frac{2\mathrm{SNR}+1}{\tilde{\rho}}+1\right)\ln\left(1+\frac{\tilde{\rho}}{2\mathrm{SNR}+1}\right)}. \tag{6.51}$$

While in the case of combined noise, assume

$$\sigma_1^2 = \frac{\mathbb{E}\{|h_A|^2\}\mathbb{E}\{|x_A|^2\}}{2}+\frac{\mathbb{E}\{|h_B|^2\}\mathbb{E}\{|x_B|^2\}}{2}+\sigma_b^2+\sigma_w^2, \tag{6.52}$$

$$\sigma_2^2 = \frac{\mathbb{E}\{|h_A|^2\}\mathbb{E}\{|x_A|^2\}}{2}+\frac{\mathbb{E}\{|h_B|^2\}\mathbb{E}\{|x_B|^2\}}{2}+\sigma_b^2+\sigma_w^2(1+\tilde{\rho}). \tag{6.53}$$

The threshold can be derived as

$$|T_{ML}^{opt}| = \sqrt{2\sigma_w^2\left(2\text{SNR}+\frac{\sigma_b^2}{\sigma_w^2}+1\right)\left(\frac{2\text{SNR}+1}{\tilde{\rho}}+\frac{\sigma_b^2}{\tilde{\rho}\sigma_w^2}+1\right)\ln\left(1+\frac{\tilde{\rho}}{2\text{SNR}+\frac{\sigma_b^2}{\sigma_w^2}+1}\right)}. \tag{6.54}$$

6.7 Maximum Likelihood Detector and LLR Computations

6.7.1 Maximum Likelihood Detector

6.7.1.1 At the Relay

The general expression of the real and imaginary components of the equalized received samples at the relay can be written as

$$p(\hat{Z}_R^r(k)) = \frac{8\sqrt{\pi}\sigma_h\sigma_\beta^2}{\Gamma(3.5)(\sigma_h|2\hat{Z}_R^r(k)|+\sqrt{2}\sigma_\beta)^3}\,{}_2F_1\left(3,\frac{1}{2};3\frac{1}{2};\frac{\sigma_h|2\hat{Z}_R^r(k)|-\sqrt{2}\sigma_\beta}{\sigma_h|2\hat{Z}_R^r(k)|+\sqrt{2}\sigma_\beta}\right). \tag{6.55}$$

By utilizing the PDF in (6.55), the ML detector for the real and imaginary parts of the equalized signal at the relay utilizing the new derived denoise mapping at the relay in Table 6.1 can be expressed as

$$\begin{aligned}&\sum_{i=0}^{15}\left\{\frac{8\sqrt{\pi}\sigma_h\sigma_\beta^2\,{}_2F_1\left(3,\frac{1}{2};3\frac{1}{2};\frac{2\sigma_h|\hat{Y}_R-\mathbf{C}_i(b_m^R=0)|-\sqrt{2}\sigma_\beta}{2\sigma_h|\hat{Y}_R-\mathbf{C}_i(b_m^R=0)|+\sqrt{2}\sigma_\beta}\right)}{\Gamma(3.5)(2\sigma_h|\hat{Y}_R-\mathbf{C}_i(b_m^R=0)|+\sqrt{2}\sigma_\beta)^3}\right\}\underset{1}{\overset{0}{\gtrless}}\\ &\sum_{i=0}^{15}\left\{\frac{8\sqrt{\pi}\sigma_h\sigma_\beta^2\,{}_2F_1\left(3,\frac{1}{2};3\frac{1}{2};\frac{2\sigma_h|\hat{Y}_R-\mathbf{C}_i(b_m^R=1)|-\sqrt{2}\sigma_\beta}{2\sigma_h|\hat{Y}_R-\mathbf{C}_i(b_m^R=1)|+\sqrt{2}\sigma_\beta}\right)}{\Gamma(3.5)(2\sigma_h|\hat{Y}_R-\mathbf{C}_i(b_m^R=1)|+\sqrt{2}\sigma_\beta)^3}\right\},\forall\ m=0,1,\end{aligned} \tag{6.56}$$

6.7.1.2 At the Broadcast

The ML detector at the BC stage can be computed by utilizing the derived distribution in Chapter 4 for the equalized received noise samples. The ML in the case of MCAIN model, BI noise and their combination can be computed by utilizing (4.82), while in the case of BGMIN model and combined BI noise and BGMIN model can be computed by utilizing (4.84).

6.7.2 LLR Computations

6.7.2.1 At the Relay

The LLR computations at the relay using 4-QAM constellation for the new denoise mapping presented in Table 6.1 can be computed in the case of B-LDPC codes as

$$\mathrm{LLR}(b_m^R) = \log \frac{\sum_{i=0}^{15} \left\{ \frac{8\sqrt{\pi}\sigma_h\sigma_\beta^2 \ {}_2F_1\left(3,\frac{1}{2};3\frac{1}{2};\frac{2\sigma_h|\hat{Y}_R-\mathbf{C}_i(b_m^R=0)|-\sqrt{2}\sigma_\beta}{2\sigma_h|\hat{Y}_R-\mathbf{C}_i(b_m^R=0)|+\sqrt{2}\sigma_\beta}\right)}{\Gamma(3.5)(2\sigma_h|\hat{Y}_R-\mathbf{C}_i(b_m^R=0)|+\sqrt{2}\sigma_\beta)^3} \right\}}{\sum_{i=0}^{15} \left\{ \frac{8\sqrt{\pi}\sigma_h\sigma_\beta^2 \ {}_2F_1\left(3,\frac{1}{2};3\frac{1}{2};\frac{2\sigma_h|\hat{Y}_R-\mathbf{C}_i(b_m^R=1)|-\sqrt{2}\sigma_\beta}{2\sigma_h|\hat{Y}_R-\mathbf{C}_i(b_m^R=1)|+\sqrt{2}\sigma_\beta}\right)}{\Gamma(3.5)(2\sigma_h|\hat{Y}_R-\mathbf{C}_i(b_m^R=1)|+\sqrt{2}\sigma_\beta)^3} \right\}}, \ \forall\, m = 0, 1. \tag{6.57}$$

Moreover, the LLRs at the relay can be computed for NB-LDPC codes as

$$F_{q,k}^a = \log \frac{\frac{8\sqrt{\pi}\sigma_h\sigma_\beta^2 \ {}_2F_1\left(3,\frac{1}{2};3\frac{1}{2};\frac{2\sigma_h|\hat{Y}_R-\mathbf{C}(a+1)|-\sqrt{2}\sigma_\beta}{2\sigma_h|\hat{Y}_R-\mathbf{C}(a+1)|+\sqrt{2}\sigma_\beta}\right)}{\Gamma(3.5)(2\sigma_h|\hat{Y}_R-\mathbf{C}(a+1)|+\sqrt{2}\sigma_\beta)^3}}{\frac{8\sqrt{\pi}\sigma_h\sigma_\beta^2 \ {}_2F_1\left(3,\frac{1}{2};3\frac{1}{2};\frac{2\sigma_h|\hat{Y}_R-\mathbf{C}(1)|-\sqrt{2}\sigma_\beta}{2\sigma_h|\hat{Y}_R-\mathbf{C}(1)|+\sqrt{2}\sigma_\beta}\right)}{\Gamma(3.5)(2\sigma_h|\hat{Y}_R-\mathbf{C}(1)|+\sqrt{2}\sigma_\beta)^3}}, \ a \in \mathbb{F}_q \backslash \{0\}. \tag{6.58}$$

Furthermore, the LLRs at the relay can be computed for TCs by taking the negative sign of the LLRs of LDPC codes expressed as

$$\mathrm{LLR}(b_m^R) = -\log \frac{\sum_{i=0}^{15} \left\{ \frac{8\sqrt{\pi}\sigma_h\sigma_\beta^2 \ {}_2F_1\left(3,\frac{1}{2};3\frac{1}{2};\frac{2\sigma_h|\hat{Y}_R-\mathbf{C}_i(b_m^R=0)|-\sqrt{2}\sigma_\beta}{2\sigma_h|\hat{Y}_R-\mathbf{C}_i(b_m^R=0)|+\sqrt{2}\sigma_\beta}\right)}{\Gamma(3.5)(2\sigma_h|\hat{Y}_R-\mathbf{C}_i(b_m^R=0)|+\sqrt{2}\sigma_\beta)^3} \right\}}{\sum_{i=0}^{15} \left\{ \frac{8\sqrt{\pi}\sigma_h\sigma_\beta^2 \ {}_2F_1\left(3,\frac{1}{2};3\frac{1}{2};\frac{2\sigma_h|\hat{Y}_R-\mathbf{C}_i(b_m^R=1)|-\sqrt{2}\sigma_\beta}{2\sigma_h|\hat{Y}_R-\mathbf{C}_i(b_m^R=1)|+\sqrt{2}\sigma_\beta}\right)}{\Gamma(3.5)(2\sigma_h|\hat{Y}_R-\mathbf{C}_i(b_m^R=1)|+\sqrt{2}\sigma_\beta)^3} \right\}}, \ \forall\, m = 0, 1. \tag{6.59}$$

While the sub-optimal LLRs in the case of B-LDPC codes and NB-LDPC codes can be computed based on a Gaussian distribution as

$$\mathrm{LLR}(b_m^R) = \log \frac{\sum_{i=0}^{15} e^{-\left(\frac{|\hat{Y}_R-\mathbf{C}_i(b_m^R=0)|^2}{\sigma_w^2}\right)}}{\sum_{i=0}^{15} e^{-\left(\frac{|\hat{Y}_R-\mathbf{C}_i(b_m^R=1)|^2}{\sigma_w^2}\right)}}, \ \ ,\forall\, m = 0, 1, \tag{6.60}$$

$$F_{q,k}^a = \log \frac{e^{-\left(\frac{|\hat{Y}_k-\mathbf{C}(a+1)|^2}{\sigma_w^2}\right)}}{e^{-\left(\frac{|\hat{Y}_k-\mathbf{C}(1)|^2}{\sigma_w^2}\right)}}, \ a \in \mathbb{F}_q \backslash \{0\}. \tag{6.61}$$

and in the case of TCs can be computed as

$$\mathrm{LLR}(b_m^R) = \log \frac{\sum_{i=0}^{15} e^{-\left(\frac{|\hat{Y}_R - \mathbf{C}_i(b_m^R=1)|^2}{\sigma_w^2}\right)}}{\sum_{i=0}^{15} e^{-\left(\frac{|\hat{Y}_R - \mathbf{C}_i(b_m^R=0)|^2}{\sigma_w^2}\right)}}, \quad \forall\, m = 0, 1. \tag{6.62}$$

6.7.2.2 At the Broadcast

The LLR values at the BC stage can be computed by utilizing the LLR computations in Chapter 5 based on the derived equalized noise samples in Chapter 4. In the case of optimal/suboptimal detectors, the LLR values can be computed by utilizing (5.40)/(5.41) in the case of B-LDPC code, (5.42)/(5.43) in the case of NB-LDPC code and (5.44)/(5.45) in the case of TC.

6.8 Simulation Results

6.9 Investigation of the PDFs

To verify the validity of the derived PDF at the relay in (6.11), the comparison between the histogram plots for the real part of the empirical and theoretical derived noise PDF, are shown in Fig. 6.3-Fig. 6.7. The histogram has been plotted in the presence of different scenarios of MCAIN, BGMIN, BI noise, combined MCAIN and BI noise and finally combined BGMIN and BI noise over two multipath PLC channels of length 150 m with 4 path and 15 path modelled by modified Zimmermann simulation models [11], where the channel parameters of 15 path are presented in Table 4.1 and for 4 path are listed in Table 6.2 [8, 31]. The simulation parameters are set as follows: $A = 10^{-2}$ and $\rho = 10^{-1}, 10^{-2}, 10^{-3}$ for the case of MCAIN model, $\alpha = 0.3, 0.1, 0.01$ and $\tilde{\rho} = 100$ for the case of BGMIN model and $m = 0.5, 0.7$ and $\Omega = 1$ for the case of the BI noise at SNR = 20 dB.

Table 6.2: Parameters of the 4-path model.

Attenuation parameters		
$k = 1$	$a_0 = 0$	$a_1 = 7.8 \times 10^{-10}$
Path-parameters		
i	g_i	$d_i(m)$
1	0.64	200
2	0.38	222.4
3	-0.15	411
4	0.05	490

It can be seen from the Fig. 6.3 in the presence of IN modelled using the MCAIN model, for a constant $A = 0.01$,as $\rho = 10^{-3}, 10^{-2}, 10^{-1}$ increases, the variance of $\sigma_\beta^2 = \sigma_A^2 = 2.5024, 0.2525, 0.0275$ utilizing (4.13) decreases, respectively. Thus, the PDFs level is increased.

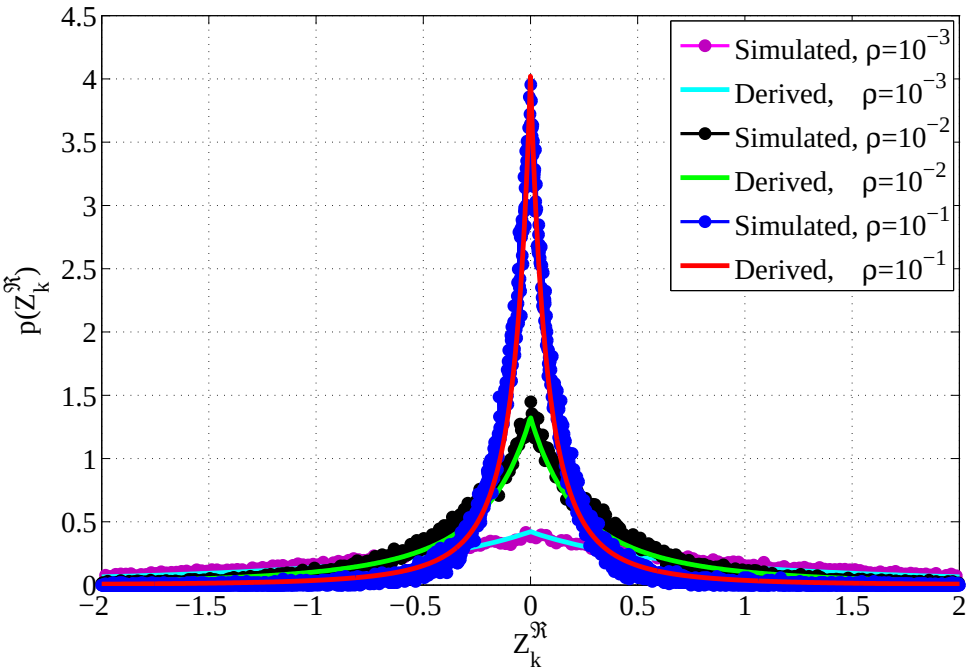

Figure 6.3: Histogram plot at the relay in the presence of IN modelled by MCAIN with $A = 0.01$ over 15-path PLC channel by utilizing the derived PDF in (6.11) where $\sigma_\beta^2 = \sigma_A^2$ at SNR = 20 dB.

While it can be seen from Fig. 6.4 in the presence of IN modelled using the BGMIN model, for a constant $\tilde{\rho} = 100$ and $\alpha = 0.3, 0.1, 0.01$, the variance of $\sigma_\beta^2 = \sigma_N^2 = 0.155, 0.055, 0.01$ using (5.3) decreases is decreasing, respectively. Thus, the PDFs level is increased.

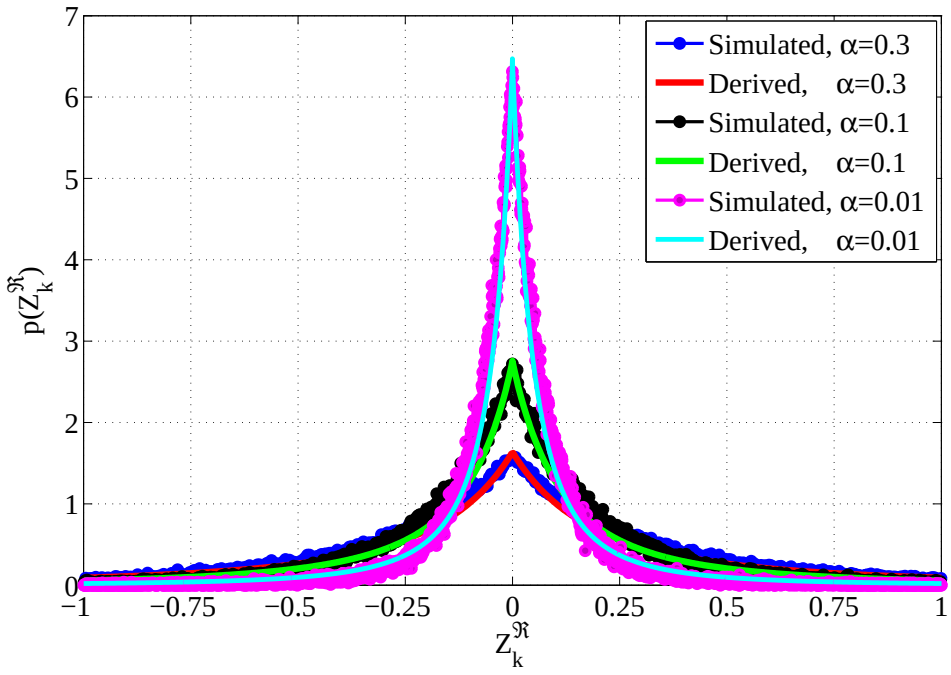

Figure 6.4: Histogram plot at the relay in the presence of IN modelled by BGMIN with $\tilde{\rho} = 100$ over 15-path PLC channel utilizing the derived PDF in (6.11) where $\sigma_\beta^2 = \sigma_N^2$ at SNR = 20 dB.

Moreover, it is observed from Fig. 6.5 in the presence of Nakagami-m BI noise with $m = 0.5, 0.7$ and $\Omega = 1$, the theoretical derived noise distribution in (6.11) $\sigma_\beta^2 = \sigma_b^2 = 0.5, 0.5$ computed using (4.62), respectively, are closely matched with their simulated distributions.

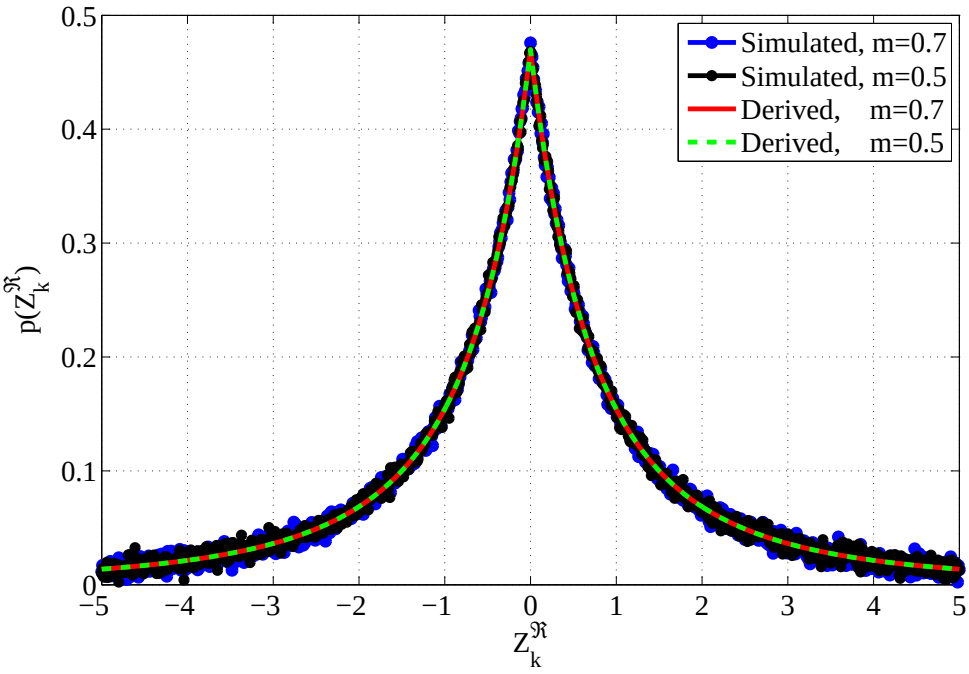

Figure 6.5: Histogram plot at the relay in the presence of Nakagami-m BI noise with $\Omega = 1$ over 15-path PLC channel by utilizing the derived PDF in (6.11) with $\sigma_\beta^2 = \sigma_b^2$.

Furthermore, it can be seen from the Fig. 6.6 in the presence of combined BI noise and MCAIN model that, as $\rho = 10^{-3}, 10^{-2}, 10^{-1}$ increases, the variance of $\sigma_\beta^2 = \sigma_b^2 + \sigma_A^2 = 3.0026, 0.7526, 0.5275$ decreases, respectively, for constant $A = 0.01$. Thus, the PDFs level increases.

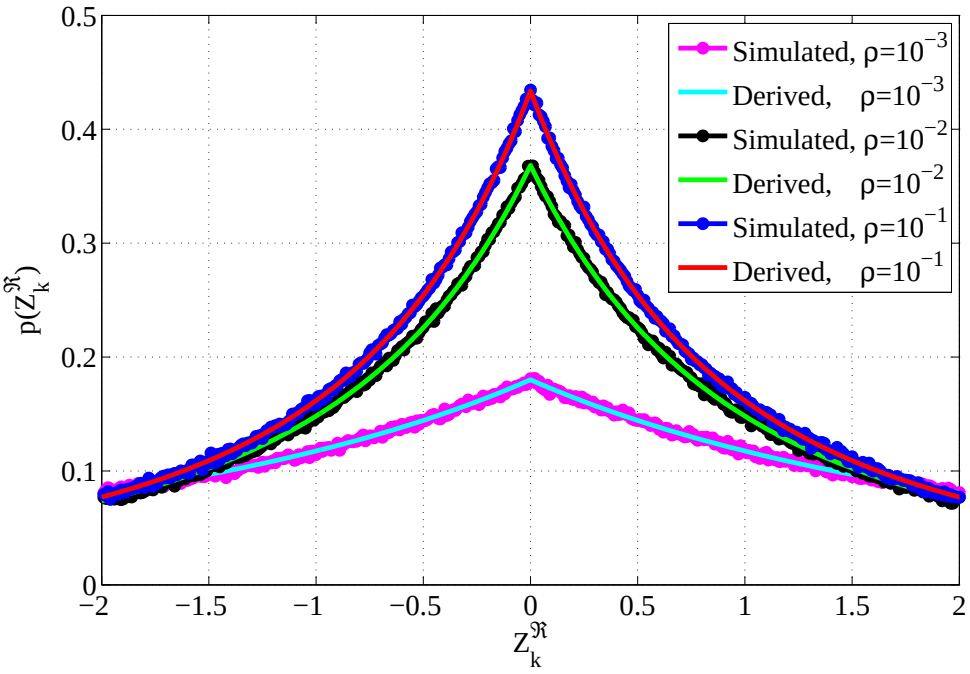

Figure 6.6: Histogram plot at the relay in the presence of combined Nakagami-m BI noise with $m = 0.7$ and MCAIN with $A = 10^{-2}$ over 15-path PLC channel at SNR = 20 dB.

Finally, it can be seen from the Fig. 6.6 in the presence of the combined BI noise and BG-MIN model that, as $\alpha = 0.3, 0.1, 0.01$ decreases, the variance of $\sigma_\beta^2 = \sigma_b^2 + \sigma_N^2 = 0.655, 0.555, 0.5099$ decreases, respectively, for a constant $\tilde{\rho} = 100$. Thus, the PDFs level is increased. It can be observed that the closed-form PDFs are closely matched with their corresponding empirically obtained distributions at the relay. Similar results can be obtained when utilizing the imaginary part. It can conclude that due to the orthogonality, the real and imaginary components of the noise exhibit identical statistical behaviours.

6.9.1 Performance Comparison of IR-B/NB-LDPC Versus Conventional IR-B-LDPC for COFDM-PLNC Systems

The BER performance of 4-QAM constellation for the OFDM-PLNC system has been compared by utilizing the rate-1/2 (1008,504) IR-B-LDPC code versus the rate-1/2 (252,126) IR-NB-LDPC code over $\mathbb{F}_{16}$, the number of decoding iterations was set to 50. The multipath PLC channels of 15-path and 4-path illustrated in table (4.1) and table (6.2) have been utilized, in

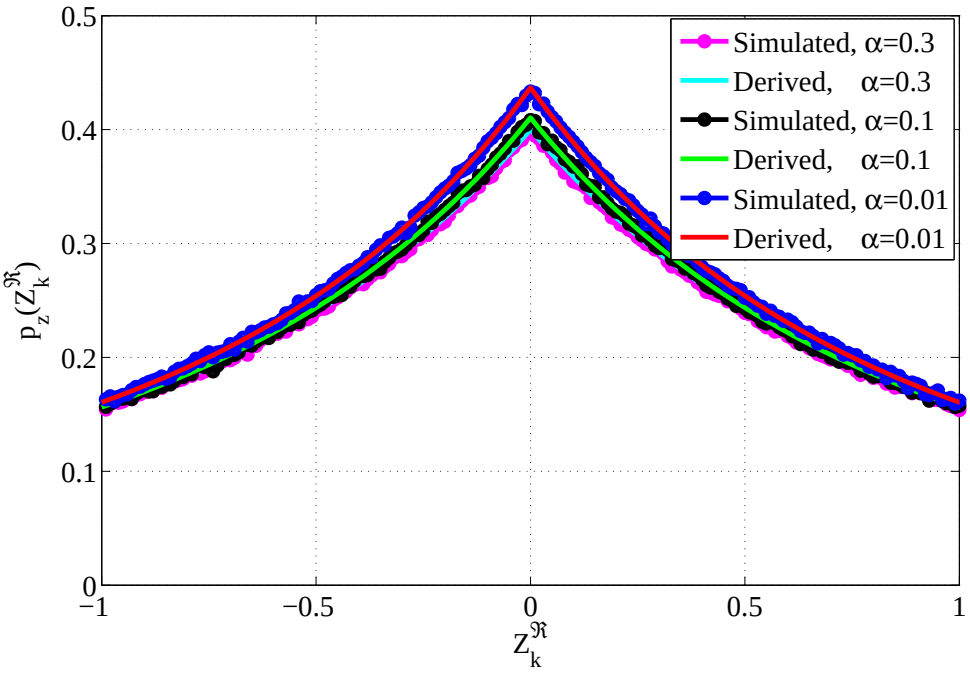

Figure 6.7: Histogram plot at the relay in the presence of combined Nakagami-m BI noise with $m = 0.7$ and BGMIN with $\tilde{\rho} = 100$ over 15-path PLC channel at SNR = 20 dB.

the presence of combined BI noise with $m = 0.7$ and IN modelled by the BGMIN model with $\alpha = 0.3, 0.1$ and $\tilde{\rho} = 100$, i.e., the IN power is 100 times higher than the Gaussian noise power, or by the MCAIN model with $A = 0.01$ and $\rho = 10^{-1}, 10^{-3}$, i.e., the Gaussian noise power is 10 and 1000 times less than the Gaussian noise power.

Fig. 6.8 investigates the performance of IR-B-LDPC-COFDM-PLNC and IR-NB-LDPC-COFDM-PLNC by utilizing the new mapping method at the relay where the LLRs are is computed based on the derived PDFs at the relay using (6.57) and (6.58) and at the end nodes using (5.40) and (5.42), respectively. The performance of IR-B/NB-LDPC-COFDM-PLNC systems is compared against the performance of a conventional system that use a blanker IN mitigation method with a blanking threshold computed based on (6.48) at the relay and (4.109) at the end nodes in the case of the combined BI noise and MCAIN model, and (6.54) at the relay and (4.122) at the end nodes in the case of the combined BI noise and BGMIN model, where the LLRs are computed based on the Gaussian PDF at the relay using (6.60) and at the end nodes using (5.41). All systems performance has been compared against the uncoded-COFDM-PLNC system. It can be seen from the figures that the proposed IR-B/NB-LDPC-COFDM-PLNC systems utilizing derived PDFs at the relay node and at the end nodes achieve superior BER performance compared to the conventional system for all scenarios of combined NGN for all values of $\frac{E_b}{N_0}$. Moreover, the IR-NB-LDPC-COFDM-PLNC system achieves superior BER per-

formance than the other systems even with the high impact of IN for all scenarios of NGN but with higher decoding complexity.

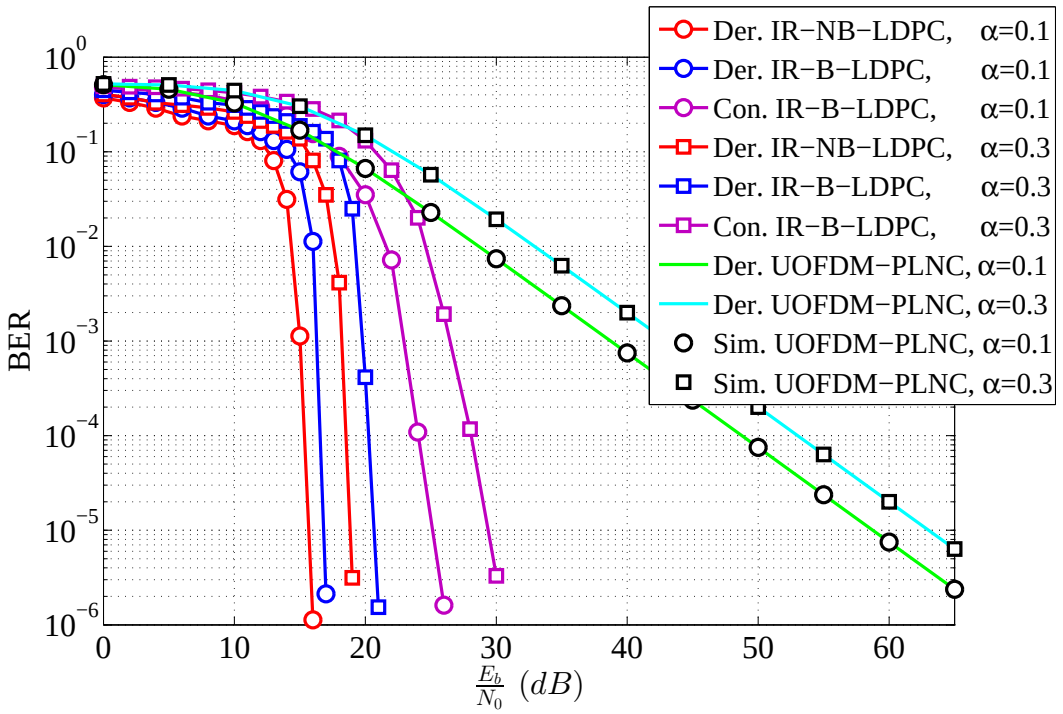

(a) Combined BI noise with $m = 0.7$ and BGMIN with $\tilde{\rho} = 100$.

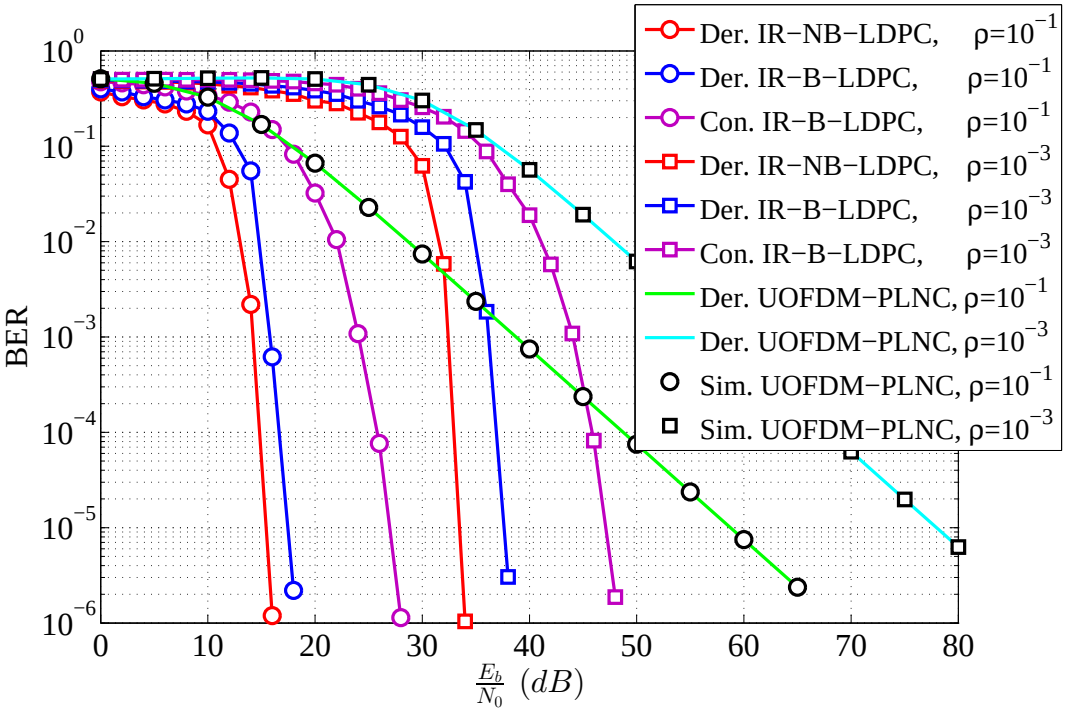

(b) Combined BI noise with $m = 0.7$ and MCAIN with $A = 0.01$.

Figure 6.8: Performance of the derived IR-B/NB-LDPC-COFDM-PLNC versus conventional IR-B-LDPC-COFDM-PLNC systems over PLC channels.

Table 6.3 shows the coding gains (CGs) of the derived IR-B/NB-LDPC-COFDM-PLNC systems versus conventional IR-B-LDPC-COFDM-PLNC system at $P_e = 10^{-5}$.

Table 6.3: CGs of the derived IR-B/NB-LDPC-COFDM-PLNC systems versus conventional IR-B-LDPC-COFDM-PLNC system at $P_e = 10^{-5}$.

$P_e = 10^{-5}$		Coding Gains in (dB)		
		Derived IR-NB-LDPC	Derived IR-B-LDPC	Conventional IR-B-LDPC
BI+BGMIN	$\alpha = 10^{-1}$	44	42.5	34
$m = 7 \times 10^{-1}$	$\alpha = 3 \times 10^{-1}$	45	43	33
BI+MCAIN	$\rho = 10^{-1}$	44.5	42	32
$m = 7 \times 10^{-1}$	$\rho = 10^{-3}$	45	41	31

6.9.2 Performance Comparison and Average Upper Bounds of T-COFDM-PLNC System Versus Conventional T-COFDM-PLNC System

The BER performance of 4-QAM constellation for the COFDM-PLNC system has been investigated by utilizing a rate-1/2 TC constructed using the generator in octal form $(1, 5/7, 5/7)_8$ with 50 decoding iterations, over two multipath PLC channels of a length of 150 m with 4-path and 15-path and modelled using the modified Zimmermann simulation model [11].

Fig. 6.9 investigates the performance of T-COFDM-PLNC by utilizing the new mapping method at the relay where the LLRs are computed from the derived PDFs at the relay using (6.59) and at the end nodes using (5.44) versus the uncoded OFDM-PLNC system over PLC channels in the presence of combined noise. The system performance has been compared against the performance of a conventional T-COFDM-PLNC that uses a blanker IN mitigation method with a blanking threshold computed based on (6.48) at the relay and (4.109) at the end nodes in the case of the combined BI noise and MCAIN model, and (6.54) at the relay and (4.122) at the end nodes in the case of the combined BI noise and BGMIN model, where the LLRs are computed from the Gaussian PDF at the relay using (6.62) and at the end nodes using (5.45). It can be seen from the figures that the proposed system utilizing the derived PDFs at the relay node and at the end nodes achieves superior BER performance compared to the traditional T-COFDM-PLNC system, even with the high impact of impulsive noise. Moreover, it is worth noting that the derived AUB achieves a close match with the simulated performance. Table 6.4 shows the CGs of the derived versus conventional T-COFDM-PLNC at $P_e = 10^{-5}$.

Table 6.4: Derived versus conventional CGs for T-COFDM-PLNC systems.

$P_e = 10^{-5}$		Coding gain in (dB)	
		Derived TC	Conventional TC
BI+BGMIN	$\alpha = 10^{-1}$	40	31
$m = 7 \times 10^{-1}$	$\alpha = 3 \times 10^{-1}$	41	30
BI+MCAIN	$\rho = 10^{-1}$	40	29
$m = 7 \times 10^{-1}$	$\rho = 10^{-3}$	41	28

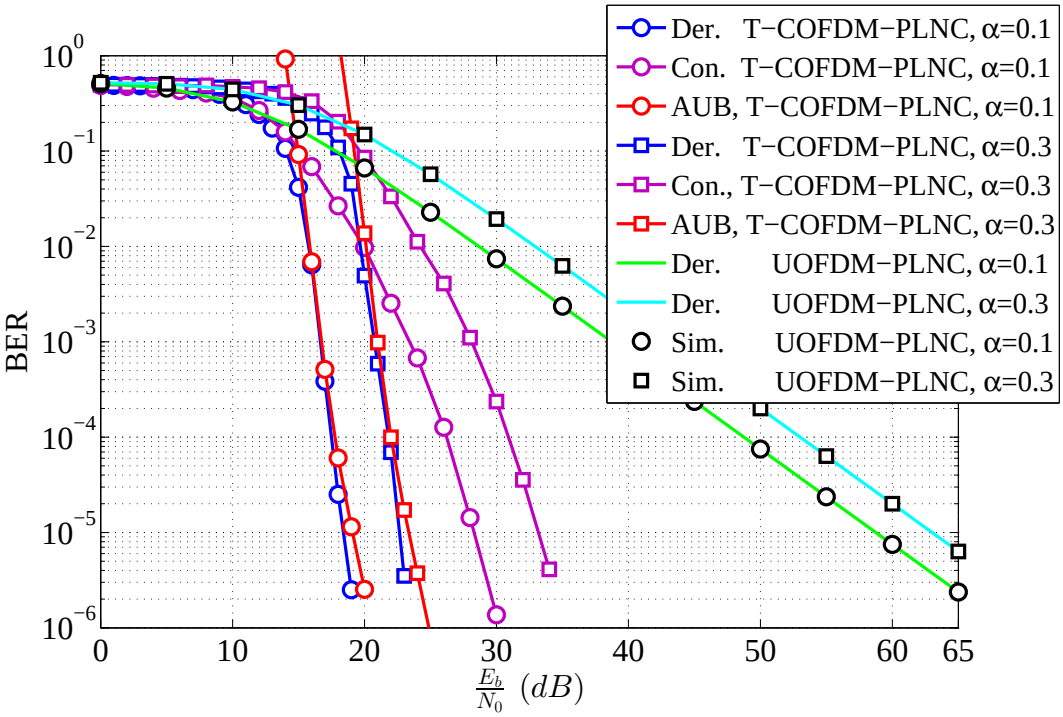

(a) Combined BI noise with $m = 0.7$ and BGMIN with $\tilde{\rho} = 100$.

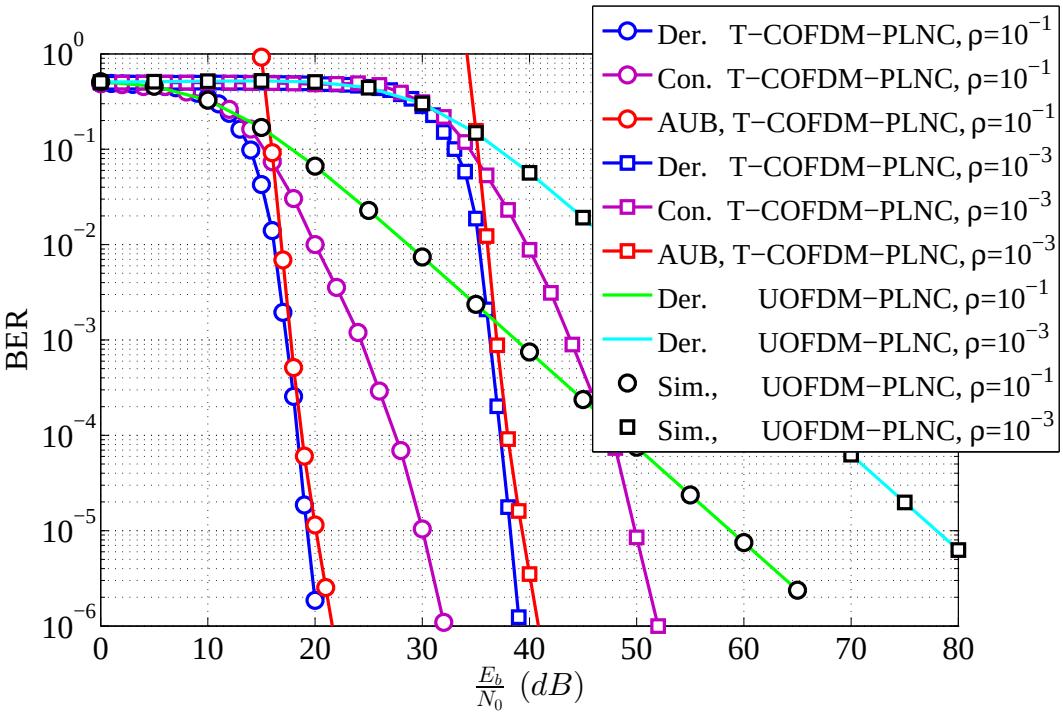

(b) Combined BI noise with $m = 0.7$ and MCAIN with $A = 0.01$.

Figure 6.9: Performance of the derived vs conventional T-COFDM-PLNC systems over PLC channels.

6.10 Summary of the Chapter

In this chapter, the performance comparisons of IR-B-LDPC code, IR-NB-LDPC code and TC for COFDM-PLNC systems over multipath PLC channels in the presence of NGN have been made and analyzed. Two multipath PLC channels have been utilized for a 150 m channel length

modelled by 15-path and 4-path. The closed form distribution based on the novel mapping method at the relay node has been derived and analyzed. Additionally, closed-form expressions of the E2E-BER, E2E-AUB and optimal thresholds are derived and presented. The simulation results obtained via Monte-Carlo simulation have confirmed the feasibility of the derived PDFs for the IR-B-LDPC code, IR-NB-LDPC code and TC for COFDM-PLNC systems and were subsequently used to improve the LLRs calculation for the iterative decoder. The performance of the proposed coded systems outperformed the conventional system that used the blanker IN mitigation method and LLRs computed based on Gaussian distribution for different scenarios of combined BI noise and IN modulated either by BGMIN or MCAIN model.

Chapter 7

Conclusions and Future Work

7.1 Conclusions

This thesis focused on communication over the existing PLs grid. PLC is a technology that allows transmitting communication signals along with electrical current power supply network. The main advantage of PLC is that it does not need any new infrastructure, hence reducing the cost. The PL grid is used to connect all digital appliances by wiring inside the building. This wiring is originally designed to carrying the electrical power, leading to PLC channel characteristics being very harsh for communication signals due to multipath frequency selective fading, attenuation and impulsive noise. The Zimmermann and Dostert model has been used for modelling PLC channels with a small number of parameters. On the other hand, the main sources of noise in the PLC channel are the BI noise modelled by Nakagami-m distribution and the IN modelled either by the MCAIN model or BGMIN model. Therefore, to achieve reliable communication over the PLC channel, these factors have to be well understood.

The multipath effects and impulsive noise are the dominant performance degradation factors in PLC. This is due to the channel frequency selectivity and the high PSD of IN, which exceeds the PSD of the BI noise by 10-15 dB and may reach up to 50 dB with random occurrence rates over a short time duration. To combat both of them, OFDM has been adopted in this thesis. OFDM is usually used with a CP to minimize effects of ISI caused by the frequency-selective multipath. Moreover, OFDM provides higher robustness against IN than SC modulation methods. It spreads the effect of IN over multiple sub-carriers after DFT operations at the receiver, hence, it requires only a simple single-tap ZF equalizer at the receiver.

For reliable communication, the challenges of the PLC channel in the presence of NGN should be addressed. This thesis focuses on deriving effective noise distributions over different

scenarios of individual and combined background noise and impulsive noise over PLC channels. The effective noise distributions are derived for the OFDM system and the OFDM-PLNC system based on the ratio of complex-valued RVs at the ZF equalizer output and at the proposed mapping method which utilizes two ZF equalizers at the relay.

Different forward error correcting codes have been used in this thesis such as IR-B-LDPC code, IR-NB-LDPC code and TC for the COFDM system and for the COFDM-PLNC system in order to reduce the negative impacts of NGN and to achieve high coding gain. The significant improvements in the BER performance over PLC channels have been achieved by utilizing optimal LLR computations based on the exact noise distributions. In this respect, the BER performance of the uncoded and coded systems are analysed and evaluated over PLC channels in the presence of different scenarios of NGN for high order M-QAM constellations.

Monte-Carlo simulations show the proposed IR-B/NB-LDPC-COFDM and T-COFDM systems that utilize 4096-QAM constellation outperform the conventional system over PLC channel. Numerical results demonstrate significant performance improvements based on CG computation. For example in the case of point-to-point, the proposed IR-B-LDPC-OFDM system outperforms the conventional IR-B-LDPC-OFDM system by 12.5 and 13.5 dB and can achieve CG about 34 and 34.5 dB for $\alpha = 0.1, 0.3$, respectively, for a constant $\tilde{\rho} = 100$. The derived system have been achieved 111 Mbps higher data throughput than the conventional system. Moreover, the derived IR-NB-LDPC-OFDM system outperforms the conventional system by 18 and 19 dB and can achieve CG about 40 and 39 dB for $\alpha = 0.1, 0.3$, respectively, for a constant $\tilde{\rho} = 100$. It can be achieved maximum data throughput of 1000 Mbps over $\mathbb{F}_{16}$ for the same $\frac{E_b}{N_0}$, BER and BW. Furthermore, the derived T-COFDM system utilizes 8192-QAM constellation outperform the conventional system. Both systems achieves CG approximately 33.1 and 28.5 dB and 33.4 and 29 dB for $\rho = 10^{-1}, 10^{-3}$, respectively, at BER=10^{-5}. On the other hands, the results are bounded within less than 1 dB from the AUB results, requiring fewer iterations to converge according to EXIT chart analyses.

Another example in the case of physical layer network coding, the proposed IR-B/NB-LDPC-COFDM-PLNC systems have superior BER performance compared to the conventional IR-B-LDPC-COFDM-PLNC system for all values of $\frac{E_b}{N_0}$. The CGs were 44, 42.5 and 34 dB by utilizing the derived IR-NB-LDPC-COFDM-PLNC, the derived IR-B-LDPC-COFDM-PLNC and the conventional IR-B-LDPC-COFDM-PLNC systems, respectively, at BER=10^{-5} in the presence of combined BI noise with $m = 0.7$ and BGMIN model with $\alpha = 0.1$ and $\tilde{\rho} = 100$. While, the CGs were 44.5, 42 and 32 dB by utilizing the derived IR-NB-LDPC-COFDM-PLNC, the derived IR-B-LDPC-COFDM-PLNC and the conventional IR-B-LDPC-COFDM-

PLNC systems, respectively, at BER=10^{-5} in the presence of combined BI noise with $m = 0.7$ and MCAIN model with $A = 0.01$ and $\rho = 10^{-3}$. Moreover, the proposed T-COFDM-PLNC system outperforms the conventional T-COFDM-PLNC system for all values of $\frac{E_b}{N_0}$. The CGs were 40 and 31 dB by utilizing the derived T-COFDM-PLNC and the conventional T-COFDM-PLNC systems, respectively, at BER=10^{-5} in the presence of combined BI noise with $m = 0.7$ and BGMIN model with $\alpha = 0.1$ and $\tilde{\rho} = 100$. While, the CGs were 40 and 29 dB by utilizing the derived T-COFDM-PLNC and the conventional T-COFDM-PLNC systems, respectively, at BER=10^{-5} in the presence of combined BI noise with $m = 0.7$ and MCAIN model with $A = 0.01$ and $\rho = 10^{-3}$.

The main works of the thesis are summarized as follows

- Chapter 4: The analysis and evaluation of BER performance of the uncoded OFDM system based on derived effective noise distributions at the ZF equalizer output over PLC channels in the presence of NGN was presented. The derived systems in the presence of individual and combined Nakagami-m BI noise and IN modelled either by the MCAIN model and BGMIN model were investigated. The ML detector has been derived based on exact noise distributions to improve the degradation in the BER performance by reducing the $\frac{E_b}{N_0}$ needed for communication over PLC channel, hence, increasing the data throughput. Moreover, the ML detector and thresholds optimization based on the derived PDFs have improved the BER performance of the conventional system in the presence of different scenarios of NGN.

- Chapter 5: The performance of IR-B-LDPC code with SPA iterative, IR-NB-LDPC code with SL-FFT iterative decoding algorithm and TC with iterative Max-Log-MAP decoding algorithm have been proposed for COFDM system to overcome the harsh environment of PLC channels. The sparse parity check matrix $\mathbf{H}$ of the IR-NB-LDPC code and the IR-B-LDPC code have been constructed using the PEG algorithm, while the TC has been generated using the parallel concatenation of two recursive systematic convolutional codes. The decoders performance has been improved by computing LLRs based on two scenarios: the first scenario has been computed by utilizing the distribution of the received signal at the OFDM demodulator output based on Euclidean Distance, while the second scenario has been computed based on the derived complex-valued ratio distributions of the noise samples at the ZF equalizer output in Chapter 4. Monte-Carlo simulation results have been obtained by utilizing derived PDFs which demonstrate significant performance improvement compared to the conventional receiver over PLC channels in the presence

of NGN, reducing the number of iterations of iterative decoding of convergence and increasing the data throughput compared to conventional COFDM system. Moreover, the IR-NB-LDPC code over $\mathbb{F}_{16}$ out performs the IR-B-LDPC code and TC and achieves a higher data throughput. Furthermore, the derived systems are very close to the AUBs in the case of T-COFDM system.

- Chapter 6: The BER performance of IR-B/NB-LDPC and TC for the COFDM-PLNC system over PLC channels have been presented in this chapter. For the MA stage, the LLRs have been computed by utilizing the new derived distribution at the relay node based on the novel mapping method in the presence of different scenarios of NGN, while, the LLRs have been computed by utilizing the derived PDFs in Chapter 4 in BC stage. Moreover, the E2E-BER, E2E-AUB and the thresholds optimization have been derived in this chapter. Monte-Carlo simulation results of the proposed IR-B/NB-LDPC and TC for COFDM-PLNC system based on the derived PDFs have superior BER performance in the presence of IN and outperform the conventional system in all scenarios of NGN, which makes the derived systems very attractive for practical purposes to mitigate the high impact of NGN over PLC channels.

- Chapter 7: This chapter concludes the important findings with new research directions for future works.

7.2 Future Research Work

The following suggestions can be considered in future research based on the work reported in this dissertation.

- To increase the systems reliability and data throughput in Chapter 5, further BER performance improvement can be achieved by increasing the diversity or multiplexing by adopting multiple-input multiple-output (MIMO) for COFDM system over PLC channels.

- In this thesis, it was assumed that perfect channel and noise parameters are available at the receiver. This implies that exact noise derived distributions can be achieved in the receiver. The channel and the noise in practice may vary over time and they need to be estimated. The studies can be extended by assuming imperfect knowledge of the channel and noise at the receiver, in which the channel can be estimated by any estimation methods

such as pilot estimation. The Middleton A parameters can be estimated using [6] and for the Gaussian mixture model using [166].

- The low complexity SL-FFT decoding algorithm with LLRs computed based on derived PDFs can achieve lower BER and lower decoding iterations which demonstrates the possibility of implementing on Digital Signal-Processing (DSP) and FPGA platforms.

- In Chapter 4 of this thesis, the derived NGN distributions at the ZF equalizer output can be extended to more advanced channel equalization techniques such as minimum mean square error (MMSE) to improve the BER of the systems. This issue can be further researched.

- Further research could also be done on the IR-NB-LDPC code for OFDM and OFDM-PLNC systems over PLCs, by computing the EXIT chart and AUB for the new derived PDFs.

- Applying the IN mitigation method in the frequency domain for OFDM and OFDM-PLNC systems over PLCs based on derived the new optimal threshold for improving the BER performance of both systems.

- Design a relay that can transmit and receive at the same time, i.e. full-duplex transmission.

- Another interesting area of research would be the investigation of the performance of the derived system with time interleaver. A complete BER analysis and performance comparison of different coding systems need to be explored.

References

[1] H. A. Latchman, S. Katar, L. Yonge, and S. Gavette, *Homeplug AV and IEEE 1901: A handbook for PLC designers and users*. John Wiley & Sons, 2013.

[2] H. Meng, Y. L. Guan, and S. Chen, "Modeling and analysis of noise effects on broadband power-line communications," *IEEE Trans. Power Del.*, vol. 20, no. 2, pp. 630–637, April 2005.

[3] Y. Kim, S. Choi, and H. M. Oh, "Closed-form expression of Nakagami-like background noise in power-line channel," *IEEE Trans. Power Del.*, vol. 23, no. 3, pp. 1410–1412, July 2008.

[4] M. Ghosh, "Analysis of the effect of impulse noise on multicarrier and single carrier QAM systems," *IEEE Trans. commun.*, vol. 44, no. 2, pp. 145–147, Feb. 1996.

[5] D. Middleton, "Statistical-physical models of electromagnetic interference," *IEEE Trans. Electromagn. Compat.*, vol. EMC-19, no. 3, pp. 106–127, 1977.

[6] ——, "Procedures for determining the parameters of the first-order canonical models of class A and class B electromagnetic interference [10]," *IEEE Trans. Electromagn. Compat.*, vol. EMC-21, no. 3, pp. 190–208, Aug 1979.

[7] ——, "Canonical and quasi-canonical probability models of class A interference," *IEEE Trans. Electromagn. Compat.*, vol. EMC-25, no. 2, pp. 76–106, 1983.

[8] M. Zimmermann and K. Dostert, "A multipath model for the powerline channel," *IEEE Trans. Commun.*, vol. 50, no. 4, pp. 553–559, Apr. 2002.

[9] S. Galli, A. Scaglione, and Z. Wang, "For the grid and through the grid: The role of power line communications in the smart grid," *Proceedings of the IEEE*, vol. 99, no. 6, pp. 998–1027, June 2011.

[10] M. Hazen, "The technology behind Homeplug AV powerline communications," *IEEE Comput.*, vol. 41, no. 6, pp. 90–92, 2008.

[11] H. Ferreira, L. Lampe, J. Newbury, and T. Swart, *Power line communications: Theory and applications for narrowband and broadband communications over power lines*. John Wiley & Sons Ltd, 2010.

[12] H. Hrasnica, A. Haidine, and R. Lehnert, *Broadband powerline communications: Network design*. John Wiley & Sons, 2005.

[13] K. Dostert, *Powerline communications*. Inc., Upper Saddle River, NJ 07458: Prentice Hall PTR,, 2001.

[14] S. Gorshe, A. Raghavan, T. Starr, and S. Galli, *Broadband access: Wireline and wireless-alternatives for internet services*. John Wiley & Sons, 2014.

[15] S. Galli and O. Logvinov, "Recent developments in the standardization of power line communications within the IEEE," *IEEE Commun. Mag.*, vol. 46, no. 7, pp. 64–71, July 2008.

[16] S. Galli, H. Koga, and N. Kodama, "Advanced signal processing for PLCs: Wavelet-OFDM," in *2008 IEEE International Symposium on Power Line Communications and Its Applications*, April 2008, pp. 187–192.

[17] Homeplug AV white paper, [Online]. Available at, $https : //www.solwise.co.uk/downloads/files/hpav - white - paper\_050818.pdf$.

[18] M. Tlich, A. Zeddam, F. Moulin, and F. Gauthier, "Indoor power-line communications channel characterization up to 100 MHz-part I: One-parameter deterministic model," *IEEE Trans. Power Del.*, vol. 23, no. 3, pp. 1392–1401, July 2008.

[19] ——, "Indoor power-line communications channel characterization up to 100 MHz-part II: Time-frequency analysis," *IEEE Trans. Power Del.*, vol. 23, no. 3, pp. 1402–1409, July 2008.

[20] S. Goldfisher and S. Tanabe, "IEEE 1901 access system: An overview of its uniqueness and motivation," *IEEE Commun. Mag.*, vol. 48, no. 10, pp. 150–157, October 2010.

[21] P. Siohan, A. Zeddam, G. Avril, P. Pagani, S. Person, M. Le Bot, E. Chevreau, O. Isson, F. Onado, and X. Mongaboure, "State of the art, application scenario & specific requirement for PLC," 2008.

[22] V. Oksman and S. Galli, "G.hn: The new ITU-T home networking standard," *IEEE Commun. Mag.*, vol. 47, no. 10, pp. 138–145, October 2009.

[23] M. S. Yousuf, S. Z. Rizvi, and M. El-Shafei, "Power line communications: An overview-part II," in *Information and Communication Technologies: From Theory to Applications. ICTTA 2008. 3rd International Conference on*. IEEE, 2008, pp. 1–6.

[24] N. Pavlidou, A. J. H. Vinck, J. Yazdani, and B. Honary, "Power line communications: State of the art and future trends," *IEEE Commun. Mag.*, vol. 41, no. 4, pp. 34–40, April 2003.

[25] O. G. Hooijen, "On the relation between network-topology and power line signal attenuation," in *ISPLC*, vol. 98, 1998, pp. 24–26.

[26] H. Philipps, "Modelling of powerline communication channels," in *Conf. IEEE Int. Symp. on Power Line Communications and Its Applications*, 1999, pp. 14–21.

[27] M. Gotz, M. Rapp, and K. Dostert, "Power line channel characteristics and their effect on communication system design," *IEEE Commun. Mag.*, vol. 42, no. 4, pp. 78–86, Apr 2004.

[28] J. Anatory, N. Theethayi, R. Thottappillil, M. M. Kissaka, and N. H. Mvungi, "An experimental validation for broadband power-line communication (BPLC) model," *IEEE Trans. Power Del.*, vol. 23, no. 3, pp. 1380–1383, July 2008.

[29] L. Lampe and A. H. Vinck, "Cooperative multihop power line communications," in *Power Line Communications and Its Applications (ISPLC), 2012 16th IEEE International Symposium on*. IEEE, 2012, pp. 1–6.

[30] P. Karols, K. Dostert, G. Griepentrog, and S. Huettinger, "Mass transit power traction networks as communication channels," *IEEE J. Sel. Areas Commun.*, vol. 24, no. 7, pp. 1339–1350, 2006.

[31] M. Zimmermann and K. Dostert, "A multi-path signal propagation model for the power line channel in the high frequency range," in *Proceedings of the 3rd International Symposium on Power-line Communications*, 1999, pp. 45–51.

[32] H. Philipps, "Development of a statistical model for powerline communications channels," in *Proceedings of the 4th International Symposium on Power-Line Communications and its Applications (ISPLC)*, 2000, pp. 5–7.

[33] S. Galli and T. C. Banwell, "A deterministic frequency-domain model for the indoor power line transfer function," *IEEE J. Sel. Areas Commun.*, vol. 24, no. 7, pp. 1304–1316, July 2006.

[34] E. Biglieri, "Coding and modulation for a horrible channel," *IEEE Commun. Mag.*, vol. 41, no. 5, pp. 92–98, May 2003.

[35] M. Zimmermann and K. Dostert, "An analysis of the broadband noise scenario in powerline networks," in *International Symposium on Powerline Communications and its Applications (ISPLC2000)*, 2000, pp. 5–7.

[36] L. D. Bert, P. Caldera, D. Schwingshackl, and A. M. Tonello, "On noise modeling for power line communications," in *2011 IEEE International Symposium on Power Line Communications and Its Applications*, April 2011, pp. 283–288.

[37] M. Zimmermann and K. Dostert, "Analysis and modeling of impulsive noise in broadband powerline communications," *IEEE Trans. Electromagn. Compat.*, vol. 44, no. 1, pp. 249–258, 2002.

[38] V. Degardin, M. Lienard, A. Zeddam, F. Gauthier, and P. Degauquel, "Classification and characterization of impulsive noise on indoor powerline used for data communications," *IEEE Trans. Consum. Electron.*, vol. 48, no. 4, pp. 913–918, Nov 2002.

[39] W. Bo, Q. Yinghao, H. Peiwei, and C. Wenhao, "Indoor powerline channel simulation and capacity analysis," 2007.

[40] H. Philipps, "Performance measurements of powerline channels at high frequencies," in *Proceedings of the International Symposium on Power Line Communications and its Applications (ISPLC)*, vol. 229237, 1998.

[41] B. Praho, M. Tlich, P. Pagani, A. Zeddam, and F. Nouvel, "Cognitive detection method of radio frequencies on power line networks," in *ISPLC2010*, March 2010, pp. 225–230.

[42] Y. Gao, E. Liu, O. Bilal, and T. O. Korhonen, "Channel modeling and modem design for broadband powerline communications," in *International Symposium on Power Line Communications, ISPLC'2004, Zaragoza*, 2004.

[43] M. Nakagami, "The m-distribution-A general formula of intensity distribution of rapid fading," *Statistical Method of Radio Propagation*, pp. 3–34, 1960.

[44] Y. Kim, S.-W. Rhee, J.-J. Lee, and S. K. Oh, "BER performance of QPSK-transmitted signal for power line communication under Nakagami-like background noise," *Journal of International Council on Electrical Engineering*, vol. 4, no. 1, pp. 54–58, 2014.

[45] A. Jeffrey and D. Zwillinger, *Table of integrals, series, and products*. Academic Press, 2007.

[46] M. R. Spiegel, *Advanced mathematics*. McGraw-Hill, Incorporated, 1991.

[47] Y. Kim, S. Choi, and H. M. Oh, "BER performance of binary transmitted signal for power line communication under Nakagami-like background noise," in *in Proc. Energy, 1st Int. Conf. Smart Grids, Green Commun. IT Energy-Aware*, vol. 5, 2011, pp. 126–129.

[48] A. Mathur and M. R. Bhatnagar, "PLC performance analysis assuming BPSK modulation over Nakagami-m additive noise," *IEEE Commun. Lett.*, vol. 18, no. 6, pp. 909–912, 2014.

[49] V. B. Balakirsky and A. H. Vinck, "Potential limits on power-line communication over impulsive noise channels," in *Proc. 7th Int. Symp. Power-Line Communications and Its Applications (ISPLC 2003)*, 2003, pp. 32–36.

[50] S. Miyamoto, M. Katayama, and N. Morinaga, "Performance analysis of QAM systems under class A impulsive noise environment," *IEEE Trans. Electromagn. Compat.*, vol. 37, no. 2, pp. 260–267, May 1995.

[51] D. Middleton, "Non-Gaussian noise models in signal processing for telecommunications: New methods an results for class A and class B noise models," *IEEE Trans. Inf. Theory*, vol. 45, no. 4, pp. 1129–1149, 1999.

[52] D. Umehara, H. Yamaguchi, and Y. Morihiro, "Turbo decoding in impulsive noise environment," in *Global Telecommun. Conf., 2004. GLOBECOM '04. IEEE*, vol. 1, Nov 2004, pp. 194–198 Vol.1.

[53] S. Miyamoto, N. Morinaga, and M. Katayama, "Receiver design using the dependence between quadrature components of impulsive radio noise," *Electronics and Communications in Japan (Part I: Communications)*, vol. 78, no. 5, pp. 44–56, 1995.

[54] W. Y. Chen, *Home networking basis: Transmission environments and wired/wireless protocols*. Prentice Hall Professional, 2003.

[55] R. Pighi, M. Franceschini, G. Ferrari, and R. Raheli, "Fundamental performance limits of communications systems impaired by impulse noise," *IEEE Trans. Commun.*, vol. 57, no. 1, pp. 171–182, January 2009.

[56] J. G. Proakis, "Digital communications. 2008," *McGraw-Hill, New York.*

[57] O. G. Hooijen, "On the channel capacity of the residential power circuit used as a digital communication medium," in *Proceedings of IEEE International Symposium on Information Theory*, Jun 1997, pp. 467–.

[58] Y. H. Ma, P. L. So, and E. Gunawan, "Performance analysis of OFDM systems for broadband power line communications under impulsive noise and multipath effects," *IEEE Trans. Power Del.*, vol. 20, no. 2, pp. 674–682, April 2005.

[59] A. Spaulding and D. Middleton, "Optimum reception in an impulsive interference environment–part I: Coherent detection," *IEEE Trans. Inf. Theory*, vol. 25, no. 9, pp. 910–923, 1977.

[60] E. N. Committee, "Radio broadcasting systems, digital audio broadcasting (DAB) to mobile, portable and fixed receivers," *Norme ETSI, Sophia-Antipolis, France, Doc. ETS*, vol. 300, no. 401, pp. 1995–1997, 1995.

[61] E. ETSI, "300 744: Digital video broadcasting (DVB)," *Framing structure, channel coding and modulation for digital terrestrial television*, vol. 1, no. 2, 2004.

[62] A. B. Alamanac, P. Burzigotti, M. Cohen, R. De Gaudenzi, G. Liva, S. Lipp, O. Pulvirenti, L. Roullet, and H. Stadali, "Performance validation of the DVB-SH standard for satellite/terrestrial hybrid mobile broadcasting networks," *IEEE Trans. Broadcast.*, vol. 57, no. 4, pp. 802–825, 2011.

[63] Y. G. Li and G. L. Stuber, *Orthogonal frequency division multiplexing for wireless communications*. Springer Science & Business Media, 2006.

[64] M. Korki, N. Hosseinzadeh, H. L. Vu, T. Moazzeni, and C. H. Foh, "A channel model for power line communication in the smart grid," in *2011 IEEE/PES Power Systems Conference and Exposition*, March 2011, pp. 1–7.

[65] J. A. Bingham, *ADSL, VDSL, and multicarrier modulation*. Wiley New York, 2000.

[66] *Digital video broadcasting (DVB) standard; frame structure channel coding and modulation for a second generation digital transmission system for cable systems (DVB-C2)*. DVB Blue Book A138, Apr. 2009.

[67] I. S. Association, "Ieee standard for broadband over power line networks: Medium access control and physical layer specifications," *IEEE Std 1901*, vol. 2010, pp. 1–1586, 2010.

[68] H. A. Suraweera, C. Chai, J. Shentu, and J. Armstrong, "Analysis of impulse noise mitigation techniques for digital television systems," in *Proc. 8th International OFDM Workshop*. Citeseer, 2003, pp. 172–176.

[69] S. Zhidkov, "Analysis and comparison of several simple impulsive noise mitigation schemes for OFDM receivers," *IEEE Trans. Commun.*, vol. 56, no. 1, pp. 5–9, January 2008.

[70] A. Mengi and A. J. H. Vinck, "Successive impulsive noise suppression in OFDM," in *ISPLC2010*, March 2010, pp. 33–37.

[71] E. Alsusa and K. M. Rabie, "Dynamic peak-based threshold estimation method for mitigating impulsive noise in power-line communication systems," *IEEE Trans. Power Del.*, vol. 28, no. 4, pp. 2201–2208, Oct. 2013.

[72] S. V. Zhidkov, "Impulsive noise suppression in OFDM-based communication systems," *IEEE Trans. Consum. Electron.*, vol. 49, no. 4, pp. 944–948, Nov 2003.

[73] T. Hirakawa, M. Fujii, M. Itami, and K. Itoh, "A study on iterative impulse noise reduction in OFDM signal by recovering time domain samples," in *IEEE International Symposium on Power Line Communications and Its Applications*, 2006, pp. 325–330.

[74] H. Matsuo, D. Umehara, M. Kawai, and Y. Morihiro, "An iterative detection for OFDM over impulsive noise channel," in *Proceedings of the 6th International Symposium on Power-Line Communications and its Applications (ISPLC)*, 2002, pp. 27–29.

[75] H.-M. Oh, Y.-J. Park, S. Choi, J.-J. Lee, and K.-C. Whang, "Mitigation of performance degradation by impulsive noise in LDPC coded OFDM system," in *2006 IEEE International Symposium on Power Line Communications and Its Applications*, 2006, pp. 331–336.

[76] J. Haring and A. H. Vinck, "Coding for impulsive noise channels," *Proc. 2001 IEEE ISPLC*, pp. 103–108, 2001.

[77] H. Nakagawa, D. Umehara, S. Denno, and Y. Morihiro, "A decoding for low density parity check codes over impulsive noise channels," in *Proc. Inter. Symp. PLCs. and Its Appls.*, April 2005, pp. 85–89.

[78] N. Andreadou and F.-N. Pavlidou, "Mitigation of impulsive noise effect on the PLC channel with QC–LDPC codes as the outer coding scheme," *IEEE Trans. Power Del.*, vol. 25, no. 3, pp. 1440–1449, 2010.

[79] J. Haring and A. J. H. Vinck, "Iterative decoding of codes over complex numbers for impulsive noise channels," *IEEE Trans. Inf. Theory*, vol. 49, no. 5, pp. 1251–1260, May 2003.

[80] S. Zhidkov, "On the analysis of OFDM receiver with blanking nonlinearity in impulsive noise channels," in *Proc. Int. Symp. Intell. Signal Process. Commun. Syst.*, Nov 2004, pp. 492–496.

[81] ——, "Performance analysis and optimization of OFDM receiver with blanking nonlinearity in impulsive noise environment," *IEEE Trans. Veh. Technol.*, vol. 55, no. 1, pp. 234–242, Jan 2006.

[82] W. Peterson, T. Birdsall, and W. Fox, "The theory of signal detectability," *Transactions of the IRE professional group on information theory*, vol. 4, no. 4, pp. 171–212, 1954.

[83] G. Ndo, P. Siohan, and M. H. Hamon, "An adaptive procedure for impulsive noise mitigation over power line channels," in *GLOBECOM 2009 - 2009 IEEE Global Telecommun. Conf.*, Nov 2009, pp. 1–6.

[84] ——, "Adaptive noise mitigation in impulsive environment: Application to power-line communications," *IEEE Trans. Power Del.*, vol. 25, no. 2, pp. 647–656, April 2010.

[85] G. Ndo, "Optimization of impulsive noise countering strategies for high data rate communications over indoor powerlines," Ph.D. dissertation, University of Rennes 1, 2010.

[86] K. M. Rabie and E. Alsusa, "Preprocessing-based impulsive noise reduction for power-line communications," *IEEE Trans. Power Del.*, vol. 29, no. 4, pp. 1648–1658, 2014.

[87] ——, "Effective noise cancellation using single-carrier FDMA transmission in power-line channels," *IEEE Trans. Power Del.*, vol. 29, no. 5, pp. 2110–2117, 2014.

[88] ——, "Impulsive noise blanking using quantized PAPR estimates in powerline communications," in *Vehicular Technology Conference (VTC Fall), 2013 IEEE 78th*. IEEE, 2013, pp. 1–5.

[89] ——, "Performance analysis of adaptive hybrid nonlinear preprocessors for impulsive noise mitigation over power-line channels," in *IEEE International Conference on Communications (ICC)*. IEEE, 2015, pp. 728–733.

[90] ——, "On enhancing the performance of the DPTE-based noise cancellation method utilizing the PTS PAPR reduction scheme in PLC systems," in *Power Line Communications and its Applications (ISPLC), 2014 18th IEEE International Symposium on*. IEEE, 2014, pp. 334–339.

[91] E. Alsusa and K. M. Rabie, "Dynamic peak-based threshold estimation method for mitigating impulsive noise in power-line communication systems," *IEEE Trans. Power Del.*, vol. 28, no. 4, pp. 2201–2208, 2013.

[92] C. E. Shannon, "A mathematical theory of communication," *ACM SIGMOBILE Mobile Computing and Communications Review*, vol. 5, no. 1, pp. 3–55, 2001.

[93] D. J. MacKay, *Information theory, inference and learning algorithms*. Cambridge university press, 2003.

[94] C. Berrou, A. Glavieux, and P. Thitimajshima, "Near Shannon limit error-correcting coding and decoding: Turbo-codes. 1," in *Communications, 1993. ICC '93 Geneva. Technical Program, Conference Record, IEEE International Conference on*, vol. 2, May 1993, pp. 1064–1070 vol.2.

[95] D. J. C. MacKay and R. M. Neal, "Near Shannon limit performance of low density parity check codes," *Electronics Letters*, vol. 32, no. 18, pp. 1645–, Aug 1996.

[96] D. J. C. MacKay, "Good error-correcting codes based on very sparse matrices," *IEEE Trans. Inf. Theory*, vol. 45, no. 2, pp. 399–431, Mar 1999.

[97] H. Tang, J. Xu, Y. Kou, S. Lin, and K. Abdel-Ghaffar, "On algebraic construction of Gallager and circulant low-density parity-check codes," *IEEE Trans. Inf. Theory*, vol. 50, no. 6, pp. 1269–1279, June 2004.

[98] D. J. MacKay, "Fountain codes," *IEE Proceedings-Communications*, vol. 152, no. 6, pp. 1062–1068, 2005.

[99] P. G. Farrell, *Essentials of error-control coding*. John Wiley & Sons, 2006.

[100] D. Fertonani and G. Colavolpe, "On reliable communications over channels impaired by bursty impulse noise," *IEEE Trans. Commun.*, vol. 57, no. 7, pp. 2024–2030, July 2009.

[101] R. Gallager, "Low-density parity-check codes," *IRE Transactions on information theory*, vol. 8, no. 1, pp. 21–28, 1962.

[102] X. Hu, E. Eleftheriou, D.-M. Arnold, and A. Dholakia, "Efficient implementations of the sum-product algorithm for decoding LDPC codes," *GLOBECOM '01. IEEE conf.*, vol. 2, pp. 1036–1036E, 2001.

[103] T. J. Richardson and R. L. Urbanke, "The capacity of low-density parity-check codes under message-passing decoding," *IEEE Trans. Inf. Theory*, vol. 47, no. 2, pp. 599–618, Feb 2001.

[104] S.-Y. Chung, G. D. Forney, T. J. Richardson, and R. Urbanke, "On the design of low-density parity-check codes within 0.0045 db of the Shannon limit," *IEEE Commun. Lett.*, vol. 5, no. 2, pp. 58–60, Feb 2001.

[105] M. Eroz, F.-W. Sun, and L.-N. Lee, "DVB-S2 low density parity check codes with near Shannon limit performance," *International Journal of Satellite Communications and Networking*, vol. 22, no. 3, pp. 269–279, 2004.

[106] Z. Zhang, V. Anantharam, M. J. Wainwright, and B. Nikolic, "An efficient 10GBASE-T ethernet LDPC decoder design with low error floors," *IEEE J. Solid-State Circuits*, vol. 45, no. 4, pp. 843–855, 2010.

[107] R. Tanner, "A recursive approach to low complexity codes," *IEEE Trans. Inf. Theory*, vol. 27, no. 5, pp. 533–547, 1981.

[108] S. J. Johnson, *Iterative error correction: Turbo, low-density parity-check and repeat-accumulate codes*. Cambridge University Press, 2009.

[109] J. Fan and Y. Xiao, "A method of counting the number of cycles in LDPC codes," in *Signal Processing, 2006 8th International Conference on*, vol. 3. IEEE, 2006.

[110] Y. Kou, S. Lin, and M. P. Fossorier, "Low-density parity-check codes based on finite geometries: A rediscovery and new results," *IEEE Transactions on Information Theory*, vol. 47, no. 7, pp. 2711–2736, 2001.

[111] X.-Y. Hu, E. Eleftheriou, and D.-M. Arnold, "Regular and irregular progressive edge-growth Tanner graphs," *IEEE Trans. Inf. Theory*, vol. 51, no. 1, pp. 386–398, 2005.

[112] T. Etzion, A. Trachtenberg, and A. Vardy, "Which codes have cycle-free Tanner graphs?" *IEEE Trans. Inf. Theory*, vol. 45, no. 6, pp. 2173–2181, 1999.

[113] J. Chen, A. Dholakia, E. Eleftheriou, M. P. Fossorier, and X.-Y. Hu, "Reduced-complexity decoding of LDPC codes," *IEEE trans. commun.*, vol. 53, no. 8, pp. 1288–1299, 2005.

[114] D. MacKay and R. Neal, "Near Shannon limit performance of low density parity check codes," *E-Lett.*, vol. 33, no. 6, pp. 457–458, Mar 1997.

[115] J. S. Walther, "A unified algorithm for elementary functions," in *Proceedings of the May 18-20, 1971, spring joint computer conference*. ACM, 1971, pp. 379–385.

[116] X. Hu, R. G. Harber, and S. C. Bass, "Expanding the range of convergence of the cordic algorithm," *IEEE Transactions on Computers*, vol. 40, no. 1, pp. 13–21, 1991.

[117] S. ten Brink, "Convergence behavior of iteratively decoded parallel concatenated codes," *IEEE Trans. Commun.*, vol. 49, no. 10, pp. 1727–1737, Oct 2001.

[118] S. Ten Brink, G. Kramer, and A. Ashikhmin, "Design of low-density parity-check codes for modulation and detection," *IEEE Trans. commun.*, vol. 52, no. 4, pp. 670–678, April 2004.

[119] S. Ten Brink, "Designing iterative decoding schemes with the extrinsic information transfer chart," *AEU Int. J. Electron. Commun*, vol. 54, no. 6, pp. 389–398, 2000.

[120] W. Ryan and S. Lin, *Channel codes: Classical and modern*. Cambridge University Press, 2009.

[121] C. Poulliat, M. Fossorier, and D. Declercq, "Design of non binary LDPC codes using their binary image: Algebraic properties," in *2006 IEEE Int. Symp. Inf. Theory*. IEEE, 2006, pp. 93–97.

[122] S.-Y. Li, R. W. Yeung, and N. Cai, "Linear network coding," *IEEE Trans. Inf. Theory*, vol. 49, no. 2, pp. 371–381, 2003.

[123] M. Davey and D. MacKay, "Low density parity check codes over GF(q)," in *Inf. Theory Workshop*, Jun. 1998.

[124] R. A. Carrasco and M. Johnston, *Non-binary error control coding for wireless communication and data storage*. John Wiley & Sons, 2008.

[125] B. Zhou, J. Kang, S. Song, S. Lin, K. Abdel-Ghaffar, and M. Xu, "Construction of non-binary quasi-cyclic LDPC codes by arrays and array dispersions-[transactions papers]," *IEEE Trans. Commun.*, vol. 57, no. 6, 2009.

[126] D. Declercq and M. Fossorier, "Decoding algorithms for nonbinary LDPC codes over GF(q)," *IEEE Trans. Commun.*, vol. 55, no. 4, pp. 633–643, 2007.

[127] G. J. Byers and F. Takawira, "Fourier transform decoding of non-binary LDPC codes," in *Telecommun. Networks and Apps. Conf.*, 2004.

[128] M. Beermann, E. Monro, L. Schmalen, and P. Vary, "High speed decoding of non-binary irregular LDPC codes using gpus," in *Signal Process. Systems (SiPS*, Oct. 2013.

[129] H. Holma and A. Toskala, *WCDMA for UMTS: Radio access for third generation mobile communications*. John Wiley & sons, 2005.

[130] E. ETSI, "Digital video broadcasting (DVB); interaction channel for satellite distribution systems," *ETSI EN*, vol. 301, p. 790, 2005.

[131] L. Bahl, J. Cocke, F. Jelinek, and J. Raviv, "Optimal decoding of linear codes for minimizing symbol error rate," *IEEE Trans. Inf. Theory*, vol. 20, no. 2, pp. 284–287, Mar 1974.

[132] S. Benedetto, D. Divsalar, G. Montorsi, and F. Pollara, "A soft-input soft-output maximum a posteriori (MAP) module to decode parallel and serial concatenated codes," *TDA progress report*, vol. 42, no. 127, pp. 1–20, 1996.

[133] P. Robertson, E. Villebrun, and P. Hoeher, "A comparison of optimal and sub-optimal MAP decoding algorithms operating in the log domain," in *Communications, 1995. ICC'95 Seattle,'Gateway to Globalization', 1995 IEEE International Conference on*, vol. 2. IEEE, 1995, pp. 1009–1013.

[134] M. R. Soleymani, Y. Gao, and U. Vilaipornsawai, *Turbo coding for satellite and wireless communications*. Springer Science & Business Media, 2006, vol. 702.

[135] T. L. L. Hanzo and B. Yeap, *Turbo coding, turbo equalisation and spacetime coding*. Chichester, UK: Wiley, 2002.

[136] S. Benedetto and G. Montorsi, "Unveiling turbo codes: Some results on parallel concatenated coding schemes," *IEEE Trans. Inf. Theory*, vol. 42, no. 2, pp. 409–428, Mar 1996.

[137] P. Frenger, P. Orten, and T. Ottosson, "Convolutional codes with optimum distance spectrum," *IEEE Commun. Lett.*, vol. 3, no. 11, pp. 317–319, 1999.

[138] E. K. Hall and S. G. Wilson, "Design and analysis of turbo codes on Rayleigh fading channels," *IEEE J. Sel. Areas Commun.*, vol. 16, no. 2, pp. 160–174, Feb 1998.

[139] X.-Y. Hu, E. Eleftheriou, D.-M. Arnold, and A. Dholakia, "Efficient implementations of the sum-product algorithm for decoding ldpc codes," in *Global Telecommun. Conf., 2001. GLOBECOM'01. IEEE*, vol. 2. IEEE, 2001, pp. 1036–1036E.

[140] M. Karkooti, P. Radosavljevic, and J. R. Cavallaro, "Configurable ldpc decoder architectures for regular and irregular codes," *J. Signal Process. Syst.*, vol. 53, no. 1-2, pp. 73–88, 2008.

[141] H. R. Sadjadpour, "Maximum a posteriori decoding algorithms for turbo codes," in *PROC SPIE INT SOC OPT ENG*, vol. 4045, 2000, pp. 73–83.

[142] E. Arikan, "Channel polarization: A method for constructing capacity-achieving codes for symmetric binary-input memoryless channels," *IEEE Transactions on Information Theory*, vol. 55, no. 7, pp. 3051–3073, July 2009.

[143] R. M. Pyndiah, "Near-optimum decoding of product codes: Block turbo codes," *IEEE Transactions on communications*, vol. 46, no. 8, pp. 1003–1010, 1998.

[144] Y. Wu, P. A. Chou, and S.-Y. Kung, "Information exchange in wireless networks with network coding and physical-layer broadcast," MSR-TR-2004, Tech. Rep., 2005.

[145] R. H. Y. Louie, Y. Li, and B. Vucetic, "Practical physical layer network coding for two-way relay channels: Performance analysis and comparison," *IEEE Trans. Wireless Commun.*, vol. 9, no. 2, pp. 764–777, February 2010.

[146] S. Zhang, S. C. Liew, and P. P. Lam, "Hot topic: Physical-layer network coding," in *Proceedings of the 12th annual international conference on Mobile computing and networking*. ACM, 2006, pp. 358–365.

[147] P. Popovski and H. Yomo, "The anti-packets can increase the achievable throughput of a wireless multi-hop network," in *Communications, 2006. ICC'06. IEEE International Conference on*, vol. 9. IEEE, 2006, pp. 3885–3890.

[148] J. N. Laneman, G. W. Wornell, and D. N. Tse, "An efficient protocol for realizing cooperative diversity in wireless networks," in *Information Theory, 2001. Proceedings. 2001 IEEE International Symposium on*. IEEE, 2001, p. 294.

[149] T. Koike-Akino, P. Popovski, and V. Tarokh, "Optimized constellations for two-way wireless relaying with physical network coding," *IEEE J. Sel. Areas Commun.*, vol. 27, no. 5, 2009.

[150] M. Ju and I.-M. Kim, "Error performance analysis of BPSK modulation in physical-layer network-coded bidirectional relay networks," *IEEE trans. Commun.*, vol. 58, no. 10, pp. 2770–2775, 2010.

[151] S. Zhang and S.-C. Liew, "Channel coding and decoding in a relay system operated with physical-layer network coding," *IEEE J. Sel. Areas Commun.*, vol. 27, no. 5, 2009.

[152] T. Koike-Akino, P. Popovski, and V. Tarokh, "Denoising maps and constellations for wireless network coding in two-way relaying systems," in *IEEE GLOBECOM 2008.* IEEE, 2008, pp. 1–5.

[153] Z. Shengli, S.-C. Liew, and P. P. Lam, "Physical layer network coding," *arXiv preprint arXiv:0704.2475*, 2007.

[154] T. Huang, T. Yang, J. Yuan, and I. Land, "Design of irregular repeat-accumulate coded physical-layer network coding for Gaussian two-way relay channels," *IEEE Trans. Commun.*, vol. 61, no. 3, pp. 897–909, 2013.

[155] M. Mirahmadi, A. Al-Dweik, and A. Shami, "BER reduction of OFDM based broadband communication systems over multipath channels with impulsive noise," *IEEE Trans. Commun.*, vol. 61, no. 11, pp. 4602–4615, Nov. 2013.

[156] J. Anatory and N. Theethayi, *Broadband power-line communications systems: Theory & applications*. wit press, 2010.

[157] P. Billingsley, *Probability and measure*. John Wiley & Sons, 2008.

[158] M. K. Simon, *Probability distributions involving Gaussian random variables: A handbook for engineers and scientists*. Springer Science & Business Media, 2007.

[159] M. K. Simon and M.-S. Alouini, *Digital communication over fading channels*. John Wiley & Sons, 2005, vol. 95.

[160] R. V. Hogg and E. A. Tanis, *Probability and statistical inference, 6th Edition*. Macmillan New York, 2001.

[161] A. Papoulis and S. U. Pillai, *Probability, random variables, and stochastic processes*. Tata McGraw-Hill Education, 2002.

[162] J. Dutka, "The early history of the factorial function," *Archive for History of Exact Sciences*, vol. 43, no. 3, pp. 225–249, 1991.

[163] A. Mathur, M. R. Bhatnagar, and B. K. Panigrahi, "Performance evaluation of PLC under the combined effect of background and impulsive noises," *IEEE Commun. Lett.*, vol. 19, no. 7, pp. 1117–1120, July 2015.

[164] T. J. Richardson and R. L. Urbanke, "The capacity of low-density parity-check codes under message-passing decoding," *IEEE Transactions on Information Theory*, vol. 47, no. 2, pp. 599–618, Feb 2001.

[165] D. Divsalar, S. Dolinar, and F. Pollara, "Iterative turbo decoder analysis based on density evolution," *IEEE J. Sel. Areas Commun.*, vol. 19, no. 5, pp. 891–907, May 2001.

[166] K. Fukunaga and T. E. Flick, "Estimation of the parameters of a gaussian mixture using the method of moments," *IEEE Transactions on Pattern Analysis and Machine Intelligence*, no. 4, pp. 410–416, 1983.